PhD thesis

Submitted in fulfillment of the requirements for the degree of Doctor of Philosophy in optics, photonics and image processing

Aix-Marseille Université

Superresolution fluorescence microscopy with structured illumination

Awoke Negash

Defended on 29$^{\text{th}}$ of November 2017 in the presence of jury members:

Rainer HEINTZMANN	President	Friedrich-Schiller-University Jena, Germany
Jerôme MERTZ	Reviewer	Boston University, USA
Chrysanthe PREZA	Reviewer	The University of Memphis, USA
Stefan WIESER	Examiner	ICFO, Barcelona, Spain
Anne SENTENAC	Examiner	Aix-Marseille Université, France
Hugues GIOVANNINI	Thesis director	Aix-Marseille Université, France
Pablo LOZA-ALVAREZ	Thesis co-director	ICFO, Barcelona, Spain

Discipline: *Optique, photonique et traitement d'image*
École Doctorale: *Physique et sciences de la matière*, ED352

Acknowledgment

First of all, I would like to express my deepest appreciation for my director Prof. Huges Giovannini for his guidance and persistent help. I would like to thank Anne Sentenac for her continuous support and critics. She has always been interested in discussing and developing research ideas which allowed me to advance in my work. I would like to thank Kamal Belkebir and Patrick C. Chaumet for their invaluable discussion and significant help in solving some bottlenecks particularly in the computational part of the thesis. I would like to thank Marc Allain for the multiple constructive discussions throughout my work and Thomas Mangeat for your invaluable help in the experimental setup and data acquisition. Thank you for your great help and interesting discussions during my two months stay in your lab at LBCMCP, Toulouse.

I would also like to thank my second supervisor, Pablo Loza-Alvarez, for his positive comments and constructive discussions in the work during my stay at ICFO. I am particularly grateful to Omar Olarte at ICFO for all the guidance and support that he provided for my work at ICFO. His constant support and devotion to my thesis were amazing. I would not forget to thank all the members of SLN facility at ICFO. The time I spent with them in ICFO was productive. Interacting with them was inspiring and helpful for the evaluation and understanding of the experimental results.

I would like to thank Dam-bé L. Douti for the great discussions on many scientific aspects as well as for the instructive and humorous chats we had. I am grateful for Simon Labouesse for the interesting discussions on most common areas of our thesis and enjoyable times we spent together.

For the unforgettable social moments in Marseille, I would like to thank my friends Hassan Saleh, Luisa Neves and Nicolas Cochinaire. The time I spent in the last three years with you was enjoyable. I would like to thank many good friends at Institut Fresnel and at downtown Marseille for many unforgettable memories.

Most of all, I would like to thank my parents for all the unpayable things you did to me. My father's work ethic has always been an inspiration for me. My mother's care, support and encouragment was unlimited and she makes the difficult times look easy. My sisters and brothers, thank you for your constant encouragement and appreciation. Long live!

iii

Contents

List of Figures

Résumé (en langue française)

Microscopie de fluorescence super-résolution

La microscopie de fluorescence optique est l'un des outils les plus puissants pour étudier les structures cellulaires et les événements moléculaires au niveau subcellulaire. Son principe est basé sur l'imagerie de l'émission de l'échantillon marqué avec des fluorophores spécifiques lorsqu'il est éclairé par une lumière d'excitation. La résolution d'une image conventionnelle du microscope à fluorescence est cependant limitée par la diffraction, où la limite de résolution est définie par le critère de Rayleigh[1], qui atteint une résolution latérale de 200nm et axiale de 500nm[2]. Récemment, de nombreuses techniques de microscopie de fluorescence àsuper-résolution ont été développées, ce qui permis d'observer de nombreuses structures biologiques au-delà de la limite de diffraction. Les techniques principales incluent STED[3], STORM / PALM et la microscopie d'illumination structurée (SIM). La plupart de ces méthodes ont donné une amélioration de la résolution spatiale dans les trois dimensions.

De la SIM harmonique à la SIM speckle

Depuis l'introduction de la SIM, à la fin des années 1990[4], de multiples chercheurs ont démontré que la SIM peut améliorer la résolution d'un facteur deux par rapport à la microscopie de fluorescence conventionnelle.[5–8] Le principe de la SIM est basé sur l'utilisation d'une illumination structurés qui module les fréquences spatiales élevées de l'échantillon dans la région observable du microscope. L'amélioration de la résolution dépend fortement de la technique de reconstruction, qui rétablit les fréquences spatiales élevées de l'échantillon dans sa position d'origine. Les reconstructions SIM communes nécessitent une connaissance parfaite du modèle d'illumination. Cependant, contrôler parfaitement les structurées l'illuminations sur le plan d'échantillonnage n'est pas facile dans les implémentations expérimentales, ce qui rend l'éxécution expérimentale très technique. La reconstruction des images de la SIM en supposant que une parfaite connaissance des structurées d'illuminations peut, par conséquent, introduire des artefacts sur l'échantillon estimé en raison de déformation de l'illumination structurée qui peuvent se produire lors des acquisitions expérimentales. C'est un inconvénient, à moins que les aberrations causées par l'échantillon et les composants optiques ne soient négligeables. Pour remédier à cet inconvénient de la SIM, une stratégie de reconstruction qui est indépendante de l'illumination est souhaitable, ce qu'on appelle «blind-SIM».

Le développement de stratégies de reconstruction blind-SIM est également une étape importante pour étendre la SIM standard à la microscopie d'speckle qui n'ont pas besoin de contrôle, contrairement aux modèles de grille harmonique. L'utilisation de la microscopie d'speckle simplifie de façon significative la mise en œuvre expérimentale de le SIM avec une performance équivalente à le SIM standard en terme de résolution.

Stratégies de reconstruction «Blind-SIM»

Dans un microscope classique de fluorescence en plein champ, l'échantillon est illuminé par un faisceau d'intensité uniforme et la fluorescence émise est détectée dans le plan image d'un objectif de microscope. En régime linéaire, l'intensité lumineuse dans le plan image M est modélisée par une convolution de la densité de fluorescence de l'échantillon ρ par la PSF (Point Spread Function en anglais) h. Dans le cas d'une illumination speckle, l'intensité lumineuse dans le plan image pourra être modélisée comme dans la Ref.[7],

$$M_l = (I_l \rho) * h, \tag{1}$$

où $*$ désigne le produit de convolution, I_l la $l^{\text{ième}}$ intensité de l'illumination speckle et M_l l'intensité dans le plan image issue de le $l^{\text{ième}}$ illumination.

Afin d'appliquer une méthode d'inversion pour le traitement des données définissons l'erreur résuduielle r_l, pour une densité de fluorophores ρ et une excitation I_l, telle que:

$$r_l = M_l - (\rho I_l) * h. \tag{2}$$

Le principe de base de la minimisation blind-SIM est d'évaluer deux séquences relatives à la densité de fluorophores $\{\rho_n\}$ et à l'illuminations $\{I_{l,n}\}$, telle que on minimise

$$F\left(\rho, (I_l)_{l=1,\dots,L}\right) = W \sum_{l=1}^{L} ||r_l||_{\Gamma}^2, \tag{3}$$

Γ étant le (sub-set) de $\mathbb{R}^3$ où M_l a été mesuré et W le facteur de normalisation

$$W = \frac{1}{\sum_{l=1}^{L} \|M_l\|_{\Gamma}^2}. \tag{4}$$

Considérant les L images, l'objectif est de reconstruire la densité de fluorescence et les L intensités, avec $L+1$ inconnues. Le système est alors très sous déterminé. Pour éviter cela, nous allons poser comme condition que la somme des intensités incidentes soit relativement homogène sur l'échantillon. Cette condition exprime expérimentalement que l'échantillon est uniformémenet illuminé en moyenne. Soit:

$$\sum_{l=1}^{L} I_l \quad \approx \quad L I_0, \tag{5}$$

où I_0 est constant dans le plan de l'échantillon. Cette condition d'homogénéité permet de réduire le nombre d'inconnues. La dernière intensité I_L est supposée être égale à

$$I_L = L I_0 - \sum_{l=1}^{L-1} I_l, \tag{6}$$

donc, l'intensité dans le plan image issue de l'illumination peut être représentée, à partir des Eqs. (1) et (6), par

$$M_L = \left[\left(LI_0 - \sum_{l=1}^{L-1} I_l \right) \rho \right] * h, \tag{7}$$

où on peut remarquer l'absence du terme I_L.

Dans un blind-SIM joint, la densité de fluorescence et les $L-1$ intensités sont conjointement estimées de manière itérative afin de minimiser la fonctiont de coût,

$$F(\rho, I_{l=1,\dots,L-1}) = W \sum_{l=1}^{L-1} \|M_l - (I_l\rho) * h\|^2 + \left\| M_L - \left[\left(LI_0 - W \sum_{l=1}^{L-1} I_l \right) \rho \right] * h \right\|^2,$$

où $\|.\|$ représente la norme euclidienne dans l'espace image.

La densité de fluorophores ρ et les intensités I_l sont réelles et positives.

$$\begin{aligned} I_l &= i_l^2, \\ \rho &= \xi^2. \end{aligned} \tag{8}$$

Nous avons dévelopé différentes méthodes de reconstruction 3D du blind-SIM. La première, la blind-SIM joint, reconstruit simultanément la densité de fluorescence et les intensités d'illumination à partir d'une contrainte positive. Pour un calcul rapide de l'inversion, nous avons développé la deuxième technique appelée blind-SIM déconvolution séparée (blind-SIM-SD) qui ne reconstruit pas explicitement les illuminations. En introduisant la variable auxiliaire $q_l = \rho I_l$ pour $l = 1, \cdots, L$, le problème de la blind-SIM peut être définit comme

$$\mathcal{F}(q_{l=1,\cdots,L}) = W_l \sum_{l=1}^{L} \|M_l - q_l * h\|^2. \tag{9}$$

Une fois les q_l connus, l'indétermination sur ρ et I_l est levée en utilisant la contrainte d'homogénéité sur l'illumination $\sum_{l=1}^{L} I_l = I_0$ afin de former $\rho = (\sum_{l=1}^{L} q_l)/I_0$. La minimisation de $\mathcal{F}$ peut être faite en déconvoluant séparement les images SIM de chaques illuminations sous la contrainte de positivité, et accélérant de manière significative la procédure d'inversion.

L'autre technique de reconstruction, appliquée spécialement aux données SIM harmonique, est la blind-SIM filtrée. Son principe est de confiner l'intensité d'illumination dans une bande fréquencielle prédéterminée selon les pics de Fourier. Pour le faire nous introduisons un masque dans le domaine de Fourier, typiquement une gaussienne centrée autour des pics.

Illustration des reconstructions

Nous avons démontré l'efficacité de la performance de ces techniques de reconstruction par le biais des données synthétiques et expérimentales. Nous présentons et examinons les résolutions en SIM sous des illuminations de type harmonique et speckle en utilisant le même d'échantillon. Pour ce faire, nous avons enregistré des images brutes du même échantillon de filaments de vimentin à l'aide d'illuminations grille et speckle, en utilisant alternativement la configuration SIM de l'illumination
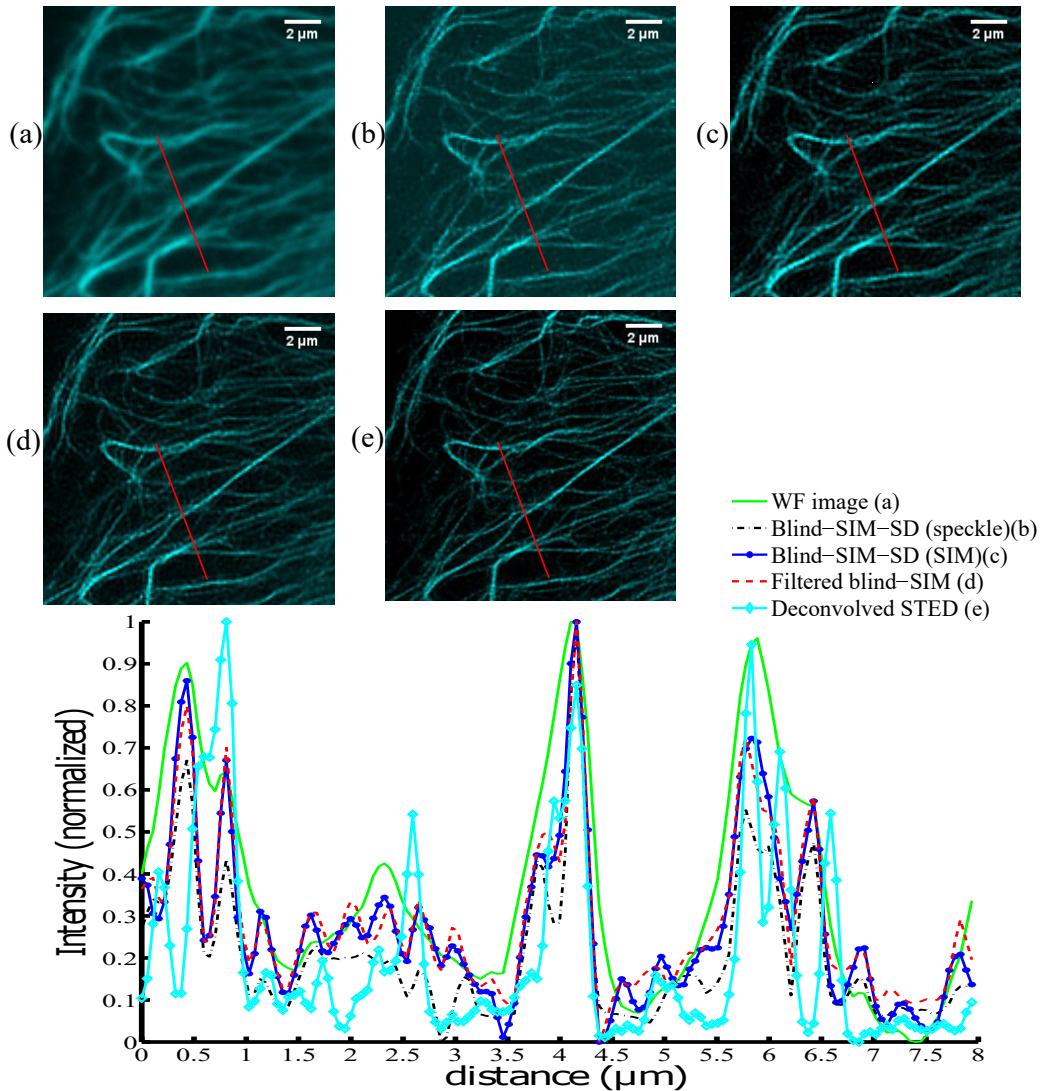
Figure 1 : *Reconstruction Blind-SIM du SIM speckle et grille. (a) Image champ large. (b) Blind-SIM-SD (speckle). (c) Blind-SIM-SD (harmonique). (d) blind-SIM filtrée. (e) STED déconvolué.*

grille/speckle à base de SLM. Nous utilisons 30 modèles harmoniques (6 orientations et 5 phases) et 800 speckles. L'échantillon est excité à 561nm de longueur d'onde et émet à 650nm. Nous utilison un objectif à huile de grandissement x60 et ouverture NA = 1.4. Pour référence, l'image champ large est illustrée dans la Figure 1(a). Le blind-SIMSD sur speckle SIM images brutes (b), le blind-SIM-SD sur des images SIM harmonique (c) et le filtrée blind-SIM sur les images SIM harmonique (d) ont tous des résolutions impressionnantes, en comparaison avec l'image champ large. Pour une comparaison équitable, l'image STED déconvolué du même échantillon est présentée en (e). Le blind-SIM filtré offre une résolution très impressionnante qui est comparable à la résolution STED déconvolué. Le blind-SIM-SD speckle est légèrement meilleur que le blind SIM-SD des données SIM harmoniques. Cela vient du fait que les speckles d'illumination ont plus de sparsité

par rapport à ceux des grilles. La super-résolution de la reconstruction des blind-SIM-SD résulte de l'activation plus fréquente de la contrainte de positivité sur les images speckle. Cependant, au contraire, les grilles satisfont mieux la contrainte d'homogénéité que les speckles. Par conséquent, la différence de résolution entre les deux n'est pas significative. Surtout, le blind-SIM filtré donne la meilleure résolution, comparable à STED, puisqu'il utilise des informations sur les motifs ainsi que la contrainte de positivité. D'autre part, en plus de l'amélioration de la résolution, la SIM speckle a un avantage sur la SIM en raison de sa simplicité pour la mise en œuvre expérimentale.

Réduction le problème de «out-of-focus» en microscopie à fluorescence

En microscopie à fluorescence, l'image focalisée d'un échantillon de fluorescence 3D souffre d'un flou de «out-of-focus» en raison de la diffraction axiale de la lumière. Cette fluorescence out-of-focus dégrade le contraste de l'image et peut entraver la visualisation des caractéristiques de l'échantillon. Afin de s'attaquer à ce problème, nous introduisons brièvement la stratégie de réduction out-of-focus basée sur la convolution informatique. Le principe de la technique dépend de la convolution des images bidimensionnelles du plan focal en utilisant des PSF tridimensionnelles, que nous appelons technique de convolution slice 3D. La Figure 2(a-d) montre l'objet au plan focal, son image de champ large, la déconvolution 2D de l'image champ large et la déconvolution 3D de la même image champ large, respectivement. Dans la Figure 2(e), nous affichons la reconstruction pour les plans entourant le plan focal. Nous observons qu'une fluorescence out-of-focus a été détectée vers ces plans. La fonction de blurring des plans de out-of-focus correspondants est également présentée en dessous de chaque estimation hors foyer. En comparant la Figure 2(c) et (d), on constate que la déconvolution 3D améliore considérablement la résolution et le contraste de l'image 2D.

En conclusion, la convolution tridimensionnelle devrait être préférée à la convolution bidimensionnelle, même lorsque les données sont limitées à une seule image plane. Elle diminue la fluorescence out-of-focus et améliore considérablement le contraste et la résolution. Elle s'agit d'un simple traitement de données qui peut être utilisé sur la plupart des configurations de microscopie. Elle a été testé à la fois sur des données synthétiques et expérimentales, bien que seules les données synthétiques soient présentées dans cette section.

Une autre façon de réduire les problèmes de out-of-focus est d'utiliser des techniques de microscopie telles que la microscopie à nappe de lumière. Le microscope à nappe de lumière dècouple le chemin d'illumination du chemin de détection et utilise une nappe de lumière pour éclairer seulement une partie de l'échantillon. Cela réduit le photobleaching de l'échantillon et le out-of-focus au plan d'imagerie. La résolution des images de nappe de lumière est cependant limitée par la diffraction. Inspiré du gain de résolution dans la théorie de la microscopie d'illumination grille/speckle, nous avons introduit l'illumination structurée à la microscopie à nappe de lumière. Cela aide à combiner les avantages des deux approches avec peu de coût de complexité lors de la mise en œuvre physique. Nous avons développé le microscope iSPIM à partir de zéro et nous avons

Synthetic microspheres
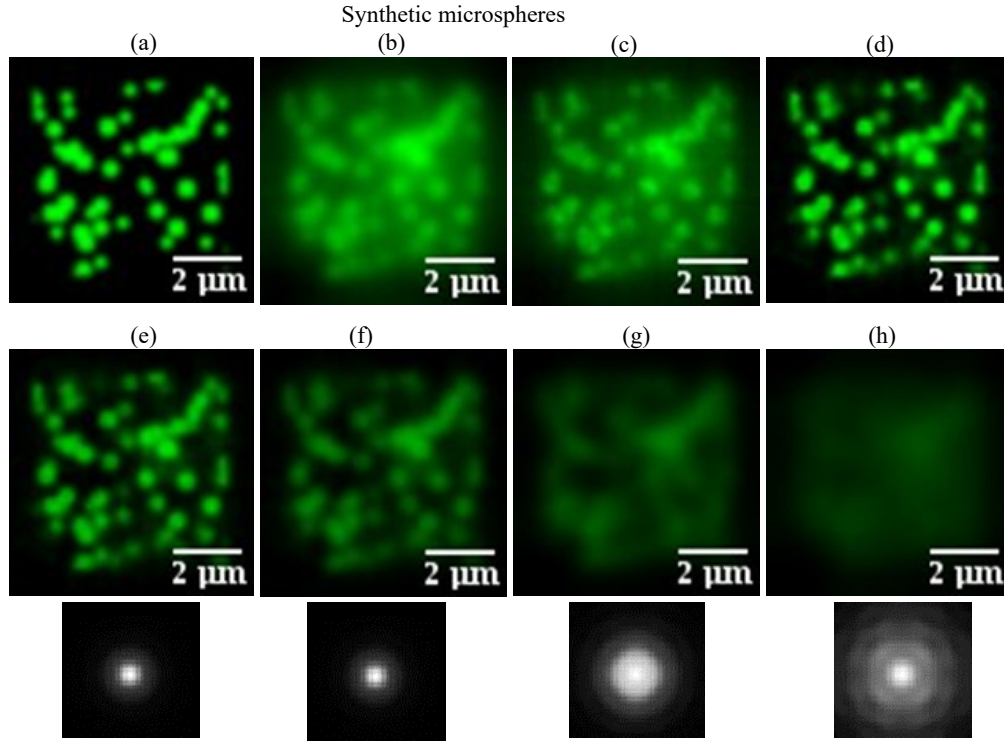
Figure 2 : *Déconvolution 3D basée sur les données synthétiques. (a) Objet au niveau focal d'un échantillon 3D épais. (b) Image de l'objet. (c) Déconvolution 2D. (d) Déconvolution 3D. (e) - (h) Contributions out-of-focus à une distance de 185nm, 370nm, 555nm et 925nm au-dessus du plan focal respectivement. La fonction de blurring respectif de chaque plan out-of-focus est affichée (en bas).*

introduit un éclairage structuré. La configuration permet de combiner les avantages des techniques de microscopie SIM et de nappe de lumière avec peu de coûts de complexité lors de la mise en œuvre physique. Dans la SIM standard, les orientations de la grille peuvent être tournées en faisant simplement tourner les réseaux la diffraction dans les configurations SIM basées sur les réasaux. C'est parce que le réseau doit être maintenu dans une orientation fixe pour avoir une nappe de lumière. La configuration est à l'étude pour avoir des illuminations structurées dans de multiples directions et développer en microscopie d'éclairage à double plan sélectif (dSPIM) combinée avec un microscope inversé. Ces développements sont cependant difficiles et dépassent la portée de ce projet. Des recherches futures sur les développements ultérieurs sont recommandées en tant que perspective.

Conclusion

Dans cette thèse, nous avons développé des stratégies tridimensionnelles de reconstruction de SIM qui évaluent itérativement l'échantillon sans nécessiter une connaissance parfaite des illuminations individuelles. Les stratégies de reconstruction sont appliquées à la fois sur la SIM grille et la

microscopie de speckle (SIM speckle). SIM speckle est avantageux pour simplifier considérablement la complexité des configurations expérimentales SIM. En plus d'améliorer la résolution des données du SIM grille/speckle à l'aide d'algorithmes de blind-SIM, nous avons également développé une technique de calcul simple qui supprime la lumière out-of-focus dans les images en champ large. Le principe de la technique consiste à reconstruire des images bidimensionnelles à l'aide d'une PSF tridimensionnelle. De plus, nous avons pratiquement mis en place une microscope qui combine l'illumination structurée avec la microscopie à nappe de lumière afin de bénéficier des avantages des deux techniques.

Introduction

The phenomenon of fluorescence was investigated in the 1800s and early 1900s[9]. Since then, multiple optical fluorescence microscopes have been developed and became extremely useful instruments in biological and medical laboratories. Currently, optical fluorescence microscopy is one of the most powerful techniques which is an indispensable tool to study cellular structures and molecular events at the subcellular level. Its principle is based on imaging the emission from the sample labeled with specific markers illuminated with an excitation light. The resolution of a conventional fluorescence microscope image is, however, diffraction limited, about a spatial resolution of 200nm lateral and 500nm axial[2]. Recently many super-resolution fluorescence microscopy techniques have been developed which allow the observation of biological structures beyond the diffraction limit, each technique varying in their principle, application and implementation. The major techniques include stimulated emission and depletion (STED)[3], stochastic optical reconstruction microscopy (STORM)/photoactivated localization microscopy (PALM)[10–13] and structured illumination microscopy (SIM)[6]. STED and PALM/STORM have yielded an order of magnitude improvement in spatial resolution in all three dimensions over conventional light microscopy. On the other hand, linear SIM can only double the resolution twice the diffraction limit[5–8] in three dimensions but can be done with standard fluorophores contrary to STED and PALM/STORM. Currently, SIM is playing a significant role in investigating cellular structures even in multicolor and live cell superresolution imaging[14–17]. SIM consists in illuminating the sample with a light grid in order to downmodulate the high spatial frequencies of the sample into the observable frequency region of the microscope. The resolution enhancement is highly dependent on the reconstruction technique which restores the high spatial frequency of the sample to its original position. Linear SIM can provide a lateral resolution of about $100nm$ and axial resolution of about $300nm$[16,17]. Common SIM reconstructions require the knowledge of the illumination pattern. However, to perfectly control the harmonic illumination patterns on the sample plane is not easy in experimental implementations. This makes the experimental implementation very technical. Pattern distortion stems from the optical components of the setup as well as from the sample itself, particularly in thick samples. Reconstructing SIM images using an inaccurate knowledge of the illumination intensity introduce artifacts on the reconstruction. To tackle this drawback, reconstruction strategies that do not require the knowledge of the illumination pattern are currently under study. These approaches allow the extension of the standard SIM to speckle illumination microscopy which uses random unknown speckle patterns. The speckle patterns are much easier to generate than the harmonic grids and require no control at all. The only requirement on the speckle illuminations is that the

temporal average of all the speckle illuminations is homogeneous over the sample. Using speckle illumination microscopy significantly simplifies the experimental implementation of SIM.

This thesis is dedicated to the study of SIM in particular speckle SIM, and to the development of blind-SIM reconstruction techniques which do not require the control of the illuminations. Blind-SIM algorithms have been developed in simplified two-dimensional configurations during the thesis of Mudry [18]. One objective of my thesis is to extend the principle of blind-SIM reconstruction to the three dimensions and apply it to speckle illumination microscopy. To this aim, we have just extended the pre-existing 2D joint blind-SIM algorithm into 3D. Then we have introduced a faster and simpler blind-SIM algorithm (blind-SIM-SD) which reconstructs the product of the illumination and the sample (Contrary to the joint blind-SIM which inverts the sample and the illuminations simultaneously). We have observed that the resolution obtained by blind-SIM-SD highly depends on the sparsity of the low-resolution images. The sparsity of the low-resolution images emanates from either sparsity of the illumination itself or the nature of the sample. For classical-SIM images, however, incorporating some information about illumination patterns is valuable. Therefore, the 3D positive filtered blind-SIM is developed which confines the iterative estimation of the illuminations in the vicinity of the Fourier peaks (using carefully designed Fourier filter masks) in the reciprocal space. The filtered blind-SIM reconstruction strategy is powerful in estimating the sample under even strong distortions of the illumination pattern.

Another contribution of this thesis is related to improving the contrast of the image. A simple computational technique which is based on reconstructing 2D data with 3D PSF is developed using blind-SIM-SD. This technique can be generally applied to any widefield image and significantly enhances the contrast of the image.

The last part of the thesis aims at introducing structured illumination into light sheet microscopy. Light sheet microscopy decreases the out of focus blur of images by illuminating the sample with a light sheet. The lateral resolution of light sheet images is still diffraction limited. We have developed a structured illumination light sheet microscope setup which combines the functionalities of SIM and light sheet microscopy. The development of the setup has been practically challenging and the structured illumination is limited only in one direction. Test results have been demonstrated using our developed reconstruction strategies, and the challenges and limitations are highlighted as a perspective.

The thesis is divided into six chapters. In the first chapter, we introduce the basics of fluorescence microscopy, briefly review the modern superresolution microscopy techniques, and explain the principles of structured illumination microscopy (SIM).

In the second chapter, the three-dimensional blind-SIM (blind-SIM-3D) reconstruction techniques that provide optical sectioning and transverse resolution improvement without requiring the control of the illuminations is presented. The principle of blind-SIM and the developed reconstruction schemes (namely, joint blind-SIM, blind-SIM Separate Deconvolution (blind-SIM-SD) and filtered blind-SIM) are explained demonstrating the interest of these approaches on synthetic data mimicking that of the standard fluorescence microscopes. The imaging mechanisms of three-dimensional microscopy and the proposed reconstruction schemes are investigated.

In the third chapter, the practical implementation of speckle illumination microscopy is presented. The blind-SIM techniques are demonstrated on multiple biological samples and resolutions

are investigated. STED images are used to compare the limits of 3D blind-SIM. The speckle SIM superresolution microscopy is also compared with the classical SIM results reconstructed through blind-SIM and filtered blind-SIM methods.

In the fourth chapter, some advanced perspectives of speckle illumination microscopy are highlighted using synthetic simulations. First, an attempt to obtain isotropic resolution (in three dimensions) using mirror-based speckle illumination microscopy is investigated. Second, the two-photon speckle illumination microscopy is investigated. The resolution improvements related to the nature of two-photon speckle illuminations is studied and characterized compared to single photon speckle illumination microscopy.

In the fifth chapter, we presented a computational technique which removes the out of focus blur in general widefield images. The in-focus image of a 3D fluorescence sample suffers from out-of-focus blur due to the axially spreading light. This out of focus fluorescence degrades the contrast of the image and may hinder the visualization of the in-focus sample features. The principle of our out of focus removal technique consists in deconvolving the image of the sample at the focal plane using a three-dimensional PSF.

In the last chapter, we have presented a proof of concept of structured illumination light sheet microscopy which enables to obtain optical sectioning (from the thin light sheet) in the axial direction and improves the two-dimensional resolution (from structured illumination). Developing this has been experimentally challenging and the structured illumination pattern is limited to a single dimension.

Fluorescence microscopy towards superresolution

Contents

The interest of this chapter is to recall the basics of fluorescence microscopy and to review the modern superresolution imaging techniques in microscopy. Resolution and contrast, the two main quality measures of an optical microscope image, are briefly discussed. Next, we present a short review of confocal and multiphoton imaging, stimulated emission depletion (STED) microscopy and stochastic reconstruction microscopy (STORM)/photo-activated localization microscopy (PALM). Then, the principles of structured illumination microscopy (SIM), its experimental implementation and its spatial resolution is discussed. Finally, the chapter is concluded with a preview of the new candidate of classical SIM which is speckle illumination microscopy.

1.1 Principle of fluorescence microscopy

1.1.1 Introduction

Fluorescence microscopy is a powerful imaging technique for biological applications. It allows investigating cellular structures and micro-organisms in three-dimensions under non-invasive conditions by assigning a fluorophore to a specific site of the biological sample. The invention of green fluorescence protein (GFP) has a huge contribution on this aspect. A Nobel Prize in chemistry is awarded in 2008 for Japanese scientist, Osamu Shimomura, and two American scientists, Martin Chalfie and Robert Y. Tsien for the development of GFP[19]. In addition to GFP, a large number of different dyes are available ranging from UV to near infrared region. The introduction of varieties of specific markers has brought about unprecedented advances in biological applications of fluorescence microscopy. Today, it is possible to label proteins with fluorescent dyes of high contrast, sensitivity, and specificity[20,21]. The fluorophores, however, need special precautions in preparation and usage. They have limited stability and they bleach with excessive illumination and produce phototoxicity.
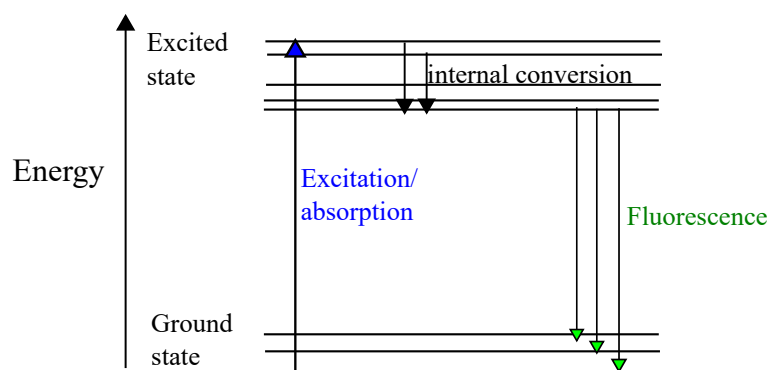
Figure 1.1 : *Simplified Jablonski diagram to show fluorescence principle*

When the sample marked with fluorophores is illuminated with appropriate light, the fluorophores absorb light and re-emit it at a longer wavelength. The fluorescence process can be explained using a simple Jablonski diagram, Figure 1.1. When fluorophore marked proteins are excited with enough energy they absorb the energy and transit to the excited electronic state. The

molecules in the excited state then relax either to the lower excited state or to the ground state. Fluorescence is the process which occurs when the excited molecules emit light in nanoseconds of time at the longer wavelength during relaxation to the ground state. Some of the molecules also non-radiatively relax to the lowest excited state which is known as the internal conversion.
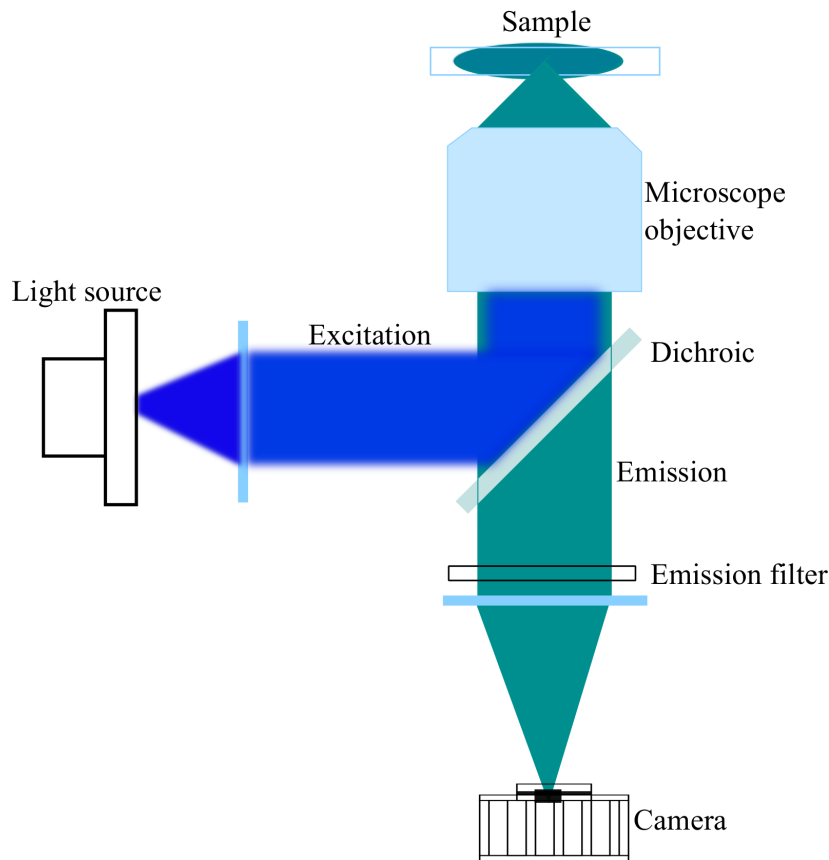
Figure 1.2 : *Basic widefield fluorescence schematic*

In a standard fluorescence microscope, the sample is illuminated by a homogeneous light at the excitation wavelength. A dichroic mirror which is positioned at 45° angle reflects photons at the excitation wavelength but allows the fluorescence light to pass through, as shown in Figure 1.2. The remaining excitation light is filtered out by the emission filter so that only the fluorescence intensity is captured by the camera. The emitted fluorescence intensity is proportional to the excitation intensity. The light emitted by each fluorophore is incoherent meaning that their intensity add up on the detector. Due to the linearity of the microscope and the incoherence of the fluorophores, the intensity recorded by the camera can be modeled as the convolution of the fluorescence distribution with a point spread function (PSF) which corresponds to the image of a single fluorophore.

1.1.2   Performance of widefield fluorescence microscope

In fluorescence microscopy, improving the resolution and the contrast of images is a strong challenge. Resolution and contrast are inseparable concepts as low contrast usually deteriorates the ability to distinguish two point objects.

1.1.2.1   Resolution and PSF

Resolution is the minimum distance between two point objects such that their spots can be separated on the image. The resolution of a conventional widefield image is *diffraction limited*. When the central point of the diffraction spot coincides with first diffraction minimum of the other diffraction spot on the image plane, the two points on the sample are said to be resolved [1]. The resolution on the xy-plane (plane perpendicular to the optical axis), $R_\parallel$, is given by

$$R_\parallel = 0.61\lambda/n\sin(\theta) = 0.61\lambda/\mathrm{NA}, \tag{1.1}$$

where θ is the half aperture angle of the objective, n is the refractive index of the medium, λ is the emission wavelength and NA is the numerical aperture.

    The resolution along the optical axis, R_z, is determined in a similar fashion using the width of the diffraction in the z-axis (the PSF along the optical axis, Figure 1.3(b)) commonly estimated using the full width half maximum (FWHM). The resolution along the z-axis is given by

$$R_z = n\lambda/(\mathrm{NA})^2. \tag{1.2}$$

High numerical apertures shrink the depth-of-field and dramatically improves the axial resolution. It is worth mentioning here that increasing the refractive index of the immersion medium of the objective does not improve the axial resolution. This is because the numerical aperture is also dependent on the same refractive index. In addition to the super-resolution microscopy, currently, there are several techniques to improve the axial resolution (also known as optical sectioning) such as confocal and light sheet microscopy techniques.

    Another way of determining resolution is based on the accessible sample spatial frequencies in the Fourier space. The spatial frequency support of the conventional widefield fluorescence microscopy is limited by the optical transfer function (OTF), which is the Fourier transform of the point spread function of the microscope. The three-dimensional OTF of the conventional microscope is a torus-like region, as shown in Figure 1.4(c). Figure 1.4(a) and (b) shows the 2D cross-sections of the support. The low-resolution information resides close to the origin, while higher resolution information resides further away. The origin of the torus has a "hole" which is the missing cone of information. The maximum sample spatial frequency accessible in the conventional widefield microscope image is therefore limited by the size of the OTF which is $k_{max} = k_0\mathrm{NA}$ where $k_0 = 2\pi n/\lambda$ for the numerical aperture of the objective NA and for the emission wavelength λ. This means a conventional microscope detects information about the sample that resides within the OTF in the reciprocal space.
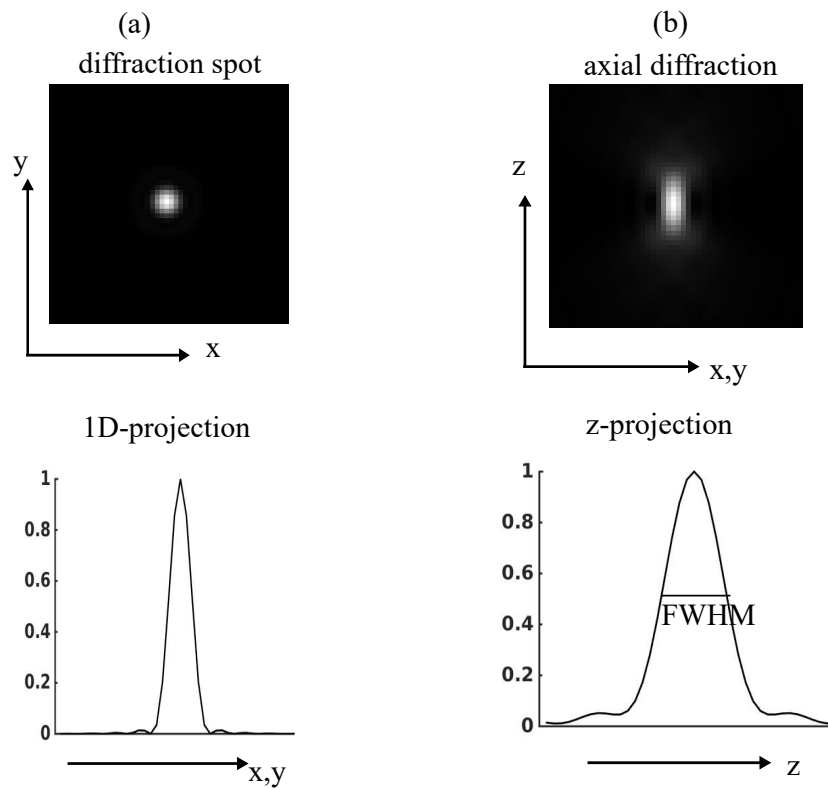
Figure 1.3 : *Microscope point spread function. (a) Lateral diffraction spot. (b) Axial diffraction spot.*
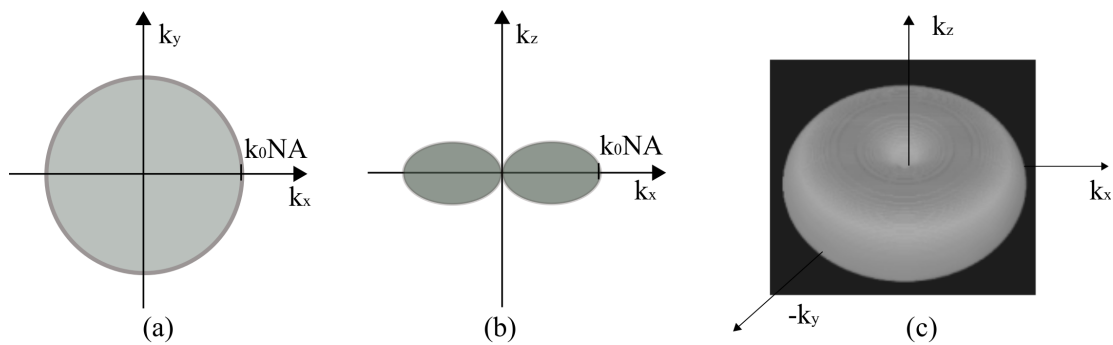
Figure 1.4 : *Conventional microscope OTF. (a) Transversal cross-section. (b) Axial cross-section and the missing cone. (c) 3D-OTF.*

1.1.2.2 Contrast

Another important parameter is the contrast or visibility of the images. Contrast is the ability to distinguish signals of the object of interest from the background. The main factor that determines contrast in conventional fluorescent microscopy is the background fluorescence. There is no optical sectioning in widefield fluorescence microscopy. In other words, a thin transverse fluorescent plane is impossible to be located using a widefield fluorescence microscope. This is because whatever the position of a fluorophore with respect to the focal plane, its intensity integrated over the plane

is always the same (from the principle of energy conservation). So the fluorescent light emitted by fluorescent structures far away from the focal plane will be recorded on the image (with low-frequency behavior) and, therefore, impact the image contrast. In addition to the background fluorescence, other factors such as imperfection of sample preparation methodologies (fixation quality, antibody penetration, evenness of staining) result in the presence of fluorophores outside the region of the molecules of interest, which once again, impacts the contrast of the image.

In this thesis, different techniques for improving resolution and contrast in fluorescence microscopy are investigated. Resolution improvement techniques include STED, STORM, SIM, speckle illumination microscopy (see Chapters 2, 3, 4). Contrast improvements can be achieved by reducing out of focus problems using computational techniques such as 3D-deconvolution of 2D images (see Chapter 5) and microscopic techniques such as confocal and light sheet microscopy (see Chapter 6).

1.2   Superresolution fluorescence microscopy techniques

The conventional standard widefield fluorescence microscope enables to achieve a spatial resolution of 200nm lateral and 500nm axial[2]. A microscopic technique that improves the resolution by afactor of 2 at least is classified as a superresolution technique[10,21]. Recently many superresolution fluorescence microscopy techniques have been developed which allow the observation of biological structures which are not resolvable in conventional fluorescence microscopy.

The superresolution techniques vary in their principle, application, and implementation. To enhance the axial resolution (optical sectioning), researchers have developed confocal microscopy in the 1960s[4,21,22]. More recently, stimulated emission and depletion (STED)[3], stochastic optical reconstruction microscopy (STORM) and photoactivated localization microscopy (PALM)[10–13], and structured illumination microscopy (SIM)[6] have been developed to improve transverse (and possibly axial) resolution beyond the diffraction limit. (Eric Betzig, Stefan W. Hell, and W. E. Moerner have been awarded the Nobel Prize in Chemistry 2014 for the development of superresolution fluorescence microscopy[23].) Most of these methods have yielded an order of magnitude improvement in spatial resolution in all three dimensions over conventional light microscopy. Before discussing the details of structured illumination microscopy, it is relevant to have a brief review of some of these techniques.

1.2.1   Confocal and multi-photon imaging

According to the point spread function (PSF) of the optical system, the diffraction pattern extends not only in the transversal direction but also in the axial dimension where the light extends above and below the focal plane. This diffraction produces out-of-focus light from the neighboring planes to the imaging plane. This out-of-focus light not only decreases the contrast of the imaging plane but also results in poor axial sectioning. Confocal microscopy is one of the earliest approaches demonstrated to reduce the out-of-focus blurring[4,24]. It uses a pinhole in the detection path to

filter out the light coming from the background away from the focal plane. The ability of the pinhole to reject the out of focus emission determines the optical sectioning. In some practical implementations, a set of conjugate apertures are used, one for the excitation illumination and the other for the emission in the detection path. The conjugate pinholes ensure that the microscope will illuminate and detect light from the same volume of the sample. Conversely, it is important to note that the use of pinholes also results in a waste of light. To collect information over the full sample the beam has to be scanned through the sample volume. A single beam scanning or multiple beam scanning (spinning disk) of the disk containing an array pinholes have been demonstrated[25–27]. In multiple beam scanning, the collimated laser beam is passed through the disk which contains multiple pinholes. When the disk rotates rapidly, it creates multiple spots on the sample plane. This approach improves the speed compared to the single beam raster scanning.

Another important point to note regarding confocal microscopy techniques is the detection system. In laser scanning microscopes point detectors such as laser diodes and photomultipliers have been commonly used. Recently, alternative ways of camera detection systems combined with post-processing using synthetic pinholes have been developed. In[28], it is shown that the 3D cross-sectional images (up to 400nm axial range) can be obtained using post-acquisition refocussing methods from just the 2D raster scanned image by applying different synthetic pinholes. The synthetic pinholes are defined by reading only specific pixels with pixel-specific weights for optimal signal to noise ratio. By the same token on laser scanning microscope, a new detector concept which does not use physical aperture pin holes is applied in the commercial Airyscan microscope of Carl Zeiss[29]. The Airyscan is a 32 channel area detector and collects a pinhole-plane image at every scan position. Each detector element functions as a single, very small pinhole. Knowing the beam path and the spatial distribution of each of the 32 detectors enables very light efficient imaging with improved resolution and signal-to-noise level.

A fast-growing technique that also provides excellent optical sectioning is the two-photon microscopy[30]. Two-photon microscopy has some advantages compared to the standard confocal microscope. First, the two-photon excitation wavelength is about twice longer than the one-photon excitation wavelength. The wide separation between the emission and excitation wavelengths guarantees that the excitation light and Raman scatterings can be completely rejected by using filters. Second, biological samples have less absorption and scattering in the near infrared region which makes the two-photon microscopy suitable for imaging thick samples. Finally, unlike the confocal microscopy, it does not use a pin hole in the detection path. It only controls the excitation volume and thus minimizes the signal loss.

1.2.2 STED

Another superresolution technique which breaks the diffraction limit is stimulated emission and depletion (STED)[3]. The principle is to reduce the excited volume by taking advantage of the non-linearity of the fluorophore-light interaction. A combination of two lasers which are called the excitation beam and the STED beam is focused on the sample. The excitation beam excites the fluorophores whereas the doughnut-shaped STED beam (depletion beam) suppresses the spontaneous emission and makes the fluorophores in the periphery of the excited region inactive. This

STED laser decreases the effective diameter of the emission area. Only the center of the excitation spot is allowed to emit fluorescence spontaneously. The STED beam and the stimulated emissions are then filtered out and only emissions localized to the center of the excitation spot are detected. The beams are then scanned across the sample to get the full widefield image. The acquisition time, of course, depends on the number of scanning points. The STED technique gives image resolution in all dimensions without any image processing. The spatial resolution is determined by the intensity of the STED beam, and it is practically limited by photobleaching of the fluorescent probes, which can occur after repeated excitation and stimulated emission.

1.2.3   PALM/STORM

Photoactivation localization microscopy (PALM) [13] and stochastic optical reconstruction microscopy (STORM) [11] are single molecule localization superresolution techniques. The principle is to excite the fluorescent molecule of the sample in a very dilute way in order to avoid the overlap of their image. Then, the position of each molecule can be localized from its diffraction spot with nanometer accuracy.

The STORM/PALM techniques use sophisticated single-molecule emitters. PALM uses photoactivable fluorescent probes and STORM uses photoswitchable or blinking fluorophores. The fluorescent probes change their emission property by light irradiation of a particular wavelength using a low-energy laser. The emission of the probes can be controlled by switching it off and on. Initially, the photoswitchable probes are turned off. They cannot be imaged in this state. Then using a weak irradiation of the switching light on the sample, a limited number of the fluorophores are turned on and can be detected using a conventional widefield microscope. These fluorophores are then turned off again before the measurement of other fluorophores in a similar fashion. Multiple images are recorded (hundreds of thousands) and processed and combined to make the final image. The final image is obtained from the precise calculation of the location of each single molecule emissions and using extensive data processing. The spatial resolution is determined by the number of photons that can be collected from each fluorophore and also from the background fluorescence.

Each superresolution technique has its own advantages and disadvantages in imaging biological samples with respect to spatial resolution, acquisition speed, the complexity of data processing and experimental setup, photobleaching, and phototoxicity. STORM/PALM follow widefield imaging approaches while STED and confocal microscopy are scanning techniques. STORM/PALM need a large number of frames for getting the full final 3D image. It also needs long acquisition times as well as intensive post-processing. On the other hand, STED and confocal requires scanning. Photo-bleaching is a challenge in STED.

Structured illumination microscopy (SIM) is a well-established superresolution technique which mediates the drawbacks of the above techniques. It is a widefield technique, unlike confocal and STED, which requires very few number of acquisitions, unlike STORM/PALM. In terms of probes, SIM uses conventional fluorescent probes while STED and PALM/STORM use sophisticated fluorophores. However, the resolution of SIM is limited about 100nm while STED and STORM/PALM can achieve up to 20nm resolution.

1.3 Structured illumination microscopy (SIM)

The introduction of structured illumination in fluorescence microscopy for improving resolution and optical sectioning goes back to the late 1990s. It is illustrated in [4] that by projecting single spatial frequency grid pattern onto the object, optical sectioning in a conventional wide-field microscope can be obtained. Images were taken at three spatial positions of the grid and processed to produce optically sectioned images that are substantially similar to those obtained with confocal microscopes.The theoretical analysis of the image formation in structured illumination microscopy and demonstration that the transfer function behavior is comparable to the confocal instrument can be found in[31]. In 1999, R. Heintzmann and C. Cremer have introduced a simple method of generating laterally modulated illumination using a diffraction grating wich results in improvement of resolution[5]. The full capability of the technique for doubling the lateral resolution is demonstrated by Gustafsson[6]. The method is then modified and developed for three-dimensional resolution doubling[7]. Since the introduction of SIM, researchers have brought in and developed multiple techniques for improving some parameters in SIM such as: improving resolution[8], enhancing image acquisition speed[32–34], multicolor imaging[14], live cell imaging[15–17] and optimizing the reconstruction technique and minimizing the artifacts in SIM[35,36].

In fluorescence microscopy, the imaging model is given by [7]

$$M(\boldsymbol{r}) = \rho(\boldsymbol{r})I(\boldsymbol{r}) * h(\boldsymbol{r}), \tag{1.3}$$

where $M(\boldsymbol{r})$ is the resulting image, $\rho(\boldsymbol{r})$ is the sample fluorophore density, $I(\boldsymbol{r})$ is the excitation intensity and $h(\boldsymbol{r})$ is the point spread function. Equivalently, using the Fourier transform, the image can be expressed in the reciprocal space as

$$\tilde{M}(\boldsymbol{k}) = [\tilde{\rho}(\boldsymbol{k}) * \tilde{I}(\boldsymbol{k})]\tilde{h}(\boldsymbol{k}). \tag{1.4}$$

˜ denotes the Fourier transform while $*$ denotes the convolution operator. From the real space equation, it is clear that the emission intensity is a pointwise product of the excitation intensity and the fluorophore density. Equivalently in the Fourier space, the emission intensity is the filtered convolution of the object and the excitation intensity frequencies. If the excitation intensity is wisely selected, it downmodulates the high sample spatial frequencies into the Fourier support of the PSF. Appropriate reconstruction strategies can then be used to recover the sample frequency information beyond the frequency cut-off of the conventional fluorescent microscope.

In a standard SIM, the excitation intensity patterns are usually created by interfering coherent plane waves at the sample plane. The 2D-SIM and 3D-SIM periodic patterns are obtained from the interference of 2 coherent beams and 3 coherent beams respectively. The general interference principle at the sample position $\boldsymbol{r} = (\boldsymbol{r}_\parallel, \boldsymbol{z}) = (\boldsymbol{x}, \boldsymbol{y}, \boldsymbol{z})$ can be represented as

$$I(\boldsymbol{r}) = |\sum_m \boldsymbol{E}_m(\boldsymbol{r})e^{i\boldsymbol{k}_m.\boldsymbol{r}}|^2. \tag{1.5}$$

Assuming each plane wave has equal amplitude distribution $\boldsymbol{E}_m(\boldsymbol{r}) = \boldsymbol{E}_0(\boldsymbol{r})$ at a given sample point $\boldsymbol{r}$, and rewriting $\boldsymbol{k}_m.\boldsymbol{r} = m\boldsymbol{k}_\parallel.\boldsymbol{r}_\parallel + k_z z$, the 2D and 3D SIM patterns can be described from

$$I(\boldsymbol{r}) = \left|\sum_m \boldsymbol{E}_0(\boldsymbol{r})e^{i(m\boldsymbol{k}_\parallel.\boldsymbol{r}_\parallel + k_z z)}\right|^2, \tag{1.6}$$

where $k_z = \sqrt{k_0^2 - |\boldsymbol{k}_\parallel|^2}$, and $k_0 = 2\pi/\lambda$. The lateral wave vector $\boldsymbol{k}_\parallel.\boldsymbol{r}_\parallel = \boldsymbol{k}_x.\boldsymbol{x} + \boldsymbol{k}_y.\boldsymbol{y}$, and the coefficient $m = 1, -1$ for 2 beam interference and $m = 1, 0, -1$ for 3 beam interference.

1.3.1   2D-SIM

The sinusoidal excitation intensity pattern is commonly obtained by using two transversally counter propagating coherent beams as

$$
\begin{aligned}
I(\boldsymbol{r}_\parallel, z) &= \left| \boldsymbol{E}_0(\boldsymbol{r})e^{i(\boldsymbol{k}_\parallel.\boldsymbol{r}_\parallel + k_z z)}e^{i\phi/2} + \boldsymbol{E}_0(\boldsymbol{r})e^{i(-\boldsymbol{k}_\parallel.\boldsymbol{r}_\parallel + k_z z)}e^{-i\phi/2} \right|^2 \\
&= 2|\boldsymbol{E}_0(\boldsymbol{r})|^2(1 + \cos(2\boldsymbol{k}_\parallel.\boldsymbol{r}_\parallel + \phi)) \\
&= I_0(1 + \cos(2\boldsymbol{k}_\parallel.\boldsymbol{r}_\parallel + \phi)).
\end{aligned} \tag{1.7}
$$

$\boldsymbol{k}_\parallel$ is the lateral wave vector of the sinusoidal pattern and ϕ is a phase which corresponds to the translation of the patterns. Using this sinusoidal pattern, the resulting image can be expressed as

$$
M(\boldsymbol{r}) = \rho(\boldsymbol{r})I_0[1 + \cos(2\boldsymbol{k}_\parallel.\boldsymbol{r}_\parallel + \phi)] * h(\boldsymbol{r}). \tag{1.8}
$$

And in the reciprocal space,

$$
\begin{aligned}
\tilde{M}(\boldsymbol{k}) &= [\tilde{\rho}(\boldsymbol{k}) * I_0(\boldsymbol{k})][\delta(\boldsymbol{k}) + 0.5\delta(\boldsymbol{k} - 2\boldsymbol{k}_\parallel)e^{i\phi} + 0.5\delta(\boldsymbol{k} + 2\boldsymbol{k}_\parallel)e^{-i\phi}]\tilde{h}(\boldsymbol{k}) \\
&= I_0[\tilde{\rho}(\boldsymbol{k}) + 0.5\tilde{\rho}(\boldsymbol{k} - 2\boldsymbol{k}_\parallel)e^{i\phi} + 0.5\tilde{\rho}(\boldsymbol{k} + 2\boldsymbol{k}_\parallel)e^{-i\phi}]\tilde{h}(\boldsymbol{k}).
\end{aligned} \tag{1.9}
$$

The image spectrum contains $\tilde{\rho}(\boldsymbol{k})$ at its original position and two additional components at
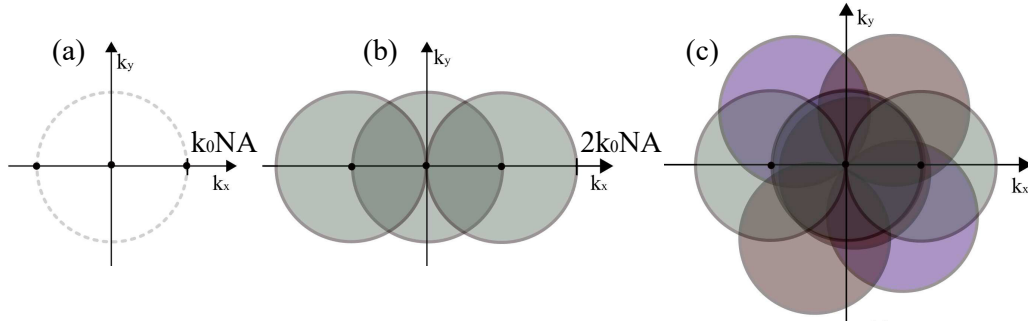
Figure 1.5 : *Observable spectrum of 2D-SIM. (a) 2D SIM illumination Fourier peaks. (b) 2D-SIM observable spectrum, single illumination pattern. (c) 2D-SIM observable spectrum (3 orientations).*

$\tilde{\rho}(\boldsymbol{k} - 2\boldsymbol{k}_\parallel)$ and $\tilde{\rho}(\boldsymbol{k} + 2\boldsymbol{k}_\parallel)$ shifted by $2\boldsymbol{k}_\parallel$ and $-2\boldsymbol{k}_\parallel$ respectively. The light grid is shifted 3 times to distinguish these components which modifies the coefficient $e^{i\phi}$ and yields an easy to solve linear system with 3 equations and 3 unknowns. To improve the resolution by the factor of two, assuming the same microscope objective is used for excitation and collection, $2\boldsymbol{k}_\parallel = k_0$ has to be satisfied. Therefore, the two beam interference shows additional two harmonic peaks $(k_0, 0)$ and $(-k_0, 0)$ (as shown in Figure 1.5(a)), in addition to the zero frequency peak $(0, 0)$, which translates the OTF to the corresponding peak centers as shown in Figure 1.5(b). Figure 1.5(c) shows the full

observable region of 2D-SIM by using harmonic patterns in three orientations. We observe here that the illumination is constant along the optical axis. This illumination can be used to study a single plane of the sample or to get a 3D stack of data by translating the object.

SIM increases the lateral resolution by a factor of 2 assuming the same microscope objective is used for illumination and collection. In order to achieve isotropic 2D lateral resolution gain, grid patterns with various orientations are used for illumination, at least 3 orientations.
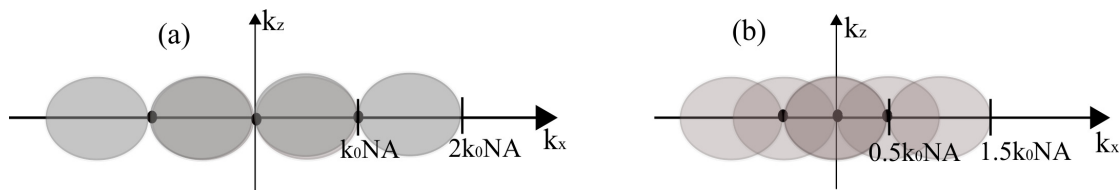
Figure 1.6 : *Filling missing cone using 2D-SIM (a) 2D-SIM maximum transverse resolution. (b) 2D-SIM missing cone filled with cost of transverse resolution.*

However, in 2D-SIM, the missing cone problem still exists which makes difficult three-dimensional resolution gain. Using a coarser illumination pattern, equivalently using patterns with shorter wave vectors closer to each other, one can fill the missing cone. This is because the three OTF components are overlapping and covering each others' missing cones [7]. This, therefore, fills the missing cone information and introduces optical sectioning. However using coarser illumination pattern (grid patterns with shorter wave vectors) deteriorates the lateral resolution. Figure 1.6 backs up this claim. When the 2D-SIM is used to obtain the maximum resolution, Figure 1.6(a), the missing cone is no sectioning. On the other hand, with the cost of the transverse resolution, the axial resolution can be improved by some factor, as shown in Figure 1.6(b). To improve further the resolution along the optical axis as well as along the transverse direction, it is better to use an illumination that is also structured along z.

1.3.2 3D-SIM

The intensity pattern of 3D-SIM can be analytically expressed starting from Eq. (1.6) using the interference of the three beams with carefully defined propagation wave vectors as

$$
\begin{aligned}
I(\boldsymbol{r}) &= |\boldsymbol{E}_0(\boldsymbol{r})e^{ik_0z} + \boldsymbol{E}_0(\boldsymbol{r})e^{i(\boldsymbol{k}_\parallel \cdot \boldsymbol{r}_\parallel + k_z z)}e^{i\phi/2} + \boldsymbol{E}_0(\boldsymbol{r})e^{i(-\boldsymbol{k}_\parallel \cdot \boldsymbol{r}_\parallel + k_z z)}e^{-i\phi/2}|^2 \\
&= |\boldsymbol{E}_0(\boldsymbol{r})|^2(3 + e^{i2\boldsymbol{k}_\parallel \cdot \boldsymbol{r}_\parallel} + e^{-i2\boldsymbol{k}_\parallel \cdot \boldsymbol{r}_\parallel} + e^{i(\boldsymbol{k}_\parallel \cdot \boldsymbol{r}_\parallel + (k_0 - k_z)z)} \\
&+ e^{-i(\boldsymbol{k}_\parallel \cdot \boldsymbol{r}_\parallel + (k_0 - k_z)z)} + e^{i(\boldsymbol{k}_\parallel \cdot \boldsymbol{r}_\parallel + (-k_0 + k_z)z)} + e^{-i(\boldsymbol{k}_\parallel \cdot \boldsymbol{r}_\parallel + (-k_0 + k_z)z)}).
\end{aligned} \tag{1.10}
$$

One can rigorously simplify Eq. (1.10) and obtain

$$
I(\boldsymbol{r}) = I_0[3 + 2\cos(\boldsymbol{k}_1 . \boldsymbol{r} + \phi) + 2\cos(\boldsymbol{k}_2 . \boldsymbol{r} + \phi) + 2\cos(\boldsymbol{k}_3 . \boldsymbol{r} + \phi)], \tag{1.11}
$$

where $I_0 = |\boldsymbol{E}_0(\boldsymbol{r})|^2$, $|\boldsymbol{k}_1| = (2|\boldsymbol{k}_\parallel|, 0)$, $|\boldsymbol{k}_2| = (|\boldsymbol{k}_\parallel|, k_0 - k_z)$, $|\boldsymbol{k}_3| = (|\boldsymbol{k}_\parallel|, -k_0 + k_z)$, $|\boldsymbol{r}| = (|\boldsymbol{r}_\parallel|, z)$ and ϕ is a phase which corresponds to the translation of a gird pattern.

The peaks in the reciprocal are obtained from the Fourier transform of the 3D intensity pattern as

$$
\begin{aligned}
\tilde{I}(\boldsymbol{k}) &= I_0[3\delta(\boldsymbol{k}) + \delta(\boldsymbol{k} - \boldsymbol{k}_1)e^{i\phi} + \delta(\boldsymbol{k} + \boldsymbol{k}_1)e^{-i\phi} + \delta(\boldsymbol{k} - \boldsymbol{k}_2)e^{i\phi} + \delta(\boldsymbol{k} + \boldsymbol{k}_2)e^{-i\phi} \\
&+ \delta(\boldsymbol{k} - \boldsymbol{k}_3)e^{i\phi} + \delta(\boldsymbol{k} + \boldsymbol{k}_3)e^{-i\phi}].
\end{aligned}
\tag{1.12}
$$

These intensity peaks are shown in Figure 1.7(a) for an arbitrary 3D illumination pattern. The image spectrum will then be

$$
\begin{aligned}
\tilde{M}(\boldsymbol{k}) &= [\tilde{\rho}(\boldsymbol{k}) * \tilde{I}(\boldsymbol{k})]\tilde{h}(\boldsymbol{k}) \\
&= I_0[3\tilde{\rho}(\boldsymbol{k}) + \tilde{\rho}(\boldsymbol{k} - \boldsymbol{k}_1)e^{i\phi} + \tilde{\rho}(\boldsymbol{k} + \boldsymbol{k}_1)e^{-i\phi} + \tilde{\rho}(\boldsymbol{k} - \boldsymbol{k}_2)e^{i\phi} + \tilde{\rho}(\boldsymbol{k} + \boldsymbol{k}_2)e^{-i\phi} \\
&+ \tilde{\rho}(\boldsymbol{k} - \boldsymbol{k}_3)e^{i\phi} + \tilde{\rho}(\boldsymbol{k} + \boldsymbol{k}_3)e^{-i\phi}]\tilde{h}(\boldsymbol{k}).
\end{aligned}
\tag{1.13}
$$

Figure 1.7(b) shows the image spectrum obtained while using an arbitrary 3 beam illumination
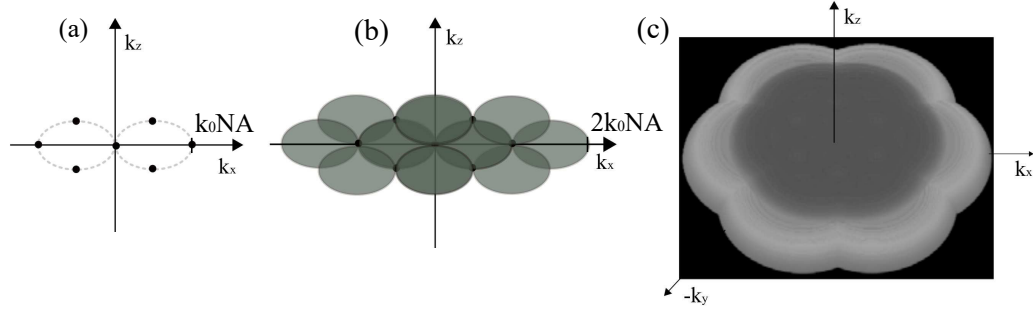
Figure 1.7 : *Observable spectrum of 3D-SIM. (a) 3D-SIM illumination Fourier peaks. (b) 3D-SIM observable spectrum, single illumination intensity. (c) 3D-SIM observable spectrum (3 orientations).*

intensity pattern of a particular orientation. Due to the convolution, the OTF of the conventional 3D microscope is translated using the illumination peaks as centers. This translation shifts the sample frequencies within the support of the OTF. Theoretically the best configuration for improving both transverse and axial resolution corresponds to $|\boldsymbol{k}_1| = |\boldsymbol{k}_2| = |\boldsymbol{k}_3| = k_0$. Figures 1.7(c) depict the three-dimensional sample spectrum that can be accessed using 3D-SIM light grid of 3 orientations.

In this section, we assume that the object does move with respect to the illumination while the 3D stack of images is recorded. This means that each image is taken using a remote focusing approach. In this case, the image formation model that we use for 3D-SIM will have the same format as the 2D-SIM. Unfortunately, this is not the technique used in most commercial systems. A thorough discussion about this crucial point will be given in Chapter 2.

The SIM images contain the overlap of shifted and non-shifted spatial frequency components that need to be separated. The reconstruction techniques extract the information and place it to the correct location beyond the OTF cutoff. To this aim, the light grid is translated to give access to the same sample spectrum with different phases and thus getting a linear system that

can unravel the different components.The reconstruction techniques will be discussed in detail in Chapter 2.

In conclusion, 3D-SIM encodes the sample spectrum twice of the lateral and axial frequency maxima of the conventional microscope OTF. The resolution is therefore doubled in both lateral and axial dimensions. SIM can provide a lateral resolution of about 100nm and axial resolution of about 300nm[16,17].

1.4 Practical implementation of 2D/3D SIM

Practically SIM can be implemented using transmission diffraction gratings[7] or spatial light modulators (SLM)[17,33] fixed in an intermediate image plane. A transmission diffraction grating splits the laser beam into 3 or more beams. Choosing 2 or 3 beams, using carefully designed spatial filters, and making them interfere at the sample produces the illumination grid. A programmable electro-optical spatial light modulator also produces the illumination grid with precise and rapid control of the excitation pattern in the specimen.
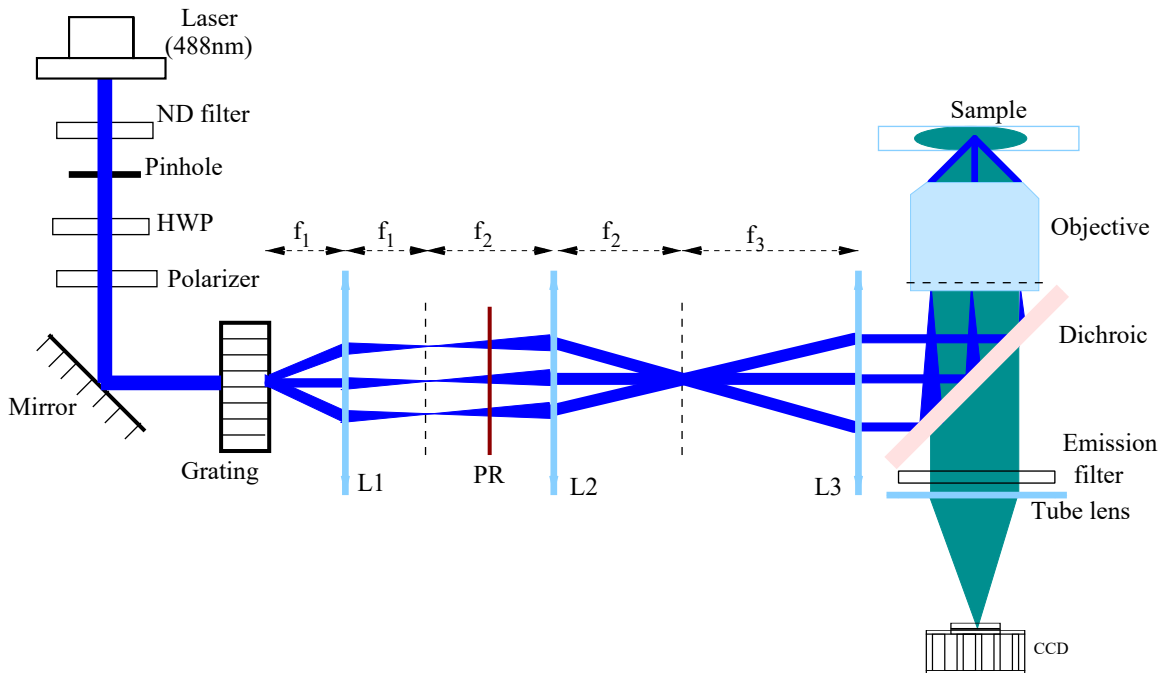
Figure 1.8 : *Schematic of SIM using transmission diffraction grating. P: polarizer, HWP: half wave plate, L1, L2, L3: Lenses, PR: polarization rotator. The polarizer and half wave plate is used to control the polarization that provides optimal contrast of the grid pattern.*

A transmission grating creates multiple diffraction orders based on its groove spacing (the number of grooves in a mm). The grating has to be mounted on the rotator and translator stage so that it can produce the required orientations and phase translations. Figure 1.8 shows a simple schematic to demonstrate the implementation of 2D/3D-SIM using transmission gratings. The two

Figure 1.9 : *SIM using SLM (Setup from Thomas Mangeat, LBCMCP, UMR 5088 CNRS - Université P. Sabatier Toulouse III).*

or three excitation beams (shown in blue) can be selected using spatial filter masks placed at the conjugate of the back focal plane of the objective (between L1 and PR).

Grating-based SIM may not switch quickly between different orientations and phases. It is mechanically manipulated and hence is slow. This impacts the image acquisition speed, especially on live imaging of biological samples. Using programmable SLM, as shown in Figure 1.9, can generate interference illumination patterns which can be altered rapidly and precisely. Unlike gratings which have commercially limited groove period, SLM is flexible and easily controllable in generating the illumination patterns. The polarization rotators are used in both configurations to maintain the polarization status at all the orders and orientations.

1.5   Performance and drawbacks of structured illumination microscopy

For SIM to exhibit resolutions about twice better than the widefield microscope, the illumination patterns have to be designed carefully with optimally-calibrated pattern period, orientations and phases. The experimental setup has to be therefore carefully calibrated and stabilized to control the illumination patterns. The perfect knowledge of the illumination patterns is very critical in SIM reconstructions.

However, to perfectly control the illumination patterns on the sample plane is not easy in physical experimental implementations. Pattern distortions can be introduced by the optical com-

ponents of the setup as well as by the sample itself, particularly in thick samples. This makes the experimental implementation very technical and limits its application to weakly scattering samples. Reconstructing SIM images assuming the perfect knowledge of the illumination intensity patterns may, therefore, introduce artifacts on the estimated sample due to the misalignment of the grid that can occur during experimental acquisitions. To tackle this drawback of SIM a reconstruction strategy which is independent of the illumination pattern is desirable. Recently, some works have been done to address the issue of inaccurate illumination knowledge[36–38].

Our work is the continuation of these studies. The development of reconstruction strategies without the knowledge of the illuminations (blind SIM) permits to extend the harmonic SIM to speckle illumination microscopy which uses random unknown patterns.

1.6   Conclusion

The development of superresolution fluorescence microscopy techniques such as STED, STORM/PALM allow investigating biological structures with nanometer resolution, beyond the diffraction limit. Each of these techniques has its own advantages and disadvantages regarding spatial resolution, acquisition speed, complexity of data processing and experimental setup, photobleaching, and phototoxicity. STORM/PALM are widefield imaging approaches and need a large number of frames for getting the full final 3D image and specific fluorophores. On the other hand, STED requires scanning, specific fluorophores and is challenged by photo-bleaching.

SIM is a good compromise among the superresolution techniques. It is a widefield technique with only a few number of acquisitions. It uses conventional fluorescent probes. On the other hand, its resolution does not reach that of STED and PALM/STORM.

The principle of SIM is based on a wisely selected illumination patterns that down-modulate the high sample spatial frequencies into the support of the OTF. By using appropriate reconstruction strategies the down-modulated high sample frequency information can be restored to its original position, which results in resolution enhancement. 3D-SIM improves the resolution up to twice of the diffraction limit in both transversal and axial dimensions. Unfortunately, the reconstruction strategies that are based on the perfect knowledge of the illumination are sensitive to the misalignment and distortion of the illumination patterns. The experimental setup, therefore, needs a careful calibration and can be challenging. Blind-SIM approaches which are able to reconstruct the sample with an approximate knowledge of the illumination are thus very interesting for simplifying and extending the application domain of SIM. This thesis is mainly devoted to the development of blind-SIM strategies and their application to 2D and 3D imaging.

Blind-SIM: reconstruction techniques

Contents

2.1 Introduction

Improving the resolution and contrast of three-dimensional images of fluorescent samples while conserving the ease of use and non-invasiveness of classical microscopy is a major challenge. The classical widefield microscopes, in which the fluorescence is excited by homogeneous intensity, exhibits, in the best case, a lateral resolution about half the emitted wavelength with an axial resolution three times bigger[39]. In addition, due to the specific shape of the optical transfer function, it is plagued by an important out of focus signal coming from the low-frequency sample structures which deteriorates significantly the image contrast.

Optical sectioning techniques, such as confocal microscopy, light sheet microscopy[40] and others[4,41] ameliorate the image contrast but give little resolution improvement over widefield. In contrast, Structured Illumination Microscopy (SIM), using harmonic patterns or random speckles, improves both the optical sectioning and the transverse resolution[7,36]. The main drawback of SIM is that it relies on reconstruction algorithms that require a precise knowledge of the illumination patterns. This careful control of the three-dimensional excitation pattern is necessary which is not always possible in thick samples. This important constraint can be met only if the illumination distortion induced by the sample or the objective aberrations is negligible and if the set-ups are carefully calibrated and stabilized to control the illumination. It limits the application domain to weakly scattering samples and make the experimental implementation very technical. Blind-SIM strategies have begun to be proposed to tackle this issue, the principle being to retrieve the sample fluorescence density without the knowledge of the illumination patterns[36,42,43]. Blind-SIM algorithms are also a major step forward to extend harmonic SIM to speckle illumination patterns since it needs no control over the illuminations and hence simplifies the experimental implementation.

In this chapter, we develop blind-SIM algorithms that are adapted to 3D imaging. The reconstructions of the techniques are demonstrated only on synthetic data since the experimental data reconstructions are mainly illustrated in the next chapter. The imaging mechanisms of three-dimensional microscopy and the proposed reconstruction schemes are investigated in Section 2.4.

2.2 Reconstruction Strategies

In classical wide-field fluorescence microscopy, the sample fluorescence is excited by a uniform light intensity and the emitted fluorescence is detected at the image plane of a microscope objective. In the linear regime, the recorded intensity M can be modelled as the convolution of the fluorescence density of the sample ρ with the microscope detection point-spread-function h. When the sample is illuminated with a non-uniform light pattern, the recorded intensity can be modelled as in[7],

$$M_l = (I_l \rho) * h, \tag{2.1}$$

where $*$ stands for the convolution product, I_l is the lth illumination intensity and M_l is the recorded image using the lth illumination pattern.

In three-dimensional (3D) SIM approach, the sample is illuminated with L different three-dimensional (3D) intensity patterns I_l, $l = 1, \cdots, L$. For each illumination, a 3D fluorescence image of the sample M_l is recorded. To keep the illumination unchanged, the scanning along the

optical axis should be done by remote focusing[44] or by using a specific device that projects on the camera, within one shot, several images taken at different focal planes[45]. Under these experimental conditions, the recorded 3D data, M_l, can be modeled as in Eq. (2.1).

2.2.1 Joint blind-SIM reconstruction

In this approach, we extended the algorithm developed by Mudry[36] for simplified 2D configurations into a 3D algorithm. The goal of the joint blind-SIM algorithm is to determine the density of fluorophores ρ and the L illuminations $\{I_l\}$ simultaneously from the knowledge of the measured intensities M_l. For a given density of fluorophores ρ and excitations I_l, one defines the residual error r_l from Eq. (2.1) as follows

$$r_l = M_l - (\rho I_l) * h. \tag{2.2}$$

The basic idea of the blind-SIM minimisation is to build up two sequences related to the density of fluorophores and illuminations $\{\rho_n\}$ and $\{I_{l,n}\}$, respectively, so as to minimise

$$F\Big(\rho, (I_l)_{l=1,\dots,L}\Big) = W \sum_{l=1}^{L} ||r_l||_\Gamma^2, \tag{2.3}$$

where Γ is the sub-set of $\mathbb{R}^3$, $\|.\|$ is an euclidean norm over the image space, M_l is measured and W is the normalisation factor

$$W = \frac{1}{\displaystyle\sum_{l=1}^{L} \|M_l\|_\Gamma^2}. \tag{2.4}$$

Given the L images, we seek to reconstruct both the fluorescence density and the L incident intensities, *i.e.* $L+1$ unknowns. The system is thus highly under-determined. To avoid this problem, we introduce the constraint that the sum of all the incident intensities be roughly homogeneous over the sample plane. This condition assumes that the sample is uniformly illuminated on average. This means

$$\sum_{l=1}^{L} I_l \quad \approx \quad L I_0, \tag{2.5}$$

where I_0 is constant over the sample plane. We use this constraint for reducing the number of unknowns. The last intensity I_L is assumed to be equal to

$$I_L = L I_0 - \sum_{l=1}^{L-1} I_l, \tag{2.6}$$

so, equivalently, the recorded image using the Lth illumination can be represented, from Eq. (2.1) and Eq. (2.6),

$$M_L = \left[\left(L I_0 - \sum_{l=1}^{L-1} I_l\right)\rho\right] * h, \tag{2.7}$$

where I_L is now absent.

The fluorescence density and the $L-1$ first illuminations are then jointly estimated iteratively in order to minimise the cost functional,

$$F(\rho, I_{l=1,...,L-1}) = W \sum_{l=1}^{L-1} \|M_l - (I_l\rho) * h\|^2 + W \left\| M_L - \left[\left(LI_0 - \sum_{l=1}^{L-1} I_l \right) \rho \right] * h \right\|^2. \quad (2.8)$$

The only assumption on the illuminations is approximate homogeneity of their sum. Note that with this approach, the residual inhomogeneity of the illumination average will be transferred to the reconstructed fluorescence density. A non-linear conjugate gradient algorithm is used to minimize this cost-functional.

The density of fluorophores ρ and intensities I_l are both real and positive. To incorporate this information in the reconstruction algorithm, positivity is imposed on the density of fluorophores and intensities, ρ and the $L-1$ first illuminations $\{I_l\}$ are written as the square of auxiliary functions ξ and $\{i_l\}$ such that

$$\begin{aligned} I_l &=& i_l^2, \\ \rho &=& \xi^2. \end{aligned} \quad (2.9)$$

The cost functional to be minimised depends now on these auxiliary functions as,

$$F(\xi, (i_l)_{l=1,...,L-1}) = W \sum_{l=1}^{L-1} \left\| M_l - (\xi^2 i_l^2) * h \right\|_\Gamma^2 + W \left\| M_L - [\xi^2 I_L] * h \right\|_\Gamma^2, \quad (2.10)$$

with $I_L = LI_0 - \sum_{l=1}^{L-1} i_l^2$. Series $\{\xi_n\}$ and $\{i_{l,n}\}$ are updated at each iteration according to the following recursive relations

$$\begin{aligned} \xi_n &=& \xi_{n-1} + \alpha_n d_{n;\xi}, \\ i_{l,n} &=& i_{l,n-1} + \beta_{l,n} d_{l,n;i}, \end{aligned} \quad (2.11)$$

where $d_{n;\xi}$ and $d_{l,n;i}$ are updating directions with respect to the auxilary quantities of the density of fluorophores ξ and illuminations $\{i_l\}$, respectively. Scalar coefficients α_n and $\beta_{l,n}$ are weights that are chosen at each iteration step such that they minimise

$$f\big(\alpha_n, (\beta_{l,n})_{l=1,...,L-1}\big) = F(\xi_{n-1} + \alpha_n d_{n;\xi}, (i_{l,n-1} + \beta_{l,n} d_{l,n;i})_{l=1,...,L-1}).$$

This choice for α_n and $\beta_{l,n}$ ensures that $\mathcal{F}\big(\xi_n, (i_{l,n})\big)$ is reduced at every step. Calculation of the function f leads to a polynomial of variables α_n and $\beta_{l,n}$ for which the minimum is obtained thanks to a Conjugate Gradient method [46,47]. The detailed analysis of the cost functional as a function of α_n and $\beta_{l,n}$ and the minimization of the polynomial is presented in the Appendix B.2.

The updating directions $d_{n;\xi}$ and $d_{l,n;i}$ are based on the gradient of the cost functional $\mathcal{F}(\rho, i_l)$: g_ξ is the gradient of the cost functional $\mathcal{F}(\xi, i_l)$ with respect to ξ assuming that the intensities i_l do not change within the domain Ω; while $g_{l,i}$ is the gradient of $\mathcal{F}(\xi, i_l)$ with respect to the l-th intensity, i_l, assuming that the density of fluorophores, and the $L-1$ other intensities do not change inside the domain Ω. The derivation of these gradients is reported in the Appendixces A.1, A.2 and A.3.

$$\begin{aligned} g_{n,\xi} &=& -4W \sum_{l=1}^{L-1} i_{l,n-1}^2 \xi_{n-1}(r_{l,n-1} * h) - 2WI_{L,n-1}\xi_{n-1}(r_{L,n-1} * h) \\ g_{l,n,i} &=& -4W\xi_{n-1}^2 i_{l,n-1}\Big((r_{l,n-1} - r_{L,n-1}) * h\Big). \end{aligned} \quad (2.12)$$

Using gradients as updating direction being generally inefficient, one prefers to use a conjugation algorithm[47]. We choose the Polak-Ribière conjugate gradient formula[48], known as one of the most efficient ones

$$
\begin{aligned}
d_{n;\xi} &= g_{n;\xi} + \gamma_{n;\xi} d_{n-1;\xi} \\
&\text{with} \quad \gamma_{n;\xi} = \frac{\langle g_{n;\xi} | g_{n;\xi} - g_{n-1;\xi} \rangle_\Omega}{||g_{n-1;\xi}||_\Omega^2}, \\
d_{n,l;i} &= g_{l,n;i} + \gamma_{n,i} d_{l,n-1;i} \\
&\text{with} \quad \gamma_{n;i} = \frac{\langle g_{l,n;i} | g_{l,n;i} - g_{l,n-1;i} \rangle_\Omega}{||g_{l,n-1;i}||_\Omega^2},
\end{aligned}
\tag{2.13}
$$

where g_ξ and g_i denote the gradients of the cost functional $\mathcal{F}$ with respect to ξ and i, respectively.

2.2.2 Separate deconvolution

The joint blind-SIM estimates the density of fluorophores and the intensities simultaneously. This significantly increases the computational time of the algorithm, mainly for three-dimensional data reconstruction. In order to accelerate the inversion procedure, we have devised a simpler reconstruction scheme, hereafter denoted by blind-SIM Separate Deconvolution (blind-SIM-SD), that does not reconstruct explicitely the illuminations. Introducing the auxiliary variable $q_l = \rho I_l$ for $l = 1, \cdots, L$, the blind-SIM problem can be stated as finding q_l positive so as to minimize,

$$
\mathcal{F}(q_{l=1,\cdots,L}) = W_l \sum_{l=1}^{L} ||M_l - \mathbf{A}(q_l)||^2.
\tag{2.14}
$$

The operator $\mathbf{A}$ describes the convolution operator considering the recorded image M_l obtained for a given illumination I_l is modelled by

$$
M_l = \mathbf{A}(q_l) = q_l * h.
\tag{2.15}
$$

Once the q_l are known, the indetermination on ρ and I_l is removed by using the homogeneity constraint on the illuminations $\sum_{l=1}^{L} I_l = I_0$ to form $\rho = (\sum_{l=1}^{L} q_l)/I_0$. The minimization of $\mathcal{F}$ can be done by deconvolving separately each low-resolution image of a pattern under positivity constraint which fastens remarkably the inversion procedure. This technique is straightforwardly adapted from the previous joint blind-SIM algorithm discussed in the previous section. Imposing positivity on q_l using an auxilary quantity η_l, $q_l = \eta_l^2$, one can estimate η_l by minimizing,

$$
\mathcal{F}(\eta_l) = W_l ||M_l - \mathbf{A}(\eta_l^2)||^2,
\tag{2.16}
$$

where $W_l = 1/||M_l||^2$. In a similar fashion as the joint blind-SIM algorithm, the minimization is performed iteratively using Polak-Ribière conjugate gradient method. A sequence (η_n) is built up according to the following recursive relation for each of the low-resolution images.

$$
\eta_n = \eta_{n-1} + \alpha_n d_n,
\tag{2.17}
$$

with η_n and η_{n-1} estimations of η for the iteration step n and $n-1$, respectively, and d_n represents the Polak-Ribière conjugate gradient direction

$$
d_n = g_{\eta;n} + \gamma_n d_{n-1},
\tag{2.18}
$$

with

$$\gamma_n = \frac{\langle g_n \mid g_{\eta;n} - g_{\eta;n-1} \rangle}{\|g_{\eta;n}\|^2}. \tag{2.19}$$

The function $g_{n,\eta}$ is the gradient of the cost functional $\mathcal{F}(\eta)$ with respect to η evaluated for the estimation η_{n-1}. Once the updating direction is computed, the real scalar α_n is determined at each iteration step by minimizing the cost function,

$$
\begin{aligned}
\mathcal{F}(\alpha_n) &= \|M - \mathbf{A}(\eta_n^2)\|^2 \\
&= \|M - \mathbf{A}(\eta_n^2) - 2\alpha_n \mathbf{A}(\eta_n d_n) - \alpha_n^2 \mathbf{A}(d_n^2)\|^2.
\end{aligned} \tag{2.20}
$$

The minimization of this cost function, which is a polynomial in α of the fourth order, is achieved numerically using the Polak-Ribière conjugation gradient method[46]. The minimization of the cost functional is also computed analytically. The details about the gradients and minimization of blind-SIM-SD is presented in Appendix C.

Comparing the cost functional F, Eq. (2.10), to $\mathcal{F}$, Eq. (2.16), and bearing in mind the homogeneity constraint, one observes that the two reconstruction schemes are basically solving the same problem. The main difference is that, in the first approach, the Lth intensity, written as $I_0 - \sum_{l=1}^{L-1} I_l$, is not always positive, while, in the second approach, all the intensities are positive. The equal treatment of all the speckle intensities and the rapidity of the minimization of $\mathcal{F}$ compared to that of F are strong assets in favor of the second scheme. However, when the illuminations are partially known, as in classical SIM with distorted illuminations, joint blind remains a better option as it can easily incorporate *a priori* information on the illumination patterns[38,49] contrary to blind-SIM-SD. The joint blind-SIM incorporating partial information of the classical SIM patterns is termed as filtered blind-SIM.

2.2.3 Filtered blind-SIM

Filtered blind-SIM is a joint blind-SIM technique adapted for classical SIM image reconstructions incorporating the knowledge of the illumination intensity patterns[38]. Reconstructing SIM images assuming the illumination intensity patterns are perfectly known may introduce artifacts due to the misalignments of the grid that can occur during experimental acquisitions. However, some information about the illumination grid can still be used with the joint blind-SIM technique. Ideally, the Fourier transform of the sinusoidal intensity grid gives sharp Fourier peaks in the reciprocal space. The Fourier peaks that are determined from the direct Fourier transform of the raw data are fuzzy, depending on the contrast of the grid pattern. It is sometimes not easy to locate the exact position of the Fourier peaks, particularly when the contrast of the illumination pattern is weak and the sample is highly sparse. However, the approximate position of the Fourier peaks can be known from the analysis of the illumination patterns or can be inferred from the experimental raw data. The fact that it requires the approximate location of the peaks could permit simplification in SIM implementation.

The principle of filtered blind-SIM is to restrict the illumination intensity during reconstruction such that its frequencies are confined in a predetermined regions about the Fourier peaks. This

is done by introducing a filter mask in the Fourier domain, that is basically a Gaussian centered about the peaks. Figure 2.1 illustrates the peaks and the restricting regions of investigation of the illumination pattern using the Fourier masks for a particular illumination pattern in 2D-SIM (a) and 3D-SIM (b).
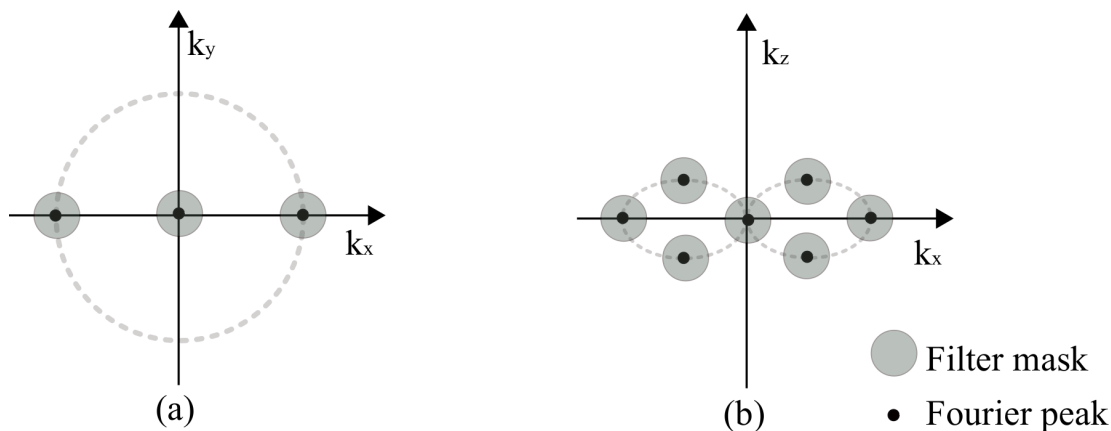
Figure 2.1 : *Principle of filtered blind-SIM: Filter masks centering the Fourier peaks of (a) 2D-SIM, (b) 3D-SIM.*

A two-dimensional filtered blind-SIM algorithm is demonstrated by Ayuk *et al.*[38] and was effective in processing SIM images even when the illuminations were distorted. However, the algorithm was restricted only to two-dimensional samples. In addition, the positivity constraint was imposed only on the fluorescence density but not on the illumination patterns. We have adapted the algorithm for three-dimensional data reconstruction. Moreover, the positivity constraint is imposed on the fluorophore density as well as on the illumination intensity.

Positivity on the fluorescence density ρ is imposed using the auxilary variable ξ as $\rho = \xi^2$. The implementation of positivity on the illumination intensity however is not straightforward. We systematically implemented positivity on the intensity I_l using a complex field $\boldsymbol{e}_l$ as an auxilary quanity which gives

$$I_l = |\boldsymbol{e}_l|^2. \tag{2.21}$$

If $\tilde{f}_l$ is the filter mask function in the Fourier space, the restriction of the illumination pattern estimations within the region defined by the filter masks can be mathimatically presented as

$$\tilde{I}_l = \widetilde{|\boldsymbol{e}_l|^2} \tilde{f}_l, \tag{2.22}$$

where ˜ represents the Fourier transform, i.e. $\widetilde{|\boldsymbol{e}_l|^2}$ is the Fourier transform of $|\boldsymbol{e}_l|^2$. Therefore, the filtered illumination in the real space is given by

$$I_l = |\boldsymbol{e}_l|^2 * f_l, \tag{2.23}$$

$*$ being the convolution operator.

The minimization principle of filtered blind-SIM is to find the minimum of the joint blind-SIM cost functional given in Eq. 2.3 for illumination patterns, I_l, belonging to the regions restiricted by

the filter mask in the Fourier space. The filter blind-SIM cost functional using positivity constraint is then conformed as

$$F_{\mathrm{s}}\Big(\xi, (\boldsymbol{e}_l)_{l=1..L-1}\Big) = W \sum_{l=1}^{L-1} \| M_l - \big(\xi^2(|\boldsymbol{e}_l|^2 * f_l)\big) * h \|_{\Gamma}^2$$

$$+W \left\| M_L - \left[\xi^2 \left(L I_0 - \sum_{l=1}^{L-1} (|\boldsymbol{e}_l|^2 * f_l) \right) \right] * h \right\|_{\Gamma}^2, \tag{2.24}$$

and ξ and $\boldsymbol{e}_l$ are jointly estimated to minimize this function for $\xi \subset \mathbb{R}^3$ and $\boldsymbol{e}_l \subset \mathbb{C}^3$. The analysis of the gradients and the polynomials of the algorithm are prsented in detail in the Appendices A.5 and B.4 respectively.

2.3 Illustration of reconstruction techniques on synthetic data

In this section, we investigate the performances of the blind-SIM approach on synthetic data stemming from various samples. Since the blind-SIM reconstruction technique on 2D data has been demonstrated by Mudry *et al.*[36], and also deeply investigated in Chapter 3 using experimental data, this section mainly focuses on the axial resolution improvement of the blind-SIM reconstruction techniques using speckle illuminations.

The blind-SIM 3D reconstructions are compared to the positive deconvolution of standard widefield and confocal images. The widefield image is obtained by summing all the speckle images, which ensures that the comparison is performed with the same photon budget. The ideal confocal image (obtained with an infinitely small pinhole) is simulated by convolving the actual fluorescence distribution of the sample with the square of the point spread function h^2 [50] and deteriorating it with Poisson noise using the same photon budget as the other techniques. In both cases, the positive deconvolution is performed with the same algorithm as that used in blind-SIM-SD. It is worth noting that the confocal image is unrealistic as it combines the use of an infinitely small pin-hole with a large number of collected photons. Actually, it should rather be considered as an indication of the ultimate axial resolution that can possibly be achieved using structured illumination than as a feasible experiment.

In all the following numerical experiments, we consider a microscope objective with NA = 0.95 and $\lambda = 550$nm where λ is the excitation and fluorescence wavelength. The voxel size of the image is $\lambda/(8\text{NA})$ in all directions. To be realistic from an experimental point of view, only one hundred different speckles were considered to generate the data. Note that with this limited number of illuminations, the speckle average exhibits a non negligible inhomogeneity. We have considered data with an average global photon budget per pixel about 10^6, it will be specified if otherwise, so that Poisson noise is negligible.

2.3.1 Speckle illumination: separate deconvolution and joint blind-SIM

The first task in simulating the micrsocope is to generate the speckle patterns and the PSF. The PSF of the microscope and the speckle, displayed in Figures 2.2(a, b) and 2.2(c, d), are modeled using a simple scalar model. Noting the space variable $\boldsymbol{r} = \boldsymbol{r}_\parallel + z\hat{\boldsymbol{z}}$ where $\hat{\boldsymbol{z}}$ indicates the optical axis, the speckle is approximated by,

$$I_l(\boldsymbol{r}) = \int_D f(\boldsymbol{k}_\parallel) e^{i\phi_l(\boldsymbol{k}_\parallel)} e^{i\sqrt{k_0^2 - k_\parallel^2}\, z} e^{i\boldsymbol{k}_\parallel \cdot \boldsymbol{r}_\parallel} \mathrm{d}\boldsymbol{k}_\parallel, \tag{2.25}$$

where $k_0 = 2\pi/\lambda$ is the illumination wavenumber, $\phi_l(\boldsymbol{k}_\parallel)$ is an uncorrelated random variable uniformly distributed between 0 and 2π and D is a disk of radius $k_0\mathrm{NA}$. The point spread function is given by,

$$h(\boldsymbol{r}) = C \int_D f(\boldsymbol{k}_\parallel) e^{i\sqrt{k_0^2 - k_\parallel^2}\, z} e^{i\boldsymbol{k}_\parallel \cdot \boldsymbol{r}_\parallel} \mathrm{d}\boldsymbol{k}_\parallel, \tag{2.26}$$

where

$$f(\boldsymbol{k}_\parallel) = \begin{cases} 1, & \text{if } |\boldsymbol{k}_\parallel| \leq \mathrm{NA}k_0 \\ 0, & \text{otherwise} \end{cases}$$

and $C = 1/\int h(\boldsymbol{r})\mathrm{d}\boldsymbol{r}$.

In a first example of our simulation, we consider a thin fluorescent star-like sample in the $y = 0$ plane whose fluorescence density is defined by

$$\rho(x, y, z) \propto [1 + \cos(30\theta)]\delta(y), \tag{2.27}$$

where $\tan\theta = z/x$, see Figure 2.3(a). This kind of target permits an easy visualization of the resolution improvement as its spatial frequencies increase as one gets closer to the star center. To get an idea about the data being processed, we display in Figure 2.3(b) an image of the sample obtained under one speckle illumination.

In Figures 2.3(c,d) the widefield image and its deconvolution are shown. As expected, the image resolution is not isotropic, in contrast to that obtained with the same sample placed in the (xy) transverse plane[36]. The lack of resolution for the quasi-horizontal sample features is the signature of the tore-shaped support of the microscope optical transfer function $\hat{h}$[50]. The grainy aspect of the reconstruction stems from the residual inhomogeneity of the speckle average which is clearly visible in Figure 2.3(c).

The reconstructions obtained with joint blind-SIM and blind-SIM-SD are given in Figures 2.3(g) and 2.3(h), respectively. Apart from the presence of some hot spots in Figure 2.3(g) which deteriorates slightly the image rendering, both reconstructions exhibit similar performances. The transverse and axial resolutions are significantly better than that of the widefield image and comparable to that of the ideal confocal image, Figures 2.3(e) and 2.3(f). These observations, which have been confirmed on many other examples (not shown), leads to two important comments. First, when there is no *a priori* information on the illuminations except the homogeneity of their sum, blind-SIM-SD is a much better option than joint blind-SIM as it is faster and less prone to the apparition of hot spots. Hereafter, all the blind-SIM reconstructions will be performed with
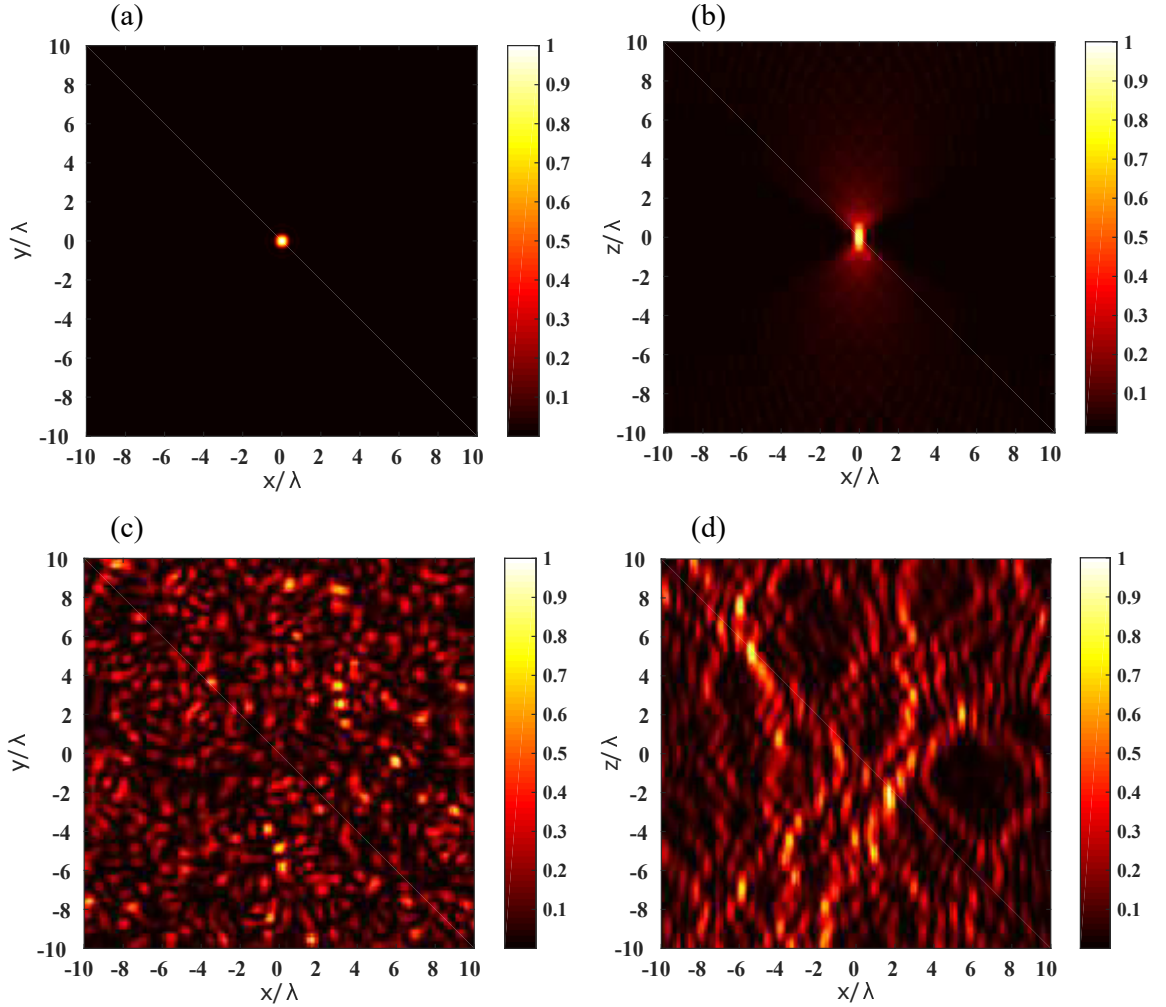
Figure 2.2 : *PSF and speckle pattern. Normalized PSF xy-view cut in the $z = 0$ plane (a) and xz-view cut in the $y = 0$ plane (b). Normalized speckle intensity xy-view cut in the $z = 0$ plane (c) and xz-view cut in the $y = 0$ plane (b).*

the blind-SIM-SD algorithm. Second, the blind-SIM-SD scheme corresponding to a simple positive deconvolution of each speckle image, the recovery of sample frequencies beyond the OTF cut-off can only be explained by the positivity constraint[51]. The better resolution of blind-SIM-SD reconstruction compared to the positive deconvolution of the widefield data stems from the more frequent activation of the positivity constraint on the speckle images than on the widefield one. Yet, it is observed that the recovery of the sample high spatial frequencies remains limited to the sample spectrum participating to the image formation Eq. (2.1). In our case, with a speckle generated with the same objective as the point spread function, the speckle images depend on the sample spectrum within the support of h^2. This property can explain the similarity between the blind-SIM and confocal images.

In Figure 2.4, we investigate more specifically the optical sectioning ability of blind-SIM-SD by considering a sample made of thin fluorescent transverse planes placed at various z, the
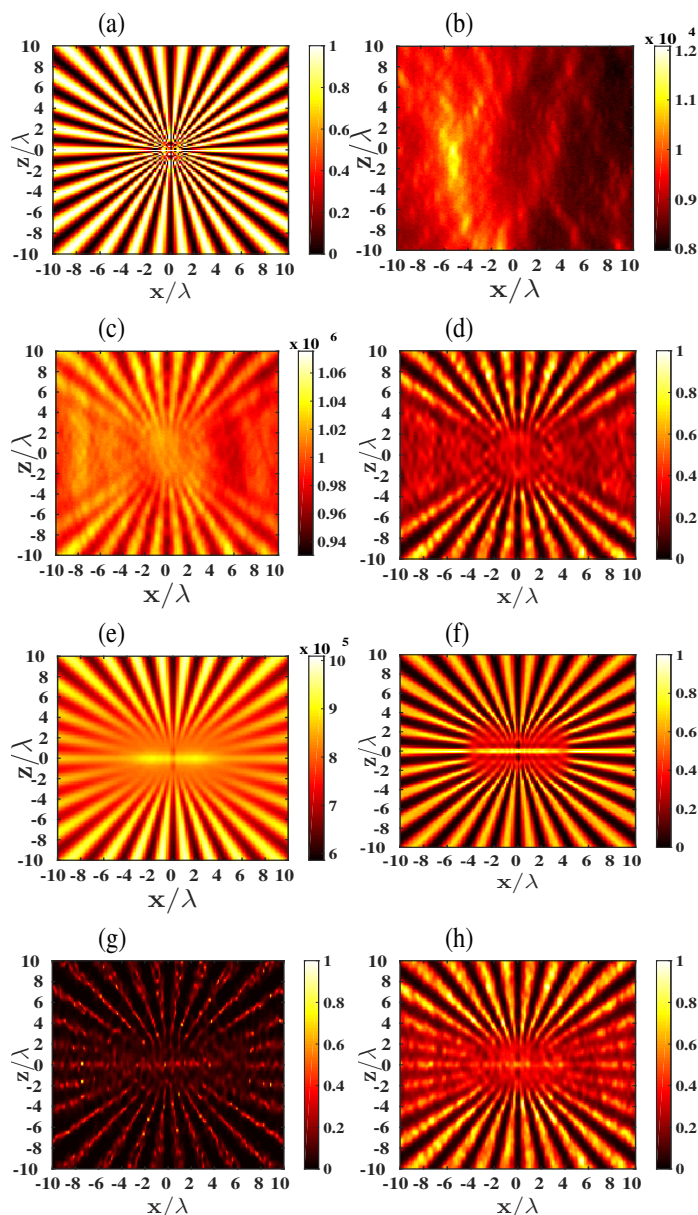
Figure 2.3 : *Reconstructions of a thin fluorescent (xz) plane with a oscillating radial fluorescence distribution (star-type sample). The sample is illuminated by 100 different speckles. (a) Fluorescence density of the sample. (b) Example of one intensity image obtained for a given speckle illumination. (c) Widefield image of the sample obtained by the summing the 100 speckles images. (d) Positive deconvolution of the widefield image (c). (e) Image of an ideal confocal microscope. (f) Positive deconvolution of the confocal image (e). (g) Reconstruction with the blind-SIM-SD algorithm. (h) Reconstruction with the blind-SIM-SD algorithm. In (b,c,e) the colorbar indicates the number of recorded photons. In (a,d,f-h) the colorbar indicates the normalized fluorescence density.*

smallest separation between the planes being 217nm. As in the previous experiment, the sample
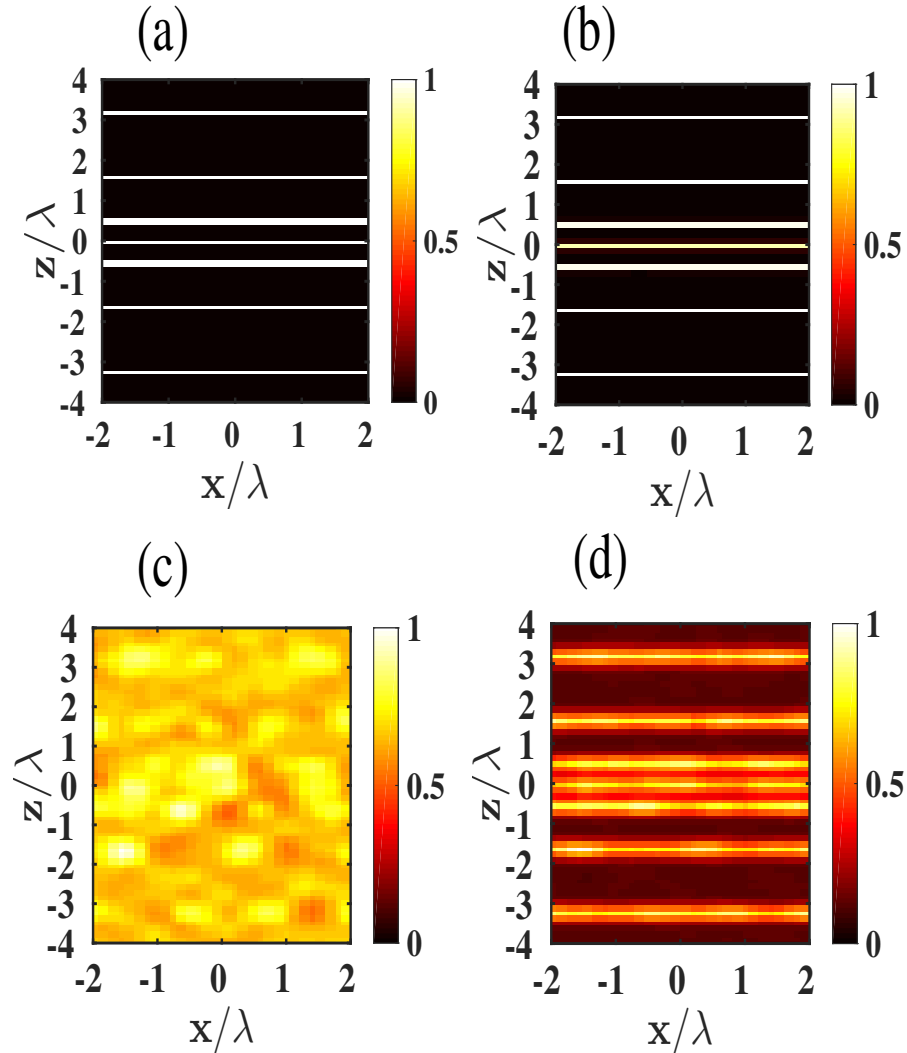
Figure 2.4 : *Reconstruction of a sample made of fluorescent thin (xy) planes placed at different distances from the focal plane. (a) Cut of the actual fluorescence distribution in the $y = 0$ plane. (b) Positive deconvolution of the ideal confocal microscope image. (c) Positive deconvolution of the widefield image. (d) Reconstruction with blind-SIM-SD. The blind-SIM approach yields an optical sectioning approaching that of the confocal image. The colorbar indicates the normalized fluorescence density.*

is illuminated by 100 different speckles. The xz-cut of the sample is depicted in Figure 2.4(a). In this example, the sample spatial frequencies are located along the z axis only. Since the optical transfer function of fluorescence microscopy removes all the sample spatial frequencies but 0 along the z- axis, the theoretical widefield image of fluorescent (xy) planes is a constant in the whole volume and so is its deconvolution. The axial cross-sectional profile is shown in Figure 2.5 and an axial resoution of 217nm is obtained with blind-SIM-SD (doted blue curve). In our experiment, the speckle average being still inhomogeneous, the deconvolution of the widefield image, Figure
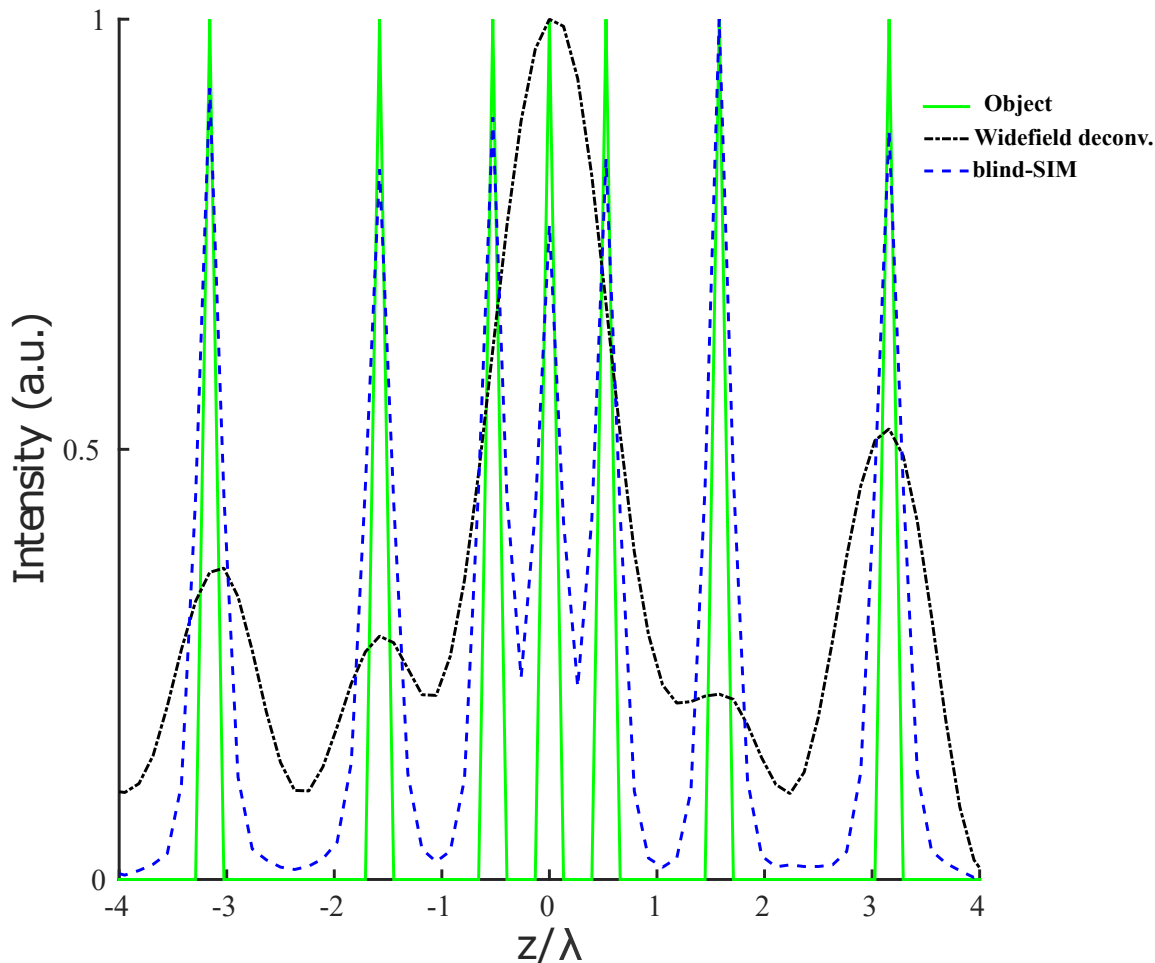
Figure 2.5 : *Optical sectioning profile from reconstruction of a sample made of fluorescent thin (xy) planes placed at different distances from the focal plane.*

2.4(c) is not a constant, also shown in Figure 2.5 dotted black line, but the fluorescent planes positions are not visible. In contrast the reconstruction obtained with blind-SIM-SD permits to distinguish the fluorescent planes, see Figure 2.4(d), with an accuracy approaching that of the confocal deconvolved image, Figure 2.4(b). Note that the spectacular accuracy of the deconvolved confocal image is attributable to the positivity constraint which is particularly efficient on sparse samples[51].

Last, in Figures 2.6 and 2.7 we study a more complex three dimensional sample made of beads inside and outside two halves of a big sphere. This specific geometry was chosen to investigate the performance of the imaging technique for surface-like objects (such as membranes) and volumic-objects. Cuts of the sample in the $y = 2.6\lambda$ and $z = -1.6\lambda$ planes are displayed in Figure 2.6(a) and Figure 2.7(a). The deconvolved confocal and widefield images and the blind-SIM-SD reconstruction in the two planes are shown in Figures 2.6(b-d) and 2.7(b-d), respectively. These results confirm the interest of the blind-SIM-SD approach as compared to the conventional widefield fluorescence
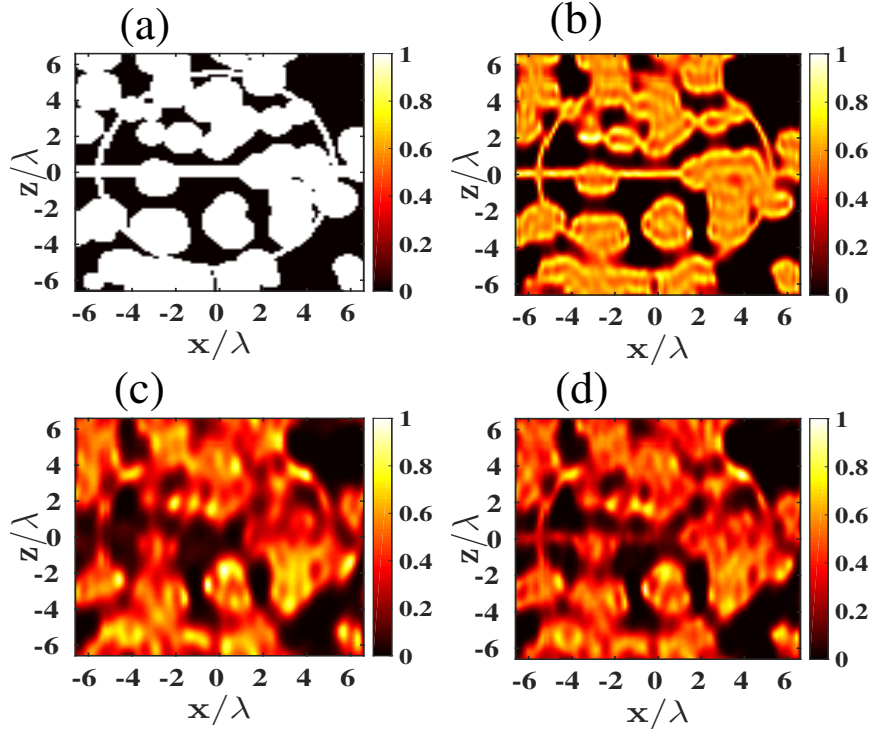
Figure 2.6 : *Reconstruction of a fluorescent sample made of beads inside and outside two halves of a big sphere (mimicking a membrane) (a) Cut of the actual fluorescence distribution in the $y = 2.6\lambda$ plane. (b) Positive deconvolution of the confocal microscope image. (c) Positive deconvolution of the widefield image. (d) Sample reconstruction with blind-SIM-SD. The blind-SIM approach yields an optical sectioning and axial resolution improvement approaching that of the confocal image. The colorbar indicates the normalized fluorescence density*

imaging. Except for the graininess aspect stemming from the residual inhomogeneity of the speckle averages, the blind-SIM reconstructions are roughly similar to that of the ideal confocal images and permit to distinguish both the surface-like and the volumic objects.

2.3.2 Speckle and harmonic illumination: separate deconvolution and filtered blind-SIM

So far, we have demonstrated the performance of the blind-SIM-SD reconstruction technique on images using unknown random speckle illuminations. For classical harmonic SIM images using *a priori* information on the illumination pattern, filtered bind-SIM, is expected to perform better as shown by Ayuk *et al.*[38] in 2D configuration. Here, we present the performance of our 3D filtered blind-SIM algorithm using a star-like sample in the $z = 0$ plane whose fluorescence density is defined by $\rho(x,y,z) \propto [1 + \cos(40\theta)]\delta(z)$, where $\tan\theta = y/x$ for $\theta \in [0\ \pi/2]$, shown in Figure 2.8(a). The 3D filtered blind-SIM reconstruction of 3D classical SIM experimental data is presented in Chapter 3.
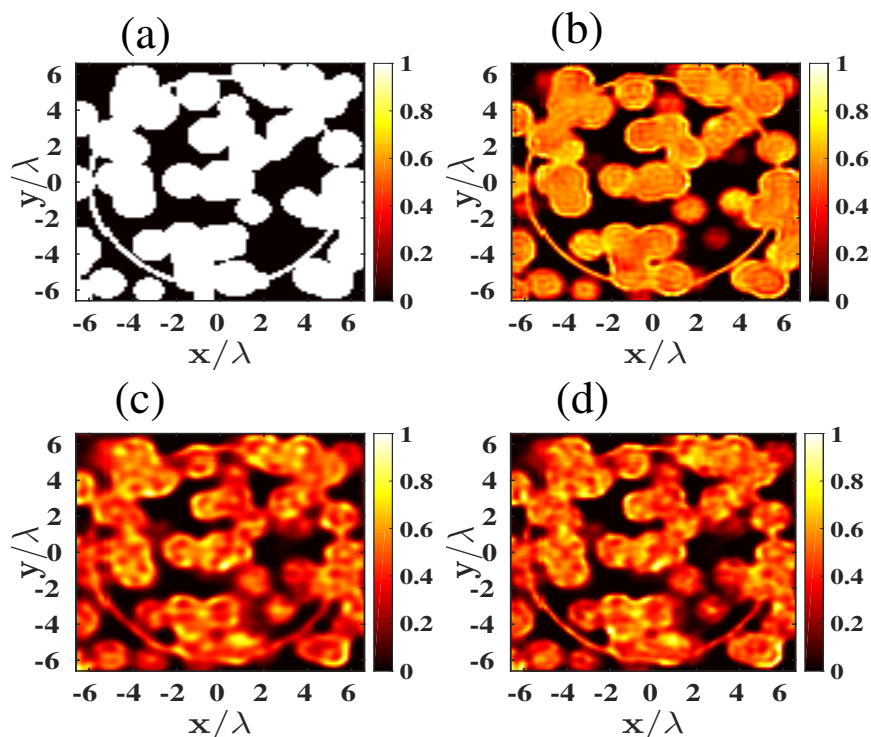
Figure 2.7 : *same as Figure 2.6 but the cut is done in the $z = -1.6\lambda$ plane. The blind-SIM approach yields a transverse resolution improvement comparable to that of the confocal image.*

The classical SIM images of the sample are obtained using grid patterns of 3 orientations, 120° separated, and 5 phases of 0, $2\pi/5$, $4\pi/5$, $6\pi/5$ and $8\pi/5$ whose frequencies are close to the OTF cutoff. The period of the grid is $\lambda/2 = 275$nm. The grid patterns are generated according to $I(r_\parallel, z = 0) = 1 + \cos(k_0 r_\parallel + \phi)$. for $r_\parallel = (x, y)$ and ϕ corresponds to the phases.

The widefield images in Figures 2.8(b) and 2.9(a) are obtained from the sum of the low-resolution images using classical SIM and 100 speckles respectively. The homogeneity of the widefield image in the former case is satisfied since the grid patterns are carefully designed to satisfy this condition while it requires an infinite number of speckles to satisfy the ideal homogeneity condition in the latter case. In order to inspect the sparsity of the low-resolution images of the sample, which highly drives the performance of blind-SIM-SD, the low-resolution images from a single speckle and a single grid pattern are shown in Figures 2.8(c,d). Since the sample contains dense structures the low-resolution images will be sparse (many zero spots in the image) if only the illumination patterns are sparse enough. The random speckle patterns give relatively sparser image than the sinusoidal grid patterns as can be seen in Figures 2.8(c,d).

Figures 2.9(b,c,d) show the reconstructions of the sample images using blind-SIM-SD on speckle data, blind-SIM-SD on classical SIM data and filtered blind-SIM respectively. The blind-SIM-SD improves the resolution under both speckle and classical SIM illuminations. Due to the sparser nature of the sample image using speckle patterns, compared to the images using the harmonic grid, blind-SIM-SD on speckles is better resolved but with some grainy spots due to the limited number of speckles (only 100 speckles). The resolution does not reach half the diffraction limit,
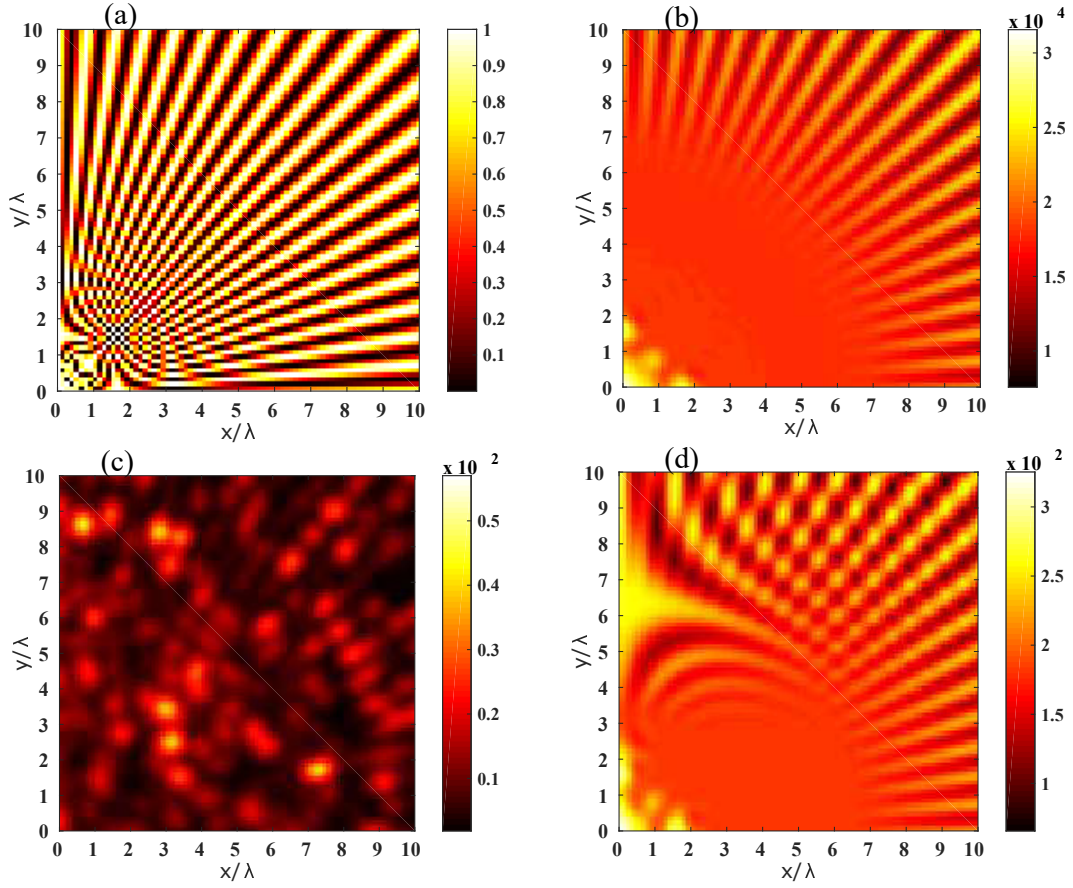
Figure 2.8 : *(a) Star-like object. (b) Widefield image. (c) Image of the sample using a single speckle pattern. (d) Image of the sample using a single light grid.*

which could theoretically be obtained with ideal SIM, due to the fact that the low-resolution speckle/harmonic SIM images are not sparse enough. The filtered blind-SIM, on the other hand, provides a significant improvement in the resolution. The resolution in filtered blind-SIM depends on the size of the filter mask used. If the filter mask radius is large enough, $\tilde{r}_{fm} >> k_0/10$, the filtered blind-SIM reconstruction result resembles the blind-SIM-SD, or equivalently the standard joint blind-SIM result, as if the illumination pattern were not known at all. On the other hand, if $\tilde{r}_{fm} << k_0/10$, the filtered blind-SIM reconstruction is equivalent to the reconstruction of SIM images with a perfect knowledge of the illuminations. From trial and error tuning of the filter mask size and investigating the filter blind-SIM reconstructions in terms of resolutions and artifacts, filter mask size of about $\tilde{r}_{fm} = k_0/10$ is optimum. In Figures 2.9, the green and blue curves on the star images correspond to the arc-periods of 350nm (the diffraction limit) and 175nm (half the diffraction limit) respectively.

In conclusion, we have developed 3D blind-SIM reconstruction strategies and studied the interest of speckle illumination for three-dimensional high resolution fluorescence microscopy (3D blind-SIM). First, the 3D version of the joint blind-SIM algorithm is developed. To speed up the
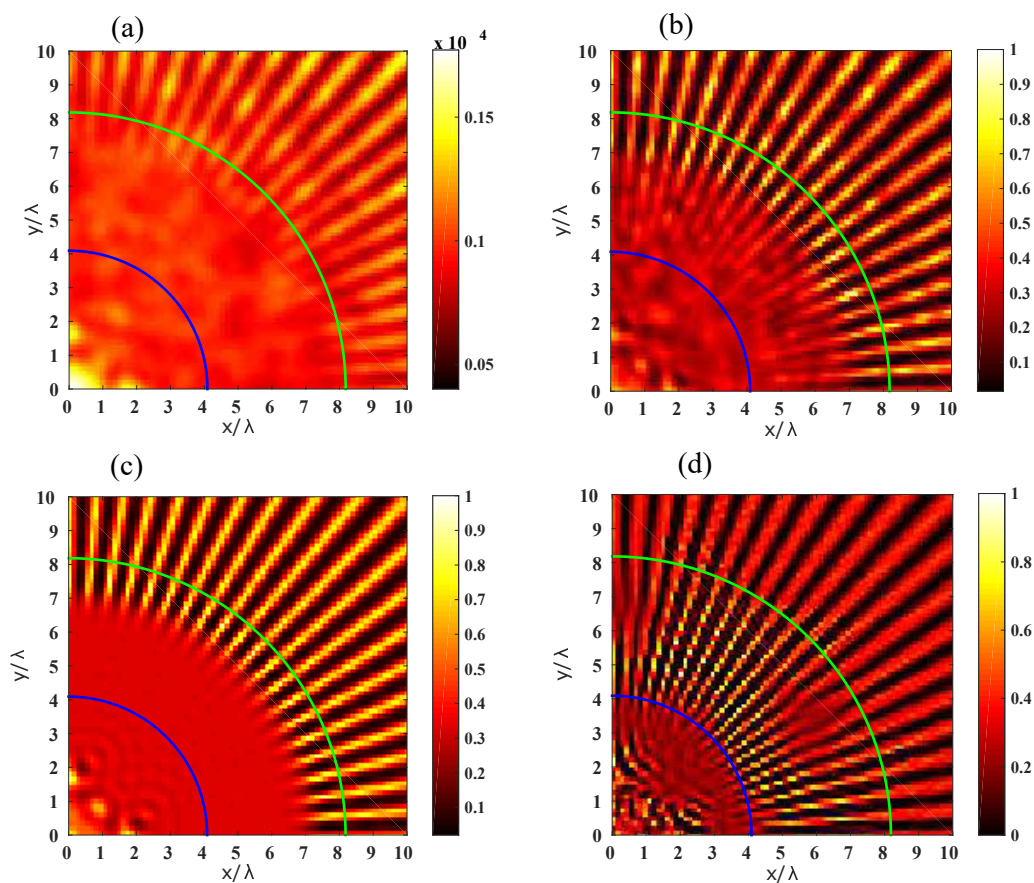
Figure 2.9 : *Filtered blind SIM reconstruction. (a) Widefield image. (b) Blind-SIM-SD on speckle SIM images. (c) Blind-SIM-SD on harmonic SIM images. (d) Filtered blind-SIM reconstruction.*

reconstruction technique, 3D blind-SIM-SD is adapted from the joint blind-SIM which can be used for speckle SIM as well as classical SIM reconstructions. For classical SIM, the filtered blind-SIM reconstruction strategy is powerful since it also uses some knowledge of the illumination patterns and reconstructs the sample under even strong distortions of the pattern.

2.3.3   Noise and number of speckle illuminations

Up to now, the simulations were performed with an important global photon budget in order to check the behavior of the algorithms in an optimal configuration. In the last example, we consider the same sample as the one used in Figures 2.6, 2.7 but we reduce the global average photon budget per pixel to 10^4. This value corresponds to an average of 100 photons per pixel per speckle image. In this case, the Poisson noise is important as illustrated by the xz-cut of a non-noisy, Figure 2.10(a), and noisy, Figure 2.10(b), single speckle image. The widefield image, obtained by adding the 100 speckle images, is displayed in Figure 2.10(c) and its deconvolution is shown in Figures 2.10(e,g). Figure 2.10(d) shows the positive deconvolution of the noisy single speckle image. Obviously, one cannot recover the fluorescent sample from just one single speckle image.

However, when the 100 deconvolved speckle images are summed, see Figures 2.10(f,h), the sample is recovered with a better resolution than that of the deconvolved widefield image.

To complete the analysis of blind SIM-SD performances, we have conducted, on the star sample depicted in Figure 2.3, a systematic study of the reconstruction accuracy with respect to the global photon budget and to the number of illuminations L. We define the error of the reconstructed fluorescence density $\hat{\rho}$ as,

$$err_\rho = \frac{\sum\limits_{n=1}^{N} \|\hat{\rho}(\boldsymbol{r}_n) - \rho(\boldsymbol{r}_n)\|^2}{\sum\limits_{n=1}^{N} \|\rho(\boldsymbol{r}_n)\|^2}. \tag{2.28}$$

Table 2.1 shows the role of the global photon budget on the reconstruction accuracy for $L = 100$ speckles. It is observed that, below 10000 photons, the reconstruction is severely impacted by the photon noise. On the other hand, above 10000 photons, the reconstruction error is mainly due to the speckle residual inhomogeneity.

Photon budget	10^6	100000	10000	5000
err_ρ	0.189	0.203	0.215	0.318

Table 2.1 : *Error on the reconstruction of the star sample depicted in   2.3 versus the global photon budget (average number of photons per pixel for the whole experiment). The number of illuminations is taken as $L = 100$.*

Table 2.2 shows the influence of the number of illuminations on the reconstruction error. The photon budget per image pixel is taken equal to 10000 so that the photon noise is negligible. We observe that the amelioration brought about by the increase of illuminations is significant up to 100 speckles but remains marginal beyond that limit. This behavior was to be expected as the standard deviation of the speckle average decreases slowly as $1/\sqrt{L}$.

Number of speckles	200	100	50	20
err_ρ	0.186	0.202	0.266	0.313

Table 2.2 : *Same as table 1, versus the number of illuminations (almost no photon noise)*

Increasing the number of illuminations strongly satisfies the homogeneity constraint and thus improves the amelioration. The homogeneity of the sum of the speckle illuminations can be measured using the coefficient of variation (CV), defined as the ratio of the standard deviation (σ_{S_L}) to the mean (μ_{S_L}) of the sum of L illuminations where S_L is the sum of L speckle illuminations. A fully developed single speckle illumination has ideally $CV = 1$ while a perfectly homogeneous illumination has $CV = 0$. Table 2.3 summarizes the coefficient of variations for the sum of selected number of illuminations from 1 to 400.
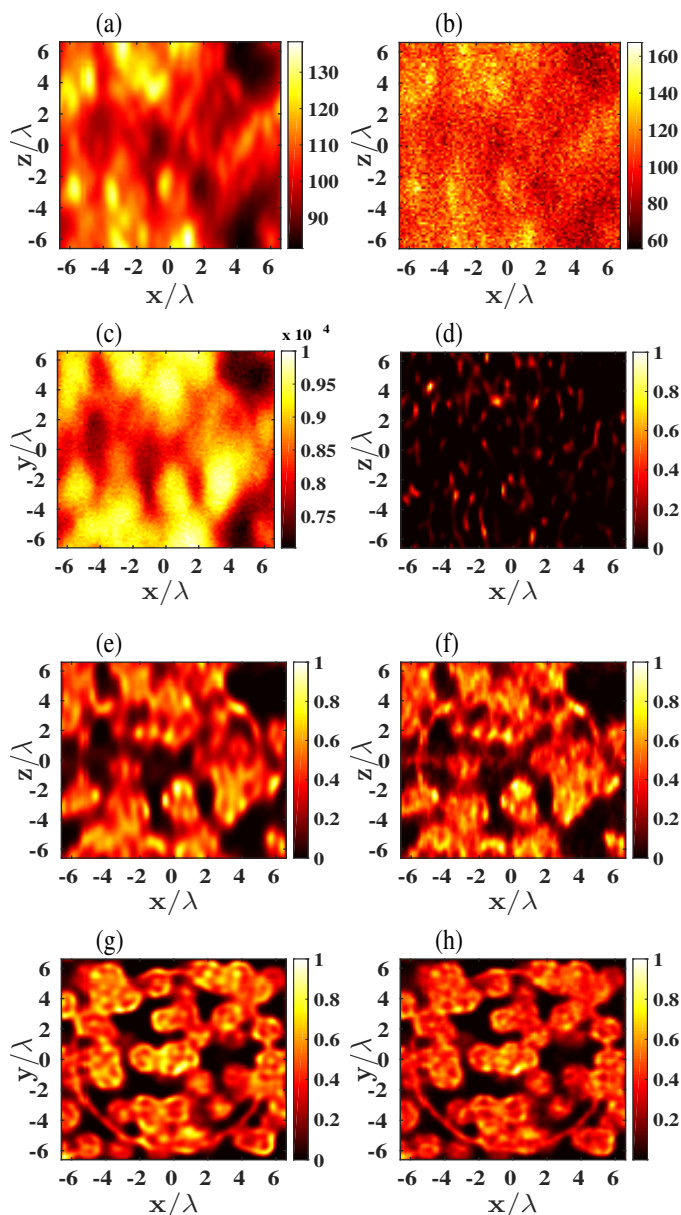
Figure 2.10 : *Reconstructions of the same sample as that of Figure 2.6 from data corrupted with realistic Poisson noise. (a) Single speckle image without noise in the $y = 2.6\lambda$ plane. (b) Same as (a) but the data are corrupted with Poisson noise. (c) Noisy widefield image obtained by summing the 100 noisy speckle images. (d) Positive deconvolution of a single speckle image in the $y = 2.6\lambda$ plane. (e) Positive deconvolution of the widefield image in the $y = 2.6\lambda$ plane. (f) Blind-SIM-SD reconstruction in the $y = 2.6\lambda$ plane. (g) Positive deconvolution of the widefield image in the $z = -1.6\lambda$ plane. (h) Blind-SIM-SD reconstruction in the $z = -1.6\lambda$ plane. In (a,b,c) the colorbar indicates the number of photons. In (d-h) the colorbar indicates the normalized fluorescence density*

These results, in agreement with that of Figure 2.10, confirm that blind SIM-SD can be used in realistic microscopy experiments with a limited number of illuminations and a reasonable global

Number of speckles, L	400	200	100	50	20	1
μ_{S_L}	0.685	0.666	0.594	0.575	0.493	0.111
σ_{S_L}	0.076	0.082	0.088	0.094	0.109	0.109
$CV = \sigma_{S_L}/\mu_{S_L}$	0.111	0.123	0.148	0.163	0.221	0.981

Table 2.3 : *Coefficient of variation as the measure of homogeneity of sum of speckle illuminations*

photon budget. More details about the physical implementation and generation experimental speckle patterns will be discussed in the next chapter.

2.3.4   Supplementary notes on the reconstruction procedures

The convolution process constitutes the main part of the computation in all our algoirthms. This convolution is implemented using 3D fast Fourier transform (FFT). Therefore, if the data has sharp edges at the borders, the reconstructions contain boundary discontinuities and some ringing artifacts. To avoid them, a smooth boundary with PSF width is included to the image frame before reconstruction. This means that the sample features in borders not meaningful. To smooth the boundaries we mainly used a trapezoidal-shape window generated using a product of hyperbolic tangent functions as,

$$w(x,y) = 1/4\big[\tanh\big(\frac{x-a}{b}\big) - \tanh\big(\frac{-x-a}{b}\big)\big]\big[\tanh\big(\frac{y-a}{b}\big) - \tanh\big(\frac{-y-a}{b}\big)\big],$$

where the coefficient a controls the boundary size and b controls the smoothing slope. Smoothing is particularly important for experimental data since the contribution of the sample features outside the field of view is significant in producing sharp boundaries. For synthetic data, since the domain of a simulated object is user defined, the borders of its image is not very sharp due to the convolution operation by the smooth PSF during imaging.

In terms of computation speed, the blind-SIM-SD is way faster than the joint blind-SIM and filtered blind SIM algorithms. The joint blind-SIM and filtered blind-SIM have L unknown coefficients. These coefficients are numerically minimized at every iteration, which significantly increases the computational time of joint blind-SIM and filtered blind-SIM techniques. In addition, L gradients are calculated in every iteration for the former. The speed of blind-SIM-SD is promising for seamless live reconstruction during image acquisitions. As FFT is the main part of the process the computational efficiency per iteration is given by $\mathcal{O}(N\log N)$, where N is the number of voxels in the data. For example, using a standard computer (Intel(R) Core (TM) i5-4670 CPU @3.4GHz, 16GB RAM), 200x200x4 pixels stack takes 45s per iteration for 100 illuminations with joint blind-SIM while it takes 4s per iteration for blind-SIM-SD for the same number of illuminations.

For the joint/filtered blind-SIM algorithms the widefield image is used as the initial estimate of the corresponding fluorescence density, $\rho_0 = \xi_0^2$ while the auxiliary functions with respect to L illuminations are assumed to be 1. And for blind-SIM-SD, similarly, the widefield image is used as an initial estimate for the product of the illumination and the fluorescence density, $q_l = \eta^2 = (\xi_l i_l)^2$. Once the initial estimates are set, the sample is iteratively estimated until the cost functional
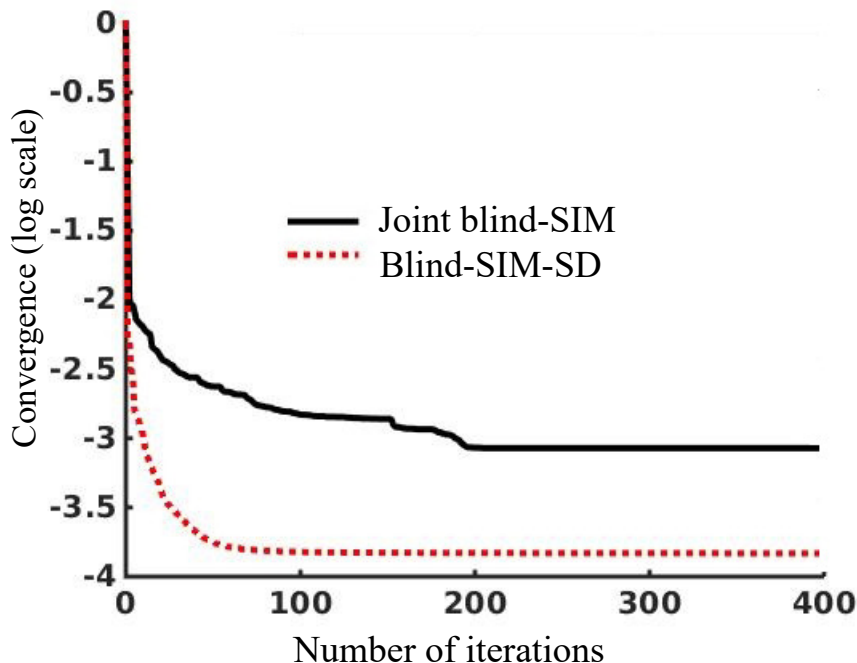
Figure 2.11 : *Convergence of joint blind-SIM and blind-SIM-SD*

.

reach the plateau. Since the conjugate-gradient is a descent method, the continued progress of the minimization is assured throughout the iterations. Figure 2.11 shows the convergence of the joint blind-SIM (black) and blind-SIM-SD (dotted red) algorithms. The blind-SIM-SD reaches the plateau faster than the joint blind-SIM algorithm. It is important to stop the iteration once it reaches the plateau or before as further iterations way deteriorate the reconstructions with the adding of high spatial frequencies stemming from noise. This "eye" preventive stop is equivalent to a Tikhonov regularization [52,53].

2.4 Investigating 3D blind-SIM microscopy

The 2D speckle/classical SIM image of thin biological samples is modeled simply as the convolution of the fluorescence emission with the detection PSF as $M = \rho I_l * h$. However, this model is not always true for 3D data depending on the 3D data acquisition configuration. In advanced multifocus acquisition microscopes where the images of the sample at various axial positions are recorded without any sample translation, the convolution model is appropriate. Recently, such multifocus microscopes are practically demonstrated using diffractive optical elements or beam splitters to image multiple focal planes [45,54,55]. The transversal and axial improvements in resolution in blind-SIM has been investigated in the preceding section assuming the use of such advanced microscope setups.

Unfortunately, most widefield imaging modalities record information from one focal plane at a time and needs an axial scanning of the object for 3D data acquisition, thus the object does not

"see" the same 3D illumination as the 3D image is recorded, and the convolution model is incorrect. In this section, we investigate the 3D image acquisitions based on both imaging configurations using a star-like object in the xz-plane at $(y = 0)$ and 100 speckle illuminations. The 3D speckle SIM data is then reconstructed using the blind-SIM-3D algorithm. The slice-by-slice blind-SIM-SD reconstruction is tested on the 3D data obtained from slice-based modality.

2.4.1 Multifocus 3D model

In multifocus or remote focussing configurations[45,54,55] the illumination pattern remains fixed in the object volume while recording the 3D data. The imaging system can be mathematically modelled as

$$
\begin{aligned}
M_l(r_\parallel, z) &= \int\int \rho(r'_\parallel, z') I_l(r'_\parallel, z') h(r_\parallel - r'_\parallel, z - z') \mathrm{d}r'_\parallel \mathrm{d}z' \\
&= \rho(r_\parallel, z) I_l(r_\parallel, z) * h(r_\parallel, z),
\end{aligned} \tag{2.29}
$$

where $(r_\parallel, z) = (x, y, z)$ and $(r'_\parallel, z') = (x', y', z')$ are the coordinates of the datasets relative to the focus of the objective lens. It is clear in this model that the 3D data of each speckle illumination M_l is obtained as the convolution of the fluorescence ρI_l with the PSF h. Therefore extracting information from the images can be computed through systematically deconvolving by the PSF, as in our blind-SIM algorithms.

The advancement of such imaging modalities is very important in biological microscopy due to its apparent advantages such as improving the speed of 3D acquisition and avoiding the perturbation on the sample that can when during mechanically scanning the sample.

2.4.2 Standard axial scan-based 3D model

Practically in most widefield configurations, 3D data is acquired by axially scanning the sample with respect to the focal plane of the microscope objective. The 3D scanning imaging microscopy can be mathematically represented as

$$
M_l(r_\parallel, z) = \int\int \rho(r'_\parallel, z' + z) I_l(r'_\parallel, z') h(r_\parallel - r'_\parallel, 0 - z') \mathrm{d}r'_\parallel \mathrm{d}z', \tag{2.30}
$$

assuming the coordinate $(r_\parallel, z) = (x, y, z) = (0, 0, 0)$ corresponds to the center of the focus of the microscope objective as a reference point. Equivalently with change of variables, $u' = z' + z$,

$$
M_l(r_\parallel, z) = \int\int \rho(r'_\parallel, u') I_l(r'_\parallel, u' - z) h(r_\parallel - r'_\parallel, z - u') \mathrm{d}r'_\parallel \mathrm{d}u'. \tag{2.31}
$$

Eqs. (2.30) and (2.31) are basically the same, the former assuming the object is axially scanned through the illumination while the latter assumes the illumination scanned through the object, or equivalently representing the physical translation of the the sample stage and the microscope objective respectively. These equations are different from the model $M_l = \rho I_l * h$. Therefore reconstruction using 3D deconvolution based algorithms is a priori incorrect, particularly for thick samples. It requires more dedicated mathematical analysis to transform this model into a convolution process, for example assuming the illumination pattern is separable into transversal and axial functions as
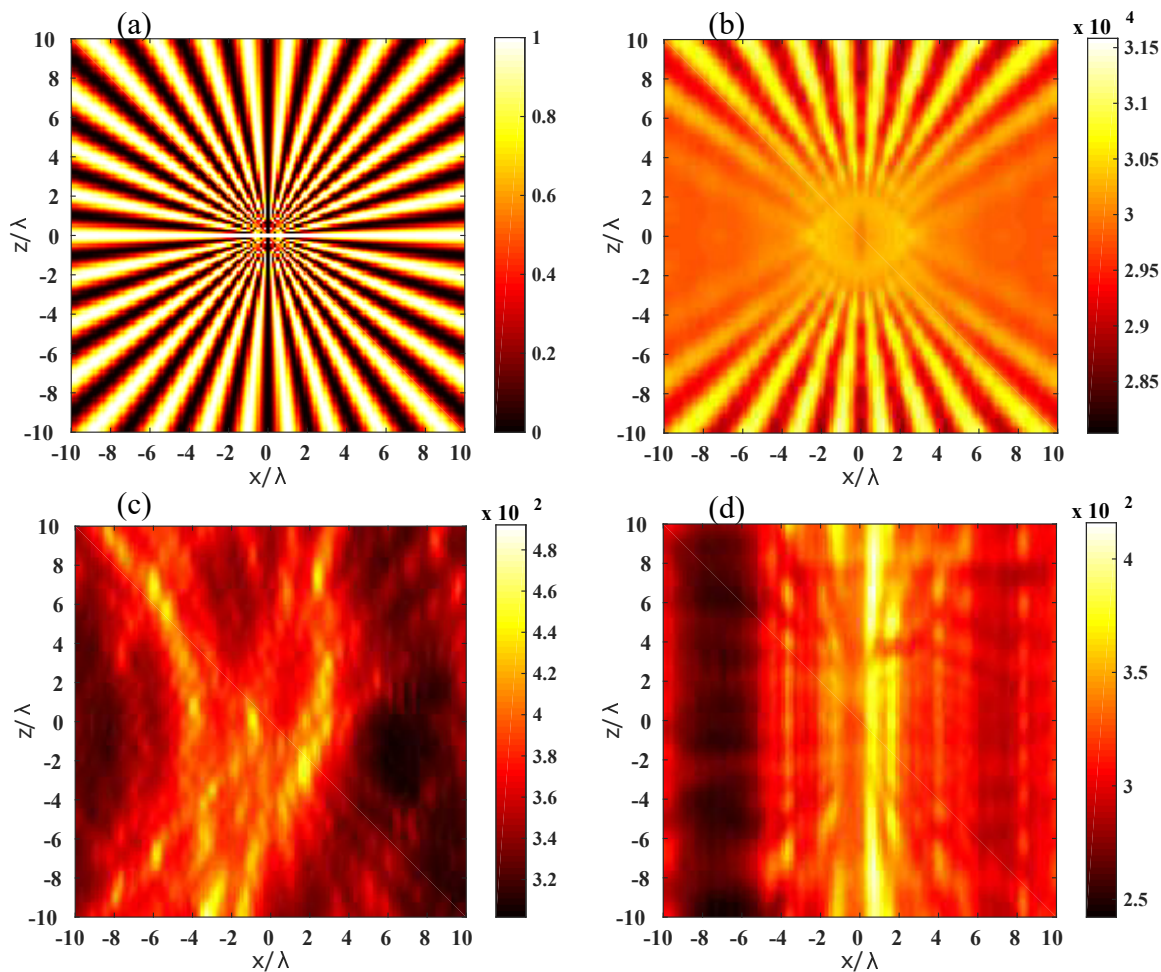
Figure 2.12 : *Imaging model illustration. (a) Star-like object xz-cut at y=0. (b) Widefield image. (c) Low-resolution image of a single speckle pattern multifocus model. (d) Low-resolution image of a single speckle pattern of axial scanning model.*

in[7]. However, if one assumes the illumination is invariant along z as $I(r_\parallel, z - d) = I(r, 0)$, which is quite plausible for thin objects, Eq. (2.31) will be

$$M_l(r_\parallel, z) = \int \int \rho(r'_\parallel, u') I_l(r'_\parallel, u') h(r_\parallel - r'_\parallel, z - u') \mathrm{d}r'_\parallel \mathrm{d}u', \tag{2.32}$$

which is a convolution process. Of course, there will not be axial resolution gain by assuming the illumination invariant along z. However, some optical sectioning can be obtained because of the shift of the object in the (k_x, k_y) plane and one get the improvement of transverse resolution as usual. Therefore the 3D blind-SIM algorithm is expected to give some optical sectioning for thin samples recorded using scan-based microscope configurations.

Figure 2.12 shows the object (a), the widefield image of the object (b), the image of the object in multifocus model using a single speckle (c) and the image of the object in a scan-based model using a single speckle (d). The vertical line appearing in the scan-based images comes from the
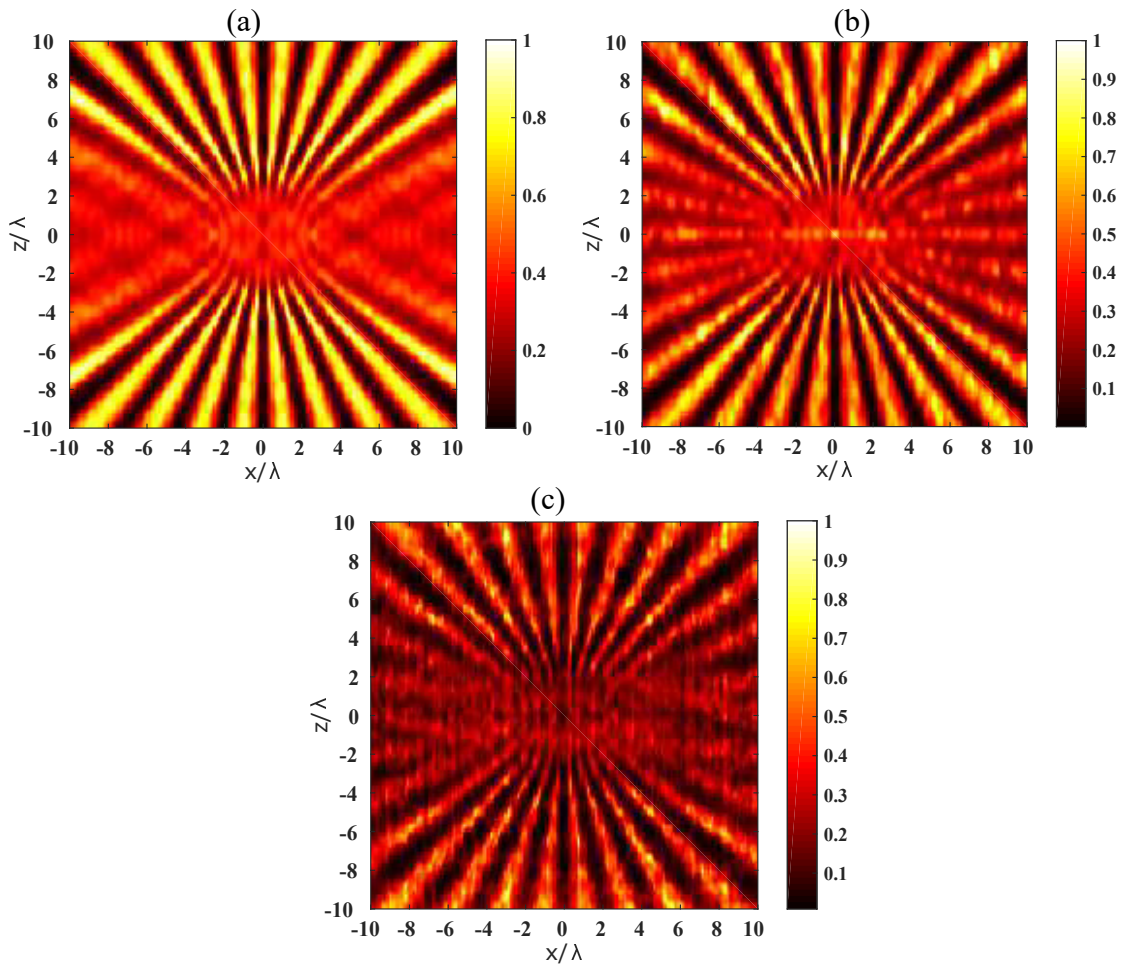
Figure 2.13 : *Reconstructions for multifocus and axial scanning models. (a) Widefield deconvolution. (b) blind-SIM-SD in multifocus model. (c) 3D blind-SIM-SD on images from axial scanning model.*

fact that the object is translated through the speckle for every axial position. So, the dark and bright spots of the speckle at the focus plane plays a major role. The speckle SIM images are recorded in both models using 100 patterns.

Figure 2.13 shows the reconstructions of the mages from both models. The deconvolution of the widefield image is shown in Figure 2.13(a).The blind-SIM-SD reconstruction of the speckle SIM images of multifocus model, Figure 2.13 (b), shows the resolution improvement and optical sectioning, as discussed in earlier sections. To investigate the consequences of 3D blind-SIM reconstructions on scan-based models we have tested blind-SIM-SD as shown in Figure 2.13 (c). The blind-SIM-SD algorithm on scan-based images provides some optical sectioning but with artifacts, the error mainly coming from the fact that the reconstruction is based on the multifocus model. The artifacts are clearly visible around the axial center of the image. Since the slice by slice re-

construction does not account the axial illumination variation, since it assumes axial illumination invariant, There is very little gain in optical sectioning.

2.5   Conclusion

Reconstruction of SIM images based on the theoretical knowledge of the excitation patterns may introduce artifacts in the estimated sample due to the possible illumination distortions. Inspired by the blind-SIM reconstruction technique that has been developed by Mudry *et al.*[36] for 2D data, we have developed 3D blind-SIM reconstruction strategies that retrieve the sample fluorescence density without the knowledge of the illumination patterns. We extended the existing 2D joint blind-SIM algorithm into 3D which enables one to estimate the 3D density of fluorophores and the intensities simultaneously. The 3D blind-SIM algorithm provides optical sectioning and transverse resolution not only for harmonic SIM images but also for speckle SIM data which requires no control of the individual illumination patterns.

Even though the 3D joint blind-SIM algorithm is efficient in terms of resolution, it is computationally intensive, particularly for 3D data. In order to accelerate the inversion procedure, we have proposed a simpler blind-SIM Separate Deconvolution (blind-SIM-SD) technique which consists in summing the deconvolution, under positivity constraint, of each speckle image. We obtained an improved reconstruction of the sample fluorescence that compared favorably to that of joint blind-SIM and ideal confocal microscope. The resolution obtained highly depends on the sparsity of the low-resolution images obtained by the excitation intensity patterns since it is enhanced by the positivity constraint. The sparsity of the low-resolution image comes either from the sparsity of the illumination itself or the nature of the sample. This can be understood analogously with STORM imaging techniques, and in fact, the blind-SIM-SD reconstruction technique can also be used in reconstructing STORM images.

The joint blind-SIM and blind-SIM-SD algorithms can be used not only for the speckle SIM but also for classical SIM which uses periodic light patterns, the only assumption on the illumination patterns being the homogeneity of their sum, yet with a resolution worse than that obtained with the classical algorithms using known illumination. For classical-SIM using harmonic light patterns incorporating some information about illumination patterns is valuable. We developed a 3D filtered blind-SIM which confines the iterative estimation of the illuminations in the vicinity of the Fourier peaks, in the Fourier space of the theoretical light field. The filtered blind-SIM reconstruction strategy is powerful in estimating the sample under even strong distortions of the illumination pattern.

Finally, we have investigated the 3D imaging modalities of 3D harmonic/speckle SIM. The standard 3D imaging system records a sequence of 2D images by scanning the object through the illumination (scanning-based 3D-imaging model). For 3D-SIM this model does not match the mathematical model, $M = \rho I_l * h$. For thicker objects, other imaging modalities such as multifocus[45] should be considered for our reconstruction techniques to be valid.

Blind-SIM: practical implementation

Contents

3.1 Introduction

Using a carefully calibrated and stable setup to control the illumination patterns, Structured Il-lumination Microscopy (SIM) improves both transverse and axial resolution[7] over the diffraction limited widefield images. Precise knowledge of the excitation pattern is indeed critical during re-construction. Knowing the perfect illumination pattern at the focal plane within the sample is, of course, a challenge due to the possible distortions of the patterns by the optical system and the sample itself. We have already presented, see chapter 2, the blind-SIM reconstruction techniques that provide optical sectioning and transverse resolution improvement beyond the diffraction limit without requiring precise control of the illuminations. The blind-SIM reconstruction techniques allow extending the use of illuminations from the harmonic patterns to random speckles. To allevi-ate the precise control of classical SIM illuminations and to ease experimental complexity, speckle illumination microscopy has been recently demonstrated[36,56]. The sparse nature of the speckle illuminations, which in turn produces low-resolution images with sparsity, enhances the resolution when reconstructtion is performed under positivity constraint. The only requirement on the speckle illuminations is that the temporal average of all the speckle illuminations is homogeneous over the sample. In this case, the sum of all low-resolution images is considered as a brightfield/widefield image.

In this chapter, we present speckle illumination microscopy, here after called speckle SIM, to investigate biological structures with resolution beyond the diffraction limit. Multiple speckle patterns are sequentially projected onto the sample and low-resolution speckle SIM images are acquired for each pattern. Speckle SIM images are recorded for multiple biological samples, such as podosomes, actin filaments, vimentin protein filaments, micro beads and standard calibration samples. Super resolved blind-SIM reconstructions are performed the images of these samples and the results are compared to other superresolution techniques such as STED. The speckle super resolved speckle SIM is also compared with the harmonic SIM reconstructed through blind-SIM and filtered blind-SIM methods. With the advantages of experimental setup simplicity and no need for illumination pattern control, speckle SIM provides a spatial resolution almost identical to the one of harmonic SIM. The speckle patterns can be generated using a setup based on a diffuser or spatial light modulator (SLM).

3.2 Practical speckle imaging setups

3.2.1 Diffuser-based setup

The simplest way of generating speckle patterns is passing the coherent laser beam through the diffuser. The diffuser can be a plastic sheet or flat glass with a rough surface that can randomly perturb the wave front of the laser beam. Speckle SIM requires the acquisition of many low-resolution images with various patterns, their sum giving the widefield image. Therefore, in order to generate multiple speckle patterns, the diffuser must be held with a motorized rotating and translating device. This means the diffuser has to be translated and/or rotated after every low-resolution image acquisition in order to generate a speckle pattern which is different from the

other patterns. The translation is along the plane orthogonal to the optical axis while the rotation axis is the optical axis. Figure 3.1 shows the diffuser-based speckle SIM setup. In this setup 3D acquisition is done by axial scanning of the sample for every speckle pattern. A faster way of obtaining 3D images which in addition correspond to the 3D convolution model would consist in producing an instant focal stack of 2D images using a multi-focus system or remote focusing with deformable mirror[45,57]. The diffuser-based speckle SIM setup has some physical challenges for
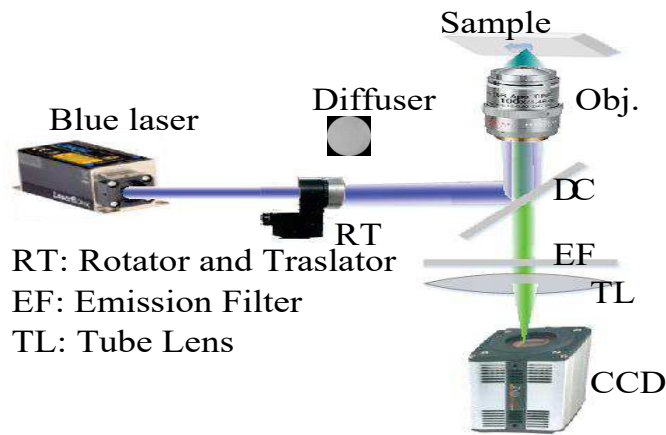
Figure 3.1 : *Diffuser-based speckle SIM setup.*

imaging biological samples. In order to generate randomly distributed speckle patterns, the diffuser has to be sufficiently translated to avoid the overlapping surfaces while recording speckle SIM images sequentially. The mechanical limit of the translating device, therefore, limits the number of speckle patterns that can be generated (<100). In addition, most of the time is consumed by the mechanical rotation and translation of the device which holds the diffuser and this makes the acquisition time longer. It takes about 0.3seconds for rotating the diffuser by 30.0^o and about 2.2seconds for 1.25mm translation of the diffuser. The translation and rotation steps are determined based on the laser beam width which interacts with the diffuser surface so that spatially independent speckle patterns can be obtained. The objective of rotation and translation of the diffuser is to pass the laser beam through a different surface of the diffuser at every acquisition. Apparently, the mechanical rotation and translation of the diffuser radically increases the image acquisition time which leads to photo bleaching and photo toxicity of the fluorophores. It is therefore practically challenging to use this setup for biological samples. In order to avoid these strong physical challenges, an alternative fast speckle setup is highly desirable.

3.2.2 SLM-based setup

To improve the acquisition speed the low-resolution speckle SIM images are recorded with an alternative fast speckle imaging technique using spatial light modulators. The fast-SIM setup for classical SIM using Spatial Light Modulator (SLM) has been proposed by Lu-Walther *et. al.*[58] and recently modified by T. Mangeat (Universitié de Toulouse, UPS, LBCMCP, 31062 Toulouse, France) in order to provide a fast, multicolor, 2D/3D SIM setup. The light from the laser block is

transmitted through a single mode polarization maintaining fiber to the SLM. The SLM produces grating patterns with the polarization of the different diffraction orders controlled by quarter wave plate (QWP) and the azimutual polarizer. The passive filter is then placed at the Fourier plane of the SLM to remove unwanted diffraction orders, as shown in reference[58]. The classical SIM setup is then adapted to be able to measure not only classical SIM but also speckle SIM images. The fast speckle SIM setup, shown in Figure 3.2, is simply modified from the fast classical SIM setup by removing some of the components such as the Fourier filter masks. This advanced setup, therefore, can measure classical SIM and speckle SIM images alternatively.
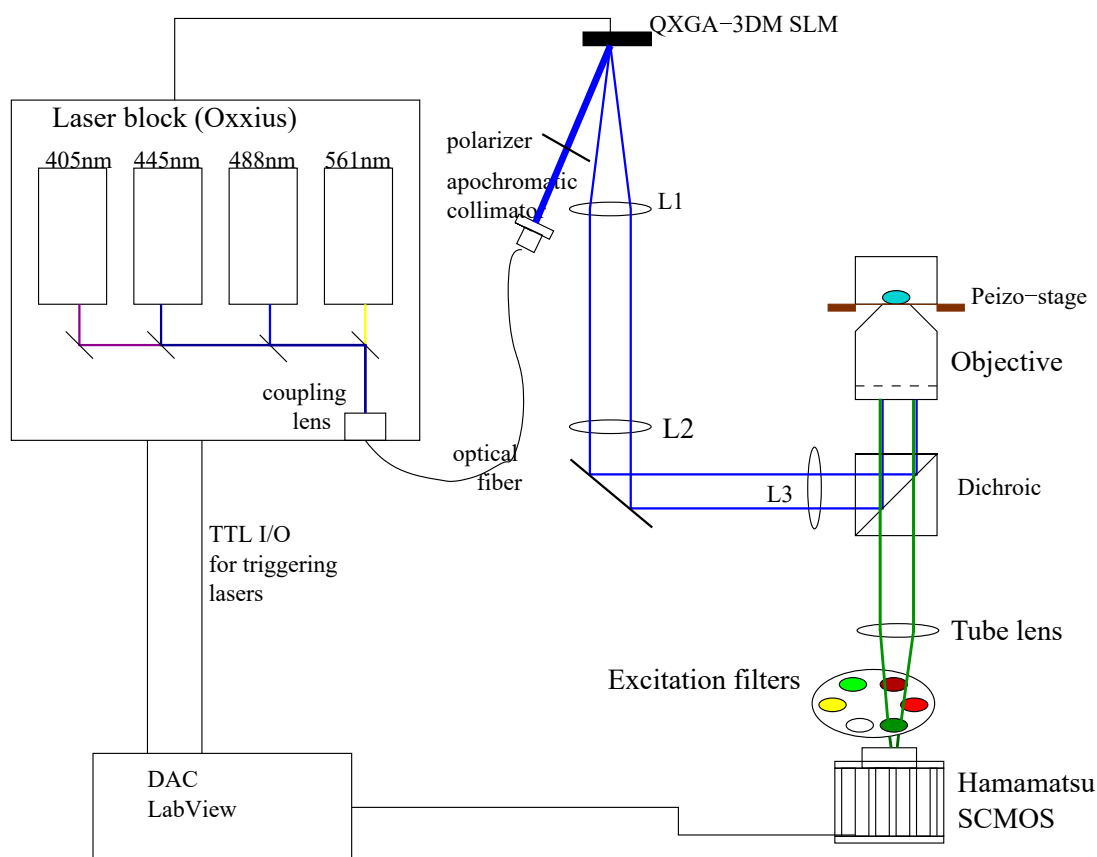
Figure 3.2 : *SLM-based speckle SIM setup. L1,L2,and L3 are achromatic doublets.*

The random binary speckle patterns are loaded on the SLM circuit board (ferroelectric LCOS, QX3GA, 4th dimensions) which is placed at the conjugate of the sample plane, as shown in Figure 3.2. Using this setup low-resolution images using 100 to 1000 random speckles can be recorded sequentially with a temporal resolution of 4ms to 15ms per frame. The experimental setup is also upgraded to multi-color speckle imaging. The speckle illumination microscopy is not only simpler from the experimental implementation point of view but also has low photo-toxicity and introduces less out-of-focus blur compared to the bright-field imaging approaches. The low-resolution speckle SIM images are sequentially captured by Orca Flash 4 sCMOS camera

which promises high speed readout. The laser, the sCMOS camera, the SLM and the stages are synchronized by the trigger timing of LabVIEW.

3.3 Data acquisition and processing

3.3.1 Sample preparations

All the biological samples are prepared in the bio-labs of Universitié de Toulouse, UPS, LBCMCP, 31062 Toulouse, France. Each sample is prepared following the immunofluorescence protocol, the procedure depending on the type of the sample. The cells are placed on the top of the coverslip. The fixation of the samples is done with 4% Paraformaldehyde in phosphate-buffered saline (PBS). Waiting 20 minutes after fixing, the permeabilization step follows, and the cells are incubated in PBS containing 0.5% Triton x-100, the most popular detergent for improving the penetration of the antibody. The cells are then incubated with 1% stain buffer of BSA (Bovine Serum Albumin protein) in PBST for 30 minutes to block unspecific binding of the antibodies. Then, the primary antibody is added at the correct dilution and put at $4°C$ overnight. Next, cells are washed in PBS. The second antibody is then added at the correct dilution at room temperature. After decantation the cells are washed again. After about an hour, the staining process is started. The final procedure is to mount the coverslip on the microscope glass with a drop of the mounting medium and perform an appropriate sealing of the coverslip to prevent drying and movement of the sample under the microscope.

3.3.2 Data acquisition

Multiple low-resolution speckle SIM images are recorded sequentially for each plane of the sample. For 3D acquisition of speckle SIM images, a different set of speckle patterns can be projected into the sample during every axial scan. But this is limited by the total number of patterns available on the SLM, the maximum being 1024. In both uses, the data acquisition does not follow the 3D deconvolution model as the illumination is kept fixed with respect to the sample. The emission by the sample fluctuates as the speckle pattern varies during acquisition. Even though a large number of speckle SIM acquisitions is required, the acquisition time of the system is fast (4ms to 15ms per frame). In addition, the fact that only parts of the sample illuminated by the hot speckle spots emit in each acquisition significantly decreases photo bleaching and photo toxicity. This, on the other hand, decreases the possible distortions that may come from the bleaching effects.

3.3.3 Data processing

Once the stack of low-resolution speckle SIM images is collected, the super resolved image is obtained using blind-SIM reconstruction algorithms. Blind-SIM permit to overcome any artifact coming from the illumination. On the other hand, it is not immune against PSF distortion (due to the sample or the optical setup). This is very critical since the reconstruction algorithms are highly dependent on the PSF, and this PSF is repeatedly used in the algorithms.

The PSF can be defined either analytically by utilizing a mathematical model of diffraction, or empirically by acquiring a three-dimensional image of microspheres. For example, the 3D PSF can be calculated using the classical diffraction based model of Gibson and Lanni[59], which can be obtained from the plugins of free imaging softwares such as ImageJ. The analytical PSF is simple to obtain, but it does not consider all the aberrations of the system. Unlike the experimentally measured PSF, the analytical PSF assumes axial and radial symmetry. This means it misinterprets the distribution of the blur in the raw image. The empirical PSF, on the other hand, deviates from the perfect symmetry. The deviation is commonly produced from misalignments in the setup and spherical aberrations from the mismatch between the refractive indices of the objective immersion medium and the mounting medium[60]. In the reconstructions of our experimental data, we have used an experimental PSF measured using $100nm$ beads.

3.4   Data reconstruction and resolution analysis

3.4.1   Data reconstruction

In Chapter 2, the principles of blind-SIM reconstruction techniques are presented using synthetic data. In this section, standard harmonic illuminations and speckle illuminations are investigated using real biological samples. Following Chapter 2, we apply blind-SIM-SD to the experimental data. Once each low-resolution image is deconvolved independently with the positivity constraint, the final image is then constructed by just simply taking the average of the reconstruction of raw images. Constructing the final image from the standard deviation image of separately deconvolved images with positivity constraint is also tested on speckle data.

3.4.2   Speckle SIM

The first interesting sample for resolution analysis is the Argo-SIM calibration sample from the ARGOLIGHT company[61]. This sample is marked with Alexa488 with $488nm/520nm$ excitation and emission wavlengths respectively. The speckle SIM images are taken using 100x, 1.49NA oil immersion objective. Figure 3.3(a) shows the widefield image of the sample, from the sum of the100 raw speckle SIM images, where the sample is composed of pairs of parallel lines between which the separation increases by 30nm starting from top right to bottom left. The widefield deconvolution is shown in Figure 3.3(b). After blind-SIM-SD, Figure 3.3(c), the two closest lines start to be visible at 97nm separation. The resolution limit is possibly between 97nm and 130nm, i.e 1.6 to 2.2 better than the diffraction limit resolution of 210nm. The respective diagonal red line profiles across the parallel lines of Figure 3.3(a-c) is plotted in the same figure (i-iii) respectively. Looking at the figures and the plot profiles, we can define the resolution limit of speckle SIM. The respective resolutions are 162nm for widefield deconvolution, 97nm to 130 nm for blind-SIM-SD.

Second, we have considered 100nm fluorescent beads using the same objective, and wavelength parameters. As a reference, the widefield image, obtained from the sum of 100 speckle SIM images is given in Figure 3.4(a). The resolution of the reconstructions improves from the widefield deconvolution (b) to blind-SIM-SD (c). The profile plots across the small, vertical red bar (d)
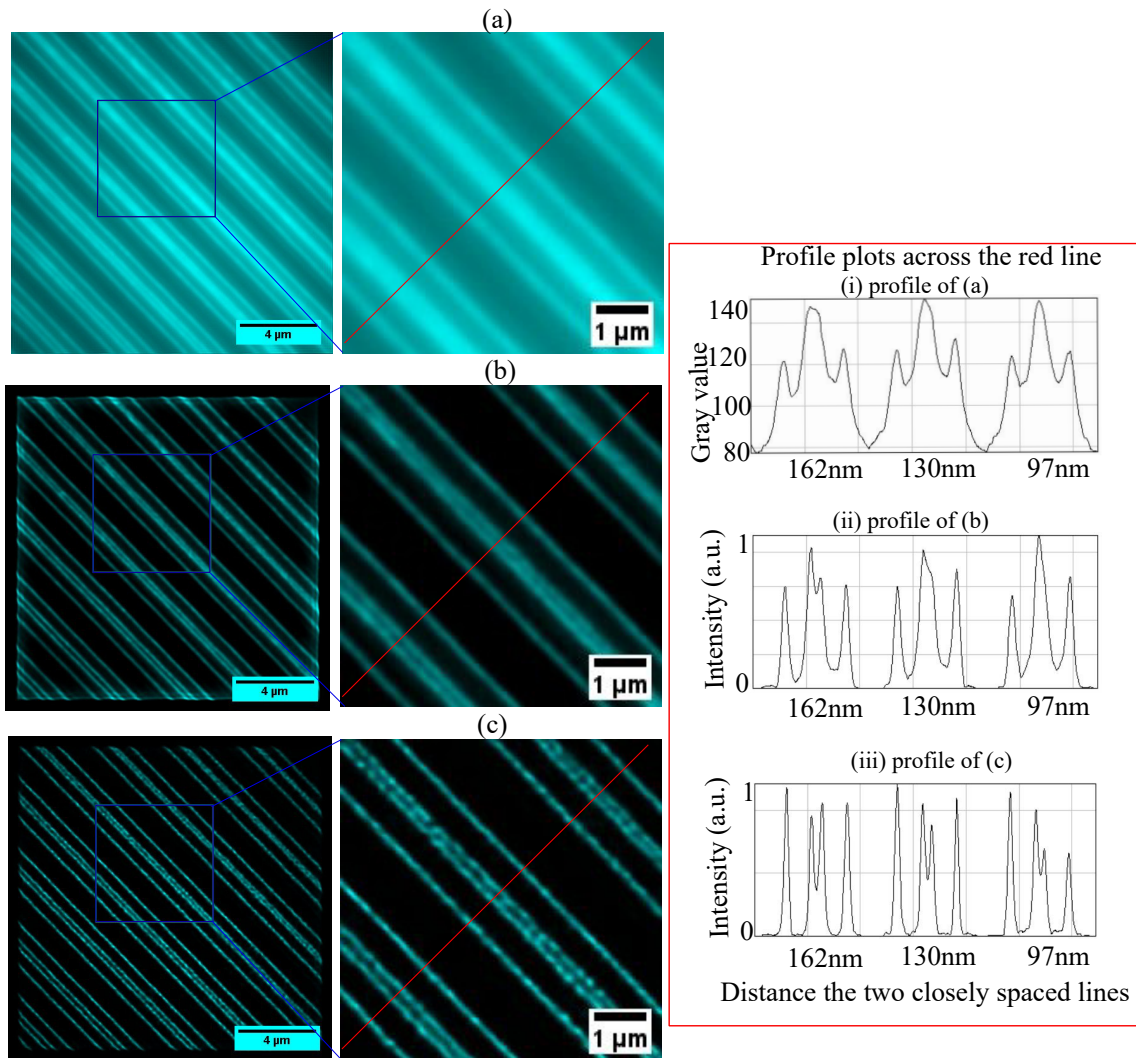
Figure 3.3 : *Argolight calibration sample speckle-SIM reconstructions. (a) Widefield image. (b) Widefield deconvolution. (c) Blind-SIM-SD. Plots from (i)-(iii) shows the profiles across the red line of figures (a)-(c) in respective order.*

clearly illustrates the power of blind-SIM-SD in isolating the beads compared to the widefield image and the widefield deconvolution.

So far we have considered sparse samples whose images are made sparser using speckle illuminations. This is the most favourable case for obtaining superresolution. Now, let's study the performance of the blind SIM on dense actin and vimentin filament structures. Figure 3.5(a-c) show the widefield image, the widefield deconvolution and blind-SIM-SD respectively. Since this actin sample is very dense, the sparsity of speckle SIM image comes mainly from the speckle patterns. The blind-SIM-SD Figure 3.5(c) shows more resolved filaments with better contrast compared to the widefield image and the widefield deconvolution. The raw images are taken with x100, 1.49 NA oil immersion objective. And the excitation and emission center wavelengths are 488nm and 520nm respectively.
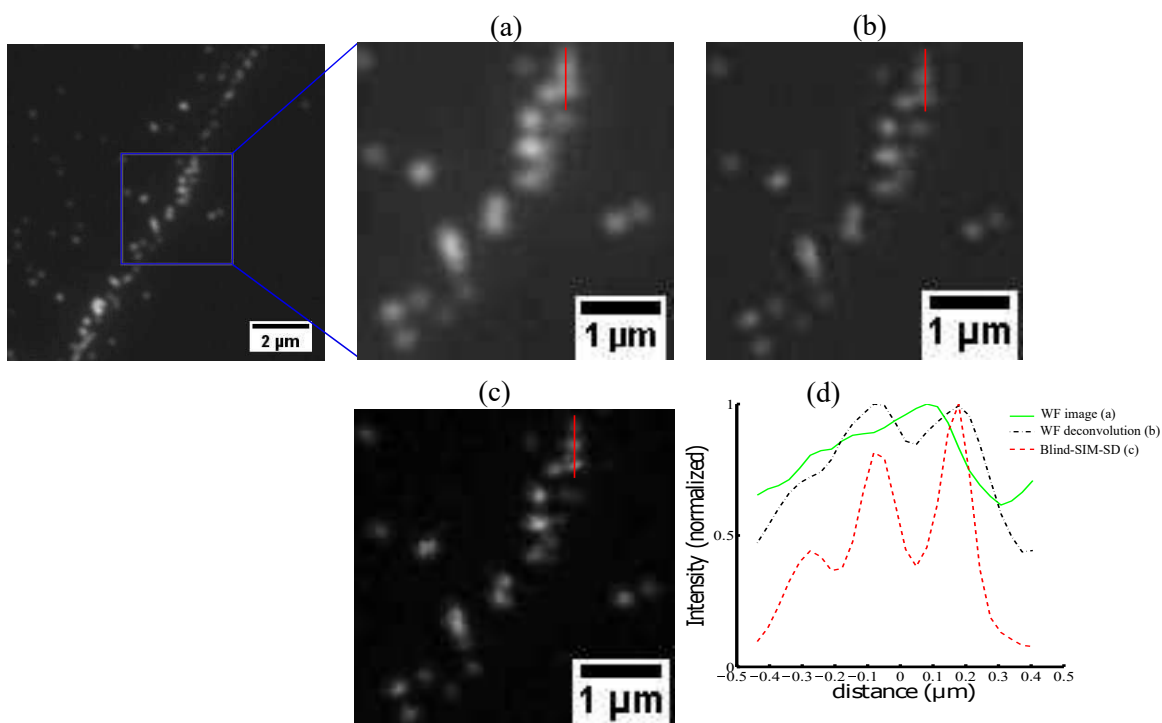
Figure 3.4 : *100nm microspheres speckle-SIM reconstructions. (a) Widefield image. (b) Widefield deconvolution. (c) Blind-SIM-SD (mean) . (d) profile plot across the vertical red bar of figures (a-c).*
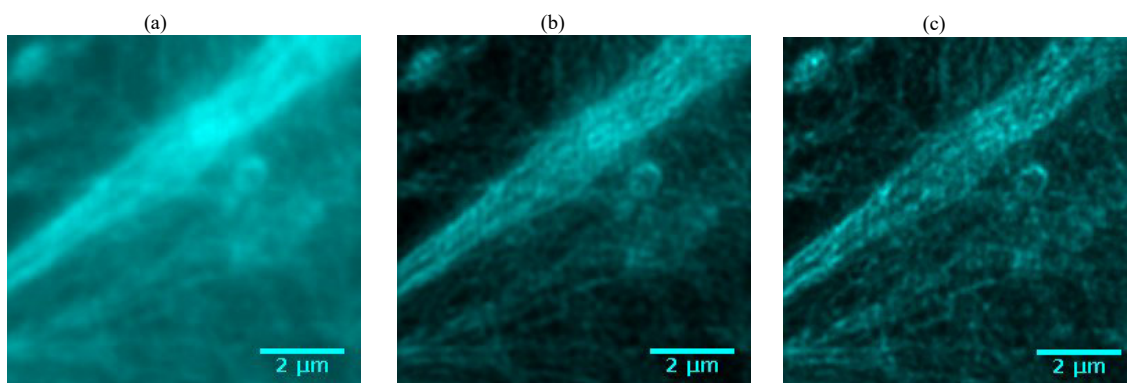
Figure 3.5 : *Dense actin speckle-SIM reconstructions. (a) Widefield image. (b) Widefield deconvolution. (c) Blind-SIM-SD.*

Let's see another 2D sample which is the vimentin filament proteins. This sample is taken using a 60x, 1.4NA oil immersion objective. Again, 488nm/520nm is the excitation/emission wavelength. From Figure 3.6, the contrast and resolution of blind-SIM-SD (c) is clearly better than the widefield deconvolution (b) and the widefield image (a).
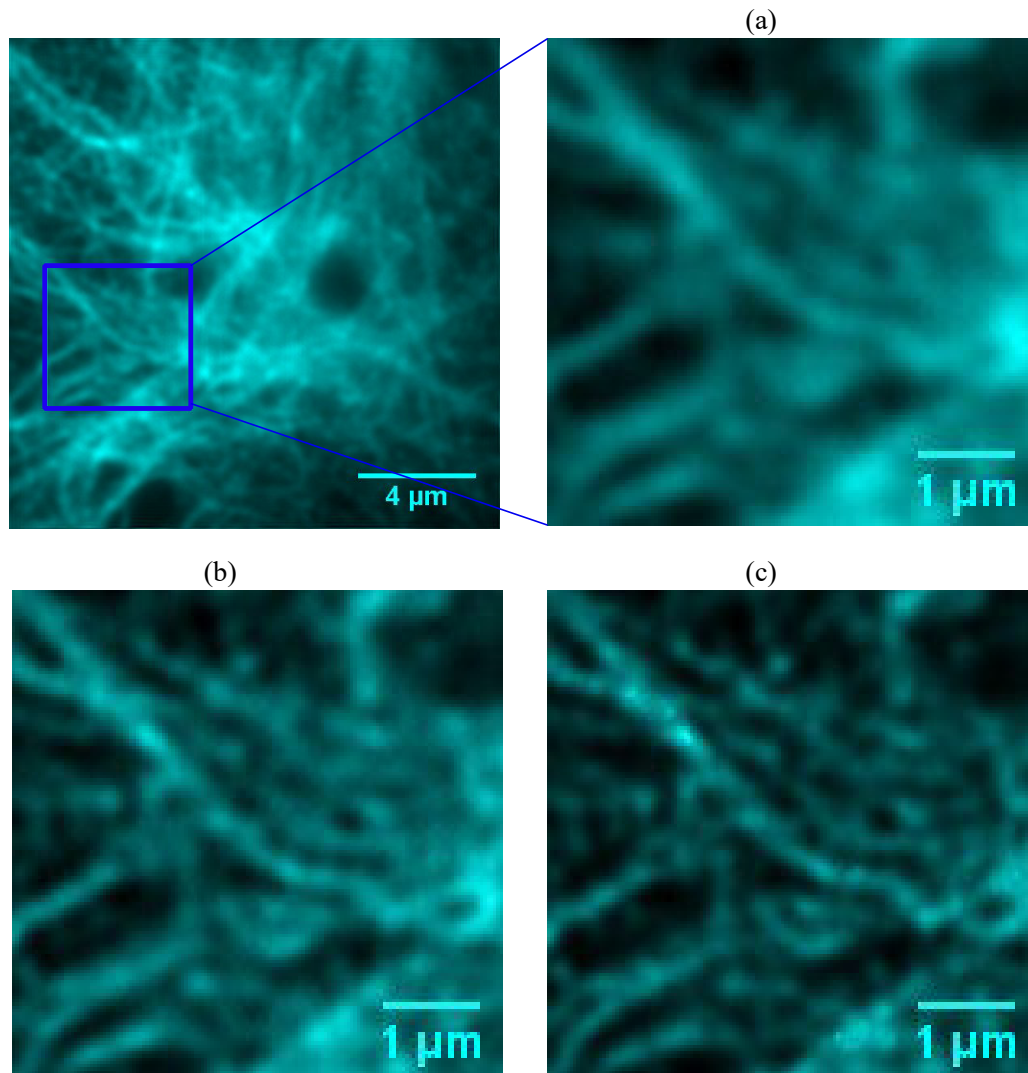
Figure 3.6 : *Vimentin speckle-SIM reconstructions. (a) Widefield image. (b) Widefield deconvolution. (c) Blind-SIM-SD .*

3.4.3 2D speckle SIM and harmonic SIM

In this section, we compare the resolutions of SIM under harmonic and speckle illuminations using the same type of sample. To do so, we recorded raw images of the same sample of vimentin filaments using speckle and harmonic illuminations alternatively using the SLM-based speckle/harmonic SIM setup. We use 30 harmonic patterns (6 orientations and 5 phases) and 800 speckle patterns. Figure 3.7 shows a single speckle pattern (a) and the low-resolution speckle SIM image (c), as well as the classical SIM patterns (6 orientations, single phase) (b) and a raw harmonic SIM image (d). The sample is excited at 561nm wavelength and emits at 650nm. An oil immersion x60, 1.4NA excitation/collection objective is used.

For reference, the widefield image is depicted in Figure 3.8(a). The blind-SIM-SD on speckle SIM raw images Figure 3.8(b), the blind-SIM-SD on classical raw SIM images Figure 3.8(c) and filtered blind-SIM on harmonic SIM images Figure 3.8(d) all have impressive resolution compared

(a)

(b)

(c)

(d)
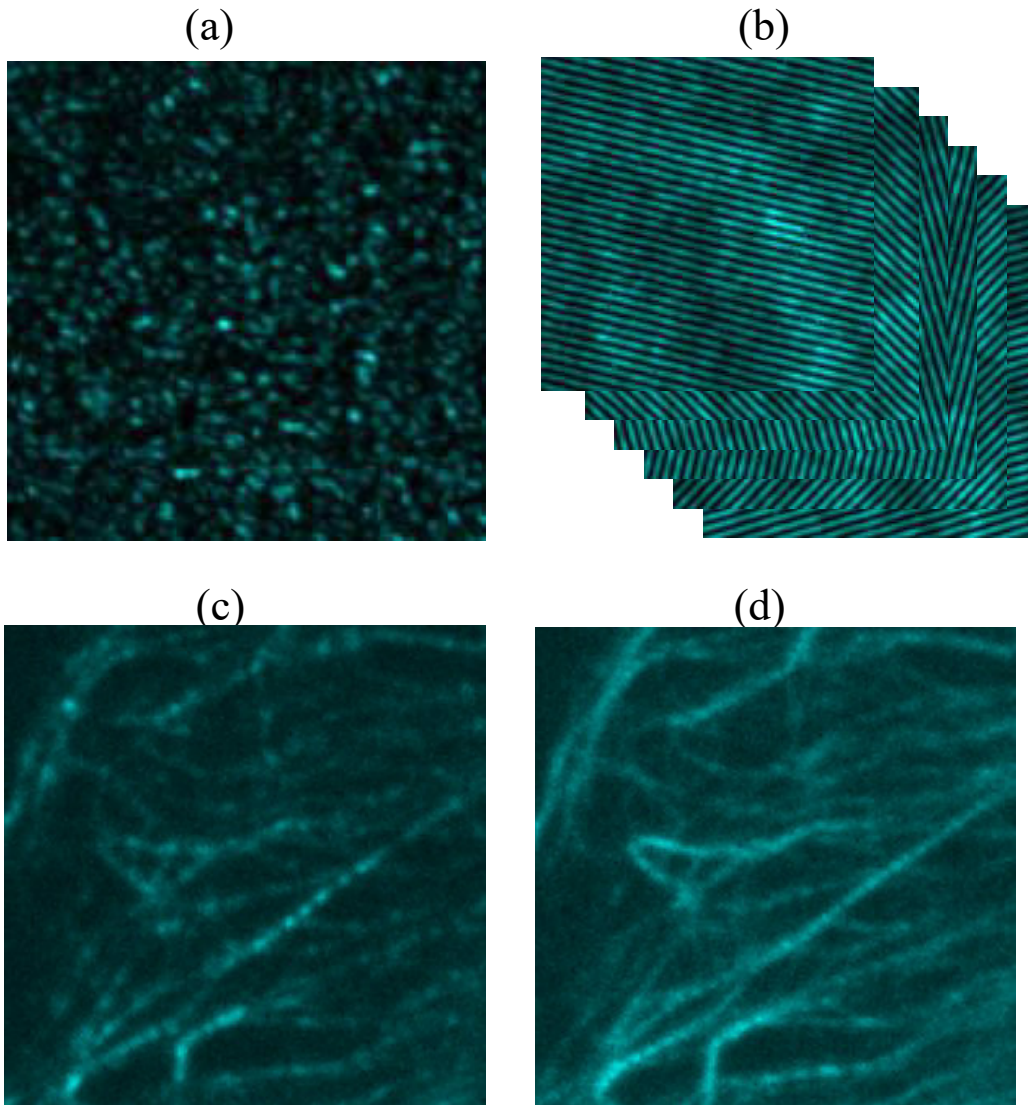
Figure 3.7 : *Harmonic SIM and speckle patterns (mirror reflection) and raw single pattern images. (a) Single speckle pattern. (b) Harmonic grid patterns (6 orientations). (c) Raw speckle-SIM low-resolution image. (d) Raw harmonic-SIM low-resolution image.*

to the widefield image. The profile plots across the red bar on the images is also presented to in Figure 3.8. For comparison, the deconvolved STED image of the same sample is presented in Figure 3.9. Due to the implementation differences of STED and SIM, we observed some inaccuracies in the positions of the peaks between the profile curves of deconvolved STED and blind-SIM. This curve is, indeed, still helpful to compare the resolutions of blind-SIM reconstructions to STED.

The filtered bind-SIM provides a resolution which is comparable to the deconvolved STED resolution. The speckle blind-SIM-SD is slightly better than blind-SIM-SD of harmonic SIM data. This comes from the fact the speckle illumination patterns have more sparsity compared to the harmonic grid patterns. However, the harmonic grid patterns satisfy the homogeneity constraint
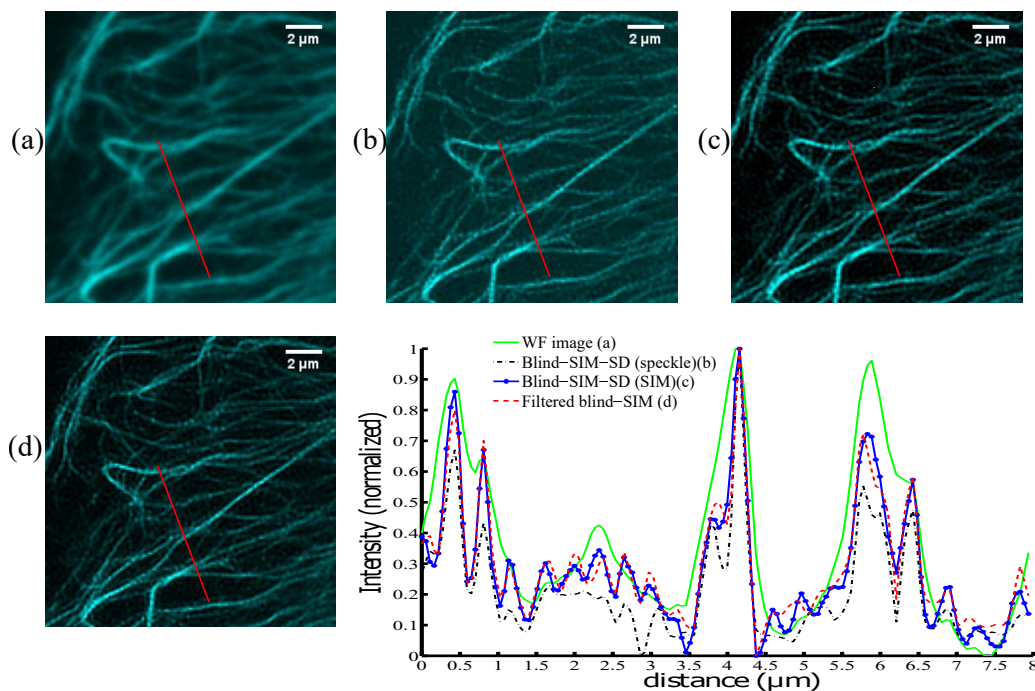
Figure 3.8 : *Blind-SIM reconstructions of harmonic and speckle SIM.(a) Wide-field image. (b) Blind-SIM-SD (speckle). (c) Blind-SIM-SD, harmonic SIM. (d) Filtered blind-SIM. The profile plots are shown across the red line for images (a-d).*
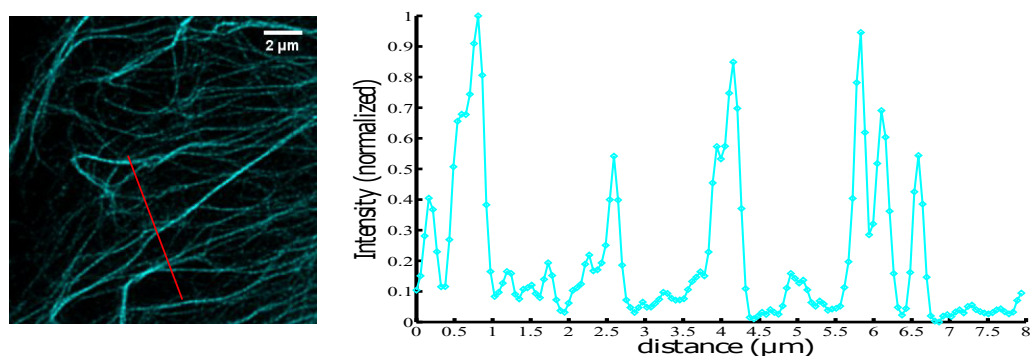
Figure 3.9 : *Deconvolved STED image and profile plot across the red bar.*

better than speckle patterns. Therefore, the resolution difference between the two is not significant, at least in this data. Above all, filter blind-SIM gives the best resolution, comparable to STED, since it uses some information about the patterns together with the positivity constraint. On the other hand, in addition to its resolution enhancement, speckle SIM has an advantage over SIM due to its simplicity for experimental implementation.

In terms of computational speed, blind-SIM-SD is substantially faster than filtered blind-SIM. The filter blind-SIM is slower since it simultaneously estimates the fluorophore density and the illumination patterns. For example, to reconstruct a data with frame size 256x256 pixels and a stack of 30 harmonic SIM images, blind-SIM-SD takes 0.5 seconds per iteration and filtered blind-SIM takes 5.5 seconds per iteration. The optimal number of iterations required are 30 for

blind-SIM-SD and 100 for filtered blind-SIM. Therefore, the total reconstruction times are 15 seconds for blind-SIM-SD and 9 minutes for filtered blind-SIM. A total of 7 minutes is consumed to reconstruct a stack of 800 speckle SIM data with a frame size of 256x256 pixels.

3.4.4   3D harmonic SIM
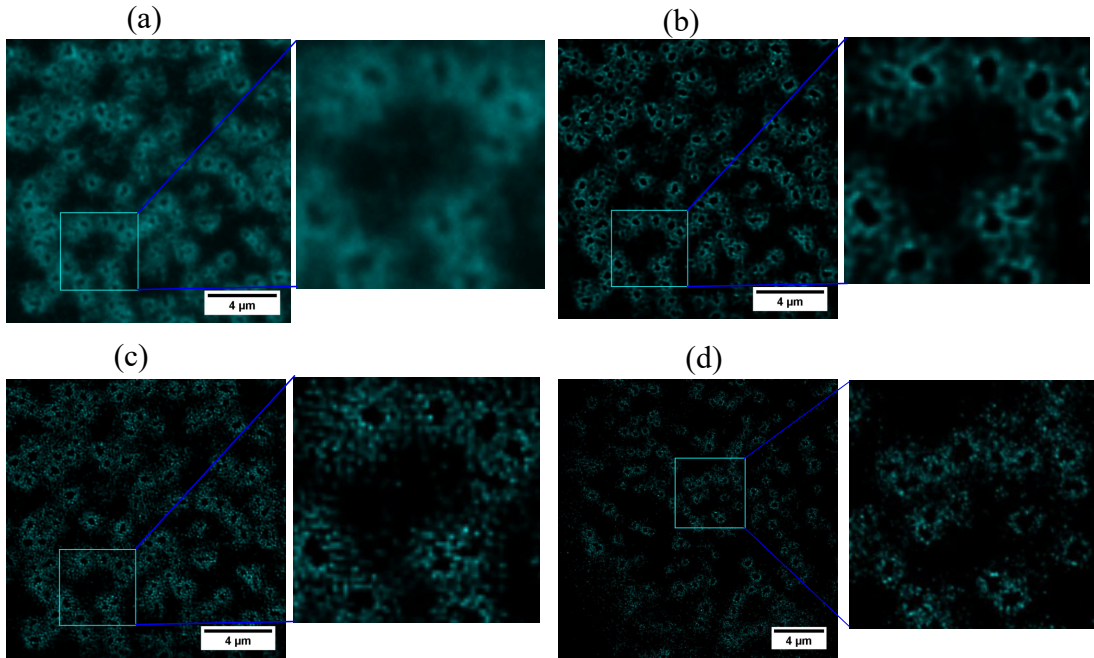
Figure 3.10 : *3D SIM reconstructions on podosome.(a) Widefield image (sum of 15 raw SIM images). (b) Blind-SIM-SD. (c) Filtered blind-SIM. (d) Deconvolved STED.*

We pursue our checking of blind-SIM reconstruction performances on podosome samples. Podosomes are conical actin-rich structures found on the outer surface of the plasma membrane of animal cells. They are highly dynamic structures which consist of an actin core surrounded by a ring-like protein such as vinculin with size $0.5 - 1.0\mu m$ in diameter[62,63]. The interest of the reconstruction of podosome data is to resolve the ring-like vinculin structures.

We implement 3D filtered blind SIM on the 3D raw images (512x512 pixels, and 15 z-scans). In Figure 3.10, we have chosen a small region in the sample (at the center sample plane) to illustrate the power of 3D filter blind SIM (c) compared to the blind-SIM-SD (b), while a single raw SIM image is shown in (a). For a fair comparison, we have also presented a deconvolved STED podosome image, shown in (d). Note that the STED image is taken from a different sample. But it is sufficient for comparison based on the knowledge of vinculin structures. Clearly, the filtered blind-SIM (c) is more efficient compared to the blind-SIM-SD. Surprisingly, it has almost equivalent performance as STED. In addition to recovering high spatial frequencies of the sample introduced into the image by the structured illumination, the positivity constraint which can be enhanced by sparsity further contributes for the superresolution in the filtered blind SIM-SD.
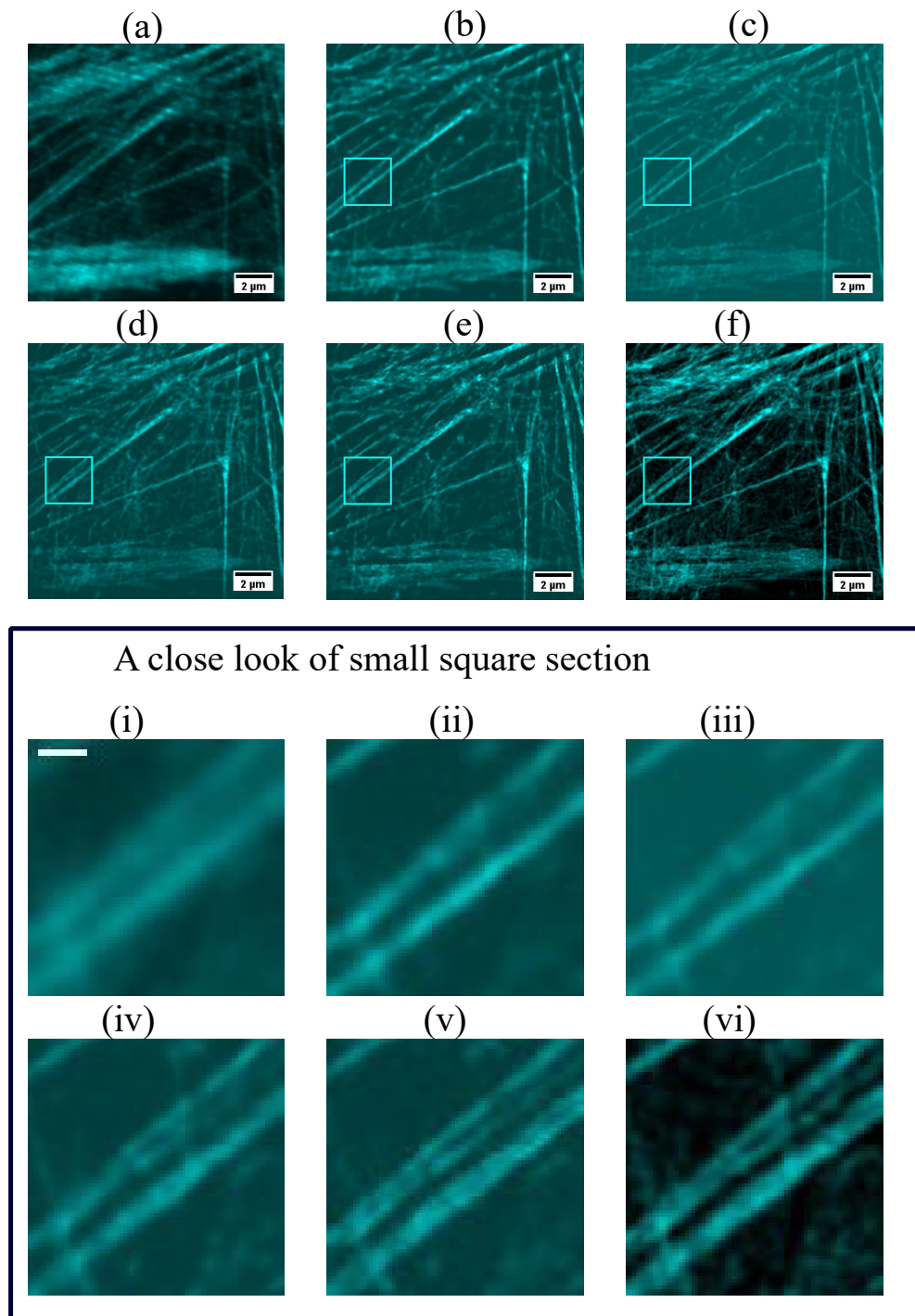
Figure 3.11 : *3D SIM reconstructions.(a) Raw SIM image. (b) Richardson Lucy widefield deconvolution. (c) Widefield deconvolution. (d) Blind-SIM-SD. (e) Filtered blind-SIM. (f) Commercial Elyra SIM reconstruction. (i)-(vi) Crops on small square section of Widefield image and (b)-(f) respectively. The length of the scale bar in (i) is $0.5\mu m$.*

We have compared our processing methods with the existing commercial softwares using a sample of actin filaments, see Figure 3.11. The raw SIM images are captured using the grating-

based commercial ELYRA S.1 SR-SIM instrument. The raw SIM images are taken using 3D structured illumination pattern with 3 orientations and 5 phases. The 3D structured pattern is created by the interference of three beams. For each axial plane, the 15 different patterns (3 orientations, 5 phases) were acquired before switching to the next axial plane[17]. The imaging parameters of the microscope are, medium refractive index 1.4-1.42, NA 1.42, pixel size 64.8nm, z-step size 100nm, and excitation/emission wavelengths 488nm/520nm.

Selected 2D small regions are shown in Figure 3.11, the main interest is the comparison of the filtered blind-SIM reconstruction with the commercially available (from Zeiss ELYRA S.1 SR-SIM machine) SIM data reconstruction software. A single plane raw SIM image is shown in (a). The widefield image can be obtained simply by summing the raw SIM images for the 15 patterns. The Richardson-Lucy (RL) deconvolution and the widefield deconvolution with our technique (conjugate gradient based iterative deconvolution) are shown in (b) and (c) respectively and show similar performance. The filtered blind-SIM (e) is slightly better than the commercial reconstruction (f). Both the filtered blind-SIM and the commercial reconstructions exhibit better resolution than the blind-SIM-SD image (d).
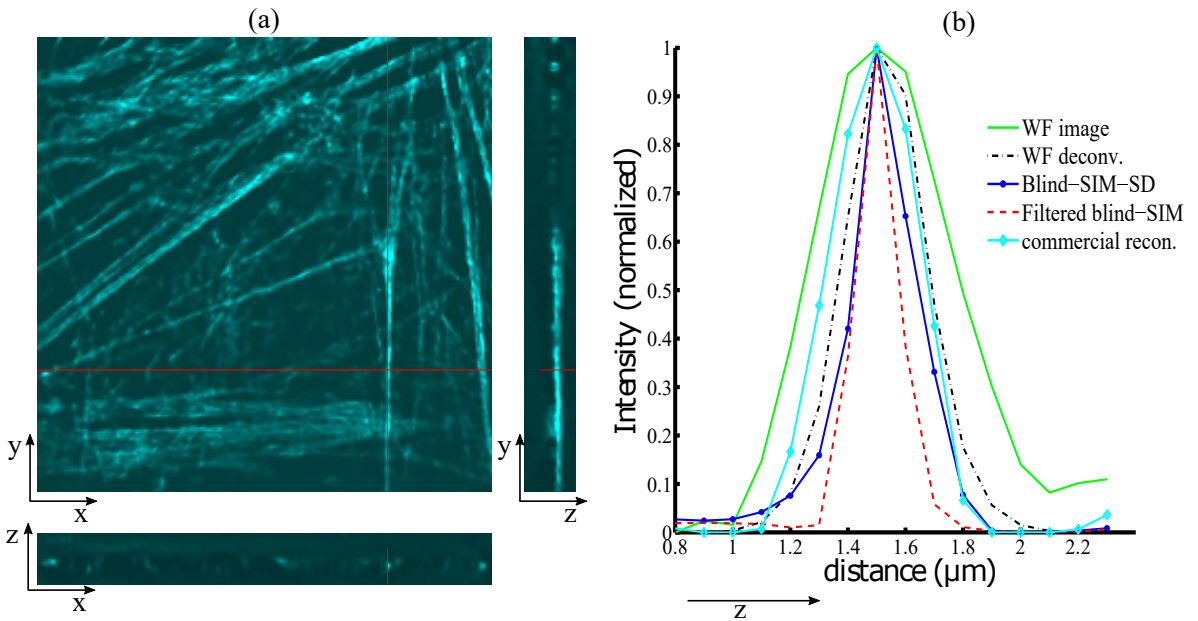
Figure 3.12 : *3D SIM axial resolution. (a) Orthogonal view of filtered blind-SIM reconstruction. (b) Axial profile at the intersection of red lines in (a).*

In Figure 3.11, we have studied the improvement of lateral resolution using blind-SIM techniques by selecting a single 2D plane from the reconstruction of 3D data. We now turn to the study of the improvement in optical sectioning. To this aim, we plot the z-profile of the fluorescence distribution at a given transverse position, as shown in Figure 3.12. The selected transverse position is chosen at the cross-section of the red lines, shown in the xy-view of the figure. The same point is selected to plot the axial profiles from the 3D widefield image, the widefield deconvolution, the blind-SIM-SD, the filtered blind-SIM and the commercial reconstruction. The z-profiles are plotted altogether as shown in Figure 3.12. The filtered blind-SIM provides the best resolution among

all. Surprisingly, the blind-SIM reconstructions provide better axial resolution (200nm by filtered blind-SIM and 250nm by blind-SIM-SD) compared to the commercial one (350nm). Bearing in mind that our model is not really appropriate, to our surprise, we btain a better optical sectioning than the commercial software. The resolutions can be estimated by calculating the half maximum widths of the profile plots.

3.5 Conclusion

In this chapter, we have compared on experimental data the performances of speckle blind-SIM to standard-SIM and brightfield. As expected speckle blind-SIM was slightly below SIM in terms of resolution but significantly superior to brightfield, with a considerably simpler experimental implementation than SIM.

In addition we compared the reconstruction from the commercial software to the filtered blind-SIM on SIM images. Filtered blind-SIM gives similar results to the commercial reconstruction without requiring the accurate knowledge of the illumination. Only the period of the light grid shoud be given within a 20% accuracy. This is a strong asset in favor of filtered blind-SIM. Finally we compared filtered blind-SIM with STED and obtained suprisingly similar results.

Advanced speckle illumination microscopy techniques

Contents

4.1 Mirror-based speckle illumination microscopy

In widefield and confocal microscopy, when the incident excitation beam is focused by the objective lens, the diffraction spot width is much larger in the axial direction than the lateral one. The size of the diffraction spot determines the 3D resolution, the axial resolution being at least 3 times worse than the lateral one. For obtaining an isotropic resolution, the illumination and collection must be done from all directions, which is experimentally challenging. The 4pi confocal microscope, for example, which uses two objectives facing each other achieves quasi-isotropic illumination and collection and therefore improves the axial resolution[64]. Similarly, image interference widefield microscopy is demonstrated by Gustafsson *et al.*[65] where a fluorescent sample is mounted between two opposing objective lenses, each of them focusing on the same focal plane within the sample. The sample is illuminated and observed from both sides simultaneously using two opposing objective lenses. A quasi-isotropic resolution can be obtained using such configurations.

Isotropic diffraction spot could be experimentally produced, in a similar way as demonstrated by Mudry *et al.*[66], by placing the sample on the reflecting mirror and shaping the incident beam so that the incident and reflected beam converge toward the same spot within the sample. With the same token, Le Moal *et al.* has extended generating an isotropic spot for two-photon microscopy, similarly, by shaping the incident beam and using a mirror in place of a standard glass slide to support the sample[67]. Using one objective and one mirror, this approach is simpler to implement than the 4pi microscope. In this work, we investigated the interest of extending the mirror concept to speckle imaging. We consider only the multifocus configuration for which the 3D data can be modeled as $\rho I * h$ (see Chapter 2 for the imaging model).

4.1.1 Mirror speckle patterns and Mirror PSF

Mirror-based speckle illumination assumes that the sample is placed in the vicinity of a reflecting mirror. All the study is based on synthetic data. First, assuming a scalar model, we recall the expression of 3D PSF, $h(\boldsymbol{r})$, and speckle illuminations, $I_l(\boldsymbol{r})$, in a homogeneous medium as

$$h(\boldsymbol{r}) = |\boldsymbol{e}(\boldsymbol{r})|^2 = C|\int_D f(\boldsymbol{k}_\parallel)e^{i\sqrt{k_0^2-k_\parallel^2}z}e^{i\boldsymbol{k}_\parallel\cdot\boldsymbol{r}_\parallel}\mathrm{d}\boldsymbol{k}_\parallel|^2, \tag{4.1}$$

and

$$I_l(\boldsymbol{r}) = |\boldsymbol{e}_{\phi_l}(\boldsymbol{r})|^2 = |\int_D f(\boldsymbol{k}_\parallel)e^{i\phi_l(\boldsymbol{k}_\parallel)}e^{i\sqrt{k_0^2-k_\parallel^2}z}e^{i\boldsymbol{k}_\parallel\cdot\boldsymbol{r}_\parallel}\mathrm{d}\boldsymbol{k}_\parallel|^2, \tag{4.2}$$

respectively.

$$f(\boldsymbol{k}_\parallel) = \begin{cases} 1, & \text{if } |\boldsymbol{k}_\parallel| \leq NAk_0 \\ 0, & \text{otherwise} \end{cases}$$

and, $C = 1/\int h(\boldsymbol{r})\mathrm{d}\boldsymbol{r}$, $\boldsymbol{r} = \boldsymbol{r}_\parallel + z\hat{\boldsymbol{z}}$ where $\hat{\boldsymbol{z}}$ indicates the optical axis, $k_0 = 2\pi/\lambda$ is the illumination wavenumber, $\phi_l(\boldsymbol{k}_\parallel)$ is an uncorrelated random variable uniformly distributed between 0 and 2π and D is a disk of radius NAk_0. This PSF and a single speckle pattern are shown in Figure 4.1(a, c) respectively.

For the mirror-based configuration, the effective speckle pattern is the interference of the incident field with the field reflected by the mirror. In this scalar modeling, we assume that the

reflection coefficient is one. So, the speckle in the presence of the mirror reads,

$$
I_{l,m}(\boldsymbol{r}) = |\boldsymbol{e}_{i,\phi_l}(\boldsymbol{r}) + \boldsymbol{e}_{r,\phi_l}(\boldsymbol{r})|^2 = |\int_D \big(f(\boldsymbol{k}_\parallel)e^{i\phi_l(\boldsymbol{k}_\parallel)}e^{i\sqrt{k_0^2-k_\parallel^2}z}e^{i\boldsymbol{k}_\parallel\cdot\boldsymbol{r}_\parallel}
$$
$$
+f(\boldsymbol{k}_\parallel)e^{i\phi_l(\boldsymbol{k}_\parallel)}e^{-i\sqrt{k_0^2-k_\parallel^2}z}e^{i\boldsymbol{k}_\parallel\cdot\boldsymbol{r}_\parallel}\big)\mathrm{d}\boldsymbol{k}_\parallel|^2, \tag{4.3}
$$

where $I_{l,m}(\boldsymbol{r})$ is the mirror speckle and $\boldsymbol{e}_{i,\phi_l}(\boldsymbol{r})$ is the incident field while $\boldsymbol{e}_{r,\phi_l}(\boldsymbol{r})$ is the reflected field from the mirror. The phase of the reflected field is considered to be the same from the incident one assuming that the additional random phase introduced by the reflecting mirror is not significant. The mirror speckle patterns consists of dense smaller spots within the volume, Figure 4.1(d), compared to the normal "free space" speckle patterns, Figure 4.1(c), that are axially elongated.

In a similar fashion, assuming the sample is laid close to the mirror within the coherence length of the emission light and that the appropriate wavefront shaping has been introduced in the observation part, the emitted fluorescence field and the reflected one interfere at the sample on the focal plane and produce a quasi-isotropic central spot with axial sidelobes, shown in Figure 4.1(b). This PSF is generated as

$$
h_m(\boldsymbol{r}) = |\boldsymbol{e}_{\boldsymbol{i}}(\boldsymbol{r}) + \boldsymbol{e}_{\boldsymbol{r}}(\boldsymbol{r})|^2 = C|\int_D \big(f(\boldsymbol{k}_\parallel)e^{i\sqrt{k_0^2-k_\parallel^2}z}e^{i\boldsymbol{k}_\parallel\cdot\boldsymbol{r}_\parallel}
$$
$$
+f(\boldsymbol{k}_\parallel)e^{-i\sqrt{k_0^2-k_\parallel^2}z}e^{i\boldsymbol{k}_\parallel\cdot\boldsymbol{r}_\parallel}\big)\mathrm{d}\boldsymbol{k}_\parallel|^2, \tag{4.4}
$$

$\boldsymbol{e}_{\boldsymbol{i}}(\boldsymbol{r})$ and $\boldsymbol{e}_{\boldsymbol{r}}(\boldsymbol{r})$ being the incident and reflected emissions respectively. The resulting effect of the axial sidelobes on the images can be removed during the reconstruction procedures. Note that the difference between Eq. (4.3) and Eq. (4.4) is that random phases are introduced in the former while there is no random phase in the latter.

4.1.2   Mirror speckle SIM reconstructions

Having the normal and mirror speckle patterns, and PSFs, three imaging conditions are considered on a 3D object (200x4x200 pixels) with a star-like profile on the xz-plane. First, a standard microscope image, no mirror, of the star object is taken using normal speckle illuminations, following $M_l = \rho I_l * h$. The object (xz-view), the widefield image from summing 100 low-resolution images is shown in Figure 4.2(a,b) respectively. The widefield deconvolution, Figure 4.2(c), and blind-SIM-SD reconstruction on the low-resolution images, Figure 4.2(d), are depicted here for reference. Apparently, the blind-SIM-SD provides impressive lateral and axial resolution improvement compared to the widefield image as well as the widefield deconvolution. Details of such reconstruction performances are discussed in Chapters 2 and 3.

Second, we assume that the effect of the mirror is only on the coherent excitation illumination, its effect on the emission being negligible, the low-resolution images are modeled using mirror speckles as $M_l = \rho I_{l,m} * h$, $I_{l,m}$ being the mirror speckle and the PSF. In this case, even though we expected a better resolution due to the smaller size of the speckle spots, we observed a resolution comparable to that using normal speckle illuminations. This can be seen from the blind-SIM reconstructions of low-resolution images using mirror speckle Figure 4.2(e), and using normal
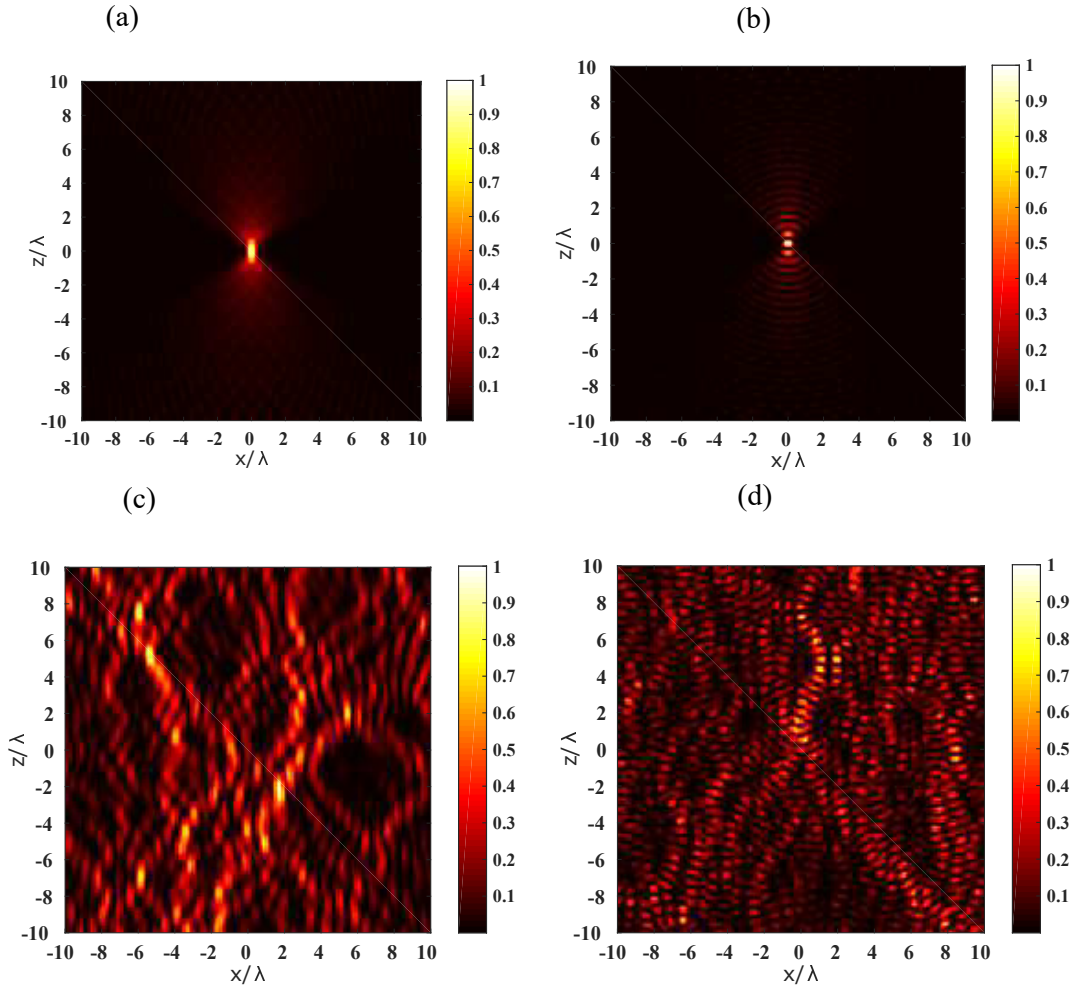
Figure 4.1 : *PSF and speckle. (a) Normal PSF (b) Mirror PSF. (c) Normal Speckle. (d) Mirror Speckle.*

speckle Figure 4.2(d). Thus, even though the mirror speckle frequency spectrum was larger than that of the normal spectrum, the reconstruction failed in recovering the additional information. Actually, we recall that in blind-SIM-SD the superresolution stems from the sparsity of the images. Now the mirror speckle spots are smaller but denser so that the sparsity of the mirror image is comparable to the sparsity of the "normal" image.

Third, assuming the position of the mirror from the focal plane is within the coherence length of the emitted fluorescence, the effective mirror PSF from the interference of incident and reflected emissions is used in imaging as $M_l = \rho I_{l,m} * h_m$, $I_{l,m}$ being the mirror speckle and h_m being the effective mirror PSF. In such cases, the blind-SIM-SD reconstruction of the low-resolution images significantly improves the axial resolution and is almost isotropic as shown in Figure 4.2(f). The contribution of the sidelobes on the images is removed during the deconvolution procedures using a PSF characterized by a central isotropic spot and axial sidelobes. However, this configuration requires wavefront shaping in the obeservation path and coherent enough emission light.
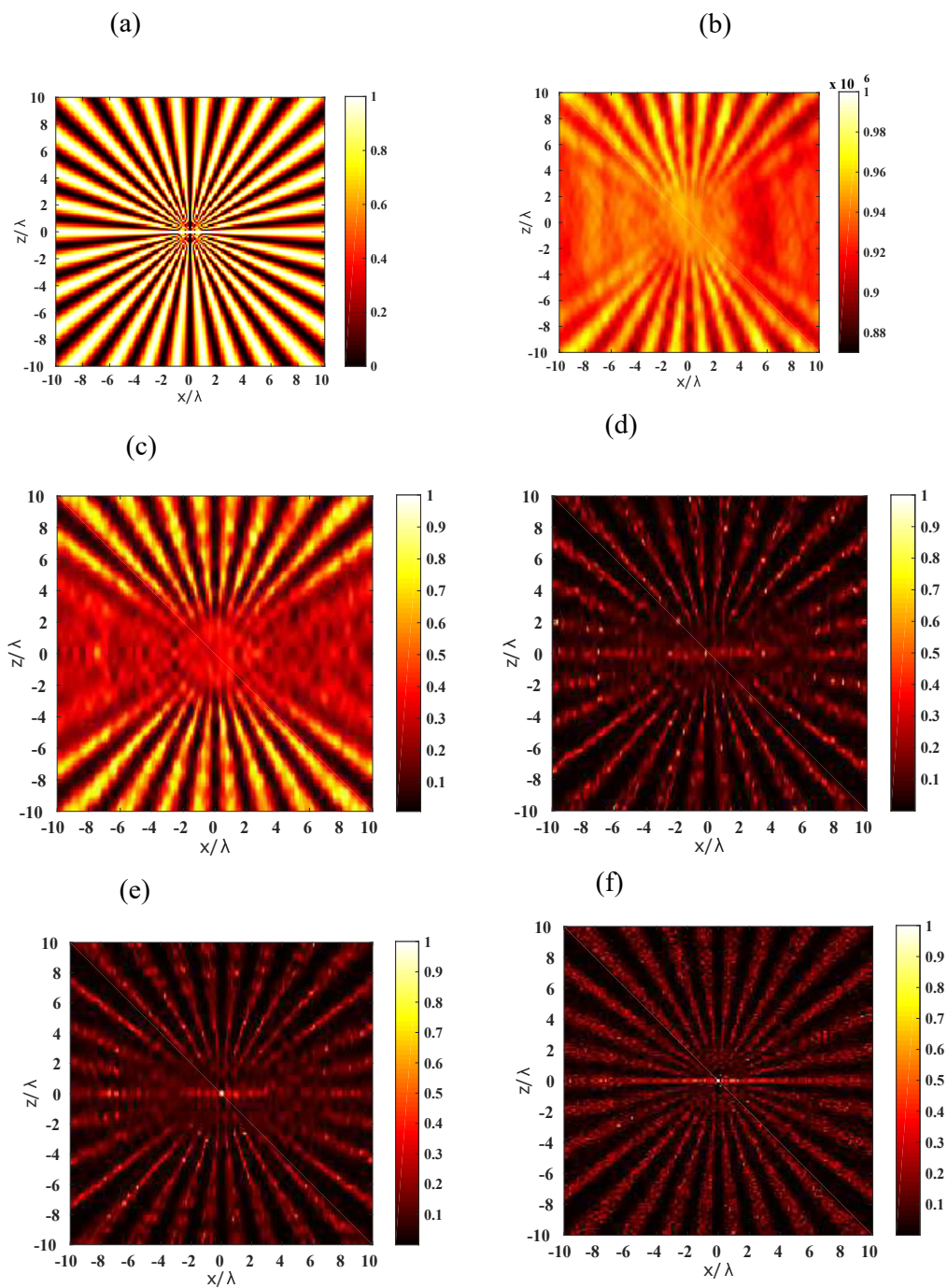
Figure 4.2 : *Mirror-based speckle illumination microscopy (a) Sample (b) Widefield image. (c) Widefield deconvolution. Blind-SIM reconstructions on low-resolution images (d) normal speckle, normal PSF. (e) mirror speckle, normal PSF. (f) mirror speckle, mirror PSF.*

4.2   Two photon Speckle illumination microscopy

Two photon microscopy is widely used for imaging deep into scattering tissues[68]. In a standard multiphoton microscope, the sample is scanned using a single diffraction limited focal spot at the focus of an objective and all the emitted two photon fluorescence is collected on a large detector. To avoid the slow scanning process, several full-field two-photon schemes have also been developed[69–71]. These approaches have been made possible by the increase in power of the exciting pulsed laser. In widefield illumination multiphoton microscope, the idea is to excite an entire plane in the focal plane of the objective, instead of exciting a single point, and then detect the emitted multiphoton fluorescence with a high resolution on a camera. Thus the entire image plane is excited simultaneously with a much higher average beam power than that used for a point focus with a high numerical aperture (NA) objective.

Up to now, two photon microscopy has seldom been considered as a means towards superresolution imaging. In the scanning mode, the resolution is monitored by the size of the excitation focus spot which is about 300nm in the transverse plane and 900nm in the axial direction[68] for a numerical aperture of 1.25 and an excitation wavelength of 960nm. In the full-field configuration, the resolution is monitored by the size of the observation point spread function and is about the same as that of the scanning mode. In both cases, the transverse and axial resolutions of two photon microscopy are far from matching that of classical single photon confocal microscopy. In fact, the doubling of the illumination wavelength and the widefield detection are detrimental to the two photon excitation (2PE) microscope resolution which remains much larger than that of a confocal single photon excitation (1PE) microscope. Recently some attempts have been made to ameliorate the two photon microscopy resolution. Multifocal structured illumination microscopy have been used to enable efficient two-photon excitation and improve resolution[72]. A superresolution method that combines two photon excitation with structured illumination microscopy (SIM) is also presented[73]. These techniques required a tight control of the illumination scheme and yielded a resolution that remained below that of a confocal microscope.

We propose to replace these controlled illuminations by speckles. In a speckle 2PE microscopy experiment, the sample is illuminated by a speckle at wavelength λ and the fluorescence is collected at $\lambda/2$. The ability to obtain 2PE excitation using speckle illumination is still an open question, but recent work on widefield 2PE microscopy[69,70,74] have already demonstrated that present lasers have enough power for exciting 2PE fluorescence on extended domains. In these references, it is shown that widefield two photon microscopy can be an alternative to widefield one photon and scanning two photon microscopy for imaging biological tissues. The absence of scanning and the low photobleaching made this approach promising. In this work, we propose to use uncontrolled speckle illumination for ameliorating the resolution of two photon microscopy.

The resolution improvements related to the nature of two-photon speckle illuminations is investigated and characterized compared to single photon speckle illuminations. The significance of the excitation and collection objective numerical apertures are demonstrated as well. We have demonstrated the technique only on synthetic data recommending the experimental demonstration for future research.

4.2.1 Two photon excitation speckle patterns
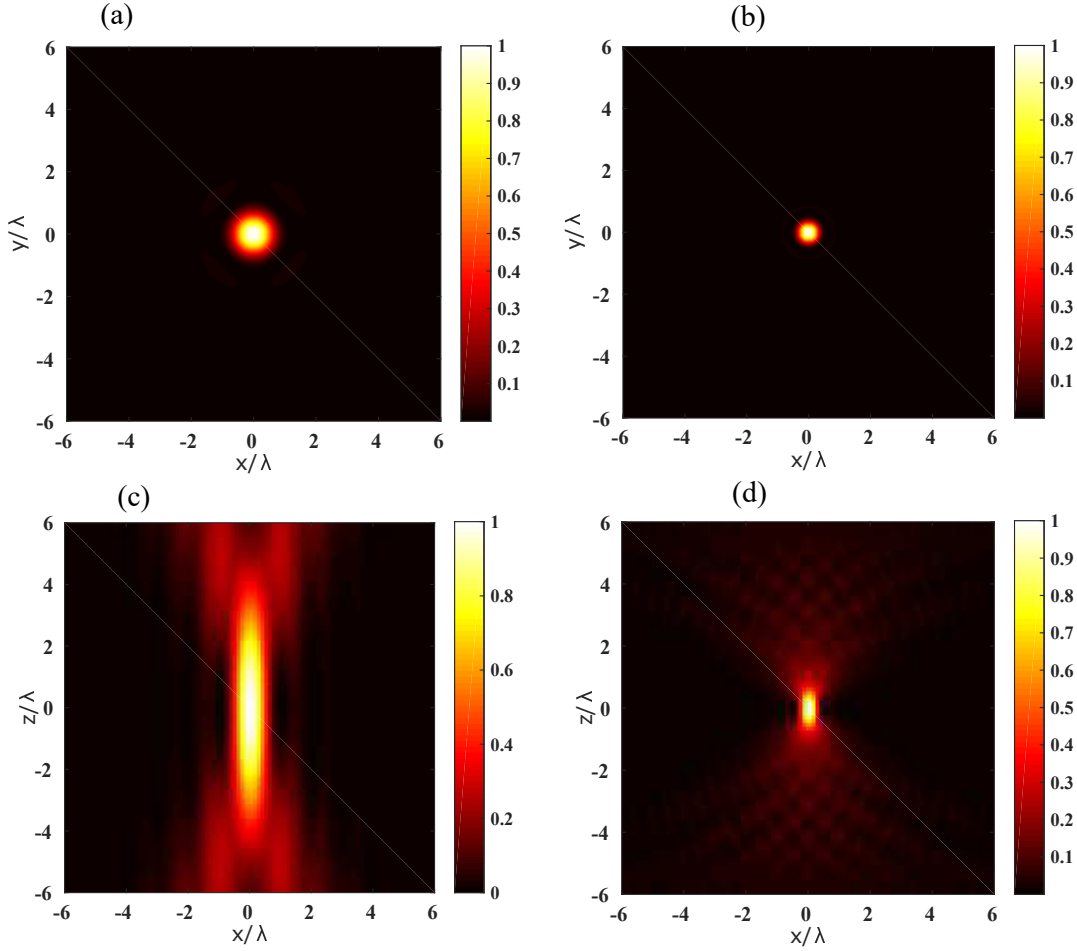
Figure 4.3 : *PSF. (a)* NA $= 0.5$, *(x,y).* *(b)* NA $= 1.0$, *(x,y).* *(c)* NA $= 0.5$, *(x,z).* *(d)* NA $= 1.0$ *(x,z).*

The 1PE and 2PE speckle illumination microscopes are simulated for collection objectives of numerical aperture (NA) 0.5 and 1.0, whose collection PSFs are shown in Figure 4.3 showing transverse PSF (top) for NA = 0.5 (a), NA = 1.0 (b) and axial PSF (bottom) for NA = 0.5 (c), NA = 1.0 (d).

The 2PE speckle excitation, at a wavlength of 1100nm, and the coutnterpart 1PE speckle excitation, at a wavelength of 550nm, are shown in Figure 4.4 (transverse) and in Figure 4.5(axial). In both figures, the top (a,b) shows 1PE speckle pattern while the botton (c, d) shows the 2PE speckle pattern. The two photon illumination speckle patterns are synthetically generated as

$$I_{l,2pe}(\boldsymbol{r}) = |\int_{D} f(\boldsymbol{k}_{\|})e^{i\phi_l(\boldsymbol{k}_{\|})}e^{i\sqrt{k_0^2-k_{\|}^2}z}e^{i\boldsymbol{k}_{\|}\cdot\boldsymbol{r}_{\|}}\mathrm{d}\boldsymbol{k}_{\|}|^4, \tag{4.5}$$

given that $\boldsymbol{r} = \boldsymbol{r}_{\|} + z\hat{\boldsymbol{z}}$ where $\hat{\boldsymbol{z}}$ indicates the optical axis, $k_0 = 2\pi/\lambda_{2pe}$ is the illumination wavenumber, $\phi_l(\boldsymbol{k}_{\|})$ is an uncorrelated random variable uniformly distributed between 0 and 2π and D is a disk of radius NAk_0. λ_{2pe} is the two photon excitation wavelength, which is twice
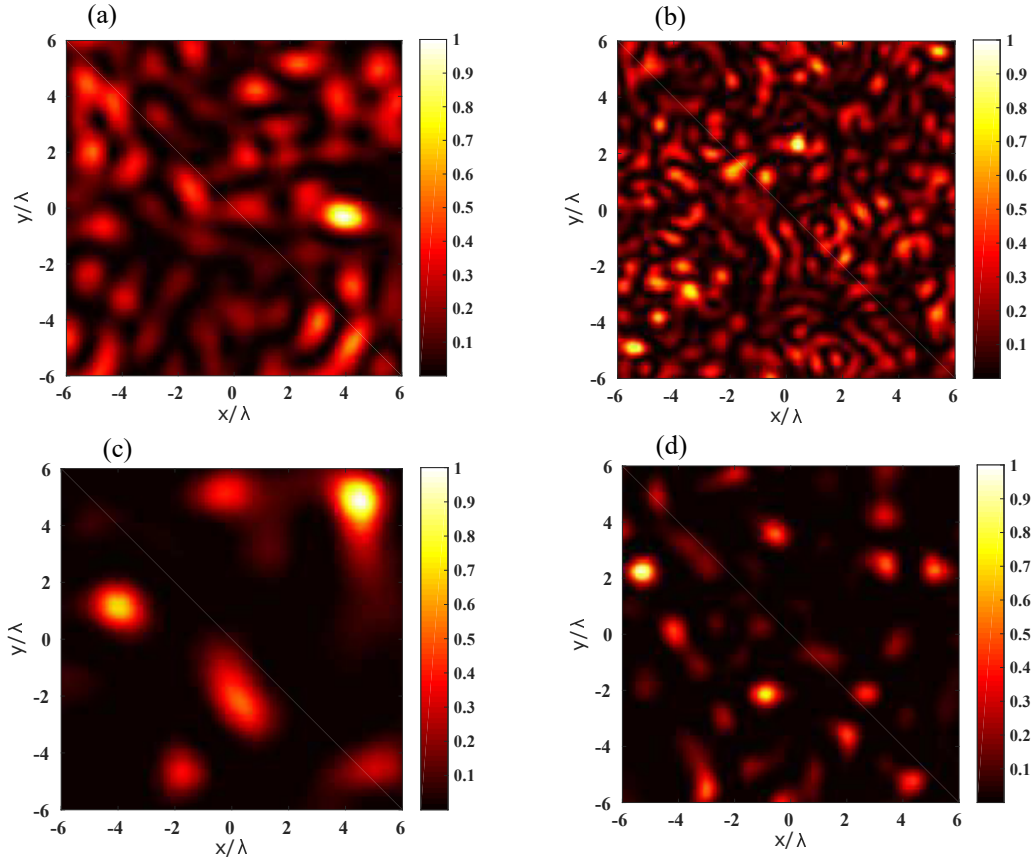
Figure 4.4 : *Speckles (x, y). (a) 1PE, $NA_{ill} = 0.5$ (b) 1PE, $NA_{ill} = 1.0$. (c) 2PE, $NA_{ill} = 0.5$. (d) 2PE, $NA_{ill} = 1.0$.*

longer than the single photon excitation wavelength. In other words, the 2PE speckle pattern is generated by squaring the speckle pattern generated at twice the 1PE wavelength. We assumed that the spectral width of the pulsed beam is small enough for considering the monochromatic interference pattern, at least over tens of microns about the temporal focusing plane[75].

From the speckle patterns, apparently, the 2PE speckle grains have larger spot size than the 1PE patterns. However, As explained in Chapter 2, the positivity constraint on sparse low-resolution images using speckle illuminations plays a substantial role in the superresolved reconstruction of our blind-SIM algorithms. Now the sparsity of the 2PE speckle is more pronounced than that of the 1PE speckle. Therefore, depending on the collection numerical aperture NA_{coll}, the 2PE speckle patterns are expected to provide better resolved reconstruction.

4.2.2   Two photon speckle SIM reconstructions

In this section, we explore the interest of 3D widefield two photon speckle illumination microscopy and compare its performance to that of one photon speckle microscopy.

We first investigate the performance of 2PE speckle microscopy on the transverse resolution. We consider a quarter of the star sample placed in the (x,y) plane as a resolution target. We simulate the widefield 1PE speckle microscopy and 2PE speckle microscopy for certain NA. For
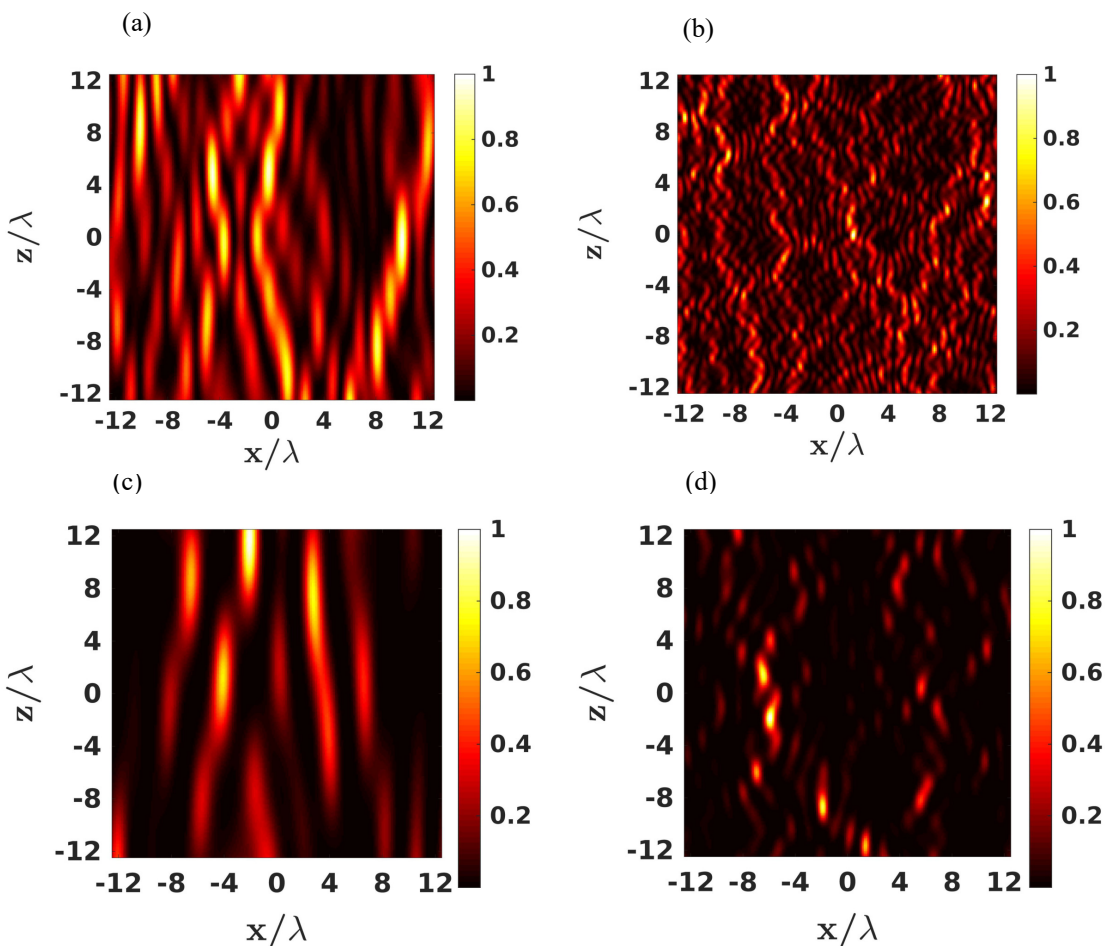
Figure 4.5 : *Speckles (x, z). (a) 1PE, $NA_{ill} = 0.5$ (b) 1PE, $NA_{ill} = 1.0$. (c) 2PE, $NA_{ill} = 0.5$. (d) 2PE, $NA_{ill} = 1.0$.*

reference, Figure 4.6(a,b,c) show the object, the widefield image (sum of 100 1PE low resolution images) for $NA_{ill} = NA_{coll} = 0.5$ and the widefield image for $NA_{ill} = 0.5 NA_{coll} = 0.5$ respectively.

For the same excitation and collection objectives $NA_{ill} = NA_{coll} = 0.5$, The 2PE speckles provide slight resolution improvement compared to the corresponding 1PE speckles as can be seen by comparing Figures 4.6(d) and (g). On the other hand, there is a significant resolution improvement by the 2PE speckles for the case of $NA_{ill} = 2 NA_{coll} = 1.0$, comparing Figures 4.6(e) and (h). This is an important result as it means that using 2PE speckles, one can handle poor collection PSF without deteriorating the resolution as long as the speckle is provided with a hign NA. When $NA_{ill} = 0.5 NA_{coll} = 0.5$, we observed no resolution improvement by the 2PE speckles, from the comparison of Figures 4.6(f) and (i). The origin of this superresolution in blind-SIM-SD is certainly the sparsity of the excitation illumination patterns which yield sparse low-resolution images. This sparsity substantially activates the positivity constraint and enhances the resolution.

Second, we investigate the performance of 2PE speckle microscopy on the axial resolution. The resolution target is now placed in the (x,z) plane, Figure 4.7(a). The widefield images (sum of 100
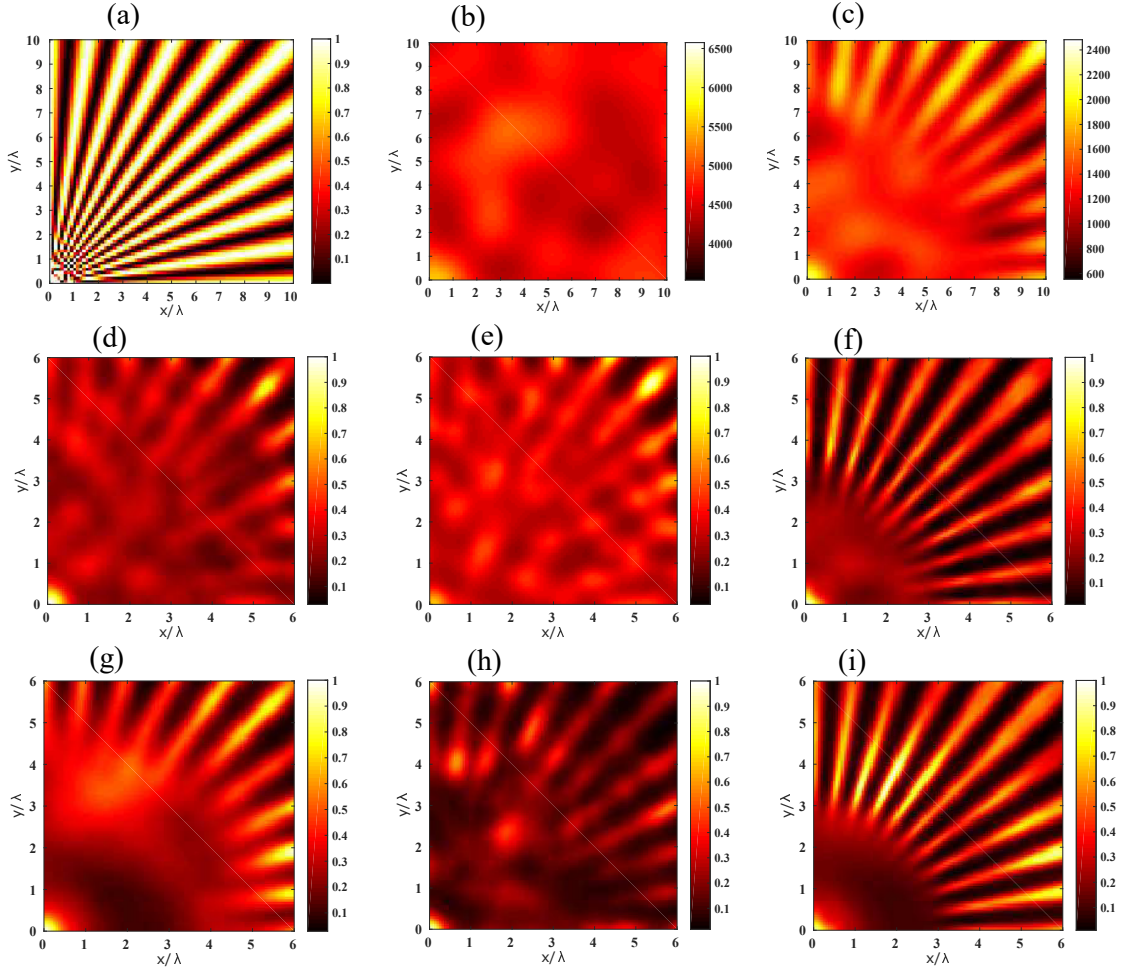
Figure 4.6 : *Reconstruction comparisons of 1PE and 2PE (xy-view).(a) Object. (b) Widefield image,* $NA_{coll} = 0.5$*. (c) Widefield image,* $NA_{coll} = 1.0$*. (d) 1PE,* $NA_{ill} = 0.5$*,* $NA_{coll} = 0.5$*. (e) 1PE,* $NA_{ill} = 1.0$*,* $NA_{coll} = 0.5$*. (f) 1PE,* $NA_{ill} = 0.5$*,* $NA_{coll} = 1.0$*. (g) 2PE,* $NA_{ill} = 0.5$*,* $NA_{coll} = 0.5$*. (h) 2PE,* $NA_{ill} = 1.0$*,* $NA_{coll} = 0.5$*. (i) 2PE,* $NA_{ill} = 0.5$*,* $NA_{coll} = 1.0$*.*

1PE low resolution images) for $NA_{ill} = NA_{coll} = 0.5$ and $NA_{ill} = 0.5 NA_{coll} = 0.5$ are presented in Figures 4.7(b) and (c) respectively.

The axial resolution improvements can be explained with the same logic as the transverse one, referring to the 1PE and 2PE figures with the corresponding NA specifications. Note that the grainy nature of the blind-SIM reconstructions emanates from the fact that we only use 100 speckle illuminations to be close to reality. Using a large number of speckle patterns smooths out the grainy aspect since it satisfies the homogeneity constraint on the illuminations better but increases the experimental cost. The study over the increasing number of speckle patterns is presented in Chapter 2.

For comparison, the analytical scanning 2PE deconvolution are demonstrated in Figure 4.8. The model for the analytical scanning 2PE imaging assumes a focused illumination, and detects
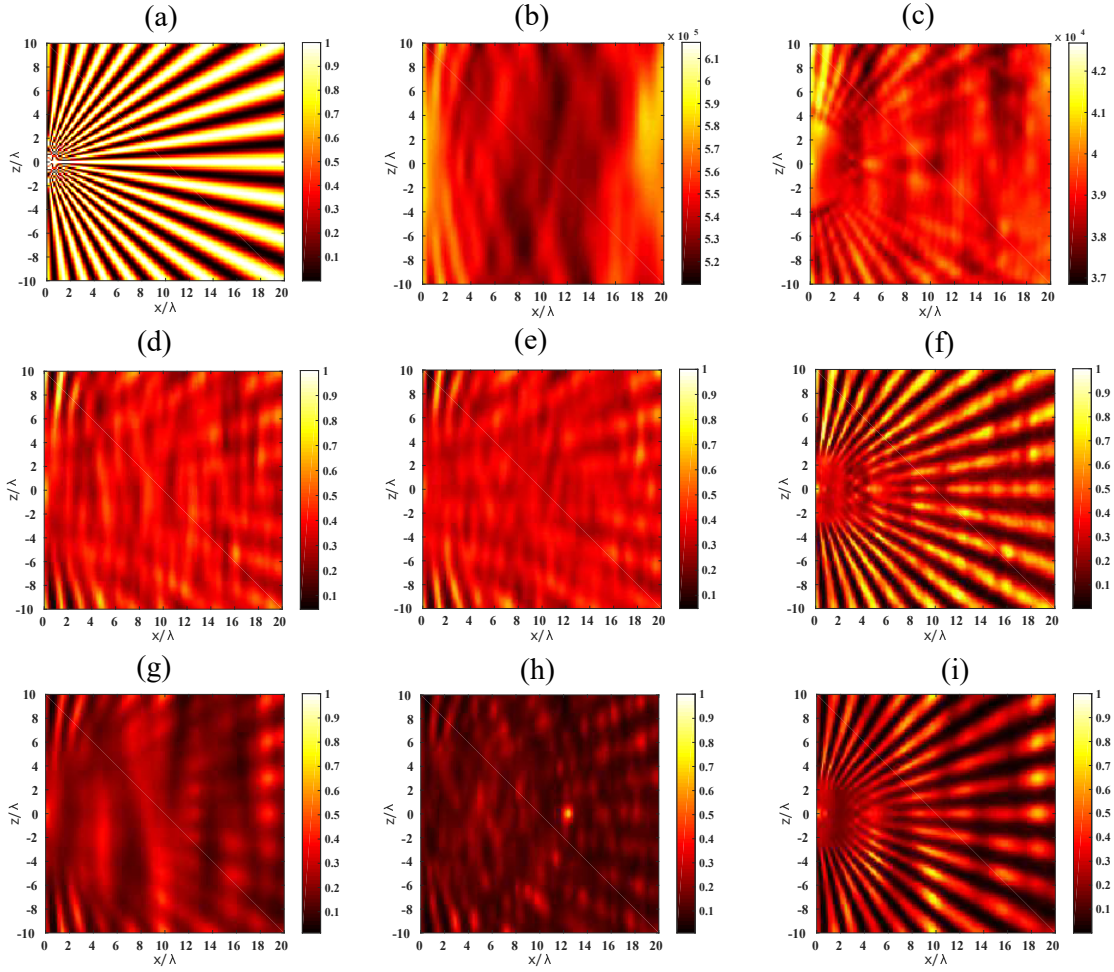
Figure 4.7 : *Reconstruction comparisons of 1PE and 2PE (xz-view).(a) Object. (b) Widefield image,* $NA_{coll} = 0.5$. *(c) Widefield image,* $NA_{coll} = 1.0$. *(d) 1PE,* $NA_{ill} = 0.5$, $NA_{coll} = 0.5$. *(e) 1PE,* $NA_{ill} = 1.0$, $NA_{coll} = 0.5$. *(f) 1PE,* $NA_{ill} = 0.5$, $NA_{coll} = 1.0$. *(g) 2PE,* $NA_{ill} = 0.5$, $NA_{coll} = 0.5$. *(h) 2PE,* $NA_{ill} = 1.0$, $NA_{coll} = 0.5$. *(i) 2PE,* $NA_{ill} = 0.5$, $NA_{coll} = 1.0$.

all collected photons. This means that, unlike confocal, there is no detection pinhole. The focused illumination is scanned across the sample to obtain the widefield image. The analytical scanning 2PE image is simulated as the convolution of the object with the PSF squared, $M = \rho * h^2$. We observed that, for transverse resolution, 2PE blind-SIM reconstruction (Figure 4.6(f,i)) is more resolved than the scanning 2PE deconvolution (Figure 4.8(a), shown for collection NA = 1.0). Similarly for axial resolution, the 2PE blind-SIM reconstruction (Figure 4.7(f,i)) is better than the scanning 2PE deconvolution (Figure 4.8(b) for collection NA = 1.0).
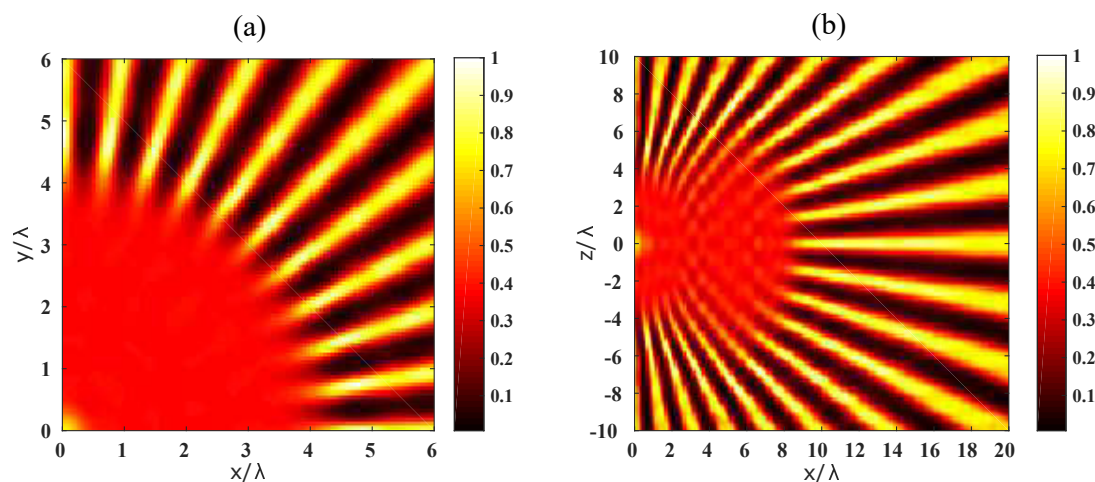
Figure 4.8 : *Analytic scanning 2PE deconvolution. (a)* NA = 1.0*, (x, y). (b)* NA = 1.0*, (x, z).*

4.3   Conclusion

In this chapter, with optimism for future practical study, we have investigated mirror based isotropic resolution and two photon microscopy using speckle illumination microscopy by numerical simulation. Assuming the position of the mirror from the focal plane is within the coherence length of the emitted fluorescence, the blind-SIM reconstruction significantly improves the axial resolution and provides almost isotropic resolution in three dimensions.

From the investigation of single photon and two photon excitation speckle patterns, the two photon configuration provide impressive resolution under blind-SIM reconstruction even compared to the single photon configuration. The source of superresolution is thought to be coming from the sparsity of the 2PE excitation patterns.

3D deconvolution for reducing out-of-focus blur

Contents

5.1 Introduction

In fluorescence microscopy, the light emitted by any source above or below the focal plane will eventually reach the detection. The in-focus image of a 3D fluorescence sample suffers from out-of-focus blur due to the light coming from the spreading cone of light. This out-of-focus fluorescence degrades the contrast of the image and may hinder the visualization of in-focus sample features. Over the past few years, varieties of strategies have been invented and implemented to minimize the effect of out-of-focus contributions either optically or computationally. Two-photon microscopy, confocal microscopy and light sheet microscopy are some of the main microscopy techniques available today. In addition to the experimental strategies, out-of-focus reducing techniques can be obtained computationally using deconvolution algorithms.

This chapter briefly reviews the available techniques and introduces a computational deconvolution based out-of-focus reduction strategy. The principle of the technique depends on deconvolving the image of the focal plane using a three-dimensional PSF (see Section 5.2). This method is first demonstrated using standard fluorescence microscopy images and then extended to speckle illumination microscopy (see Section 5.3).

5.1.1 Microscopy techniques

The first strategy that possibly comes to mind is to avoid illuminating out of the focal plane. If there is no background fluorescence it will not appear in the image. Two-photon excitation fluorescence microscopy, where the fluorescence signal is produced only in a small volume confined at the focus due to a nonlinear interaction between the excitation light and matter, is an example of such a technique. Therefore, the out-of-focus background is not generated. Another strategy is to selectively illuminate a section of the specimen using a thin light sheet which is orthogonal to the optical axis of the detection objective[76] (see Chapter 6). Only features of the sample illuminated by the sheet of light produce fluorescent signal whereas the out-of-focus background is not illuminated. However, the amount of optical sectioning is limited by the light sheet thickness. Confocal microscopy techniques[24,26] are based on rejecting the background out-of-focus fluorescence before the detection process. A detection pinhole mask placed at the image plane of the tube lens physically blocks the light coming from the planes above and below the focal plane. The field of illumination can be limited and the field of view can be restricted using pinholes in the excitation path. The pinholes block most of the out-of-focus light while significantly limiting the detection signal level. All these microscoy techniques reduce the out-of-focus blur and provide optical sectioning.

5.1.2 SIM-based techniques

A simple method of obtaining optical sectioning in a conventional wide-field microscope has been demonstrated by Neil *et al.*[4,77] based on projecting a single spatial frequency structured illumination onto the specimen. In their technique images taken at three spatial positions of the grid are processed in real time to produce optically sectioned images equivalent to the confocal microscopy. The structured illumination brings variations in the image that would not have appeared otherwise.

The contrast of the variation can serve as an indicator of how much the sample is in focus. If the structure appears highly contrasted, the sample must be thin and mostly in focus; if the structure appears weakly contrasted, the sample must be mostly out of focus. The idea of removing the out-of-focus background is done by quantifying and decoding the in-focus information using the decoding algorithm proposed by Neil *et al.* Three raw images with an adjacent phase shift of $2\pi/3$ are obtained by translating the grid structure. Computing the root mean square (RMS) of the differences between each two adjacent images reconstructs an optically sectioned image. This technique is also reviewed by Jerome Mertz[40] and Qian *et al.*[78].

Recently, Jerome Mertz[40] also introduced a new algorithm on HiLo microscopy to synthesize an optically sectioned image, which uses two wide-field images; one acquired under uniform, and the other under structured illumination. The demodulation is performed spatially with the single structured image rather than temporally with a sequence of structured images. The inevitable loss of resolution from single-image-based demodulation is compensated by a recovery of the lost resolution directly from the uniform illumination image. In the references[41,79], it is also demonstrated that an optical sectioning comparable to confocal microscopy could be obtained using two widefield images: one under uniform illumination and the other under speckle illumination. In a similar fashion, as sinusoidal grid pattern is used, the speckle-illumination image provides an optically sectioned image with low resolution. This is then complemented with high-resolution information obtained from the uniform-illumination image. A fusion of both images leads to a full resolution image that is optically sectioned across all spatial frequencies.

5.1.3   Computational techniques

Computational techniques are mainly out-of-focus removal strategies applied on conventional widefield images after the detection process. In other words, numerical deconvolution algorithms are implemented on the images where the focal and out-of-focus signals are superimposed[80]. A number of image-processing algorithms have been applied with various degrees of success in this domain[81]. One of the deconvolution techniques follows the nearest neighbor algorithm for image restoration[82–84] where the images of the nearest out-of-focus planes to the focal plane are subtracted. In the nearest neighbor algorithm, the first out of focus planes above and below the focal plane image are blurred by the PSF of the respective planes and then subtracted from the focal plane image. the result is then deblurred using the focal plane PSF. This method considers only the out-of-focus contributions from nearest-neighbor focal planes in the specimen. The nearest neighbor deblurring algorithm is fundamentally 2D because they apply an operation plane-by-plane to each 2D plane of a 3D image stack[60].

5.2   Deconvolution of 2D images using a 3D PSF

Recently, preliminary work in the framework of SIM has hinted that an appropriate three-dimensional deconvolution could be used on 2D images to remove the out-of-focus fluorescence[49]. The suggested reconstruction scheme had been implemented using a joint blind-SIM algorithm which estimates sequentially the sample and the illuminations.

In this thesis, we have implemented a slice-based three-dimensional deconvolution based on the blind-SIM separate deconvolution (blind-SIM-SD) algorithm, as seen in Chapter 2, this approach is significantly simpler and faster compared to the joint blind-SIM. The two-dimensional (2D) image is deconvolved using the three-dimensional (3D) point spread function of the microscope, which we now on call the algorithm as slice 3D deconvolution for brightfield images and slice blind-SIM-SD for speckle SIM images.

The imaging model of brightfield fluorescence microscopy reads as

$$M = s * h, \tag{5.1}$$

where $*$ is the convolution, s is the 3D fluorescence density, h is the 3D point spread function and M is the 2D recorded image. The slice 3D deconvolution procedure minimizes the cost functional (under positivity, $s = \xi^2$)

$$F(\xi) = \|M - \mathbf{A}(\xi^2 * h)\|^2, \tag{5.2}$$

where $M \in \mathbb{R}^{N_x \times N_y}$ and $\xi, h \in \mathbb{R}^{N_x \times N_y \times N_z}$ while $N_x \times N_y$ indicates the size of the image frame and N_z indicates the z-dimension of the fluorescence density and the PSF. Note that M is a 2D image slice whereas $\xi^2 * h$ is 3D. The operation $\mathbf{A}$ therefore transforms a 3D quantity into 2D, $\mathbf{A} : \mathbb{R}^{N_x \times N_y \times N_z} \longrightarrow \mathbb{R}^{N_x \times N_y}$. This operation is done by restricting the minimization to the central plane which corresponds to the focal plane, i.e. restricted to the center plane of $\xi^2 * h$ in every iteration. When the iteration stops ξ^2, the fluorescence density, is investigated in the volume where the central plane is actually the estimated sample of interest.

And, for speckle SIM, the imaging model reads as

$$M_l = I_l s * h, \tag{5.3}$$

where I_l is the lth 3D speckle pattern and M_l is the 2D speckle SIM image recorded using the specified speckle pattern. The slice 3D blind-SIM-SD minimizes the cost functional (following the positivity and homogeneity constraints explained in Chapter 2)

$$F(\eta_{l_{l=1,\ldots,L}}) = W \sum_{l=1}^{L} \|M_l - \mathbf{A}(\eta_l^2 * h)\|_\Gamma^2, \tag{5.4}$$

where the normalization factor,

$$W = \frac{1}{\sum_{l=1}^{L} \|M_l\|_\Gamma^2}.$$

Here again, $M \in \mathbb{R}^{N_x \times N_y}$, $\xi, h \in \mathbb{R}^{N_x \times N_y \times N_z}$ and $\mathbf{A} : \mathbb{R}^{N_x \times N_y \times N_z} \longrightarrow \mathbb{R}^{N_x \times N_y}$. After certain iterations a 3D fluorescence density is calculated from the estimated η_l^2, using positivity ($I_l s = i_l^2 \xi^2 = \eta_l^2$) and homogoneity ($\sum_{l=1}^{L} I_l = I_0$). This gives $\xi^2 = \sum_{l=1}^{L} \eta_l^2 / I_0$, where the constant, $I_0 = 1$.

In conclusion, one defines an investigation volume in which a three-dimensional sample is reconstructed so that its 3D convolution restricted to the focal plane best matches the recorded image. To improve the reconstruction, the deconvolution is performed under positivity constraint. This technique re-allocates the out-of-focus light from the focal image to its original source. Of

course, the sample estimate outside the focal plane is not accurate, due to the lack of constraining data. However, it is expected to carry out some of the out-of-focus fluorescence.

The convolution operation is the prevalent process in this reconstruction algorithm. It is repeated several times in every iteration for each illumination. The convolution is computed using Fast Fourier Transform (FFT), therefore, the computational efficiency is given by $\mathcal{O}(N_z N_p \log N_z N_p)$, where N_p is the number of pixels in the 2D image frame and N_z is the number of slices (reconstructed planes). Clearly, the computational efficiency depends on the number of reconstructed planes which is chosen by the user. Large N_z enables an efficient rejection of the out-of-focus contribution while increasing the computational time. Therefore, the choice of the number of planes must be wisely determined considering the depth of field of the detection microscope objective. For example, using a standard computer (Intel(R) Core (TM) i5-4670 CPU @3.4GHz, 16GB RAM), 100x100x1 pixels stack takes $230ms$ per iteration for 100 illuminations under 2D separate blind-SIM-SD while 100x100x50 voxels stack takes 290ms per iteration for 100 illuminations under 3D blind-SIM-SD.

5.3   3D slice deconvolution on brightfield images

We first checked our algorithm on brightfield fluorescence microscopy using synthetic data. We have generated a synthetic three-dimensional object composed of randomly distributed microspheres (of diameter $0.6\mu m$) in a volume of $100x100x50$ voxels, as shown in Figure 5.1(a). We assume a wavelength of $550nm$, numerical aperture of 0.95, pixel size of $69nm$ and axial step-size of $183nm$. A three-dimensional image has been obtained assuming a linear convolution of the object and the PSF using homogeneous illumination. The sample of interest at the axial center of the 3D object is shown in Figure 5.1(b). We then investigate the performance of the 3D deconvolution on the image frame at the axial-center of the 3D stack (z-slice 26). This image frame is deconvolved by a 3D PSF, as well as a 2D PSF for comparison.
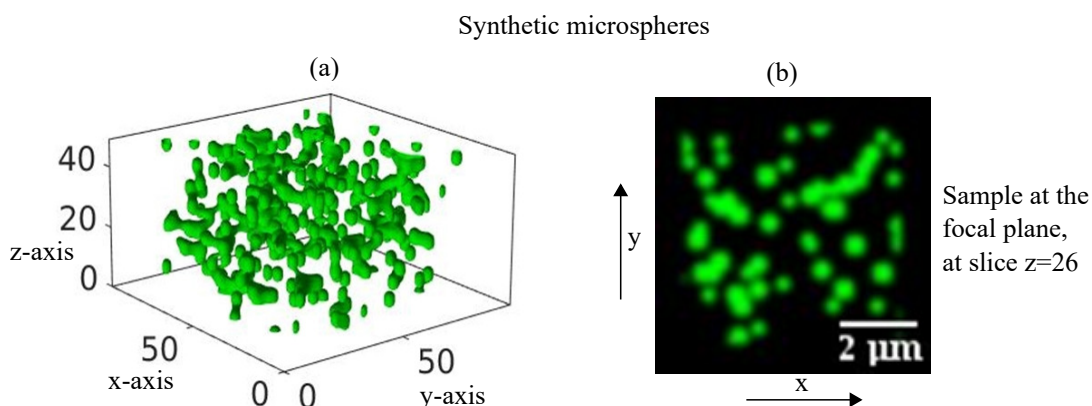
Figure 5.1 : *Synthetic data. (a) Thick 3D sample composed of randomly distributed microspheres. (b) Selected xy-slice through the center of the 3D sample.*

Synthetic microspheres
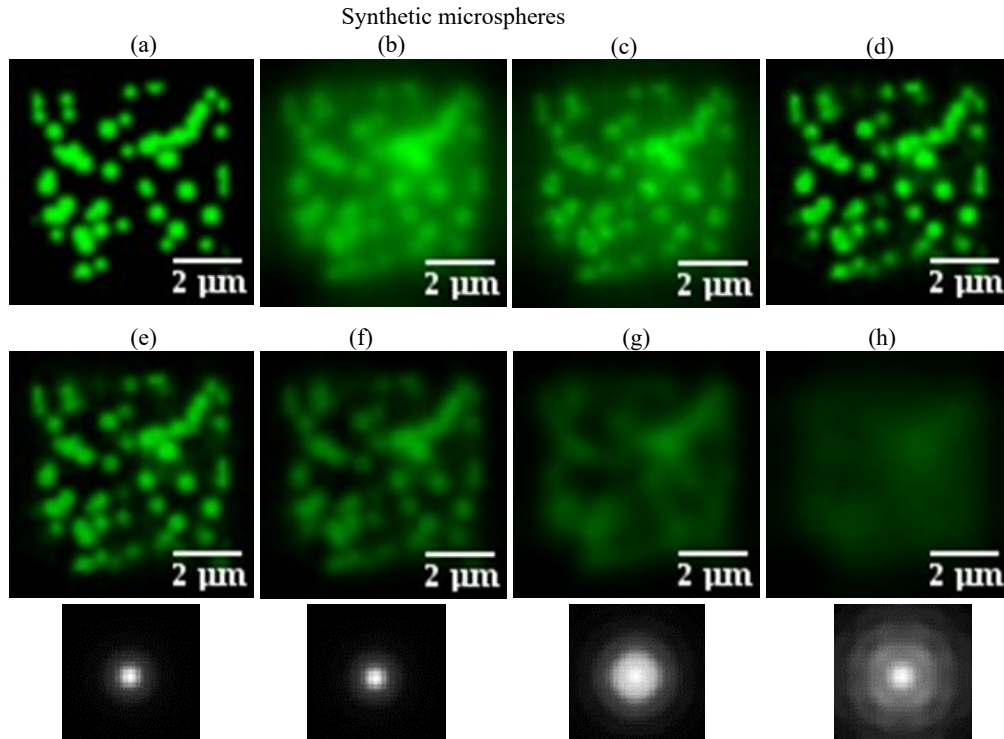
Figure 5.2 : *Slice-based 3D deconvolution on synthetic data. (a) Object at the focal plane of a thick 3D sample. (b) Image of the object. (c) 2D deconvolution. (d) 3D deconvolution. (e)-(h) Estimated out-of-focus contributions at a distance of 185nm, 370nm, 555nm and 925nm above the focal plane respectively. The respective blurring function of each out-of-focus plane is shown (bottom).*

Figure 5.2(a-d) show the object at the focal plane, its widefield image, the 2D deconvolution of the widefield image, and the 3D deconvolution of the same widefield image respectively. In Figure 5.2(e-h) we display the reconstruction for the planes surrounding the focal plane. We observe that some out-of-focus fluorescence has been detected towards these planes. The blurring function of the corresponding out-of-focus planes, obtained from the PSF, is also shown below each out-of-focus estimations. Comparing Figure 5.2(c) and Figure 5.2(d), one observes that the 3D deconvolution significantly ameliorates the resolution and contrast of the 2D image.

We have also illustrated the potential of the technique on experimental data such as vimentin filaments, podosomes, and dense actin filaments. For the experimental data, 100x,1.49NA oil immersion objective is used. The emission is at 670nm for vimentin filament and 520nm for podosomes and actin filaments. And, the number z-slices in 3D deconvolution is considered to be 9 taking into account of the depth of field. Increasing the number of slices improves the resolution and contrast, but with increasing computational time. Figure 5.3 compares again the 2D deconvolution (c) and 3D deconvolution (d) for a 2D image (b).

The improved contrast and resolution is clearly apparent on the podosomes and actin filament images, in Figure 5.4. After 2D deconvolution (b), the ring-like vinculin structures at the focal

Vimentin filaments
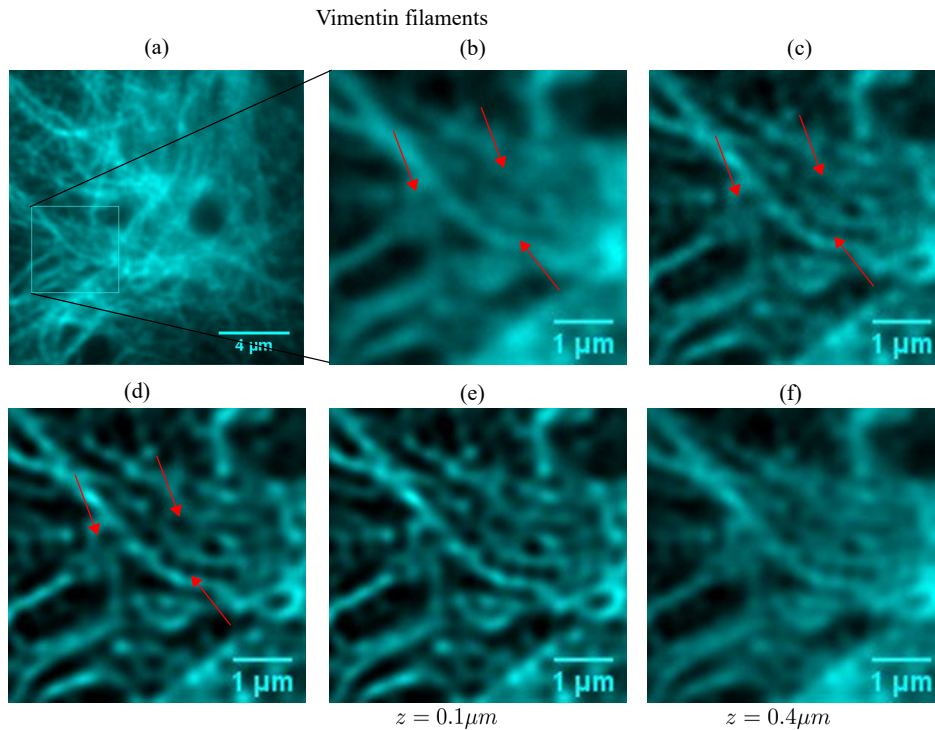
Figure 5.3 : *Slice-based 3D deconvolution on vimentin filaments.(a) Widefield image. (b) Widefield image (zoom of a section). (c) 2D deconvolution. (d) 3D deconvolution. (e)-(f) Estimated out-of-focus contributions at a distance of* $100nm$ *and* $400nm$ *above the focal plane respectively.*

plane in podosome are still highly blurred from the background out-of-focus signal. The 3D deconvolution, however, deblurrs image and improves the resolution and contrast (c). Similarly, more contrasted actin filaments are obtained after 3D deconvolution.

In conclusion, on brightfield fluorescence microscopy data, we have shown that the 3D deconvolution approach improves substantially the transverse resolution of the image. It yields considerably better results than the two-dimensional deconvolution that is usually performed on these images (with minimal additional computational costs). In the following section, we extend the technique for fluorescence microscopy using speckle illuminations.

5.4 Extending the technique towards speckle illumination microscopy

The capability of speckle illuminations for super resolution has been discussed in detail in the previous chapters (see Chapters 2 and 3). Here, we have illustrated the contrast enhancements on experimental data using the 3D blind-SIM-SD on 2D low-resolution data captured using unknown random speckle illuminations. Each raw 2D low-resolution frame is deconvolved using a 3D-PSF for 200 speckle illuminations. Each deconvolution results in the sample estimate at the focal plane

Podosome and actin filaments
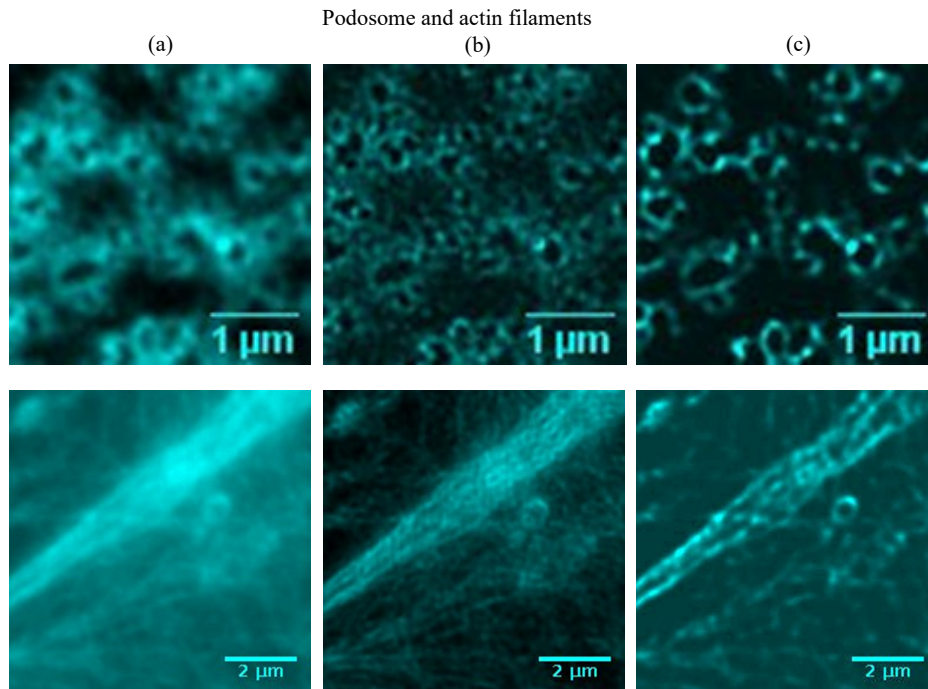
Figure 5.4 : *Slice-based 3D deconvolution on podosomes (top) and dense actin filaments (bottom). (a) Widefield images. (b) 2D deconvolution. (c) 3D deconvoluton.*

plus the background fluorescence on the out-of-focus planes which constitute the investigation volume. The final sample estimate and the background fluorescence is obtained by averaging over all the estimates. The reconstructed slice of interest is the one at the focal plane.

Figure 5.5 compares the 2D blind-SIM-SD and the 3D blind-SIM-SD, (a) and (b) respectively. There are visible contrast differences between the 2D and 3D deconvolution. Apparently, the 3D deconvolution result provides better visibility. The red arrows show some of the spots where the difference is clearly visible. It is important to note that the 2D blind-SIM-SD by itself enhances the resolution and the contrast significantly (see Chapters 2 and 3). Yet, the 3D blind-SIM-SD improves the contrast further. The contents of the estimated object at 100nm and 400nm distances above the focal plane are shown in Figure 5.5(c) and (d) respectively. These account for some background fluorescence signal from the corresponding out-of-focus planes.

The application of this algorithm for 3D raw data depends on the forward imaging model. If the object is scanned in every acquisition, which is usually is the case in many experimental setups, we can apply the 3D deconvolution technique for each slice. However, if the data is obtained using multifocus setups, where the signal from multiple axial positions is captured without moving the sample, 3D deconvolution can be applied directly to the full 3D stack: i.e. there is no need to do slice 3D deconvolution in such cases.

Vimentin filaments
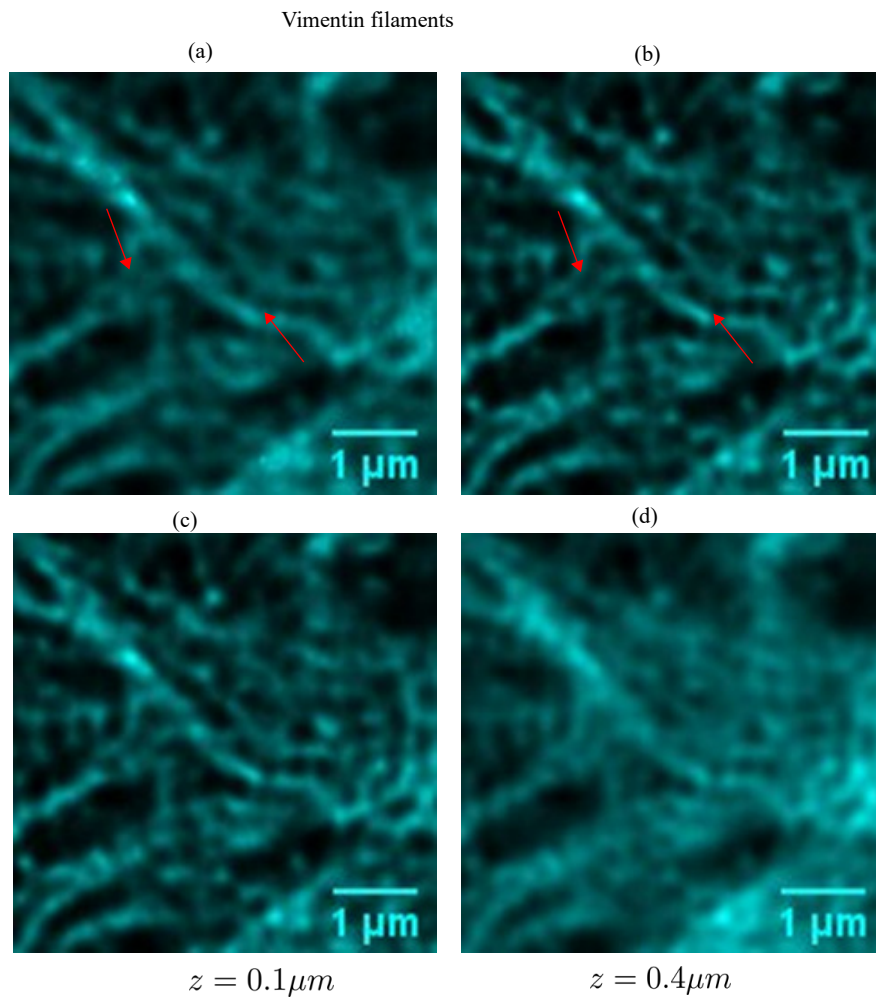
Figure 5.5 : *Slice-based 3D deconvolution on speckle illumination microscopy.*
(a) 2D blind-SIM-SD . (b) 3D blind-SIM-SD. (c, d) 3D blind-SIM-SD out-of-focus
estimate at 100nm *and* 400nm *above the focal plane respectively.*

5.5   Conclusion

In conclusion, three-dimensional deconvolution should be preferred to two-dimensional deconvolu-
tion even when the data are restricted to a single plane image. It dims the out-of-focus fluorescence
and significantly ameliorates the contrast and resolution. It is a simple data processing which can
be used on most microscopy configurations. We have demonstrated the technique on synthetic
and experimental data. On experimental data, it is sometimes difficult to actually tell which
of the reconstructions are closer to reality due to lack of ground-truth information, yet on syn-
thetic data there was clear evidence that using slice 3D deconvolution improved the contrast and
resolution compared to the two dimensional reconstruction appraoch. To summarize, Figure 5.6
depicts the 2D and 3D deconvolutions on brightfield as well as speckle SIM data and shows the
above-mentioned improvements.

Vimentin filaments
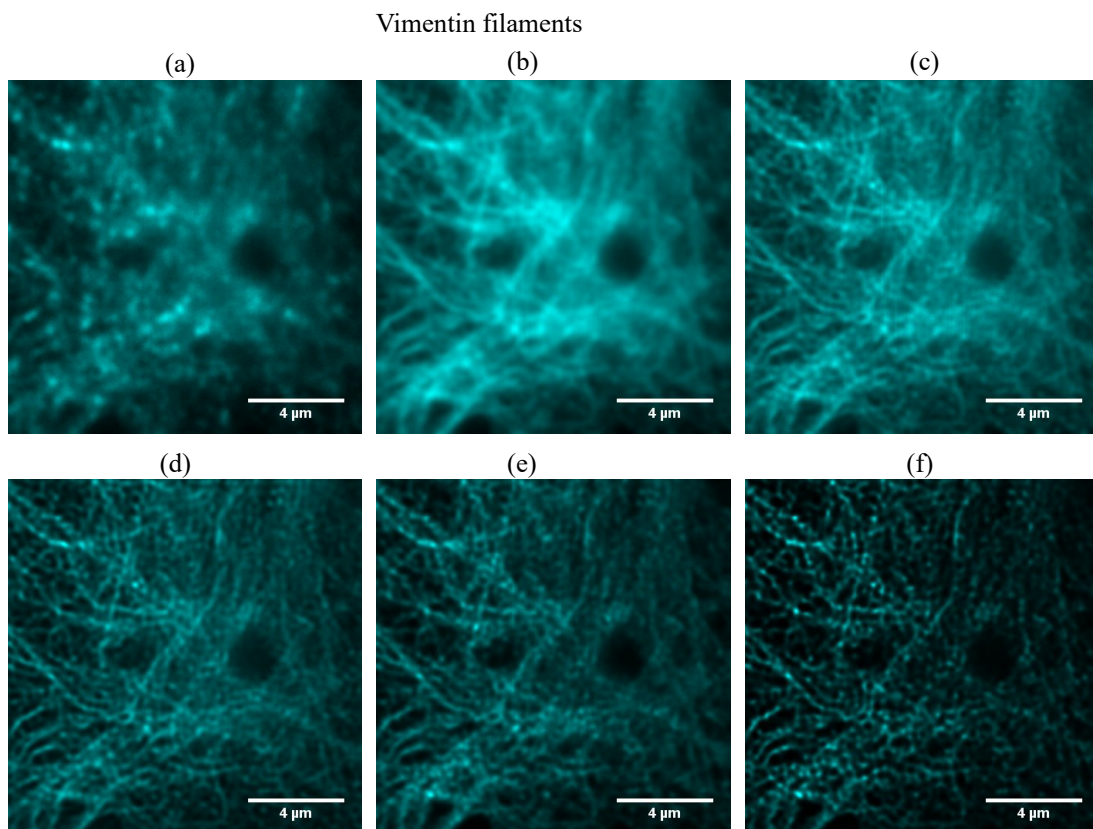
Figure 5.6 : *Slice 3D deconvolution. (a) Raw speckle SIM image . (b) Brightfield image. (c) 2D deconvolution of brightfield image. (d) Slice 3D deconvolution of brightfield image. (e) 2D Blind-SIM-SD on speckle SIM data. (f) slice 3D blind-SIM-SD on speckle SIM data.*

Light sheet Microscopy with Structured Illumination

Contents

6.1   Introduction

In the previous chapters, we have presented the standard SIM and speckle illumination microscopy techniques for super resolution enhancement in three dimensions. Indeed, these techniques have been implemented with epi-fluorescence microscope configurations where the same objective is used for illumination and collection. In such configurations, the out-of-focus blur at the imaging plane is inevitable as planes above and below the focal plane are also illuminated. Obviously, the in-focus image degradation is even worse when using thick samples. Light sheet illumination microscopy uncouples the illumination path from the detection path and uses a thin layer of light to illuminate only a section of the sample. This reduces photobleaching of the sample and out-of-focus blur at the imaging plane. The resolution of light sheet images is, however, still diffraction limited. Inspired by the resolution gain in the well-developed theory of structured illumination/speckle illumination microscopy, using our dedicated reconstruction algorithms, we introduced the structured illumination to light sheet illumination microscopy. This helps to combine the benefits of both approaches with little increase of complexity.

In this chapter, we present the efforts that we have put to experimentally combine both techniques. The blind-SIM reconstruction algorithms are then accommodated for reconstructing the images captured with the custom made structured light sheet microscopy. The goal of the microscope is to obtain optical sectioning in the axial direction using a thin light sheet and improve the two-dimensional resolution using structured patterns. In section 6.2, we present the basic principles of light sheet microscopy. We highlight the different approaches of generating light sheet, benefits of each implementation and its application domains. Section 6.3 presents the overview of structured illumination in light sheet microscopy for resolution improvement. The inverted selective plane structured illumination microscopy (iSPIM-SIM) implementation is presented in section 6.4. This section focuses on the details of the experimental setup and the challenges faced during practical implementation. The patterns of the illuminations on the light sheet are characterized and the light sheet properties are also investigated. Section 6.5 presents data acquisition, image analysis, and reconstruction procedures. In section 6.6, I present the iSPIM-SIM images and resolution enhancements after reconstruction. I finally conclude the chapter by discussing the pros and cons of iSPIM-SIM, and by suggesting recommendation for its developments to full three-dimensional configurations.

6.2   Principle of light sheet microscopy

The idea of light sheet illumination traces back to 1903[85]. The first application of light sheet microscopy to biological specimens is however introduced in 1993[86]. Huisken et al. introduced a groundbreaking selective plane illumination microscopy (SPIM) technique in 2004[76]. It is shown in[87] that SPIM performs very well at low numerical apertures (<0.8) and complements conventional confocal and two-photon fluorescence microscopy techniques. Since then, a large number of innovative implementations of light sheet fluorescence microscopy for a wide range of application has been developed including commercial light-sheet fluorescence microscopes.

The concept of light sheet microscopy is actually simple. A thin sheet of excitation laser illumination which is orthogonal to the detection path is projected onto the sample by using an excitation microscope objective, see Figure 6.1. The center of the excitation light-sheet has to match with the focal plane of the detection objective. Unlike confocal microscopy which uses pinholes, light sheet microscopy introduces instantaneous optical sectioning by the thickness of the light sheet. Only a slice of the three-dimensional sample is illuminated by the light sheet and imaged by the detection objective.
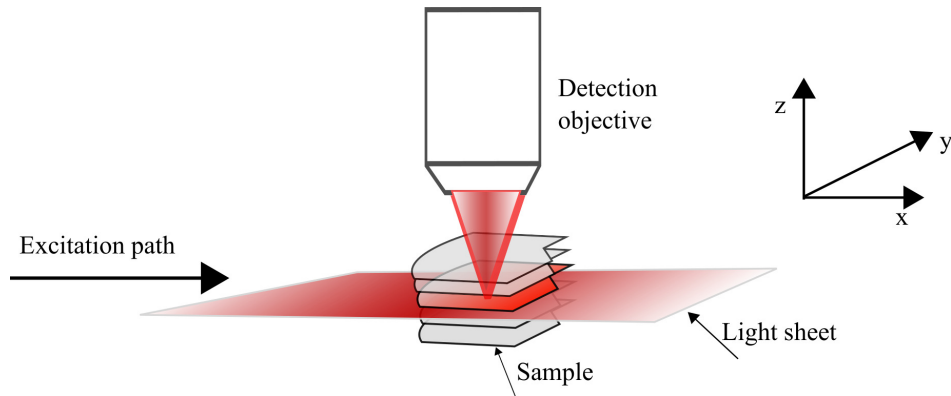
Figure 6.1 : *Basic principle of light sheet microscopy*

Optical sectioning is not the only benefit of light-sheet configurations. The thinness of the light-sheet also decreases the out-of-focus blurring problems. Since the whole volume of the sample is not illuminated during image acquisition it also incurs an advantage in significant reduction of photo-toxicity and photo-bleaching and it increases the longevity of live samples[88,89]. In contrast to confocal microscopy, light sheet microscopy is much faster since it images the full widefield at once.

Obviously the thinner the light sheet, the better the optical sectioning and its related advantages. However, due to the diffraction limit, it is not always straight forward to achieve very thin light sheets. The high NA objectives produce thinner light sheets but with a shorter field of view. The latter controls the light sheet uniformity. Commonly the thickness of the light sheet is between $2\mu m - 6\mu m$ with the field of view ranging from $60\mu m$ to $300\mu m$ respectively[90]. One has to therefore carefully design and choose the objectives based on the application areas of interest. Low NA and long working distance objectives are beneficial for large samples.

One of the applications of light sheet microscopy is for imaging morphogenesis and spatiotemporal patterns of cells during embryogenesis of model organisms such as Drosophila and Zebrafish[91]. It is also applied in imaging of morphogenesis and cellular dynamics in embryos and small organisms with emphasis on cardiac development, blood flow, vascular development and neuro-development. It has been also used for structural imaging of fixed organisms and for much more other applications. Mostly light sheet microscopy is used when long-term live imaging is required and for thick samples.

Based on the application of interest and the methods of generating light sheet, its practical implementation may be different even though they follow the same fundamental principle. The basic and simpler way to generate light sheet is using beam shaping cylindrical lenses which modify

the beam only in a single axis. Based on the choice of the NA, cylindrical lenses may produce uneven thickness with high numerical aperture and thicker light-sheet with low numerical aperture. The most common implementation of cylindrical lenses for light sheet generation is the SPIM configuration[92]. Advanced techniques such as wavefront coding have been demonstrated in[93] to extend the depth of field of the detection optics and obtain optical sectioning by loosening the tight-coupling of the illuminated volume with the detection optics. Another approach of generating light sheet is using Bessel beams[94]. This beams can be generated using the axicon (conical lens element) or by placing an annular aperture at the back focal plane of the excitation objective. Unlike Gaussian beams, the light sheet of Bessel-beams which are non-diffractive remains constant for a longer field of view. If the beam is partially obstructed it will reform further in the path which makes the beam preferable in thick inhomogeneous samples. Conversely, it requires advanced implementation and image processing skills. DSLM (Digitally scanned laser light sheet microscopy) is another implementation of light sheet microscopy[95]. By controlling the laser properties it is possible to generate structured light sheet patterns using DSLM.

6.3 Preview of structured illumination in light sheet microscopy

Structured illumination microscopy has been introduced to light sheet microscopy by few research groups so far. Tobias *et al.* in[96] have demonstrated the combination of the static light sheet (thickness between 3-4um) and structured illumination using patterned scanned light sheet. The structured illumination is produced by intensity modulation of the laser light using an acousto-optic modulator. In their demonstration, structured illumination produces superior contrast compared to both the uniform static and scanned light-sheets. Similarly, structured illumination is combined with the light sheet in[97] using the HiLo mechanism to suppress the background noise. The contrast is improved by using background removal demodulation techniques. The HiLo term describes a process in which the in-focus high-frequency content of the sample is obtained under uniform illumination and the in-focus low-frequency content can be extracted from structured illumination images. This technique is implemented on large samples (<15mm) in diameter. Even though the approach improves the contrast, the gain in resolution is not obtained. On the same token, Keller et al. have demonstrated optimization of the contrast of the in-focus image and discrimination of the specimen-related scattered background from signal fluorescence by combining DSLM with incoherent structured illumination created by digitally controlled modulation of the laser intensity[91]. Multiple light sheets (structure in the axial direction) are obtained by using carefully designed spatial filters placed at the back focal plane of the cylindrical lens[98,99]. Yet again, the spatial resolution gain from the above techniques is not clearly presented. The superresolution improvement in light sheet microscopy is clearly illustrated, at least in one dimension, by Betzig et al. which uses lattice light sheets using SLM and carefully designed annular masks to create periodic patterns on the sample[100].

Motivated by the results of superresolution gains using 2D lattice sheets, we have put the effort to combine structured illumination to standard light sheet microscopy. We use the carefully selected diffraction grating for the former and cylindrical lens for the latter. The purpose of this project is to exhibit the proof of concept, unveil the technical challenges, exhibit merits and limitations in combining SIM with light sheet microscopy. The light sheet images obtained using structured illumination passes through blind-SIM reconstruction algorithm adapted for light sheet images. For reasons which will become clear later, an inclined selective plane illumination (iSPIM) configuration is selected.

6.4 Inverted selective plane structured illumination microscopy (iSPIM-SIM)

6.4.1 Modalities of LSFM configuration

Before discussing the designs and implementation of our experimental setup, it is worth reminding the light sheet imaging configurations. Basic light sheet fluorescence microscopy is implemented using SPIM configuration, Figure 6.2(a). In such configuration, the excitation light illuminates the sample which is placed in an appropriate imaging sample chamber. The fluorescence light is then collected with an orthogonally placed detection objective. The sample is suitably suspended in the chamber using FEP (Fluorinated Ethylene Propylene) tubes with the help of support mediums such as agarose. The full three-dimensional acquisition is obtained by translating and rotating the FEP tube along the axial axis of the common focus of the two objectives.
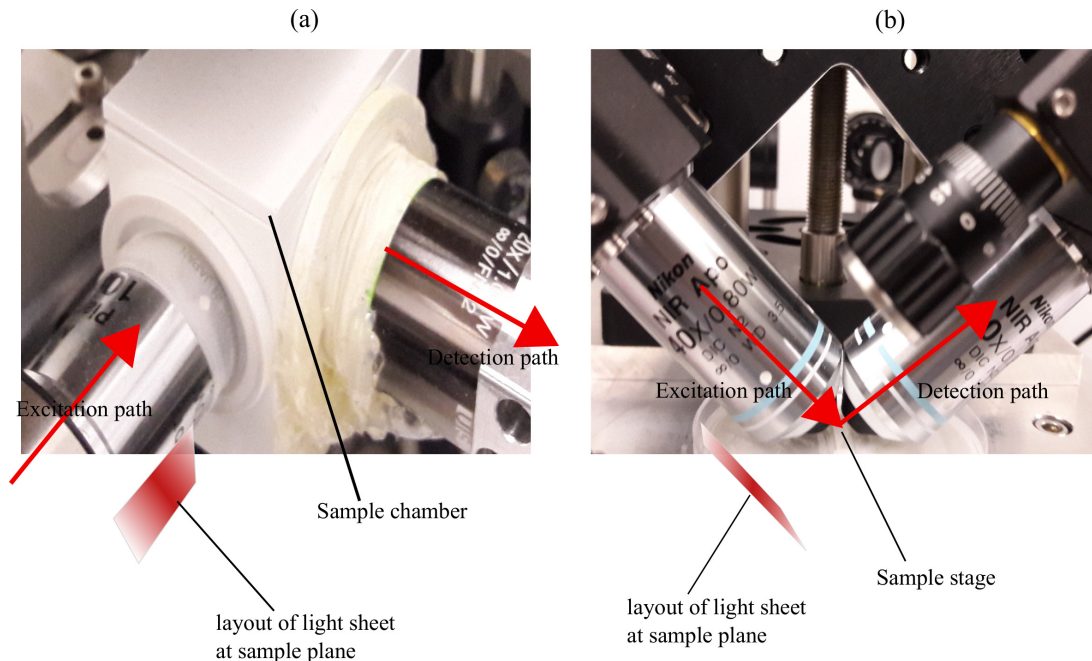
Figure 6.2 : *Modalities of light sheet configureation. (a) SPIM. (b) iSPIM.*

The other configuration, which is chosen for our demonstration, is the inverted selective plane illumination microscope (iSPIM). As depicted in Figure 6.2(b), the excitation source is guided to the sample in a 45° inclination. Correspondingly, the fluorescence is collected with another objective in 45° inclination again, orthogonal to the excitation path. This modality allows using standard sample preparation techniques on cover glasses. Unlike in the SPIM where the sample is suspended, in the latter is the sample is resting on the custom-made flat sample holder. In addition, with the support of gravity, this configuration is suitable for using the immersion media. The objectives can easily dip into the medium and there is no leaking problem in iSPIM. It is demonstrated in [101,102] that iSPIM can be extended in dual view imaging arrangements the excitation and detection paths can be alternatively used as detection and excitation respectively, in order to yield higher-resolution isotropic volumes. As a limitation, the iSPIM approach has a restriction on working distance, and the objectives have to be carefully selected.

6.4.2   Design of iSPIM-SIM

As explained in the previous sections, the objective of this experiment is to demonstrate a proof of concept by combining standard structured illumination microscopy with the conventional light sheet microscopy in order to improve the resolution at least in one-dimension. The feasibility of the experiment, the experimental challenges, the benefits, and limitations will be discussed. iSPIM light sheet modality is chosen for the experimental implementation based on the merits of the configuration. When the setup in such configurations is combined with the standard inverted microscope, the conventional light path can be used to image the sample and find the structures fast. As a proof of concept demonstration, we only focus on the structured illumination characterization and resolution improvements only in one or possibly two-dimensions.

The cylindrical lens and the transmission grating are the two basic optical components which are respectively key in the light sheet and the structured illumination in this coupled experiment. The cylindrical lens, CL, is used for beam shaping, to create the thin light sheet whereas the transmission grating, DG, splits the light sheet into diffraction orders, as has been implemented in conventional structured illumination microscopy. Starting from the cylindrical lens, the dimensions of the propagating beams are different in the two orthogonal directions. This makes the design of conventional structured light sheet microscopy more technical, particularly on the selection of appropriate optical components through the beam path. We start the design of the experiment with the two Nikon 40x,0.8NA (3.5mm working distance) water objectives for the excitation and detection. The objectives are selected based on a compromising consideration of the resolution, the field of view, the light sheet thickness, the working distance and the immersion medium. Then, starting from the output of the laser the optical components are designed such that the beam passes through the back focal aperture of the objective without clipping (within 8mm pupil size of the objective) and with adequate frequency support. The schematic of the optical setup is shown in Figure 6.3. Before the detailed explanation of the design, we assume a directional convention: x-axis shows the propagation direction of the beams, and y- and z- axes show the orthogonal directions which correspond to the field of view and the thickness of the light sheet respectively.

Figure 6.3 : *Schematic of iSPIM-SIM. HWP: half wave plate, P: linear polarizer, PH: pin hole, DG: diffraction grating (110grooves/mm), CL: cylinderical lens, GM: single axis galvo-mirror, FM: filter mask, EF: Emission filter, TL: Tube lens, L1-L7: Achromatic doublets, and M1-M4: mirrors. The focal lengths of the lenses are L1(f=35mm), L2(f=50mm), CL(f=10mm), L3(f=50mm), L4(f=150mm), L5(f=50mm), L6(f=200mm) and L7(f=200mm). P0, P1 and P2 are conjugates of the sample plane. F0 and F1 are the conjugates of the back focal plane of the objective (F2).*

The beam from a red laser (633nm, LHRP-0501 cylindrical HeNe laser, research electro optics inc.) is vertically polarized by using a half-wave plate and a polarizer. This beam is measured to

Figure 6.4 : *The xz- and yz-schematic of the iSPIM-SIM: CL: cylinderical lens, DG: diffraction grating (110grooves/mm), GM: single axis galvo-mirror, FM: filter mask, EF: Emission filter, TL: Tube lens, L3-L7: Achromatic doublets, and M1-M4: mirrors. P0, P1 and P2 are conjugates of the sample plane. F0 and F1 are the conjugates of the back focal plane of the objective (F2).*

have the beam width of 1.07mm. The achromatic doublets L1 and L2 (Thorlabs, AC254-035-A-ML, and AC254-050-A-ML respectively) are used optionally to expand the beam by a factor of 1.4 times. Until the cylindrical lens, the beam width is symmetrical in the orthogonal axes of the beam path which is chosen to be 1.07mm. A short focal length plano-convex cylindrical lens (Thorlabs, LJ1878L1-A, N-BK7 A Coat Plano Convex Cyl Lens, H=10.0 L=12.0 f=10.0) focuses the beam in the z-axis at its focal distance where we put the transmission grating. A visible transmission grating beamsplitter (110 Grooves/mm) splits the elliptical beam into diffraction orders which the first orders and the zero order accounts each 25% of the incident power, whereas the second diffraction orders (not shown in the schematic) accounts each 5% typical distribution of power at 632nm wavelength.

Starting from the cylindrical lens, the beam sizes are not symmetrical around the propagation direction. Since the cylindrical lens shapes the beam only in one direction, the width of the beams in orthogonal directions to the propagation axis have no longer the same sizes. It is, therefore, elegant to refer to the schematic in both dimensions perpendicular to the optical axis, in the xy- and the xz-view, where the x-axis is conventionally assumed to be the propagation direction. A part of the excitation path of Figure 6.3 is redrawn in the two orthogonal planes as shown in Figure 6.4.

The cylindrical lens focuses the beam (in the z-axis) at the position of the diffraction grating, *P*0. This visible transmission grating beam splitter is placed at the conjugate plane of the sample

plane. The grating does not affect the beam dimensions in the respective orthogonal directions but separates the beam into multiple orders. Furthermore, the optical lenses after the diffraction grating serve as not only to focus and collimate the beams of the multiple diffraction orders collectively but also to compress and expand the beams of individual diffraction orders through the optical path. After the transmission grating beam splitter, the elliptical diffraction order beams are then collimated using 50mm achromatic doublet lens, L3, (Thorlabs, AC254-050-A-ML). The beams at lens L3 have 1.07mm width in the minor (y-) axis and (5.35mm) width in the major (z-) axis. The separation between the zero order and the first orders is 3.50mm. This beam is then collimated by L3, and only the diffraction orders of interest selected by using a custom-made filter mask at the Fourier plane, F0. The position of the filter masks is at the conjugate of the back pupil plane of the objective. In Figures 6.3 and 6.4, it is shown that the zero order is blocked. By choosing an appropriate mask, it is possible to obtain two-beam or three-beam interference fringes at the sample plane. The lenses L3 and L4 (Thorlabs, AC254-150-A-ML) expand the beams in the minor axis by a factor of 3, whereas the size of the beam in the major axis remains to be 5.35mm. Hence, the beam sizes at lens L4 would be 3.21mm in the minor axis and 5.35mm in the major axis. Conversely, lenses L4 and L5 (Thorlabs, AC254-050-A-ML) compresses the beam in the major axis to 1.78mm and collimates the beams in the minor axis. This lens also compresses the separation between the first orders from 7mm to 2.32mm. This demagnification of the separation is critical to guide the beams into the back focal aperture without clipping. Finally the lenses L6 and L7 are used as a relay, and it conjugates F1 to the back pupil plane, F2. Even though this relay seems redundant, it is needed in order to access the back focal plane of the objective by conjugation.

At the F1, a motorized galvo-mirror (GM) is placed to introduce a slight rotation of the orientation of the elliptical beam at the back pupil plane. The position of the pattern on the sample plane in this telecentric system depends on the angle change in the Fourier plane. The slight rotation or the angle change results in translation of the periodic pattern at the sample plane. The center of the tilting movement of the mirror is the axis in the beam direction. It is important to remind that, other than the galvo-mirrors, an alternative way to get periodic translation in classical SIM is by linearly translating the grating.

The other part of the schematic of Figure 6.3 is the detection path. It consists of detection objective (40x, 0.8NA water immersion), an emission filter, a tube lens ($200mm$ focal length) and sCMOS (Orca flash, Hamamatsu) camera. With all the optical components in the excitation path set, it produces a structured light sheet at a 45° inclination to the horizontal plane at the sample through the excitation objective. The detection objective, orthogonal to the excitation one, then collects the emission and produces the image on the camera.

After careful design and selection of optical components, the practical implementation of the experimental setup has been produced. Since the setup is very sensitive to the position of the optical components due to its telecentric nature, it needs precise alignment in order to produce the optimum structured light sheet pattern according to the design.

6.4.3   Description of practical implementation

Due to the sensitivity of the excitation path for little misalignment, the setup has been carefully built. One of the very sensitive optical component in terms of positioning is the cylindrical lens. Since it is a short focal length lens, a little axial translation degrades the interference pattern at the sample. Moreover, it has to be accurately and gently placed without any tilt. A little tilt or inclination of the cylindrical lens results in a tilted light sheet. This, in turn, causes an orthogonality deflection with respect to the detection objective and decreases the effective field of view of the light sheet. To fix this problem the cylindrical lens is placed with rotational flexibility where the propagation direction is the axis of rotation. The best position of the cylindrical lens can, therefore, be optimized.

For better spatial frequency support of the illumination, we also tried to use a visible transmission grating of 300 grooves/mm. This, however, results in higher separation between the diffraction orders. It produced clipping by the back aperture of the objective, and the sinusoidal pattern on the light sheet was hardly visible. In addition, the majority of the laser intensity is in the positive first order. The interference between the negative and positive first orders, therefore, could not provide a good contrast. For a better contrast of the patterns, we have used 110 grooves/mm visible transmission grating beam splitter which improves the contrast of the illumination pattern and removes the clipping of ellipsoidal beam by the back focal aperture of the objective. Conversely, it downplays the resolution enhancement. The patterns of the illumination are characterized using a homogeneously fluorescent rectangular sample held by a customized stage.

The picture of experimental setup is shown in Figure 6.5(a). The red arrows show the path of beam propagation from the laser source to the camera. the iSPIM configuration represented in Figure 6.5(b) where the arrows show the excitation beam to the sample and the emission from the sample to the camera. This configuration requires a special customized sample stage. The custom-made sample stage, shown in Figure 6.5(c) is designed to hold the small petri-dish in which the sample holder is placed. The sample holder is designed and 3D-printed such that it will hold the sample on on a small rectangular cover slip of size 30mm by 4mm. Once we placed the sample on the sample holder, we put it on the petri dish. Since we use water immersion objectives, we fill the petridish with miliQ water wherein the objectives dip. The fact that we use a small rectangular cover slip to prepare our sample on is because of the geometrical limitation of the 40x, 0.8NA objectives which have 3.5mm working distance. In such configuration where the objectives are at 45° from the horizontal plane, the common focus point of the objectives is about 1mm above the lower surface of the objective parallel to the horizontal surface. Therefore the rectangular cover slip can pass through the gap between the objective to hold the sample at the common focal spot. Figure 6.5(d) shows the sample holder on the petri dish and the working distance of the objective. The sample is scanned horizontally through the light sheet to acquire three-dimensional data sets.

It has been discussed earlier that the visible transmission grating splits the elliptical beam into the zero order, the two first orders and the two second orders. Based on the period of the pattern and the field of view of interest we can select the desired diffraction orders and block the others. To block the undesired diffraction orders, we use the custom-made spatial filter masks
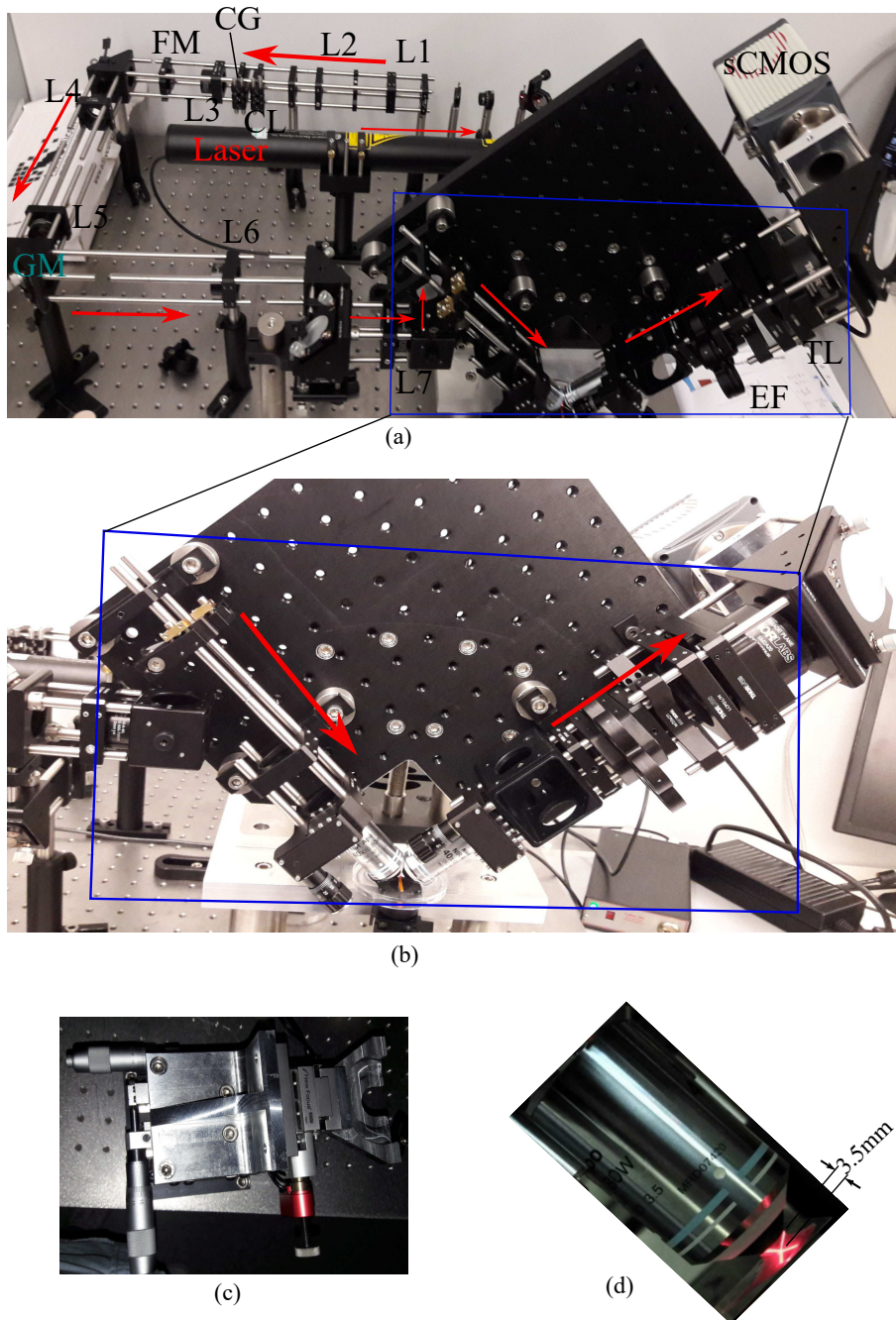
Figure 6.5 : *Experimental setup of iSPIM-SIM. (a) Setup. (b) The iSPIM con-figuration layout. (c) Custom-made sample stage. (d) Limiting working distance. The notations of components denoted in this figure are described in Figure 6.3.*

at the Fourier plane $F0$, at the focal spot of lens $L3$. We made spatial filter masks, shown in Figure 6.6, to select either the two first orders, two second orders, three beams (two first orders and zero order), and three beams (two second orders and zero order). We have mainly used the two beam interference with the first orders beams and three beam interference (two first orders and zero order). These choices produce fringe patterns with better contrast. The fact that the zero
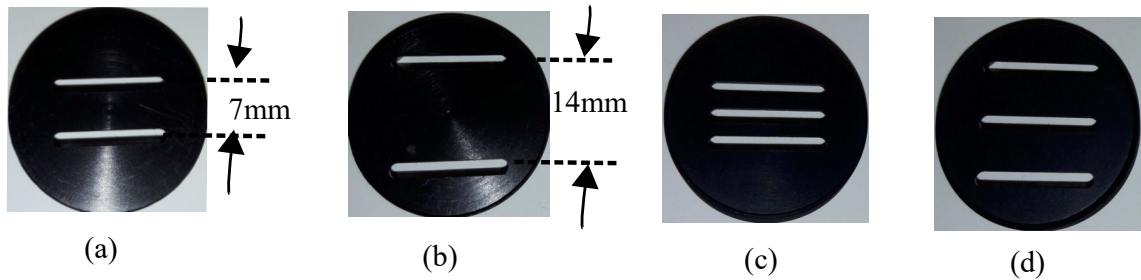
Figure 6.6 : *Spatial filters of diffraction orders. (a) 2 beam first orders. (b) 2 beam second orders. (c) 3 beam first orders and zero order. (d) 3 beam second orders and zero order.*

order and the first orders have equal fraction of power also contributes for better contrast. From the principle of structured illumination microscopy, the sample has to be recorded using multiple intensity patterns of different orientation or phase. To produce multiple patterns, we have used a piezo-controlled mirror positioned at the conjugate of the back focal plane, Fourier plane $F1$. The tilt of the mirror from one side produces an angular tilt in the Fourier space which corresponds to translation at the sample plane. By investigating the homogeneity of the sum of all the patterns, the optimum number of illuminations is found to be 20.

In general, as a proof of concept demonstration, it is possible to actually obtain two-dimensional interference patterns on the sample plane using standard SIM and LSFM principles with just simple basic cost-efficient optical components. The setup will be developed to have structured illumination patterns in multiple transversal directions to obtain symmetric two-dimensional resolution. This setup will also be advanced to dual selective plane illumination microscopy (dSPIM) combined with an inverted microscope. These developments are however beyond the scope of this project.

6.4.4 Structured light sheet illumination pattern characterization

The important parameters of interest for the structured light sheet illumination are the period of the sinusoidal pattern and the thickness and field of view of the light sheet. The period of the pattern controls the resolution enhancement, the thickness determines optical sectioning and the field of view provides the size of the image. In this section, these parameters are characterized theoretically as well as with experimental measurements.

Before talking about the quantitative characterization of the illumination properties, let us remind imaging objective and camera properties. The NIR 40x, 0.8NA water immersion objectives have a back focal pupil of 8mm. Therefore, it is important to realize that the propagating elliptical beams should not be cropped by the pupil in order to obtain the optimal light sheet quantities. The other parameter that has to be predefined is the pixel size on the sample plane. We have used the SCMOS (Hamamatsu Orca flash) camera with total field of view $2048x2048$ pixels and camera pixel size of $6.5\mu m$. it provides $162.5nm$ pixel size on the image using a $40x, 0.8NA$ objective

and 1x lens magnification of the microscope. This is less than the Nyquist pixel size for the far red emission (656nm). And, the maximum field of view of the image captured by the camera is, therefore, $332.8\mu m$ x $332.8\mu m$. Once realizing basic imaging system quantities, we are now set to study the properties of the particular parameters of the structure light sheet illumination.

6.4.4.1 Period

The period of the interference pattern on the light sheet is determined by the separation between the ellipsoidal diffraction orders at the back focal plane of the objective. In other words, the separation corresponds to the the effective numerical aperture of the system. To simplify the analysis, let us consider the interference between the +1 and -1 diffraction orders. From the geometrical optics theory, we can assume the ellipsoidal beams at the back focal plane as the output of from rectangular slits. If w_y is the width of each diffraction order at the back focal plane and d_y is the separation between the centers of the two diffraction orders (separation of the two beams), the far-field Fraunhofer diffraction pattern F (at the sample plane) is given by

$$F = w_y sinc(w_y sin(\theta)/\lambda)e^{-i\pi d_y sin(\theta)/\lambda} + w_y sinc(w_y sin(\theta)/\lambda)e^{i\pi d_y sin(\theta)/\lambda}$$
$$= 2w_y sinc(w_y sin(\theta)/\lambda)cos(\pi d_y sin(\theta)/\lambda). \tag{6.1}$$

θ is the aperture angle of the excitation objective, and λ is the excitation wavlength. The intensity, I, is then

$$I = 4w_y^2 sinc^2(w_y sin(\theta)/\lambda)cos^2(\pi d_y sin(\theta)/\lambda) \tag{6.2}$$

The one-directional pattern (in the y-direction) can be expressed using $sin(\theta) = y/f$ and the trigonometric relation $cos^2(\pi d_y sin(\theta)/\lambda) = 2cos(2\pi d_y sin(\theta)/\lambda) - 1$ as

$$I = I_0 sinc^2(w_y y/\lambda f)[1 + cos(2\pi d_y y/\lambda f)], \tag{6.3}$$

where $I_0 = 2w_y^2$, $sinc^2(w_y y/\lambda f)$ and $cos(\pi d_y y/\lambda f)$ being the diffraction factor and the interference factor respectively. The height of the slit,w_y, determines the envelope of the intensity (the field of view). The separation distance, d_y, (which limits the effective numerical aperture) contributes to the period of the light grid. The periodic distance on the sample, P_y, is determined to be $P_y = \lambda f/d_y$. Equation 6.3 is modified as follows for the immersion objective of medium refractive index n,

$$I = I_0 sinc^2(w_y y/\lambda f)[1 + cos(2\pi d_y ny/\lambda f)], \tag{6.4}$$

and the period of the pattern on the sample plane is given by

$$P_y = \lambda f/d_y n. \tag{6.5}$$

As presented in detail in the previous section, the separation distance at the back focal plane is $d_y = 2.32mm$. The period is determined to be $1.025\mu m$ from both theoretical calculations and experimental measurements. Larger separation distance, d_y decreases the period, which improves
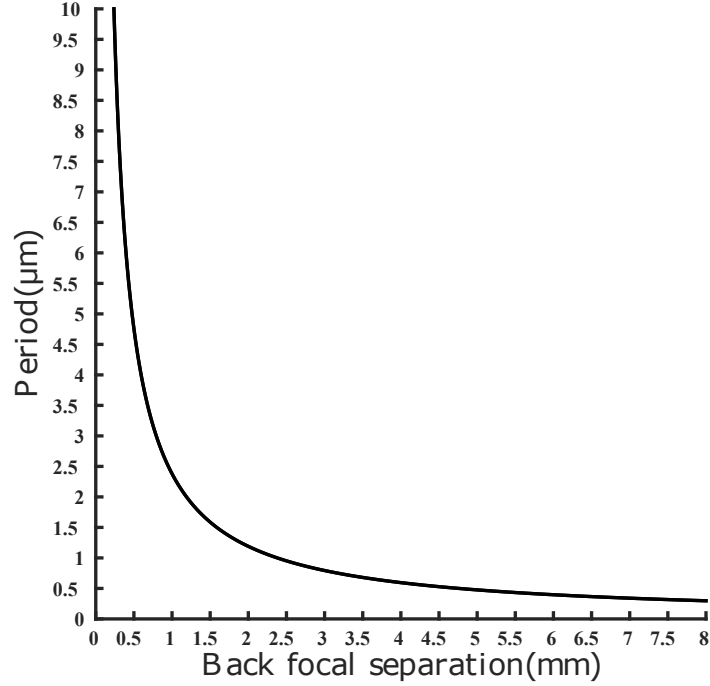
Figure 6.7 : *Period vs back focal separation of the two-beams (d_y).*

the resolution. On the other hand, it decreases the contrast. By using the interference between $+2$ and -2 diffraction orders the period is determined to be 513nm. The period on sample plane, for ranges of separation distances at the back focal aperture, is plotted in Figure 6.7. In other words, it is plotted for ranges of effective numerical apertures, $\mathrm{NA}_{eff} = \mathrm{NA}_{obj} * d_y/8mm$, where $8mm$ is the pupil diameter of the objective.

In Eq. (6.4), w_y is ideally very small such that the factor $sinc^2(w_y y/\lambda f) \approx 1$. Equation 6.4 can then be rewritten as

$$I = I_0[1 + cos(\boldsymbol{k}_{0y}.\boldsymbol{y} + \phi)], \tag{6.6}$$

where I_0 is the background fluorescence, $\boldsymbol{k}_{0y} = 2\pi d_y n/\lambda f$ is the observable spatial frequency by the objective in y-direction and ϕ specifies the phase of the illumination pattern. In fluorescence microscopy, the recorded image can be mathematically represented by

$$D(r) = [S(\boldsymbol{r})I(\boldsymbol{r})] * h(\boldsymbol{r}), \tag{6.7}$$

where $S(\boldsymbol{r})$ is the sample fluorescence density, $I(\boldsymbol{r})$ is the illumination intensity, $h(\boldsymbol{r})$ is the PSF of the detection objective and $D(\boldsymbol{r})$ is the recorded image. $\boldsymbol{r} = (\boldsymbol{x}, \boldsymbol{y}, \boldsymbol{z})$. For the illumination patterned in y-direction,

$$D(\boldsymbol{y}) = S(\boldsymbol{y})I_0[1 + cos(\boldsymbol{k}_{0y}.\boldsymbol{y} + \phi)]) * h(\boldsymbol{y}). \tag{6.8}$$

(a)   static light sheet (0-order)   (b)   -1 order   interference   +1 order

(c)   0.3k$_0$NA   (d)   0.6k$_0$NA
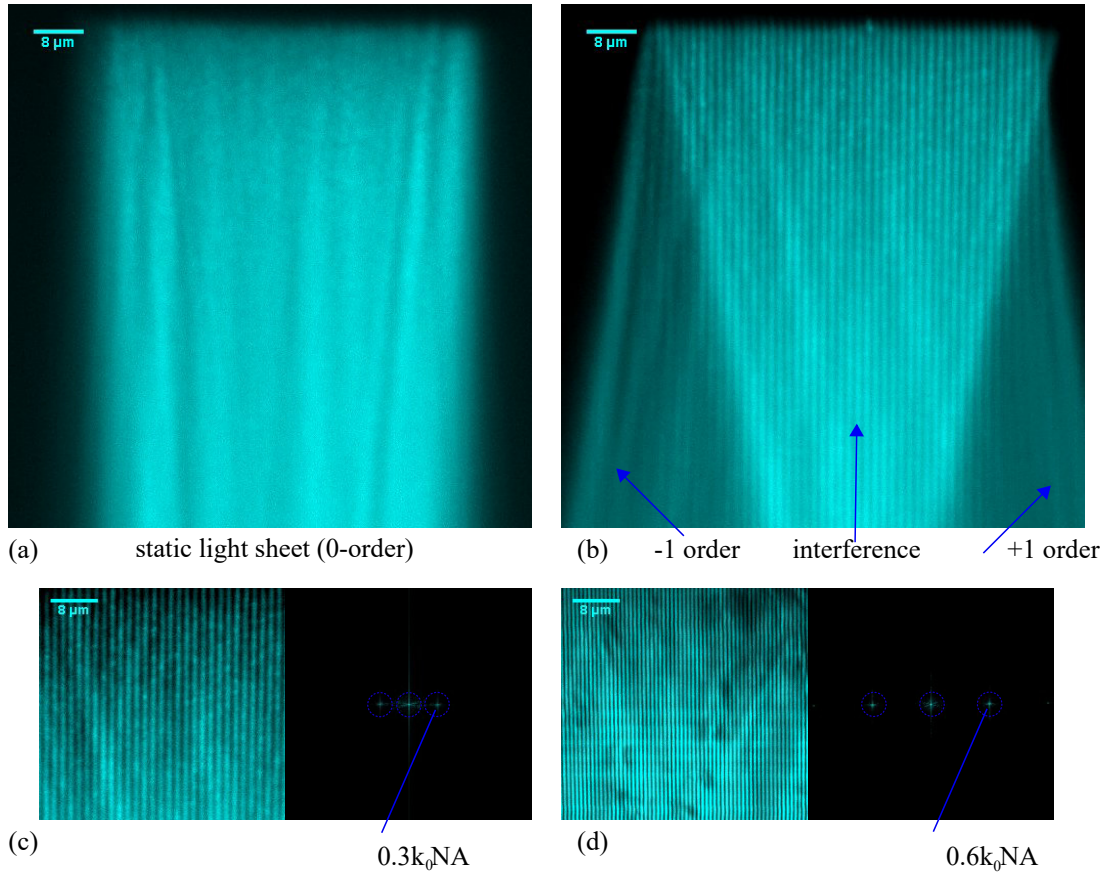
Figure 6.8 : *2beam light sheet illumination intensity patterns. (a) static light sheet (0-order beam). (b) Interference of +1 and -1 orders. (c) Intensity pattern of +1 and -1 orders and Fourier peaks. (d) Intensity pattern of +2 and -2 orders and Fourier peaks.*

In the reciprocal space,

$$\tilde{D}(\boldsymbol{k}_y) = \tilde{S}(\boldsymbol{k}_y)I_0[1 + cos(\boldsymbol{k}_{0y}.\boldsymbol{y} + \phi)]) * \tilde{h}(\boldsymbol{k}_y)$$
$$= I_0[\tilde{S}(\boldsymbol{k}_y) + 0.5\tilde{S}(\boldsymbol{k}_{0y} + \boldsymbol{k}_y)e^{i\phi} + 0.5\tilde{S}(\boldsymbol{k}_{0y} - \boldsymbol{k}_y)e^{-i\phi}. \tag{6.9}$$

The illumination frequencies, therefore, down-modulate the high sample spatial frequencies which would have been missed under uniform light sheet illuminations. The sample spatial frequencies up to $K_0NA_{obj} + K_0NA_{eff}$ can be accessible. The interference of +1 and −1 diffraction orders provides $NA_{eff} = 0.3NA_{obj}$ while the +2 and −2 orders support $NA_{eff} = 0.6NA_{obj}$. Therefore a total spatial frequency of $1.6K_0NA_{obj}$ can be accessible. Figure 6.8 shows the interfering light sheets, the interference patterns, and the corresponding Fourier peaks. Note that the light sheets in Figure 6.8 (b) and (c) are not in full field of view. Rather, they are obtained with smaller fields of view by putting a spatial filter temporarily at the conjugate of the sample plane, just for the sake illustration.

It is also possible to generate a pattern in the propagation axis from the interference of three beams (+1, -1, and 0 orders). Figure 6.9 shows the 3 beam pattern of half field of view (a) and a

small section of the pattern (b). Apparently the period in y- and x- directions are different which leads to unsymmetric transversal resolution gain. However, Due to practical challenges, we limit the demonstration to two-beam interference illumination patterns.

<p align="center">(a)   (b)</p>
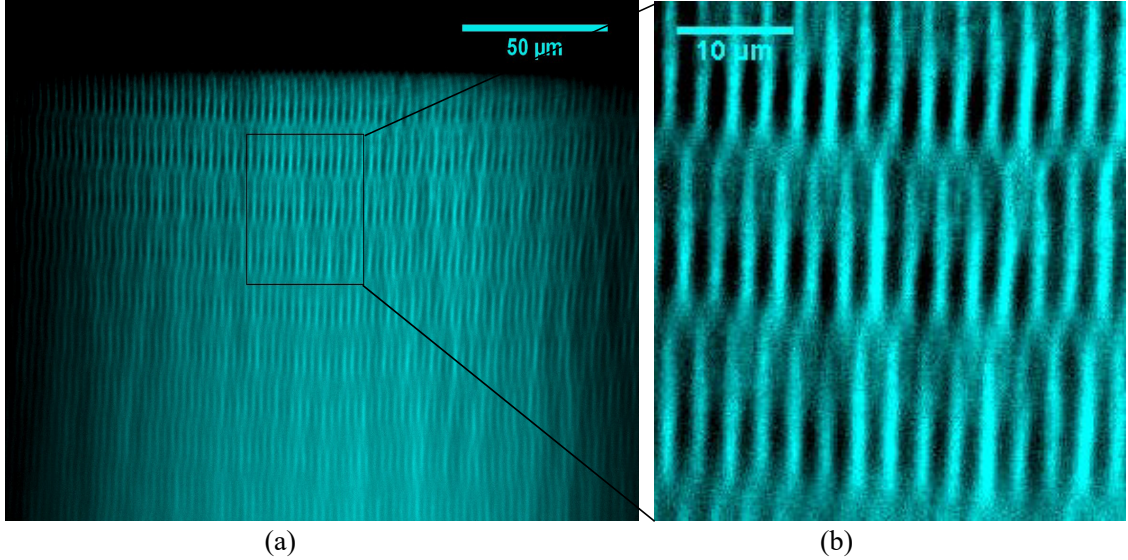
Figure 6.9 : *Three beam patterns. (a) Half of the field of view. (b) Small section of the pattern.*

6.4.4.2   Field of view and thickness

To determine the other fundamental parameters of the light sheet, the field of view and the light-sheet thickness, we can assume an elliptical Gaussian beam profile. For two beam interference, the separation distance between the two ellipsoidal beams determines the period of the pattern, while the major and minor axes of the ellipsoidal beam profiles determine the thickness and the field of view of the light sheet. According to our convention, the z-axis is the major axis which controls the thickness, the y-axis is the minor axis which determines the field of view in y-direction and x-axis is the propagation direction of the excitation beam. Based on the elliptical Gaussian beam profile, the Rayleigh range and the objective aperture angle can be expressed as

$$R_x = \pi n w_{oz}^2 / \lambda_o \tag{6.10}$$

and

$$\theta_z = \lambda_o / \pi n w_{oz} \tag{6.11}$$

respectively. R_x is half of the Rayleigh range, w_{oz} is the beam-waist in the collection (z-) axis. The aperture size is also related to the effective numerical aperture, $n sin\theta_z$.

$$n sin\theta_z = D_z / 2f, \tag{6.12}$$

where f is the foal length of the objective, D_z is the diameter of one of the beams in the major axis at the back focal plane of the objective and n is the immersion medium refractive index.

Finally, the field of view, FV, (in the direction of excitation propagation) and the thickness, Th, of the light-sheet are simultaneously expressed to be

$$FV = 2R_x = 2\lambda_o/\pi n[sin^{-1}(D_z/2nf)]^2 \tag{6.13}$$

and and

$$Th = 2w_{oz} = 2\lambda_o/\pi n[sin^{-1}(D_z/2nf)] \tag{6.14}$$

respectively.

From the theoretical analysis, the thickness D_z at the back focal plane is $1.78mm$. This gives a light-sheet thickness of $2.25\mu m$ and the field of view of $53\mu m$. Figure 6.10 depicts the field of view and the light sheet thickness for varying thickness of the elliptical beam at the back focal aperture. The thickness of the beam at the back focal aperture is taken in the major axis (z-axis). From Figure 6.10, we can see that when the beam size at the back focal aperture increases, the light-sheet at the sample plane gets thinner. On the other hand, the field of view also gets narrower. So it is always a compromise based on the application of interest. In our case, since we want to test the structured illumination smaller field of view is preferable.

(a)   (b)
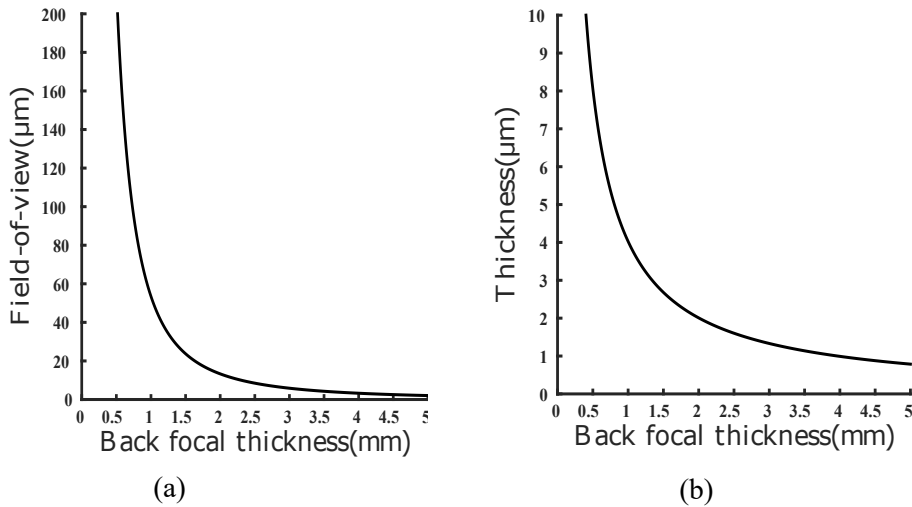
Figure 6.10 : *Thickness and field of view of the light-sheet for range of the the beam thickness at the back focal aperture.*

The field of view and the light sheet thickness has been also experimentally determined to be $2.25\mu m$ and $70\mu m$ respectively. These parameters are measured experimentally as follows:

- The scattering of the light sheet from the cover glass gives the instantaneous thickness profile of the light where it interacts with the surface of the cover glass.

- Multiple scattering profiles then measured by scanning the light sheet by slightly translating the excitation objective. This gives the in-focus and out-of-focus light sheet profiles with respect to the surface of the cover glass.

- The thickness of the detected scattering when the light sheet is in-focus actually defines the thickness of the light sheet. The field of view in the propagation direction, on the other
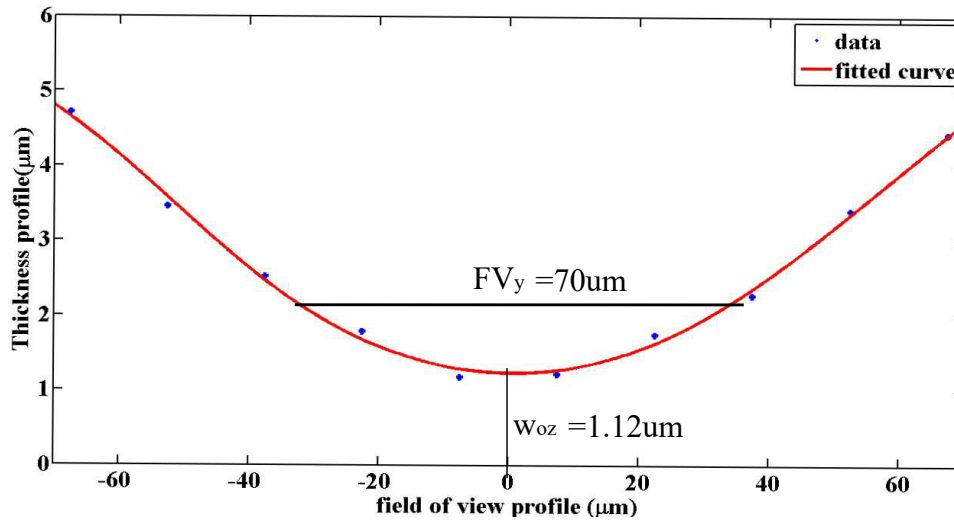
Figure 6.11 : *Experimentally measured field of view and light sheet thickness*

hand, is determined from the rate of change of the thickness profiles for multiple scans of the objective. Figure 6.11 shows the field of view and the light sheet thickness profiles. The blue dots show the measured half-thickness and the red curve fits the data. The field of view is determined from the Rayleigh range and the thickness is directly determined from the beam waist. Note that these parameters are measured while using interferences of +1 and -1 diffraction orders.

6.5 Data acquisition and reconstruction

6.5.1 Data acquisition

The iSPIM configuration needs specific sample stages which can accommodate excitation and collection objectives, each making 45° with respect to the sample holding coverslip. The sample is mounted on a small rectangular coverslip (3mm by 22mm). The sample is then translated using a linear translation stage for volumetric data acquisition. In the volumetric data, each image frame is a 45° slice of the sample (with respect to the horizontal plane which is parallel to the coverslip). Therefore, for thin samples, it is difficult to interpret the structure of iSPIM images just from the single frame. Multiple scans of the image have to be recorded and processed for visualizing the sample structures of interest. Yet again, each frame is taken with multiple phase translations of the sinusoidal pattern.

The phases of the sinusoidal pattern are generated using a scanning galvo-mirror positioned at the conjugate of the back focal plane which introduces a little tilt. The tilt angle of the beam at the conjugate of the back focal plane corresponds to the translation of the pattern (in other words the phase shift). Unlike the standard SIM phases which require 3 or 5 translations, we have used 20 phases in a period. This number is decided based characterizing the homogeneity of the sum of structured light sheet images with multiple phases. Figure 6.12 shows the static light sheet

from 0 order beam, the periodic light sheet pattern from the interference of order +1 and -1, and homogeneity of the sum of 20 structured illumination patterns with different phases.
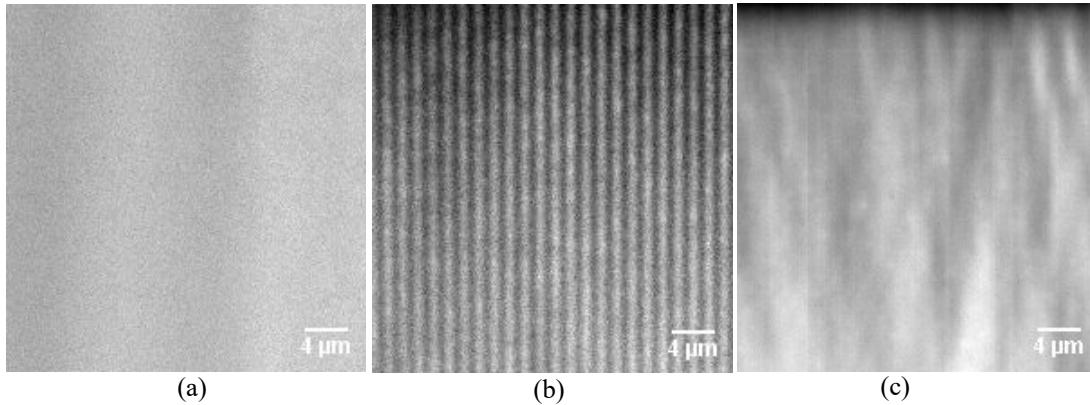
Figure 6.12 : *Generated periodic light sheet patterns. (a) Static light sheet. (b) 2 beam interference pattern. (c) Sum of 20 periodic patterns of different phases.*

Bead samples

The samples used for the test are beads (100nm and 520nm in diameter), cells fixed in mitotic phase and embryos of zebrafish. The $0.52\mu m$ beads emitting in the far red (emission at 647nm) are embedded with 2% agarose gel. The mixture is shaken and gently poured onto the small custom-made 3mm by 22mm microscope coverslip which is used in the iSPIM imaging protocol. The imaging process continues after the solution starts to fix and dry out. For resolution and PSF characterization, we have also used Invitrogen's TetraSPeck $100nm$ microspheres stained with $660/680nm$ fluorescent dyes (dark red). The microbeads are diluted with distilled water to a ratio of 1:10000. To obtain Sparse bead distribution for PSF calibrations, we put the beads on the microscope slide without the agarose solution. We need to wait until it sticks to the glass before imaging.

Cells preparation

Kidney BS-C-1 cells were seeded on 3mm by 22mm cover glasses at a density of 2.5x104 cells per Petri dish. After 48 hours, they were rinsed with phosphate buffered saline (PBS) and fixed with paraformaldehyde (3%) and glutaraldehyde (0.1%) at room temperature in PBS and the fixed sample was permeabilized in a blocking buffer (3% BSA, 0.1% Triton X-100 in PBS). They were stained with the primary antibodies against tubulin (mouse anti-a-tubulin, 1:250 dilution) and the corresponding secondary antibody was added to the sample (anti-mouse-Alexa 647, $8\mu g/mL$ concentration). The sample was then washed with a washing buffer and stored in PBS until imaging.

Once the data sets are recorded, we use our reconstruction techniques to investigate the amelioration. The following section briefly revises the reconstruction strategies.

6.5.2 Reconstruction Strategies

We reconstruct the data using two reconstruction techniques which depend on iterative algorithms. One is the blind-SIM separate deconvolution (blind-SIM-SD), and the other is the filtered blind-SIM reconstruction technique. Both reconstruction approaches require the homogeneity intensity condition. The blind-SIM-SD technique does not use the information of each individual SIM image while filter blind-SIM uses the information of the Fourier peaks (refer to Chapter 2 for details of these algorithms).

Blind-SIM-SD estimates the product of fluorescence density and illumination Intensity for each low-resolution image obtained using individual patterns. Using the homogeneity mathematical relation, the fluorescence density is calculated from the estimated product.

The filter blind-SIM approach estimates jointly both the fluorescence density and intensity. It uses little information about the illumination intensity from the Fourier peaks on the Fourier transform of raw structured illumination light sheet data. The filtered blind-SIM consists in estimating simultaneously the sample and the illuminations while iteratively minimizing a cost functional. The homogeneity constraint is introduced in the inversion scheme which assumes the sum of the structured light sheet patterns of different phases is constant within the field of view. In addition, positivity is imposed on both the illumination and fluorescent density. The imaging model, the cost functional and all the details on the reconstruction algorithms are provided in Chapter 2 and in the appendices.

6.6 Resolution analysis

It has been illustrated in earlier chapters (in Chapters 2 and 3) that the reconstruction of SIM raw images recovers the sample frequencies beyond the optical transfer function cutoff of the microscope objective. In blind-SIM-SD the resolution improvement can be explained mainly by the sparsity of the raw images activated by the positivity constraint. It stems from the more frequent activation of the positivity constraint on the raw SIM images. This technique is really powerful when the SIM images are sparse enough. The sparsity may be caused by the sparse nature of the sample or the illumination pattern. The reconstruction approaches are directly applied on the 2D structured lightsheet raw images using a 2D PSF. It is worth noting here that from the sparsity point of view the intensity pattern from the interference of +1 and -1 orders is sparser than the pattern obtained from the interference of +2 and -2 orders. Blind-SIM-SD is therefore efficient on reconstructing images of beads as shown in Figures 6.13 and 6.15.

Since we have structured illumination pattern only in one direction, resolution improvement is expected in that direction. The results of blind-SIM-SD provide the expected result on dense regions of bead images. Unlike the clustered beads, the reconstruction results of isolated beads provide close to symmetrical transversal resolution. The gain of resolution is illustrated in Figure 6.14 by focussing on the isolated bead from reconstructions. From the half-maximum width measurement, the widefield deconvolution provides 457nm whereas the blind-SIM-SD provides 184nm. Note that the raw images of the beads are sparse.

(a)

(b)

(c)
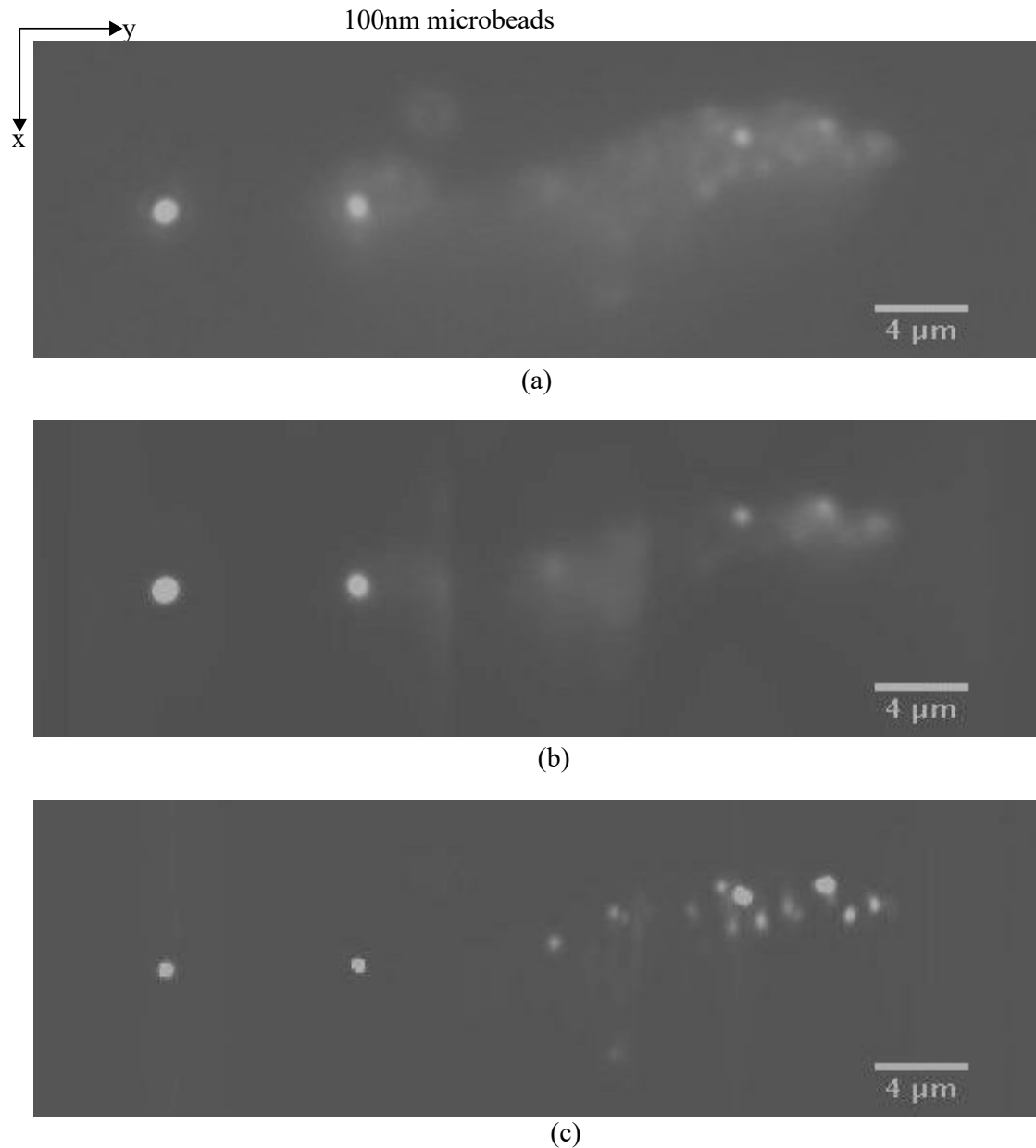
Figure 6.13 : *iSPIM-SIM resolutions on 100nm beads. (a) Widefield images obtained by summing 20 low-resolution structured illumination light sheet images. (b) Widefield deconvolution. (c) Blind-SIM-SD.*

Figure 6.15 also shows the efficiency of the technique using beads of 520nm. The beads which are not visible in the widefield image starts to be isolated using Blind-SIM-SD. The resolution gain in the y-direction is clearly better than in x-direction. This is because the beads are large enough to be modulated by the structured illumination and they are clustered as well.

In addition to beads, we have also demonstrated the iSPIM-SIM setup using biological samples such as kidney BS-C-1 cells stained with the primary antibody against tubulin (mouse anti-a-
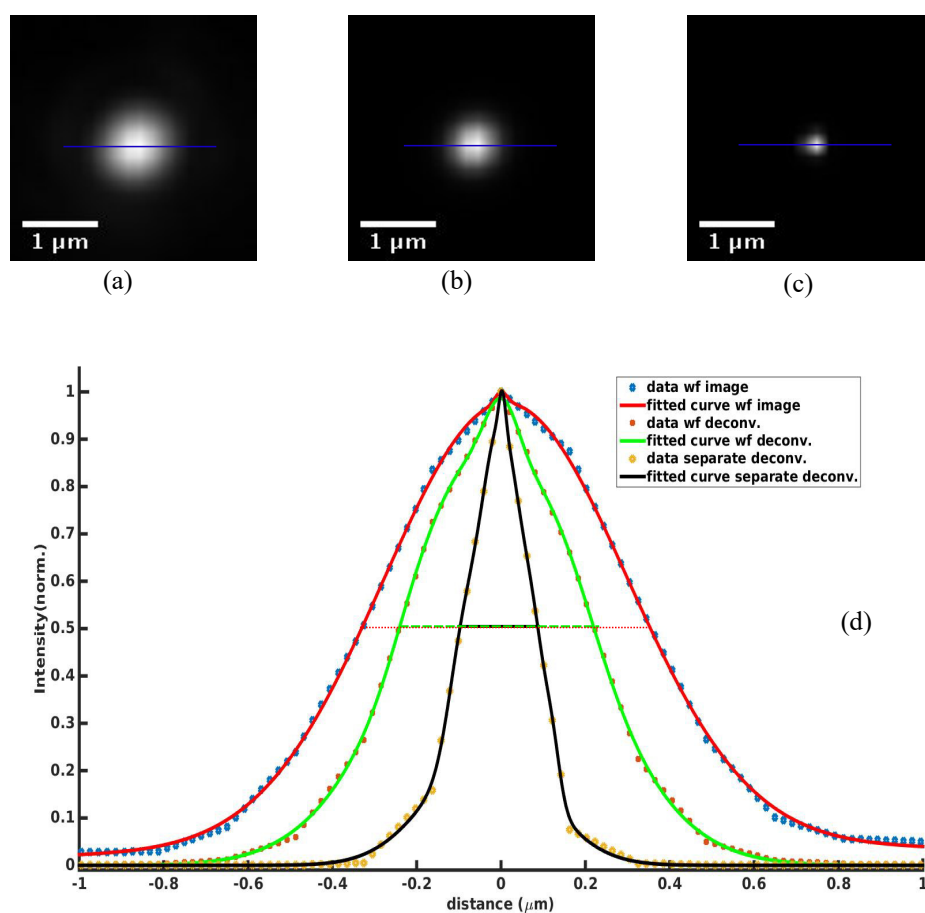
Figure 6.14 : *Illustration of resolution using images of isolated 100nm beads cropped from full-size (512x512 pixels) data reconstructions. (a) Widefield image. (b) Widefield deconvolution. (c) Blind-SIM-SD. (d) Resolution comparison using FWHM measurement.*
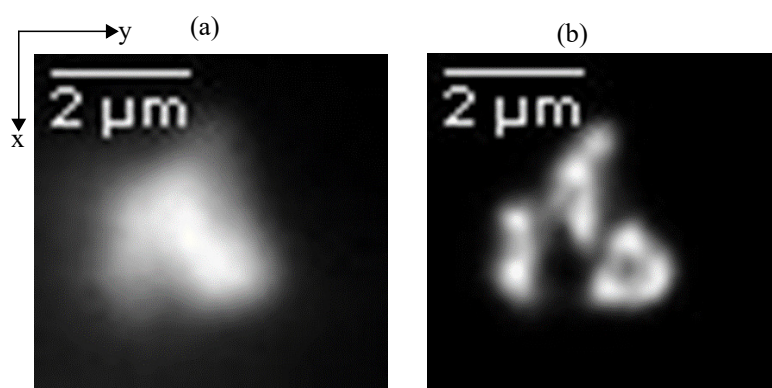
Figure 6.15 : *Structured illumination light sheet images resolution on clustrers of 0.52µm beads. (a) Widefield images obtained by summing 20 low-resolution images of translating periodic light sheet illuminations. (b) Blind-SIM-SD.*

tubulin, 1:250 dilution) and the corresponding secondary antibody (anti-mouse-Alexa 647, 8 ug/mL concentration).
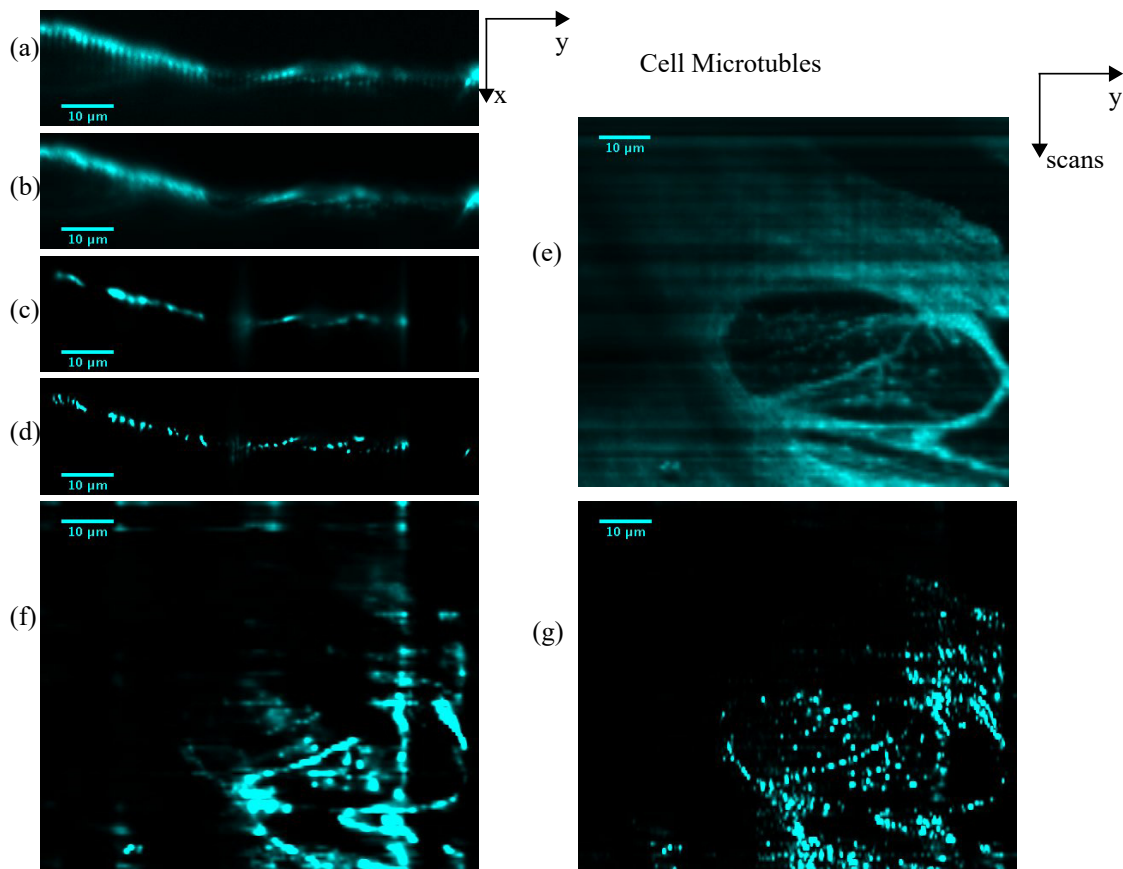
Figure 6.16 : *(a)-(d) Raw data from structured light sheet illuminiations, widefield image, widefield deconvolution and blind-SIM-SD respectively. (e)-(g) Reslices of widefield image, widefield devonvolution and blind-SIM-SD respectively.*

In iSPIM configuration, the light sheet is at 45° to the sample holding coverslip. Therefore, if the sample is thin, a single frame image just gives the thin cross section of the sample. Commonly, standard widefield microscopy provides the image of the sample features rested on the top of the cover slip (unlike iSPIM). Therefore, for interpretation of iSPIM images (particularly for thin samples), multiple transversal scans of the sample (3D acquisition) have to be taken and re-oriented. For the 3D acquisition, we translated the motorized stage horizontally. Figure 6.16 shows the images of kidney BS-C-1 cells in xy-view (a-d) and re-oriented images from 100 horizotal scans (e-g) respectively. To remind orientations, x - is the light sheet propagation direction, z - is the detection path. Therefore, the real image captured by the camera has is on the xy-plane (shown in the figure as xy-view). In Figure 6.16 (a) shows the raw image of a single sinusoidal light sheet pattern, (b) shows the widefield image (sum of 20 raw iSPIM-SIM images), (c) shows the widefield deconvolution of the widefield image, and (d) shows the blind-SIM-SD on the raw images. On the other hand, if we reslice (change the orientation of) the widefield image, the widefield deconvolution and the blind-SIM-SD image, we obtain images in (e), (f) and (g) respectively. The reslice images are shown for a selected x-position. Apparently, the sample features such as the nucleus and tubulin structures are clearly visible after reslicing the processed images.

The widefield dconvolution (c, f) and blind-SIM-SD (d, g) provide fine structures compared to the widefield image. We have a significant discontinuity problem, particularly in blind-SIM-SD. One of the reasons could be the photobleaching of some of the sample features as shown in the images since the data acquisition was very slow even though the fact that the light sheet illumination helps in reducing photobleaching. It introduces an enhanced discontinuity in the reconstructions. In addition, the coverslip, the sample/coverslip holder and stage are all custom made in the lab and it is very likely that there is instability problem. The synchronization of the camera, the sample stage, and the scanning mirror (for translating) the sinusoidal pattern was done using scripts written in python. Work is on progress in developing the setup to be more robust and fast.
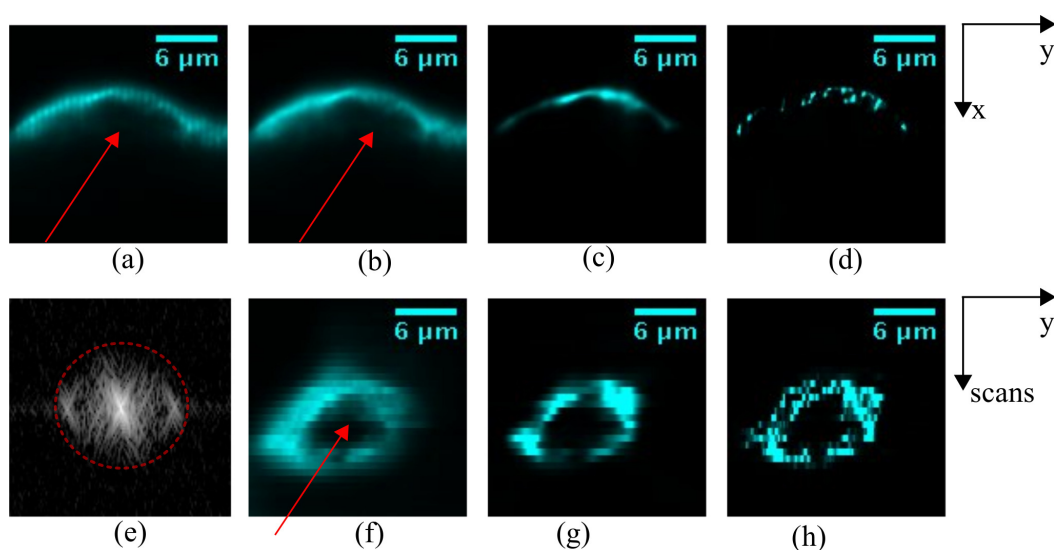
Figure 6.17 : *(a-d) Raw image from individual structured light sheet illumination, widefield image, filtered blind-SIM and blind-SIM-SD. (e) Fourier transform of raw image. (f-h) Re-slices of widefield image, filter blind-SIM and blind-SIM-SD respectively.*

A small region of the sample which shows the nucleus and nuclear membrane is selected from the 3D stack of data for illustration as shown in Figure 6.17. The data is taken from structured light sheet illumination using diffraction orders of -2 and +2. Selected images in (a-d) show the raw image from the single pattern, the widefield image, the filtered blind-SIM reconstruction and the blind-SIM-SD estimate respectively. The Fourier transform of the raw image is shown in (e). Images in (f-h) represent the reslice orientation analyzed from 32 slices of widefield image, filtered blind-SIM reconstruction, and blind-SIM-SD estimations respectively. The red arrows in the images indicate the position of the nucleus in the cell where there are no labeled tubulin structures. Even though the sample is not perfect for illustrating resolution, it somehow demonstrates the proof of concept implementation of our simple iSPIM-SIM microscope and its image interpretation. Note that the resolution improvement in y-direction due to structured illumination is not evident in this sample due to the fact that the sample has continuous structures in the y-direction.

6.7 Conclusion

To summarize, We have developed the iSPIM light sheet microscope from scratch and introduced structured illumination into it. The setup helps to combine the benefits of both SIM and light sheet microscopy techniques with little increase of complexity.

The images obtained of structured light sheet illumination are reconstructed using either blid-SIM-SD and filtered blind-SIM reconstruction technique. The inversion schemes are chosen depending on the sparsity of the recorded raw images. If the recorded images are dense, the information about the illuminations can be obtained from the raw data and filtered blind-SIM is preferable. On the other hand, If the recorded images are sparse blind-SIM-SD technique is efficient. In addition, blind-SIM-SD is computationally faster than the filtered blind-SIM reconstruction. Even though one can estimate the expected resolution gain from the illumination intensity properties, the positivity (applied in both reconstruction techniques) enhanced by sparsity also introduces some increase of the resolution. Therefore, the true resolution gain is usually determined from a comparison of the reconstructions with the widefield images.

We have shown that two-dimensional interference patterns on the sample plane can be obtained using standard SIM and LSFM principles with just simple basic cost-efficient optical components. In standard SIM the orientations of the harmonic pattern can be rotated by just rotating the grating in grating-based SIM setups. This is, however, not possible in structured illumination light sheet microscopy. This is because the grating should be kept in a fixed orientation to have a sheet of light. The setup is in progress to be developed to have structured illumination patterns in multiple transversal directions to obtain symmetric two-dimensional resolution. This setup will also be advanced to dual selective plane illumination microscopy (dSPIM) combined with an inverted microscope. These developments are however challenging and are beyond the scope of this project. Future research on further developments is recommended as a perspective.

Conclusion

Most of this thesis was devoted to the development of numerical tools aiming at improving the resolution and the contrast of 3D images in fluorescence microscopy. We have considered the superresolution approach known as structured illumination microscopy (SIM) which consists in illuminating the sample with an inhomogeneous intensity in order to down modulate the high sample spatial frequencies into the support of the optical transfer function (OTF) of the microscope. By using appropriate reconstruction strategies the down modulated high sample frequency information can be restored to their original position, which results in resolution enhancement compared to the conventional widefield images. Using a 3D illumination grid, from the interference of three coherent beams, 3D-SIM improves the resolution in both transversal and axial dimensions. However, most reconstruction techniques require the knowledge of the illuminations and are sensitive to the possible misalignments and distortions that can be introduced by the optical components and the sample itself, particularly when the sample is thick and highly scattering.

We have developed a very simple and fast reconstruction strategy that is called blind SIM separate deconvolution (blind-SIM-SD) which does not require any knowledge on the illuminations. It consists in deconvolving each raw image with positivity, then summing the deconvolved images. If the illuminations average is roughly homogeneous, the sum of the deconvolved images yield the sample reconstruction. In this case, the superresolution stems from the activation of the positivity which is frequent when the recorded data is sparse. The blind-SIM-SD algorithm is much faster than the previously developed blind-SIM algorithms which simultaneously estimate the sample and the illuminations. It is particularly advantageous when speckle illuminations are used as long as the homogeneity condition is maintained.

When the illumination is partially known (distorted light grid), it is better to account for this information in the inversion. We have developed another algorithm which simultaneously reconstructs the sample and the illuminations. Its principle consists in restricting the estimation of the illumination within a bounded region around the Fourier peaks of the theoretical light grid and simultaneously estimating the sample and the illumination pattern. We call this algorithm filtered blind-SIM. Besides doubling the resolution, the positive filtered blind-SIM reconstructs the sample even when the illumination pattern is deformed. The positivity constraint can push the resolution even more than twice better than the diffraction limit, particularly when the sample is sparse.

These reconstruction techniques were applied to synthetic and experimental data using harmonic and speckle illuminations. They yielded significantly better resolutions than the widefield and was comparable to commercial SIM reconstructions.

The simplification of the experiments that is made possible by using the blind-SIM algorithms is an incentive for pursuing in this direction. The developed 3D inversion tools assumes the 3D convolution imaging model as $M = \rho I * h$ where ρ is the sample, I is the illumination, h is the PSF and M is the recorded image. Some microscopy implementations, based on remote focussing or multifocus, can indeed be modeled by a 3D deconvolution. Unfortunately, the data coming from the commercial microscope are using the displacement of the sample to get 3D information. In this case our 3D image modeling is not adapted. An important perspective of this work would be to consider the scanning model in the inversion scheme.

In blind-SIM-SD, the superresolution stems from the sparsity of images. We have proposed to apply this technique to two photon speckle illumination microscopy and mirror-based speckle illumination microscopy to take advantage of a possible increase in the image sparsity. Both approaches were tested on synthetic data. This preliminary work could be usefully pursued on experimental data, especially for two photon speckle imaging. Indeed, the latter has been shown to improve significantly the transverse resolution compared to the one photon imaging.

In the second part of the thesis, closely related to the first one, we addressed the issue of optical sectioning and contrast. We have developed a simple computational technique which provides optical sectioning by removing the out-of- focus light in widefield images. The principle of the technique is to deconvolve the two-dimensional image using a three-dimensional PSF. It is a simple data processing approach which can be used on most widefield microscopy configurations. We have demonstrated the technique on synthetic and experimental data (brightfield and speckle), and it provides significant amelioration of the images by removing most of the out of focus contributions. As a perspective, this technique can be applied to many other imaging configurations, in particular to extended-depth-of-field microscopy.

In the last part of the thesis, we have introduced structured illumination into light sheet microscopy. Light sheet microscopy is a well known microscopy technique that provides optical sectioning. The transversal resolution of light sheet images is, however, still diffraction limited. As a proof of concept, we have practically implemented a simple microscope setup which combines structured illumination with light sheet microscopy. Due to the experimental challenges in implementing the setup the resolution improvement is limited to only one transversal direction. As a perspective of the thesis, we recommend to carry out advanced researches on combining SIM with light sheet microscopy and investigate the resolution in all directions and the optical sectioning which stems from the structured illumination and the light sheet respectively.

Appendices

Gradient analysis

A.1 Gradient definition of a functional

To define the gradient of a functional, one need first to define the directional derivative. F is a functional of the variable x, a function defined of the set Ω. For any function u of Ω, the directional derivative $\mathrm{D}_x F(u)$ along the direction u is defined as

$$\mathrm{D}_x F(u) = \lim_{t \to 0} \frac{F(x + tu) - F(x)}{t}. \tag{A.1}$$

Then g_x, the gradient of F with respect to x, is defined as

$$g_x = \arg\max_u (\mathrm{D}_x F(u) | \|u\| = 1), \tag{A.2}$$

the direction where the directional derivative is the highest.

According to this definition, gradients are normalised such that $\|g_x\| = 1$. However, since in gradient type algorithms their value is always multiplied by a constant that is optimised, we most of time neglects it.

As an example, let's see the calculation of the gradient of the least-square functional given by

$$F(\rho) = W \|M - (\rho I_0) * h\|_\Gamma^2. \tag{A.3}$$

$F(\rho + tu)$ is written

$$\begin{aligned}
F(\rho + tu) &= W \|M - [(\rho + tu)I_0] * h\|_\Gamma^2 \tag{A.4} \\
&= W \|M - (\rho I_0) * h - t(u I_0) * h\|_\Gamma^2. \tag{A.5}
\end{aligned}$$

For the sake of simplicity, one notes

$$P_0 = M - (\rho I_0) * h. \tag{A.6}$$

$F(\rho + tu)$ is then

$$\begin{aligned}
F(\rho + tu) &= W \|P_0 - t(u I_0) * h\|_\Gamma^2 \\
&= W \langle P_0 - t(u I_0) * h | P_0 - t(u I_0) * h \rangle_\Gamma \\
&= W \|P_0\|_\Gamma^2 - 2tW \langle P_0 | (u I_0) * h \rangle_\Gamma + t^2 W \|(u I_0) * h\|_\Gamma^2 \\
&= F(\rho) - 2tW \langle P_0 | (u I_0) * h \rangle_\Gamma + O(t^2). \tag{A.7}
\end{aligned}$$

Finally,

$$
\begin{aligned}
\mathrm{D}_\rho F(u) &= \lim_{t \to 0} \frac{F(\rho + tu) - F(\rho)}{t} \\
&= -2W \langle P_0 | (uI_0) * h \rangle_\Gamma.
\end{aligned}
\tag{A.8}
$$

$$
\begin{aligned}
\langle P_0 | (uI_0) * h \rangle_\Gamma &= \langle P_0 * h^\dagger | uI_0 \rangle_\Omega \\
&= \langle I_0 (P_0 * h^\dagger) | u \rangle_\Omega,
\end{aligned}
\tag{A.9}
$$

where $h^\dagger$ is the Hermitian conjugate of h, i.e. given $h = f(\boldsymbol{r})$ then $h^\dagger = f^*(-\boldsymbol{r})$, that leads to

$$
\begin{aligned}
\mathrm{D}_\rho F(u) &= -2W \langle I_0 (P_0 * h^\dagger) | u \rangle_\Omega \\
&= \langle -2W I_0 (P_0 * h^\dagger) | u \rangle_\Omega.
\end{aligned}
\tag{A.10}
$$

To find the gradient $g_\rho = \arg\max_u (\mathrm{D}_\rho F(u) | \|u\| = 1)$, one uses a theorem that states that $u = \frac{a}{\|a\|}$ maximises $(\langle a | u \rangle | \|u\| = 1)$. Thus from Eq. (A.10), one gets

$$
g_\rho = \frac{-2W I_0 (P_0 * h^\dagger)}{\|2W I_0 (P_0 * h^\dagger)\|_\Omega}.
\tag{A.11}
$$

The normalisation factor does not matter in the Conjugate Gradient algorithm. We finally have

$$
\boxed{g_\rho = -2W I_0 (P_0 * h^\dagger).}
\tag{A.12}
$$

If we impose the positivity of ρ. This is done in optimising an auxiliary function ξ such that $\rho = \xi^2$. The new functional is

$$
F(\xi) = W \| M - (\xi^2 I_0) * h \|_\Gamma^2.
\tag{A.13}
$$

Of course, g_ξ can be derived from the cost functional using a similar analysis. However, one can avoid these tedious calculations using the chain rule

$$
g_\xi = \frac{\partial \rho}{\partial \xi} g_\rho.
\tag{A.14}
$$

Using this relation and the definition of $\rho(\xi)$ we find

$$
g_\xi = 2\xi g_\rho
\tag{A.15}
$$

and using Eq. (A.12) one finally gets

$$
\boxed{g_\xi = -4W \xi I_0 (P_0 * h^\dagger).}
\tag{A.16}
$$

Assuming h as a real, even and symmetic : $\forall x \in \Omega$, one can write $h^\dagger = h$. And the gradient can then be written as

$$
\boxed{g_\xi = -4W \xi I_0 (P_0 * h).}
\tag{A.17}
$$

But the symmetry may not be always true, particularly for three dimensional PSF.

A.2 Gradients for the blind-SIM algorithm with no positivity constraint

The gradients for the blind-SIM algorithm derives from the functional

$$F(\rho, (I_l)_{l=1,\ldots,L-1}) = W \sum_{l=1}^{L-1} \|M_l - (\rho I_l) * h\|_\Gamma^2 + W \left\| M_L - \left[\rho \left(L I_0 - \sum_{l=1}^{L-1} I_l \right) \right] * h \right\|_\Gamma^2. \quad (A.18)$$

g_ρ is the gradient of F when the I_l are assumed to be constant. It is, by definition,

$$g_\rho \quad = \quad \arg \max_u (\mathrm{D}_\rho F(u) | \|u\| = 1) \quad \text{for} \quad (A.19)$$

$$\mathrm{D}_\rho F(u) \quad = \quad \lim_{t \to 0} \frac{F(\rho + tu, (I_l)_{l=1,\ldots,L}) - F(\rho, (I_l)_{l=1,\ldots,L})}{t}. \quad (A.20)$$

For the sake of simplicity, one notes

$$I_L = L I_0 - \sum_{l=1}^{L-1} I_l \quad (A.21)$$

and, for $l = 1, \ldots, L$,

$$P_{0,l} = M_l - (\rho I_l) * h, \quad (A.22)$$

called the l-th residue.

$F(\rho + tu, (I_l)_{l=1,\ldots,L})$ is written

$$
\begin{aligned}
F(\rho + tu, (I_l)_{l=1,\ldots,L}) \quad &= \quad W \sum_{l=1}^{L} \|M_l - [(\rho + tu)I_l] * h\|_\Gamma^2 \\
&= \quad W \sum_{l=1}^{L} \|M_l - (\rho I_l) * h - t(u I_l) * h\|_\Gamma^2. \quad (A.23)
\end{aligned}
$$

$F(\rho + tu)$ is then

$$
\begin{aligned}
F(\rho + tu, (I_l)_{l=1,\ldots,L}) &= W \sum_{l=1}^{L} \|P_{0,l} - t(u I_l) * h\|_\Gamma^2 \\
&= W \sum_{l=1}^{L} \left(\|P_{0,l}\|_\Gamma^2 - 2t \langle P_{0,l} | (u I_l) * h \rangle_\Gamma + t^2 \|(u I_l) * h\|_\Gamma^2 \right) \\
&= F(\rho) - 2tW \sum_{l=1}^{L} \langle P_{0,l} | (u I_l) * h \rangle_\Gamma + O(t^2). \quad (A.24)
\end{aligned}
$$

Finally,

$$\mathrm{D}_\rho F(u) = -2W \sum_{l=1}^{L} \langle P_{0,l} | (u I_l) * h \rangle_\Gamma \quad (A.25)$$

$$
\begin{aligned}
\mathrm{D}_\rho F(u) &= -2W \sum_{l=1}^{L} \langle P_{0,l} * h^\dagger | u I_l \rangle_\Omega \\
&= -2W \sum_{l=1}^{L} \langle I_l (P_{0,l} * h^\dagger) | u \rangle_\Omega \\
&= \left\langle -2W \sum_{l=1}^{L} I_l (P_{0,l} * h^\dagger) \, \middle| \, u \right\rangle_\Omega, \quad (A.26)
\end{aligned}
$$

where $h^\dagger$ is the Hermitian conjugate of h, i.e. given $h = f(\boldsymbol{r})$ then $h^\dagger = f^*(-\boldsymbol{r})$.

Using the theorem of maximality cited in the previous section, one finally has

$$g_\rho = -2W \sum_{l=1}^{L} I_l (P_{0,l} * h^\dagger). \tag{A.27}$$

$g_{l;I}$ is the gradient of F when ρ and the $(L-2)$ other I_m are assumed to be constant. It is by definition,

$$g_{l;I} = \arg\max_u (D_{l;I} F(u) | \|u\| = 1) \quad \text{for} \tag{A.28}$$

$$D_{l;I} F(u) = \lim_{t \to 0} \frac{F(\rho, I_l + tu, (I_m)_{m=1,\dots,L-1,m\neq l}) - F(\rho, (I_m)_{m=1,\dots,L-1})}{t}. \tag{A.29}$$

Expanding $F(\rho, I_l + tu, (I_m)_{m=1,\dots,L-1,m\neq l})$, one gets

$$F(\rho, I_l + tu, (I_m)_{m=1,\dots,L-1,m\neq l}) = W \sum_{m=1,m\neq l}^{L-1} \|P_{0,m}\|_\Gamma^2 + W \|M_l - (\rho(I_l + tu)) * h\|_\Gamma^2$$

$$+ W \left\| M_L - \left[\rho \left(LI_0 - \sum_{m=1,m\neq l}^{L-1} I_m - (I_l + tu) \right) \right] * h \right\|_\Gamma^2$$

$$= W \sum_{m=1,m\neq l}^{L-1} \|P_{0,m}\|_\Gamma^2 + W \|P_{0,l} - t(\rho u) * h\|_\Gamma^2$$

$$+ W \|M_L - [\rho(I_L - tu)] * h\|_\Gamma^2$$

$$= W \sum_{m=1,m\neq l}^{L-1} \|P_{0,m}\|_\Gamma^2 + W \|P_{0,l} - t(\rho u) * h\|_\Gamma^2$$

$$+ W \|P_{0,L} + t(\rho u) * h\|_\Gamma^2$$

$$= W \sum_{m=1}^{L} \|P_{0,m}\|_\Gamma^2 - 2tW \langle P_{0,l} | (\rho u) * h \rangle_\Gamma$$

$$+ 2tW \langle P_{0,L} | (\rho u) * h \rangle_\Gamma + O(t^2)$$

$$= F(\rho, (I_l)_{l=1,\dots,L-1}) - 2tW \langle P_{0,l} - P_{0,L} | (\rho u) * h \rangle_\Gamma + O(t^2). \tag{A.30}$$

This leads to

$$D_{l;I} F(u) = -2W \langle P_{0,l} - P_{0,L} | (\rho u) * h \rangle_\Gamma$$

$$= -2W \langle (P_{0,l} - P_{0,L}) * h^\dagger | \rho u \rangle_\Omega$$

$$= \langle -2W \rho [(P_{0,l} - P_{0,L}) * h^\dagger] | u \rangle_\Omega \tag{A.31}$$

that implies

$$g_{l;I} = -2W \rho [(P_{0,l} - P_{0,L}) * h^\dagger]. \tag{A.32}$$

A.3 Gradients for the blind-SIM algorithm with positivity constraint

The functional is modified to impose a positivity constraint using the auxiliary functions i_l and ξ defined by

$$I_l = i_l^2,$$
$$\rho = \xi^2.$$

The new functional is given by

$$F(\xi, (i_l)_{l=1,\ldots,L-1}) = W \sum_{l=1}^{L-1} \|M_l - (\xi^2 i_l^2) * h\|_\Gamma^2 + W \left\| M_L - \left[\xi^2 \left(L I_0 - \sum_{l=1}^{L-1} i_l^2 \right) \right] * h \right\|_\Gamma^2. \quad (A.33)$$

The gradients can be immediately derived from Eq.(A.27) and Eq.(A.32) respectively, using the chain rule,

$$g_\xi \;=\; -4W \sum_{l=1}^{L} \xi i_l^2 (P_{0,l} * h^\dagger) \quad (A.34)$$

and

$$g_{l;i} \;=\; -4W \xi^2 i_l [(P_{0,l} - P_{0,L}) * h^\dagger]. \quad (A.35)$$

A.4 Gradients for the filtered blind-SIM: positivity only on density

The algorithm is described, minimising the functional

$$F(\rho, (I_l)_{l=1,\ldots,L-1}) = W \sum_{l=1}^{L-1} \|M_l - (\rho I_l) * h\|_\Gamma^2 + W \left\| M_L - \left[\rho \left(L I_0 - \sum_{l=1}^{L-1} I_l \right) \right] * h \right\|_\Gamma^2 \quad (A.36)$$

for $\rho \in \Omega$ and $I_l \in \tilde{\mathcal{S}}$, $\tilde{\mathcal{S}}$ being the set of real functions with value in Ω whose Fourier transform has its support included in $\mathcal{S}$, a sub-set of R^2.

In this case, there is no modification on the calculations leading to g_ρ in Eq. (A.27). If positivity is assumed on the density the gradient with respect to auxilary density variable holds the expression shown in Eq. (A.34). However, the gradients $g_{l;I}$ will be modified. As the functional is unchanged,

$$\mathrm{D}_{l;I} F(u) = \langle -2W \rho[(P_{0,l} - P_{0,L}) * h^\dagger] | u \rangle_\Omega. \quad (A.37)$$

$g_{l;I}$ is the direction that minimises $\mathrm{D}_{l;I} F(u)$ inside $\tilde{\mathcal{S}}$. Formally it is defined, noting $v = -2W \rho[(P_{0,l} - P_{0,L}) * h]$, by

$$g_{l;I} = \arg \max_u (\mathrm{D}_{l;I} F(u) | \|u\|_\Omega = 1, u \in \tilde{\mathcal{S}})$$
$$= \arg \max_u (\langle v | u \rangle_\Omega | \|u\|_\Omega = 1, u \in \tilde{\mathcal{S}}). \quad (A.38)$$

The condition of membership of $\tilde{\mathcal{S}}$ hinders the use of the maximality theorem. One has to find an expression of $\mathrm{D}_{l;I}F(u)$ that includes this condition.

Defining f the function whose Fourier transform verifies

$$\tilde{f}(\boldsymbol{k}) = \begin{cases} 1 & \text{if } \boldsymbol{k} \in \mathcal{S} \\ 0 & \text{otherwise,} \end{cases} \tag{A.39}$$

(note that $f(\boldsymbol{k})$ can also be a gaussian Fourier mask that its FWHM is an element of $\mathcal{S}$) one has $\forall u \in \tilde{\mathcal{S}}, \tilde{f}\tilde{u} = \tilde{u}$ thus $\forall u \in \tilde{\mathcal{S}}, u * f = u$ and $\forall u \in \Omega, f * u \in \tilde{\mathcal{S}}$. Then,

$$\begin{aligned} \mathrm{D}_{l;I}F(u) &= \langle v|u * f\rangle_\Omega \\ &= \langle v * f^\dagger|u\rangle_\Omega. \end{aligned} \tag{A.40}$$

$\dfrac{v * f^\dagger}{\|v * f^\dagger\|}$ maximises $(\langle v * f^\dagger|u\rangle)|\|u\| = 1)$ and $v * f^\dagger \in \tilde{\mathcal{S}}$, thus

$$\frac{v * f^\dagger}{\|v * f^\dagger\|} = \arg\max_u(\mathrm{D}_{l;I}F(u)|\|u\|_\Omega = 1, u \in \tilde{\mathcal{S}}).$$

This proves that

$$\boxed{g_{l;I} = -2W\left(\rho[(P_{0,l} - P_{0,L}) * h^\dagger]\right) * f^\dagger.} \tag{A.41}$$

A.5 Gradients for positive filter blind SIM

The filter mask in the Fourier space is designed based on the location of the Fourier peaks of the intensity. The filtering is defined as

$$\tilde{I}_l = \tilde{\hat{I}}_l\tilde{f}_l, \tag{A.42}$$

where $\tilde{\hat{I}}_l$ represents the Fourier transform of the illumination pattern, and f_l represents the filter mask in the Fourier space centering of the frequency peaks of the grid pattern.

With special imposition of positivity on the illumination as

$$\hat{I}_l = |\boldsymbol{e}_l|^2, \tag{A.43}$$

The filtered illumination in the reciprocal space is then written as

$$I_l = \hat{I}_l * f_l = |\boldsymbol{e}_l|^2 * f_l, \tag{A.44}$$

where $\boldsymbol{e}_l$ is the lth field. The cost functional, with positivity on both the density and the illumination intensity, is then expressed as

$$\begin{aligned} F(\xi, (\boldsymbol{e}_l)_{l=1,\ldots,L-1}) =&W \sum_{l=1}^{L-1} \|M_l - (\xi^2|\boldsymbol{e}_l|^2 * f_l) * h\|_\Gamma^2 + \\ &W \left\|M_L - \left[\xi^2\left(LI_0 - \sum_{l=1}^{L-1}(|\boldsymbol{e}_l|^2 * f_l)\right)\right] * h\right\|_\Gamma^2, \end{aligned} \tag{A.45}$$

for $\xi \in \Omega$ and $I_l \in \mathcal{S}$, $\mathcal{S}$ being the set of real functions with value in Ω whose Fourier transform has its support included in $\tilde{\mathcal{S}}$, a sub-set of $\mathcal{R}^3$. The density auxilary variable is a real quantity while the auxilary intensity variable is a complex quantity. First let us define some operators before computing the gradient with respect to the intensity.

$$\boldsymbol{A} : f \to f * h,$$

$$\boldsymbol{B} : g \to g * f_l,$$

$$\boldsymbol{A}^\dagger : f \to f * h^\dagger,$$

(the Hermitian conjugates)

$$\boldsymbol{B}^\dagger : g \to g * f_l^\dagger,$$

where h is the PSF and $h^\dagger$ its Hermitian conjugate, f_l and $f_l^\dagger$ are the filter function and its Hermitian conjugate in real space. The cost functional is rewritten as

$$F(\xi, (\boldsymbol{e}_l)_{l=1,\ldots,L-1}) = W \sum_{l=1}^{L-1} \| M_l - \boldsymbol{A} \left[\xi^2 \boldsymbol{B}(|\boldsymbol{e}_l|^2) \right] \|_\Gamma^2 +$$

$$W \left\| M_L - \boldsymbol{A} \left[\xi^2 \left(L I_0 - \sum_{l=1}^{L-1} (\boldsymbol{B}(|\boldsymbol{e}_l|^2)) \right) \right] \right\|_\Gamma^2$$

$$= W \sum_{l=1}^{L-1} \| P_{0,l} \|_\Gamma^2 + W \| P_{0,L} \|_\Gamma^2. \tag{A.46}$$

Gradient with respect to ξ

$$F(\xi + tu, (\boldsymbol{e}_l)_{l=1,\ldots,L-1}) = W \sum_{l=1}^{L-1} \| M_l - \boldsymbol{A} \left[(\xi^2 + 2t\xi u + t^2 u^2) \boldsymbol{B}(|\boldsymbol{e}_l|^2) \right] \|_\Gamma^2$$

$$+ W \left\| M_L - \boldsymbol{A} \left[(\xi^2 + 2t\xi u + t^2 u^2) \left(L I_0 - \sum_{l=1}^{L-1} (\boldsymbol{B}(|\boldsymbol{e}_l|^2)) \right) \right] \right\|_\Gamma^2, \quad \text{(A.47)}$$

where $\xi, u \in R$.

$$F(\xi + tu, \{(\boldsymbol{e}_l)\}) = W \sum_{l=1}^{L-1} \| M_l - \boldsymbol{A} \left[\xi^2 \boldsymbol{B}(|\boldsymbol{e}_l|^2) \right] - 2t\boldsymbol{A} \left[\xi u \boldsymbol{B}(|\boldsymbol{e}_l|^2) \right] - t^2 \boldsymbol{A} \left[u^2 \boldsymbol{B}(|\boldsymbol{e}_l|^2) \right] \|_\Gamma^2$$

$$+ W \left\| M_L - \boldsymbol{A} \left[(\xi^2 I_L) + 2t\boldsymbol{A} \left[\xi u I_L \right] + t^2 \boldsymbol{A} \left[u^2 I_L \right] \right\|_\Gamma^2, \tag{A.48}$$

where

$$I_L = \left(L I_0 - \sum_{l=1}^{L-1} (\boldsymbol{B}(|\boldsymbol{e}_l|^2)) \right).$$

$$F(\xi + tu, (\boldsymbol{e}_l)_{l=1,\ldots,L-1}) = W \sum_{l=1}^{L-1} \| P_{0,l} - 2t\boldsymbol{A} \left[\xi u \boldsymbol{B}(|\boldsymbol{e}_l|^2) \right] - t^2 \boldsymbol{A} \left[u^2 \boldsymbol{B}(|\boldsymbol{e}_l|^2) \right] \|_\Gamma^2$$

$$+ W \left\| P_{0,L} + 2t\boldsymbol{A} \left[\xi u \left(L I_0 - \sum_{l=1}^{L-1} (\boldsymbol{B}(|\boldsymbol{e}_l|^2)) \right) \right] + t^2 \boldsymbol{A} \left[u^2 \left(L I_0 - \sum_{l=1}^{L-1} (\boldsymbol{B}(|\boldsymbol{e}_l|^2)) \right) \right] \right\|_\Gamma^2. \quad \text{(A.49)}$$

The gradient is calculated as

$$g_\xi = \arg\max_u \lim_{t\to 0} \frac{F(\xi + tu, (\boldsymbol{e}_l)_{l=1,\ldots,L-1}) - F(\xi, (\boldsymbol{e}_l)_{l=1,\ldots,L-1})}{t} \tag{A.50}$$

$$g_\xi = \arg\max_u -4W \sum_{l=1}^{L-1} \langle P_{0,l}, \boldsymbol{A}\left[\xi u \boldsymbol{B}(|\boldsymbol{e}_l|^2)\right]\rangle - 4W \langle P_{0,L}, \boldsymbol{A}\left[\xi u \left(LI_0 - \sum_{l=1}^{L-1}(\boldsymbol{B}(|\boldsymbol{e}_l|^2))\right)\right]\rangle$$

$$= \arg\max_u -4W \sum_{l=1}^{L-1} \langle \boldsymbol{A}^\dagger\left[P_{0,l}\right], \xi u \boldsymbol{B}(|\boldsymbol{e}_l|^2)\rangle - 4W \langle \boldsymbol{A}^\dagger\left[P_{0,L}\right], \xi u \left(LI_0 - \sum_{l=1}^{L-1}(\boldsymbol{B}(|\boldsymbol{e}_l|^2))\right)\rangle$$

$$= \arg\max_u -4W \sum_{l=1}^{L} \langle \boldsymbol{A}^\dagger\left[P_{0,l}\right], \xi u \boldsymbol{B}(|\boldsymbol{e}_l|^2)\rangle$$

$$= \arg\max_u -4W \sum_{l=1}^{L} \langle \xi \boldsymbol{B}^\dagger(\boldsymbol{A}^\dagger\left[P_{0,l}\right]), u|\boldsymbol{e}_l|^2\rangle$$

$$= \arg\max_u -4W \sum_{l=1}^{L} \langle \xi|\boldsymbol{e}_l|^2 \boldsymbol{B}^\dagger(\boldsymbol{A}^\dagger\left[P_{0,l}\right]), u\rangle$$

$$= -4W \sum_{l=1}^{L} \xi|\boldsymbol{e}_l|^2 \boldsymbol{B}^\dagger(\boldsymbol{A}^\dagger\left[P_{0,l}\right])$$

$$= -4W \sum_{l=1}^{L} \xi|\boldsymbol{e}_l|^2(\left[P_{0,l} * h^\dagger\right]) * f_l^\dagger. \tag{A.51}$$

Note that the gradient with respect to the density can also be easily obtained following Eq. (A.34) by substituting i^2 with $|\boldsymbol{e}_l|^2 * f_l^\dagger$ as

$$g_\xi = -4W \sum_{l=1}^{L} \xi(|\boldsymbol{e}_l|^2 * f_l^\dagger)(P_{0,l} * h^\dagger).$$

Gradient with respect to $\boldsymbol{e}_l$

In computing the gradient with respect to $\boldsymbol{e}_l$, ξ and the other $L - 2$ fields are assumed to be constant.

$$F(\xi, \{\boldsymbol{e}_m\}, \boldsymbol{e}_l + t\boldsymbol{u}) = W \sum_{m=1,m\neq l}^{L-1} \|M_m - \boldsymbol{A}\left[\xi^2 \boldsymbol{B}(|\boldsymbol{e}_m|^2)\right]\|_\Gamma^2 + W\|M_l - \boldsymbol{A}\left[\xi^2 \boldsymbol{B}(|\boldsymbol{e}_l + t\boldsymbol{u}|^2)\right]\|_\Gamma^2$$

$$+ W\left\|M_L - \boldsymbol{A}\left[\xi^2\left(LI_0 - \sum_{m=1,m\neq l}^{L-1}(\boldsymbol{B}(|\boldsymbol{e}_m|^2) - \boldsymbol{B}(|\boldsymbol{e}_l + t\boldsymbol{u}|^2))\right)\right]\right\|_\Gamma^2$$

$$= W \sum_{m=1,m\neq l}^{L-1} \|P_{0,m}\|_\Gamma^2 + W\|M_l - \boldsymbol{A}\left[\xi^2 \boldsymbol{B}(|\boldsymbol{e}_l + t\boldsymbol{u}|^2)\right]\|_\Gamma^2$$

$$+ W\left\|M_L - \boldsymbol{A}\left[\xi^2\left(LI_0 - \sum_{m=1,m\neq l}^{L-1}(\boldsymbol{B}(|\boldsymbol{e}_m|^2) - \boldsymbol{B}(|\boldsymbol{e}_l + t\boldsymbol{u}|^2))\right)\right]\right\|_\Gamma^2. \tag{A.52}$$

Note that

$$\boldsymbol{B}(|\boldsymbol{e}_l + t\boldsymbol{u}|^2) = f_l * \left[|\boldsymbol{e}_l|^2 + 2tRe\{\boldsymbol{e^*}_l\boldsymbol{u}\} + t^2|\boldsymbol{u}|^2\right].$$

The functional is then given by

$$
\begin{aligned}
F(\xi, \{\boldsymbol{e}_m\}, \boldsymbol{e}_l + t\boldsymbol{u}) &= W \sum_{m=1, m\neq l}^{L-1} \|P_{0,m}\|_\Gamma^2 + W\|P_{0,l} - 2t\xi^2 \boldsymbol{A}\left[f_l * Re\{\boldsymbol{e}_l^*\boldsymbol{u}\}\right] - \mathcal{O}(t^2)\|_\Gamma^2 \\
&\quad + W\|P_{0,L} + 2t\xi^2 \boldsymbol{A}\left[f_l * Re\{\boldsymbol{e}_l^*\boldsymbol{u}\}\right] + \mathcal{O}(t^2)|_\Gamma^2 \\
&= W \sum_{m=1, m\neq l}^{L-1} \|P_{0,m}\|_\Gamma^2 + \|P_{0,l}\|_\Gamma^2 - 4Wt\langle P_{0,l}, \xi^2 \boldsymbol{A}\left[f_l * Re\{\boldsymbol{e}_l^*\boldsymbol{u}\}\right]\rangle - \mathcal{O}(t^2) \\
&\quad + W\|P_{0,L}|_\Gamma^2 + 4Wt\langle P_{0,L}, \boldsymbol{A}\left[\xi^2 f_l * Re\{\boldsymbol{e}_l^*\boldsymbol{u}\}\right]\rangle - \mathcal{O}(t^2).
\end{aligned}
\tag{A.53}
$$

From the definition of the gradient,

$$
\begin{aligned}
g_{\boldsymbol{e}_l} &= \arg\max_{u} \lim_{t\to 0} \frac{F(\xi, \{\boldsymbol{e}_m\}, \boldsymbol{e}_l + t\boldsymbol{u}) - F(\xi, (\boldsymbol{e}_l)_{l=1,\dots,L-1})}{t} \\
&= \arg\max_{u} -4W\langle P_{0,l}, \xi^2 \boldsymbol{A}\left[f_l * Re\{\boldsymbol{e}_l^*\boldsymbol{u}\}\right]\rangle + 4W\langle P_{0,L}, \boldsymbol{A}\left[\xi^2 f_l * Re\{\boldsymbol{e}_l^*\boldsymbol{u}\}\right]\rangle \\
&= \arg\max_{u} -4W\langle P_{0,l} - P_{0,L}, \xi^2 \boldsymbol{A}\left[f_l * Re\{\boldsymbol{e}_l^*\boldsymbol{u}\}\right]\rangle \\
&= \arg\max_{u} -4W\langle \boldsymbol{A}^\dagger\left[\xi^2(P_{0,l} - P_{0,L})\right], f_l * Re\{\boldsymbol{e}_l^*\boldsymbol{u}\}\rangle \\
&= \arg\max_{u} -4W\langle f_l^\dagger * \boldsymbol{A}^\dagger\left[\xi^2(P_{0,l} - P_{0,L})\right], 1/2(\boldsymbol{e}_l^*\boldsymbol{u} + \boldsymbol{e}_l\boldsymbol{u}^*)\rangle.
\end{aligned}
\tag{A.54}
$$

Here, it is enough to find the $\boldsymbol{u}$ that maximaizes one of the two terms on the right side. Since they are conjugate terms, the value which maximizes one of the terms also miximizes the other, its conjugate. Therefore,

$$g_{\boldsymbol{e}_l} = \arg\max_{u} -2W\langle f_l^\dagger * \boldsymbol{A}^\dagger\left[\xi^2(P_{0,l} - P_{0,L})\right], \boldsymbol{e}_l^*\boldsymbol{u}\rangle, \tag{A.55}$$

or

$$g_{\boldsymbol{e}_l} = \arg\max_{u} -2W\langle f_l^\dagger * \boldsymbol{A}^\dagger\left[\xi^2(P_{0,l} - P_{0,L})\right], \boldsymbol{e}_l\boldsymbol{u}^*\rangle. \tag{A.56}$$

And finally,

$$g_{\boldsymbol{e}_l} = -2W\boldsymbol{e}_l f_l^\dagger * \boldsymbol{A}^\dagger\left[\xi^2(P_{0,l} - P_{0,L})\right]. \tag{A.57}$$

Gradients for the positve density and non-postive intensity

The gradient of with respect to the auxilary density variable remains similar to the gradient of the positive blind SIM case. However, the gradient with respect to the intensity is modified as follows,

$$g_{I_l} = -2W f_l^\dagger * \boldsymbol{A}^\dagger\left[\xi^2(P_{0,l} - P_{0,L})\right]. \tag{A.58}$$

Polynomials in blind-SIM

In gradient-type algorithms involving least-square functionals, the line minimisation can be sped up by polynomial expansion. One notes here f the function deriving from the functional F.

In blind-SIM, functionals F can be decomposed in two terms: a sequential terms F_s, a sum of contributions coming independently for each illumination; and a cross term F_x, involving all the illumination together. For the sake of simplicity, one studies the sequential terms first, then the cross term that requires more care.

B.1 Blind-SIM: no positivity constraint

In the non-positive version (where there is no positivity on the fluorescent density as well as the intensity), the functional can be decomposed as $F = F_\mathrm{s} + F_\mathrm{x}$ with

$$F_\mathrm{s}\Big(\rho, (I_l)_{l=1..L-1}\Big) = W \sum_{l=1}^{L-1} \|M_l - (\rho I_l) * h\|_\Gamma^2$$

$$F_\mathrm{x}\Big(\rho, (I_l)_{l=1..L-1}\Big) = W \left\|M_L - \left[\rho\left(LI_0 - \sum_{l=1}^{L-1} I_l\right)\right] * h\right\|_\Gamma^2.$$

Sequential terms

f_s is defined by
$$f_\mathrm{s}\big(\alpha, (\beta_l)_{l=1..L-1}\big) = F_\mathrm{s}(\rho + \alpha d_\rho, (I_l + \beta_l d_{l;I})_{l=1..L-1}).$$

It can be expanded in

$$f_\mathrm{s}\big(\alpha, (\beta_l)_{l=1..L-1}\big) = W \sum_{l=1}^{L-1} ||M_l - [(\rho + \alpha d_\rho)(I_l + \beta_l d_{l;I})] * h||_\Gamma^2$$
$$= W \sum_{l=1}^{L-1} ||M_l - (\rho I_l) * h - \alpha(d_\rho I_l) * h - \beta_l(\rho d_{l;I}) * h - \alpha\beta_l(d_\rho d_{l;I}) * h||_\Gamma^2.$$

$$(\mathrm{B.1})$$

Noting

$$P_{0,l} = M_l - (\rho I_l) * h$$
$$P_{1,l} = (d_\rho I_l) * h$$
$$P_{2,l} = (\rho d_{l;I}) * h$$
$$P_{3,l} = (d_\rho d_{l;I}) * h, \tag{B.2}$$

f_s can be rewritten as

$$f_s\big(\alpha, (\beta_l)_{l=1..L-1}\big) = W \sum_{l=1}^{L-1} \|P_{0,l} - \alpha P_{1,l} - \beta_l P_{2,l} - \alpha\beta_l P_{3,l}\|_\Gamma^2$$

$$= W \sum_{l=1}^{L-1} \langle P_{0,l} - \alpha P_{1,l} - \beta_l P_{2,l} - \alpha\beta_l P_{3,l} | P_{0,l} - \alpha P_{1,l} - \beta_l P_{2,l} - \alpha\beta_l P_{3,l} \rangle_\Gamma.$$

Noting

$$P_{ij,lm} = \langle P_{i,l} | P_{j,m} \rangle_\Gamma,$$

One finally obtains the polynomial

$$f_s\big(\alpha, (\beta_l)_{l=1..L-1}\big) = W \sum_{l=1}^{L-1} \big(P_{00,ll} \quad -2\alpha P_{01,ll} \quad -2\beta_l P_{02,ll} \quad -2\alpha\beta_l P_{03,ll}$$
$$+ \alpha^2 P_{11,ll} \quad +2\alpha\beta_l P_{12,ll} \quad +2\alpha^2\beta_l P_{13,ll} \tag{B.3}$$
$$+ \beta_l^2 P_{22,ll} \quad +2\alpha\beta_l^2 P_{23,ll}$$
$$+ \alpha^2\beta_l^2 P_{33,ll} \big).$$

As we are using the conjugate gradient method[46] p 413, we need to compute at each minimisation iteration the derivative of f along all its components. We find the derivatives easily as

$$\frac{\partial f_s}{\partial \alpha} = W \sum_{l=1}^{L-1} \big(-2P_{01,ll} \quad\quad\quad -2\beta_l P_{03,ll}$$
$$+2\alpha P_{11,ll} \quad +2\beta_l P_{12,ll} \quad +4\alpha\beta_l P_{13,ll} \tag{B.4}$$
$$+2\beta_l^2 P_{23,ll}$$
$$+2\alpha\beta_l^2 P_{33,ll} \big)$$

and

$$\frac{\partial f_s}{\partial \beta_l} = W \sum_{l=1}^{L-1} \big(-2P_{02,ll} \quad -2\alpha P_{03,ll}$$
$$+2\alpha P_{12,ll} \quad +2\alpha^2 P_{13,ll} \tag{B.5}$$
$$+2\beta_l P_{22,ll} \quad +4\alpha\beta_l P_{23,ll}$$
$$+2\alpha^2\beta_l P_{33,ll} \big).$$

Cross terms

f_x is defined by

$$f_x\big(\alpha, (\beta_l)_{l=1..L-1}\big) = F_x(\rho + \alpha d_\rho, (I_l + \beta_l d_{l;I})_{l=1..L-1}).$$

It can be expanded in

$$f_{\mathrm{x}}\big(\alpha, (\beta_l)_{l=1..L-1}\big) = W \left\| M_L - \left[(\rho + \alpha d_\rho) \left(LI_0 - \sum_{l=1}^{L-1} (I_l + \beta_l d_{l;I}) \right) \right] * h \right\|_\Gamma^2$$

$$= W \left\| M_l - \left[\rho \left(LI_0 - \sum_{l=1}^{L-1} I_l \right) \right] * h - \alpha \left[d_\rho \left(LI_0 - \sum_{l=1}^{L-1} I_l \right) \right] * h \right.$$

$$\left. + \sum_{l=1}^{L-1} \beta_l (\rho d_{l;I}) * h + \sum_{l=1}^{L-1} \alpha \beta_l (d_\rho d_{l;I}) * h \right\|_\Gamma^2. \tag{B.6}$$

Noting

$$P_{0,L} = M_l - \left[\rho \left(LI_0 - \sum_{l=1}^{L-1} I_l \right) \right] * h$$

$$P_{1,L} = \left[d_\rho \left(LI_0 - \sum_{l=1}^{L-1} I_l \right) \right] * h, \tag{B.7}$$

f_{x} can be rewritten as

$$f_{\mathrm{x}}\big(\alpha, (\beta_l)_{l=1..L-1}\big) \quad = W \left\| P_{0,L} - \alpha P_{1,L} + \sum_{l=1}^{L-1} \beta_l P_{2,l} + \sum_{l=1}^{L-1} \alpha \beta_l P_{3,l} \right\|_\Gamma^2. \tag{B.8}$$

One finally obtains the polynomial

$$f_{\mathrm{x}}\big(\alpha, (\beta_l)_{l=1..L-1}\big) = W \Bigg(P_{00,LL} - 2\alpha P_{01,LL} + \alpha^2 P_{11,LL}$$

$$+ 2\sum_{l=1}^{L-1} \beta_l P_{02,Ll} + 2\sum_{l=1}^{L-1} \alpha \beta_l P_{03,Ll} - 2\sum_{l=1}^{L-1} \alpha \beta_l P_{12,Ll} - 2\sum_{l=1}^{L-1} \alpha^2 \beta_l P_{13,Ll}$$

$$+ \sum_{l=1}^{L-1} \sum_{m=1}^{L-1} \beta_l \beta_m P_{22,lm} + 2\sum_{l=1}^{L-1} \sum_{m=1}^{L-1} \alpha \beta_l \beta_m P_{23,lm} + \sum_{l=1}^{L-1} \sum_{m=1}^{L-1} \alpha^2 \beta_l \beta_m P_{33,lm} \Bigg). \tag{B.9}$$

The derivative of f_{x} by respect to α is easily found

$$\frac{\partial f_{\mathrm{x}}}{\partial \alpha} = W \Bigg(-2P_{01,LL} + 2\alpha P_{11,LL}$$

$$+ 2\sum_{l=1}^{L-1} \beta_l P_{03,Ll} - 2\sum_{l=1}^{L-1} \beta_l P_{12,Ll} - 4\sum_{l=1}^{L-1} \alpha \beta_l P_{13,Ll}$$

$$+ 2\sum_{l=1}^{L-1} \sum_{m=1}^{L-1} \beta_l \beta_m P_{23,lm} + 2\sum_{l=1}^{L-1} \sum_{m=1}^{L-1} \alpha \beta_l \beta_m P_{33,lm} \Bigg). \tag{B.10}$$

The derivative of f_{x} with respect to β_l is a bit more technical. Indeed the terms involving a double summation include terms both in β_l and β_l^2. A direct term-to-term derivation would be tedious and confusing. A simpler solution is to use the formula $\partial \|u\|^2 / \partial \beta_l = 2\langle \partial u / \partial \beta_l | u \rangle$, for any function u. This and Eq. (B.8) leads to

$$\frac{\partial f_{\mathrm{x}}}{\partial \beta_l} = 2W \left\langle P_{2,l} + \alpha P_{3,l} \middle| P_{0,L} - \alpha P_{1,L} + \sum_{m=1}^{L-1} \beta_m P_{2,m} + \sum_{m=1}^{L-1} \alpha \beta_m P_{3,m} \right\rangle_\Gamma,$$

$$\frac{\partial f_{\mathrm{x}}}{\partial \beta_l} = W \left(2P_{02,Ll} - 2\alpha P_{12,Ll} + 2\alpha P_{03,Ll} - 2\alpha^2 P_{13,Ll} + 2 \sum_{m=1}^{L-1} \beta_m P_{22,lm} \right.$$

$$\left. + 2 \sum_{m=1}^{L-1} \alpha\beta_m P_{23,lm} + 2 \sum_{m=1}^{L-1} \alpha\beta_m P_{23,ml} + 2 \sum_{m=1}^{L-1} \alpha^2 \beta_m P_{33,lm} \right). \tag{B.11}$$

Note that the only difference between the second and third term of the second line of Eq. (B.11) is the exchange of indices l and m. They cannot be taken as equal as $P_{23;lm} = \langle P_{2,l} | P_{3,m} \rangle_\Gamma \neq P_{23;ml} = \langle P_{2,m} | P_{3,l} \rangle_\Gamma$.

B.2 Positive blind-SIM: positivity on density and intensity

The positive blind-SIM functional can be decomposed into sequential and cross terms to simplify the analysis as $F = F_{\mathrm{s}} + F_{\mathrm{x}}$ with

$$F_{\mathrm{s}}\Big(\xi, (i_l)_{l=1..L-1}\Big) = W \sum_{l=1}^{L-1} \|M_l - (\xi^2 i_l^2) * h\|_\Gamma^2 \tag{B.12}$$

$$F_{\mathrm{x}}\Big(\xi, (i_l)_{l=1..L-1}\Big) = W \left\| M_L - \left[\xi^2 \left(LI_0 - \sum_{l=1}^{L-1} i_l^2 \right) \right] * h \right\|_\Gamma^2. \tag{B.13}$$

Sequential terms

f_{s} is defined by

$$f_{\mathrm{s}}\big(\alpha, (\beta_l)_{l=1..L-1}\big) = F_{\mathrm{s}}(\xi + \alpha d_\xi, (i_l + \beta_l d_{l;i})_{l=1..L-1}).$$

It can be expanded as

$$f_{\mathrm{s}}\big(\alpha, (\beta_l)_{l=1..L-1}\big) = W \sum_{l=1}^{L-1} \|M_l - [(\xi + \alpha d_\xi)^2 (i_l + \beta_l d_{l;i})^2] * h\|_\Gamma^2$$

$$= W \sum_{l=1}^{L-1} \|M_l - [(\xi^2 + 2\alpha\xi d_\xi + \alpha^2 d_\xi^2)(i_l^2 + 2\beta_l i_l d_{l;i} + \beta_l^2 d_{l;i}^2)] * h\|_\Gamma^2$$

$$= W \sum_{l=1}^{L-1} \|M_l - (\xi^2 i_l^2) * h - 2\alpha(\xi d_\xi i_l^2) * h - \alpha^2(d_\xi^2 i_l^2) * h$$

$$- 2\beta_l(\xi^2 i_l d_{l;i}) * h - 4\alpha\beta_l(\xi d_\xi i_l d_{l;i}) * h - 2\alpha^2 \beta_l(d_\xi^2 i_l d_{l;i}) * h$$

$$- \beta_l^2(\xi^2 d_{l;i}^2) * h - 2\alpha\beta_l^2(\xi d_\xi d_{l;i}^2) * h - \alpha^2 \beta_l^2(d_\xi^2 d_{l;i}^2) * h\|_\Gamma^2.$$

Noting

$$P_{0,l} = M_l - (\xi^2 i_l^2) * h$$
$$P_{1,l} = (\xi d_\xi i_l^2) * h$$
$$P_{2,l} = (d_\xi^2 i_l^2) * h$$
$$P_{3,l} = (\xi^2 i_l d_{l;i}) * h$$
$$P_{4,l} = (\xi d_\xi i_l d_{l;i}) * h \quad \text{(B.14)}$$
$$P_{5,l} = (d_\xi^2 i_l d_{l;i}) * h$$
$$P_{6,l} = (\xi^2 d_{l;i}^2) * h$$
$$P_{7,l} = (\xi d_\xi d_{l;i}^2) * h$$
$$P_{8,l} = (d_\xi^2 d_{l;i}^2) * h,$$

f_{s} can be rewritten as

$$f_{\text{s}}\big(\alpha, (\beta_l)_{l=1..L-1}\big) = W \sum_{l=1}^{L-1} \| P_{0,l} - 2\alpha P_{1,l} - \alpha^2 P_{2,l} - 2\beta_l P_{3,l} - 4\alpha\beta_l P_{4,l} - 2\alpha^2 \beta_l P_{5,l}$$
$$- \beta_l^2 P_{6,l} - 2\alpha\beta_l^2 P_{7,l} - \alpha^2 \beta_l^2 P_{8,l} \|_\Gamma^2. \quad \text{(B.15)}$$

Noting

$$P_{ij,lm} = \langle P_{i,l} | P_{j,m} \rangle_\Gamma,$$

it can be expanded as the polynomial

$$f_{\text{s}}\big(\alpha, (\beta_l)_{l=1..L-1}\big) = W \sum_{l=1}^{L-1} \Big($$

$$P_{00,ll} - 4\alpha P_{01,ll} - 2\alpha^2 P_{02ll} - 4\beta_l P_{03,ll} - 8\alpha\beta_l P_{04,ll} - 4\alpha^2 \beta_l P_{05,ll} - 2\beta_l^2 P_{06,ll}$$
$$- 4\alpha\beta_l^2 P_{07,ll} - 2\alpha^2 \beta_l^2 P_{08,ll}$$
$$+ 4\alpha^2 P_{11,ll} + 4\alpha^3 P_{12,ll} + 8\alpha\beta_l P_{13,ll} + 16\alpha^2 \beta_l P_{14,ll} + 8\alpha^3 \beta_l P_{15,ll} + 4\alpha\beta_l^2 P_{16,ll}$$
$$+ 8\alpha^2 \beta_l^2 P_{17,ll} + 4\alpha^3 \beta_l^2 P_{18,ll}$$
$$+ \alpha^4 P_{22,ll} + 4\alpha^2 \beta_l P_{23,ll} + 8\alpha^3 \beta_l P_{24,ll} + 4\alpha^4 \beta_l P_{25,ll} + 2\alpha^2 \beta_l^2 P_{26,ll}$$
$$+ 4\alpha^3 \beta_l^2 P_{27,ll} + 2\alpha^4 \beta_l^2 P_{28,ll}$$
$$+ 4\beta_l^2 P_{33,ll} + 16\alpha\beta_l^2 P_{34,ll} + 8\alpha^2 \beta_l^2 P_{35,ll} + 4\beta_l^3 P_{36,ll} + 8\alpha\beta_l^3 P_{37,ll}$$
$$+ 4\alpha^2 \beta_l^3 P_{38,ll}$$
$$+ 16\alpha^2 \beta_l^2 P_{44,ll} + 16\alpha^3 \beta_l^2 P_{45,ll} + 8\alpha\beta_l^3 P_{46,ll} + 16\alpha^2 \beta_l^3 P_{47,ll} + 8\alpha^3 \beta_l^3 P_{48,ll}$$
$$+ 4\alpha^4 \beta_l^2 P_{55,ll} + 4\alpha^2 \beta_l^3 P_{56,ll} + 8\alpha^3 \beta_l^3 P_{57,ll} + 4\alpha^4 \beta_l^3 P_{58,ll}$$
$$+ \beta_l^4 P_{66,ll} + 4\alpha\beta_l^4 P_{67,ll} + 2\alpha^2 \beta_l^4 P_{68,ll}$$
$$+ 4\alpha^2 \beta_l^4 P_{77,ll} + 4\alpha^3 \beta_l^4 P_{78,ll}$$
$$+ \alpha^4 \beta_l^4 P_{88,ll}$$

$$\Big).$$

The derivative $\partial f_{\text{s}}/\partial\alpha$ and $\partial f_{\text{s}}/\partial\beta_l$ can be easily calculated by term-to-term derivation of this sum.

Cross terms

f_{x} is defined by

$$f_{\mathrm{x}}\big(\alpha, (\beta_l)_{l=1..L-1}\big) = F_{\mathrm{x}}(\xi + \alpha d_\xi, (i_l + \beta_l d_{l;i})_{l=1..L-1}).$$

It can be expanded in

$$
\begin{aligned}
f_{\mathrm{x}}\big(\alpha, (\beta_l)_{l=1..L-1}\big) &= W \left\| M_L - \left[(\xi + \alpha d_\xi)^2 \left(LI_0 - \sum_{l=1}^{L-1} (i_l + \beta_l d_{l;i})^2 \right) \right] * h \right\|_\Gamma^2 \\
&= W \left\| M_l - \left[(\xi^2 + 2\alpha\xi d_\xi + \alpha^2 d_\xi^2) \left(LI_0 - \sum_{l=1}^{L-1} i_l^2 \right) \right] * h \right. \\
&\quad \left. + \sum_{l=1}^{L-1} \left[(\xi^2 + 2\alpha\xi d_\xi + \alpha^2 d_\xi^2)(2\beta_l i_l d_{l;i} + \beta_l^2 d_{l;i}^2) \right] * h \right\|_\Gamma^2 \\
&= W \left\| M_l - \left[\xi^2 \left(LI_0 - \sum_{l=1}^{L-1} i_l^2 \right) \right] * h - 2\alpha \left[\xi d_\xi \left(LI_0 - \sum_{l=1}^{L-1} i_l^2 \right) \right] * h \right. \\
&\quad - \alpha^2 \left[d_\xi^2 \left(LI_0 - \sum_{l=1}^{L-1} i_l^2 \right) \right] * h + 2 \sum_{l=1}^{L-1} \beta_l (\xi^2 i_l d_{l;i}) * h \\
&\quad + 4 \sum_{l=1}^{L-1} \alpha\beta_l (\xi d_\xi i_l d_{l;i}) * h + 2 \sum_{l=1}^{L-1} \alpha^2 \beta_l (d_\xi^2 i_l d_{l;i}) * h \\
&\quad \left. + \sum_{l=1}^{L-1} \beta_l^2 (\xi^2 d_{l;i}^2) * h + 2 \sum_{l=1}^{L-1} \alpha\beta_l^2 (\xi d_\xi d_{l;i}^2) * h + \sum_{l=1}^{L-1} \alpha^2 \beta_l^2 (d_\xi^2 d_{l;i}^2) * h \right\|_\Gamma^2 .
\end{aligned}
$$

Noting

$$
\begin{aligned}
P_{0,L} &= M_l - \left[\xi^2 \left(LI_0 - \sum_{l=1}^{L-1} i_l^2 \right) \right] * h \\
P_{1,L} &= \left[\xi d_\xi \left(LI_0 - \sum_{l=1}^{L-1} i_l^2 \right) \right] * h \\
P_{2,L} &= \left[d_\xi^2 \left(LI_0 - \sum_{l=1}^{L-1} i_l^2 \right) \right] * h,
\end{aligned}
\tag{B.16}
$$

f_{x} can be rewritten as

$$
\begin{aligned}
f_{\mathrm{x}}\big(\alpha, (\beta_l)_{l=1..L-1}\big) &= W \left\| P_{0,L} - 2\alpha P_{1,L} - \alpha^2 P_{2,L} + 2 \sum_{l=1}^{L-1} \beta_l P_{3,l} \right. \\
&\quad + 4 \sum_{l=1}^{L-1} \alpha\beta_l P_{4,l} + 2 \sum_{l=1}^{L-1} \alpha^2 \beta_l P_{5,l} + \sum_{l=1}^{L-1} \beta_l^2 P_{6,l} \\
&\quad \left. + 2 \sum_{l=1}^{L-1} \alpha\beta_l^2 P_{7,l} + \sum_{l=1}^{L-1} \alpha^2 \beta_l^2 P_{8,l} \right\|_\Gamma^2 .
\end{aligned}
\tag{B.17}
$$

One finally obtains the polynomial

$$
\begin{aligned}
f_{\mathrm{x}}\big(\alpha, (\beta_l)_{l=1..L-1}\big) = W\bigg(& P_{00;LL} - 4\alpha P_{01;LL} - 2\alpha^2 P_{02;LL} + 4\alpha^2 P_{11;LL} + 4\alpha^3 P_{12;LL} + \alpha^4 P_{22;LL} \\
& + 4\sum_{l=1}^{L-1}\beta_l P_{03;Ll} + 8\sum_{l=1}^{L-1}\alpha\beta_l P_{04;Ll} \quad + 4\sum_{l=1}^{L-1}\alpha^2\beta_l P_{05;Ll} \quad + 2\sum_{l=1}^{L-1}\beta_l^2 P_{06;Ll} \quad + 4\sum_{l=1}^{L-1}\alpha\beta_l^2 P_{07;Ll} \\
& \hspace{9cm} + 2\sum_{l=1}^{L-1}\alpha^2\beta_l^2 P_{08;Ll} \\
& - 8\sum_{l=1}^{L-1}\alpha\beta_l P_{13;Ll} - 16\sum_{l=1}^{L-1}\alpha^2\beta_l P_{14;Ll} - 8\sum_{l=1}^{L-1}\alpha^3\beta_l P_{15;Ll} - 4\sum_{l=1}^{L-1}\alpha\beta_l^2 P_{16;Ll} - 8\sum_{l=1}^{L-1}\alpha^2\beta_l^2 P_{17;Ll} \\
& \hspace{9cm} - 4\sum_{l=1}^{L-1}\alpha^3\beta_l^2 P_{18;Ll} \\
& - 4\sum_{l=1}^{L-1}\alpha^2\beta_l P_{23;Ll} - 8\sum_{l=1}^{L-1}\alpha^3\beta_l P_{24;Ll} - 4\sum_{l=1}^{L-1}\alpha^4\beta_l P_{25;Ll} - 2\sum_{l=1}^{L-1}\alpha^2\beta_l^2 P_{26;Ll} - 4\sum_{l=1}^{L-1}\alpha^3\beta_l^2 P_{27;Ll} \\
& \hspace{9cm} - 2\sum_{l=1}^{L-1}\alpha^4\beta_l^2 P_{28;Ll} \\
& + 4\sum_{l=1}^{L-1}\sum_{m=1}^{L-1}\beta_l\beta_m P_{33;lm} + 16\sum_{l=1}^{L-1}\sum_{m=1}^{L-1}\alpha\beta_l\beta_m P_{34;lm} + 8\sum_{l=1}^{L-1}\sum_{m=1}^{L-1}\alpha^2\beta_l\beta_m P_{35;lm} + 4\sum_{l=1}^{L-1}\sum_{m=1}^{L-1}\beta_l\beta_m^2 P_{36;lm} \\
& \hspace{5cm} + 8\sum_{l=1}^{L-1}\sum_{m=1}^{L-1}\alpha\beta_l\beta_m^2 P_{37;lm} + 4\sum_{l=1}^{L-1}\sum_{m=1}^{L-1}\alpha^2\beta_l\beta_m^2 P_{38;lm} \\
& + 16\sum_{l=1}^{L-1}\sum_{m=1}^{L-1}\alpha^2\beta_l\beta_m P_{44;lm} + 16\sum_{l=1}^{L-1}\sum_{m=1}^{L-1}\alpha^3\beta_l\beta_m P_{45;lm} + 8\sum_{l=1}^{L-1}\sum_{m=1}^{L-1}\alpha\beta_l\beta_m^2 P_{46;lm} \\
& \hspace{5cm} + 16\sum_{l=1}^{L-1}\sum_{m=1}^{L-1}\alpha^2\beta_l\beta_m^2 P_{47;lm} + 8\sum_{l=1}^{L-1}\sum_{m=1}^{L-1}\alpha^3\beta_l\beta_m^2 P_{48;lm} \\
& + 4\sum_{l=1}^{L-1}\sum_{m=1}^{L-1}\alpha^4\beta_l\beta_m P_{55;lm} + 4\sum_{l=1}^{L-1}\sum_{m=1}^{L-1}\alpha^2\beta_l\beta_m^2 P_{56;lm} + 8\sum_{l=1}^{L-1}\sum_{m=1}^{L-1}\alpha^3\beta_l\beta_m^2 P_{57;lm} \\
& \hspace{9cm} + 4\sum_{l=1}^{L-1}\sum_{m=1}^{L-1}\alpha^4\beta_l\beta_m^2 P_{58;lm} \\
& + \sum_{l=1}^{L-1}\sum_{m=1}^{L-1}\beta_l^2\beta_m^2 P_{66;lm} + 4\sum_{l=1}^{L-1}\sum_{m=1}^{L-1}\alpha\beta_l^2\beta_m^2 P_{67;lm} + 2\sum_{l=1}^{L-1}\sum_{m=1}^{L-1}\alpha^2\beta_l^2\beta_m^2 P_{68;lm} \\
& \hspace{5cm} + 4\sum_{l=1}^{L-1}\sum_{m=1}^{L-1}\alpha^2\beta_l^2\beta_m^2 P_{77;lm} + 4\sum_{l=1}^{L-1}\sum_{m=1}^{L-1}\alpha^3\beta_l^2\beta_m^2 P_{78;lm} \\
& \hspace{9cm} + \sum_{l=1}^{L-1}\sum_{m=1}^{L-1}\alpha^4\beta_l^2\beta_m^2 P_{88;lm} \bigg).
\end{aligned}
$$

The derivative of f_{x} by respect to α is easily found by term-to-term derivation

$$
\begin{aligned}
\frac{\partial f_{\mathrm{x}}}{\partial \alpha} = W\Bigg(&-4P_{01,LL} - 4\alpha P_{02,LL} + 8\alpha P_{11,LL} + 12\alpha^2 P_{12,LL} + 4\alpha^3 P_{22,LL} \\
&+ 8\sum_{l=1}^{L-1}\beta_l P_{04,Ll} \quad + 8\sum_{l=1}^{L-1}\alpha\beta_l P_{05,Ll} + 4\sum_{l=1}^{L-1}\beta_l^2 P_{07,Ll} + 4\sum_{l=1}^{L-1}\alpha\beta_l^2 P_{08,Ll} \\
&- 8\sum_{l=1}^{L-1}\beta_l P_{13,Ll} - 32\sum_{l=1}^{L-1}\alpha\beta_l P_{14,Ll} - 24\sum_{l=1}^{L-1}\alpha^2\beta_l P_{15,Ll} - 4\sum_{l=1}^{L-1}\beta_l^2 P_{16,Ll} \\
&- 16\sum_{l=1}^{L-1}\alpha\beta_l^2 P_{17,Ll} - 12\sum_{l=1}^{L-1}\alpha^2\beta_l^2 P_{18,Ll} \\
&- 8\sum_{l=1}^{L-1}\alpha\beta_l P_{23,Ll} - 24\sum_{l=1}^{L-1}\alpha^2\beta_l P_{24,Ll} - 16\sum_{l=1}^{L-1}\alpha^3\beta_l P_{25,Ll} - 4\sum_{l=1}^{L-1}\alpha\beta_l^2 P_{26,Ll} \\
&- 12\sum_{l=1}^{L-1}\alpha^2\beta_l^2 P_{27,Ll} - 8\sum_{l=1}^{L-1}\alpha^3\beta_l^2 P_{28,Ll} \\
&+ 16\sum_{l=1}^{L-1}\sum_{m=1}^{L-1}\beta_l\beta_m P_{34,lm} + 16\sum_{l=1}^{L-1}\sum_{m=1}^{L-1}\alpha\beta_l\beta_m P_{35,lm} + 8\sum_{l=1}^{L-1}\sum_{m=1}^{L-1}\beta_l\beta_m^2 P_{37,lm} \\
&+ 8\sum_{l=1}^{L-1}\sum_{m=1}^{L-1}\alpha\beta_l\beta_m^2 P_{38,lm} \\
&+ 32\sum_{l=1}^{L-1}\sum_{m=1}^{L-1}\alpha\beta_l\beta_m P_{44,lm} + 48\sum_{l=1}^{L-1}\sum_{m=1}^{L-1}\alpha^2\beta_l\beta_m P_{45,lm} + 8\sum_{l=1}^{L-1}\sum_{m=1}^{L-1}\beta_l\beta_m^2 P_{46,lm} \\
&+ 32\sum_{l=1}^{L-1}\sum_{m=1}^{L-1}\alpha\beta_l\beta_m^2 P_{47,lm} + 24\sum_{l=1}^{L-1}\sum_{m=1}^{L-1}\alpha^2\beta_l\beta_m^2 P_{48,lm} \\
&+ 16\sum_{l=1}^{L-1}\sum_{m=1}^{L-1}\alpha^3\beta_l\beta_m P_{55,lm} + 8\sum_{l=1}^{L-1}\sum_{m=1}^{L-1}\alpha\beta_l\beta_m^2 P_{56,lm} + 24\sum_{l=1}^{L-1}\sum_{m=1}^{L-1}\alpha^2\beta_l\beta_m^2 P_{57,lm} \\
&+ 16\sum_{l=1}^{L-1}\sum_{m=1}^{L-1}\alpha^3\beta_l\beta_m^2 P_{58,lm} \\
&+ 4\sum_{l=1}^{L-1}\sum_{m=1}^{L-1}\beta_l^2\beta_m^2 P_{67,lm} + 4\sum_{l=1}^{L-1}\sum_{m=1}^{L-1}\alpha\beta_l^2\beta_m^2 P_{68,lm} \\
&+ 8\sum_{l=1}^{L-1}\sum_{m=1}^{L-1}\alpha\beta_l^2\beta_m^2 P_{77,lm} + 12\sum_{l=1}^{L-1}\sum_{m=1}^{L-1}\alpha^2\beta_l^2\beta_m^2 P_{78,lm} \\
&+ 4\sum_{l=1}^{L-1}\sum_{m=1}^{L-1}\alpha^3\beta_l^2\beta_m^2 P_{88,lm}\Bigg).
\end{aligned}
$$

The derivative of f_x by respect to β_l is obtained as

$$
\frac{\partial f_\mathrm{x}}{\partial \beta_l} = 2W \left\langle 2P_{3,l} + 4\alpha P_{4,l} + 2\alpha^2 P_{5,l} + 2\beta_l P_{6,l} + 4\alpha\beta_l P_{7,l} + 2\alpha^2\beta_l P_{8,l} \right|
$$

$$
P_{0,L} - 2\alpha P_{1,L} - \alpha^2 P_{2,L} + 2\sum_{m=1}^{L-1}\beta_l P_{3,m} + 4\sum_{m=1}^{L-1}\alpha\beta_l P_{4,m} + 2\sum_{m=1}^{L-1}\alpha^2\beta_l P_{5,m}
$$

$$
\left. + \sum_{m=1}^{L-1}\beta_l^2 P_{6,m} + 2\sum_{m=1}^{L-1}\alpha\beta_l^2 P_{7,m} + \sum_{m=1}^{L-1}\alpha^2\beta_l^2 P_{8,m} \right\rangle_\Gamma , \quad \text{(B.18)}
$$

$$
\frac{\partial f_\mathrm{x}}{\partial \beta_l} = W\Big(4P_{03,Ll} + 8\alpha P_{04,Ll} - 4\alpha^2 P_{05,Ll} + 4\beta_l P_{06,Ll} + 8\alpha\beta_l P_{07,Ll} + 4\alpha^2\beta_l P_{08,Ll}
$$

$$
- 8\alpha P_{13,Ll} - 16\alpha^2 P_{14,Ll} - 8\alpha^3 P_{15,Ll} - 8\alpha\beta_l P_{16,Ll} - 16\alpha^2\beta_l P_{17,Ll} - 8\alpha^3\beta_l P_{18,Ll}
$$

$$
- 4\alpha^2 P_{23,Ll} - 8\alpha^3 P_{24,Ll} - 4\alpha^4 P_{25,Ll} - 4\alpha^2\beta_l P_{26,Ll} - 8\alpha^3\beta_l P_{27,Ll} - 4\alpha^4\beta_l P_{28,Ll}
$$

$$
+ 8\sum_{m=1}^{L-1}\beta_m P_{33,ml} + 16\sum_{m=1}^{L-1}\alpha\beta_m P_{34,ml} + 8\sum_{m=1}^{L-1}\alpha^2\beta_m P_{35,ml} + 8\sum_{m=1}^{L-1}\beta_l\beta_m P_{36,ml}
$$

$$
+ 16\sum_{m=1}^{L-1}\alpha\beta_l\beta_m P_{37,ml} + 8\sum_{m=1}^{L-1}\alpha^2\beta_l\beta_m P_{38,ml}
$$

$$
+ 16\sum_{m=1}^{L-1}\alpha\beta_m P_{34,lm} + 32\sum_{m=1}^{L-1}\alpha^2\beta_m P_{44,ml} + 16\sum_{m=1}^{L-1}\alpha^3\beta_m P_{45,ml} + 16\sum_{m=1}^{L-1}\alpha\beta_l\beta_m P_{46,ml}
$$

$$
+ 32\sum_{m=1}^{L-1}\alpha^2\beta_l\beta_m P_{47,ml} + 16\sum_{m=1}^{L-1}\alpha^3\beta_l\beta_m P_{48,ml}
$$

$$
+ 8\sum_{m=1}^{L-1}\alpha^2\beta_m P_{35,lm} + 16\sum_{m=1}^{L-1}\alpha^3\beta_m P_{45,lm} + 8\sum_{m=1}^{L-1}\alpha^4\beta_m P_{55,ml} + 8\sum_{m=1}^{L-1}\alpha^2\beta_l\beta_m P_{56,ml}
$$

$$
+ 16\sum_{m=1}^{L-1}\alpha^3\beta_l\beta_m P_{57,ml} + 8\sum_{m=1}^{L-1}\alpha^4\beta_l\beta_m P_{58,ml}
$$

$$
+ 4\sum_{m=1}^{L-1}\beta_m^2 P_{36,lm} + 8\sum_{m=1}^{L-1}\alpha\beta_m^2 P_{46,lm} + 4\sum_{m=1}^{L-1}\alpha^2\beta_m^2 P_{56,lm} + 4\sum_{m=1}^{L-1}\beta_l\beta_m^2 P_{66,ml}
$$

$$
+ 8\sum_{m=1}^{L-1}\alpha\beta_l\beta_m^2 P_{67,ml} + 4\sum_{m=1}^{L-1}\alpha^2\beta_l\beta_m^2 P_{68,ml}
$$

$$
+ 8\sum_{m=1}^{L-1}\alpha\beta_m^2 P_{37,lm} + 16\sum_{m=1}^{L-1}\alpha^2\beta_m^2 P_{47,lm} + 8\sum_{m=1}^{L-1}\alpha^3\beta_m^2 P_{57,lm} + 8\sum_{m=1}^{L-1}\alpha\beta_l\beta_m^2 P_{67,lm}
$$

$$
+ 16\sum_{m=1}^{L-1}\alpha^2\beta_l\beta_m^2 P_{77,ml} + 8\sum_{m=1}^{L-1}\alpha^3\beta_l\beta_m^2 P_{78,ml}
$$

$$
+ 4\sum_{m=1}^{L-1}\alpha^2\beta_m^2 P_{38,lm} + 8\sum_{m=1}^{L-1}\alpha^3\beta_m^2 P_{48,lm} + 4\sum_{m=1}^{L-1}\alpha^4\beta_m^2 P_{58,lm} + 4\sum_{m=1}^{L-1}\alpha^2\beta_l\beta_m^2 P_{68,lm}
$$

$$
+ 8\sum_{m=1}^{L-1}\alpha^3\beta_l\beta_m^2 P_{78,lm} + 4\sum_{m=1}^{L-1}\alpha^4\beta_l\beta_m^2 P_{88,ml} \Big).
$$

B.3   Filtered blind-SIM: positivity constraint only on density

In density positive filtered blind-SIM the positivity assumption is only on the fluorophore density. The cost functional is, once again, $F = F_\mathrm{s} + F_\mathrm{x}$ with

$$F_\mathrm{s}\Big(\xi, (I_l)_{l=1..L-1}\Big) = W \sum_{l=1}^{L-1} \|M_l - (\xi^2 I_l) * h\|_\Gamma^2 \tag{B.19}$$

$$F_\mathrm{x}\Big(\xi, (i_l)_{l=1..L-1}\Big) = W \left\| M_L - \left[\xi^2 \left(L I_0 - \sum_{l=1}^{L-1} I_l\right)\right] * h \right\|_\Gamma^2. \tag{B.20}$$

Each of the illuminations, $\hat{I}_l$, $l = 1, 2, ..., L - 1$ are the filtered are filtered in every iteration. The filter mask is implemented on the incidents in the Fourier space and then inverse transformed.

Sequential terms

f_s is defined by

$$f_\mathrm{s}\big(\alpha, (\beta_l)_{l=1..L-1}\big) = F_\mathrm{s}(\xi + \alpha d_\xi, ((\hat{I}_l + \beta_l \hat{d}_{l;I}) * f)_{l=1..L-1}).$$

where f is the inverse Fourier transform of the Fourier filter mask. Now if we assume $(I_l = \hat{I}_l * f$ and $d_{l;I} = \hat{d}_{l;I} * f$ It can be expanded as

$$\begin{aligned}
f_\mathrm{s}\big(\alpha, (\beta_l)_{l=1..L-1}\big) &= W \sum_{l=1}^{L-1} \|M_l - [(\xi + \alpha d_\xi)^2 (I_l + \beta_l d_{l;I})] * h\|_\Gamma^2 \\
&= W \sum_{l=1}^{L-1} \|M_l - [(\xi^2 + 2\alpha\xi d_\xi + \alpha^2 d_\xi^2)(I_l + \beta_l d_{l;I})] * h\|_\Gamma^2 \\
&= W \sum_{l=1}^{L-1} \|M_l - (\xi^2 I_l) * h - 2\alpha(\xi d_\xi I_l) * h - \alpha^2 (d_\xi^2 I_l) * h \\
&\quad - \beta_l(\xi^2 d_{l;I}) * h - 2\alpha\beta_l(\xi d_\xi d_{l;I}) * h - \alpha^2 \beta_l(d_\xi^2 d_{l;I}) * h\|_\Gamma^2.
\end{aligned}$$

Noting

$$\begin{aligned}
P_{0,l} &= M_l - (\xi^2 I_l) * h \\
P_{1,l} &= (\xi d_\xi I_l) * h \\
P_{2,l} &= (d_\xi^2 I_l) * h \\
P_{3,l} &= (\xi^2 d_{l;I}) * h \\
P_{4,l} &= (\xi d_\xi d_{l;I}) * h \\
P_{5,l} &= (d_\xi^2 d_{l;I}) * h,
\end{aligned} \tag{B.21}$$

f_s can be rewritten as

$$f_\mathrm{s}\big(\alpha, (\beta_l)_{l=1..L-1}\big) = W \sum_{l=1}^{L-1} \|P_{0,l} - 2\alpha P_{1,l} - \alpha^2 P_{2,l} - \beta_l P_{3,l} - 2\alpha\beta_l P_{4,l} - \alpha^2 \beta_l P_{5,l}\|_\Gamma^2. \tag{B.22}$$

Noting

$$P_{ij,lm} = \langle P_{i,l} | P_{j,m} \rangle_\Gamma,$$

it can be expanded as the polynomial

$$f_s\big(\alpha, (\beta_l)_{l=1..L-1}\big) = W \sum_{l=1}^{L-1} \big($$

$$P_{00,ll} - 4\alpha P_{01,ll} - 2\alpha^2 P_{02ll} - 2\beta_l P_{03,ll} - 4\alpha\beta_l P_{04,ll} - 2\alpha^2\beta_l P_{05,ll}$$
$$+4\alpha^2 P_{11,ll} + 4\alpha^3 P_{12,ll} + 4\alpha\beta_l P_{13,ll} + 8\alpha^2\beta_l P_{14,ll} + 4\alpha^3\beta_l P_{15,ll}$$
$$+\alpha^4 P_{22,ll} + 2\alpha^2\beta_l P_{23,ll} + 4\alpha^3\beta_l P_{24,ll} + 2\alpha^4\beta_l P_{25,ll}$$
$$+\beta_l^2 P_{33,ll} + 4\alpha\beta_l^2 P_{34,ll} + 2\alpha^2\beta_l^2 P_{35,ll}$$
$$+4\alpha^2\beta_l^2 P_{44,ll} + 4\alpha^3\beta_l^2 P_{45,ll}$$
$$+\alpha^4\beta_l^2 P_{55,ll}.$$
$$\big).$$

The derivative $\partial f_s/\partial\alpha$ and $\partial f_s/\partial\beta_l$ can be easily calculated by term-to-term derivation of this sum.

Cross terms

f_x is defined by

$$f_x\big(\alpha, (\beta_l)_{l=1..L-1}\big) = F_x(\xi + \alpha d_\xi, (I_l + \beta_l d_{l;i})_{l=1..L-1}).$$

It can be expanded as

$$f_x\big(\alpha, (\beta_l)_{l=1..L-1}\big) = W \left\| M_L - \left[(\xi + \alpha d_\xi)^2 \left(LI_0 - \sum_{l=1}^{L-1}(I_l + \beta_l d_{l;i}) \right) \right] * h \right\|_\Gamma^2$$

$$= W \left\| M_l - \left[(\xi^2 + 2\alpha\xi d_\xi + \alpha^2 d_\xi^2) \left(LI_0 - \sum_{l=1}^{L-1} I_l \right) \right] * h \right.$$

$$\left. + \sum_{l=1}^{L-1} \left[(\xi^2 + 2\alpha\xi d_\xi + \alpha^2 d_\xi^2)(\beta_l d_{l;I}) \right] * h \right\|_\Gamma^2$$

$$= W \left\| M_l - \left[\xi^2 \left(LI_0 - \sum_{l=1}^{L-1} I_l \right) \right] * h - 2\alpha \left[\xi d_\xi \left(LI_0 - \sum_{l=1}^{L-1} I_l \right) \right] * h \right.$$

$$-\alpha^2 \left[d_\xi^2 \left(LI_0 - \sum_{l=1}^{L-1} I_l \right) \right] * h + \sum_{l=1}^{L-1} \beta_l(\xi^2 d_{l;I}) * h$$

$$\left. + 2\sum_{l=1}^{L-1} \alpha\beta_l(\xi d_\xi d_{l;I}) * h + \sum_{l=1}^{L-1} \alpha^2\beta_l(d_\xi^2 d_{l;I}) * h \right\|_\Gamma^2. \tag{B.23}$$

Noting

$$P_{0,L} = M_l - \left[\xi^2 \left(LI_0 - \sum_{l=1}^{L-1} I_l \right) \right] * h \tag{B.24}$$

$$P_{1,L} = \left[\xi d_\xi \left(LI_0 - \sum_{l=1}^{L-1} I_l \right) \right] * h \tag{B.25}$$

$$P_{2,L} = \left[d_\xi^2 \left(LI_0 - \sum_{l=1}^{L-1} I_l \right) \right] * h, \tag{B.26}$$

f_x can be rewritten as

$$f_\text{x}\big(\alpha, (\beta_l)_{l=1..L-1}\big) = W \left\| P_{0,L} - 2\alpha P_{1,L} - \alpha^2 P_{2,L} + \sum_{l=1}^{L-1} \beta_l P_{3,l} + 2\sum_{l=1}^{L-1} \alpha\beta_l P_{4,l} + \sum_{l=1}^{L-1} \alpha^2\beta_l P_{5,l} \right\|_\Gamma^2. \tag{B.27}$$

One finally obtains the polynomial

$$f_\text{x}\big(\alpha, (\beta_l)_{l=1..L-1}\big) = W \Bigg(P_{00;LL} - 4\alpha P_{01;LL} - 2\alpha^2 P_{02;LL} + 4\alpha^2 P_{11;LL} + 4\alpha^3 P_{12;LL} + \alpha^4 P_{22;LL}$$

$$+ 2\sum_{l=1}^{L-1} \beta_l P_{03;Ll} + 4\sum_{l=1}^{L-1} \alpha\beta_l P_{04;Ll} + 2\sum_{l=1}^{L-1} \alpha^2\beta_l P_{05;Ll}$$

$$- 4\sum_{l=1}^{L-1} \alpha\beta_l P_{13;Ll} - 8\sum_{l=1}^{L-1} \alpha^2\beta_l P_{14;Ll} - 4\sum_{l=1}^{L-1} \alpha^3\beta_l P_{15;Ll}$$

$$- 2\sum_{l=1}^{L-1} \alpha^2\beta_l P_{23;Ll} - 4\sum_{l=1}^{L-1} \alpha^3\beta_l P_{24;Ll} - 2\sum_{l=1}^{L-1} \alpha^4\beta_l P_{25;Ll}$$

$$+ \sum_{l=1}^{L-1}\sum_{m=1}^{L-1} \beta_l\beta_m P_{33;lm} + 4\sum_{l=1}^{L-1}\sum_{m=1}^{L-1} \alpha\beta_l\beta_m P_{34;lm} + 2\sum_{l=1}^{L-1}\sum_{m=1}^{L-1} \alpha^2\beta_l\beta_m P_{35;lm}$$

$$+ 4\sum_{l=1}^{L-1}\sum_{m=1}^{L-1} \alpha^2\beta_l\beta_m P_{44;lm} + 4\sum_{l=1}^{L-1}\sum_{m=1}^{L-1} \alpha^3\beta_l\beta_m P_{45;lm}$$

$$+ \sum_{l=1}^{L-1}\sum_{m=1}^{L-1} \alpha^4\beta_l\beta_m P_{55;lm} \Bigg).$$

The derivatives of f_x with respect to α and β_l can easily be computed by term-to-term derivation.

B.4 Filtered blind-SIM: positivity on both density and intensity

The postivity assumption on both the fluorophore density and Intensity is considered. Computation of the polynomials follows the same procedure as of the positive blind-SIM, except some changes

caused by the definition of the filtering. The filter and the positivity together on the Intensity is defined as

$$I_l = \hat{I}_{l;i} * f_l = |\boldsymbol{e}_{l;i}|^2 * f_l.$$

In the positive version of blind-SIM, the functional decomposed as $F = F_{\mathrm{s}} + F_{\mathrm{x}}$, is given by

$$F_{\mathrm{s}}\Big(\xi, (\boldsymbol{e}_{l;i})_{l=1..L-1}\Big) = W \sum_{l=1}^{L-1} \|M_l - \big(\xi^2(|\boldsymbol{e}_{l;i}|^2 * f_l)\big) * h\|_\Gamma^2 \tag{B.28}$$

$$F_{\mathrm{x}}\Big(\xi, (\boldsymbol{e}_{l;i})_{l=1..L-1}\Big) = W \left\| M_L - \left[\xi^2 \left(LI_0 - \sum_{l=1}^{L-1} (|\boldsymbol{e}_{l;i}|^2 * f_l) \right) \right] * h \right\|_\Gamma^2. \tag{B.29}$$

Sequential terms

f_{s} is defined by

$$f_{\mathrm{s}}\big(\alpha, (\beta_l)_{l=1..L-1}\big) = F_{\mathrm{s}}(\xi + \alpha d_\xi, (\boldsymbol{e}_{l;i} + \beta_l \boldsymbol{d}_{l;i})_{l=1..L-1}),$$

where $\boldsymbol{e}_{l;i}$ and $\boldsymbol{d}_{l;i}$ are complex. It can be expanded as

$$
\begin{aligned}
f_{\mathrm{s}}\big(\alpha, (\beta_l)_{l=1..L-1}\big) &= W \sum_{l=1}^{L-1} \|M_l - [(\xi + \alpha d_\xi)^2(|\boldsymbol{e}_{l;i} + \beta_l \boldsymbol{d}_{l;i}|^2 * f_l)] * h\|_\Gamma^2 \\
&= W \sum_{l=1}^{L-1} \|M_l - [(\xi + \alpha d_\xi)^2((\boldsymbol{e}_{l;i} + \beta_l \boldsymbol{d}_{l;i})(\boldsymbol{e}_{l;i}^* + \beta_l \boldsymbol{d}_{l;i}^*) * f_l)] * h\|_\Gamma^2 \\
&= W \sum_{l=1}^{L-1} \|M_l - [(\xi^2 + 2\alpha\xi d_\xi + \alpha^2 d_\xi^2)(|\boldsymbol{e}_{l;i}|^2 + 2\beta_l Re\{\boldsymbol{e}_{l;i}^* \boldsymbol{d}_{l;i}\} \\
&\quad + \beta_l^2 |\boldsymbol{d}_{l;i}|^2) * f_l] * h\|_\Gamma^2 \tag{B.30} \\
&= W \sum_{l=1}^{L-1} \|M_l - (\xi^2 |\boldsymbol{e}_{l;i}|^2 * f_l) * h - 2\alpha(\xi d_\xi |\boldsymbol{e}_{l;i}|^2 * f_l) * h \\
&\quad - \alpha^2(d_\xi^2 |\boldsymbol{e}_{l;i}|_l^2 * f_l) * h - 2\beta_l(\xi^2 Re\{\boldsymbol{e}_{l;i}^* \boldsymbol{d}_{l;i}\} * f_l) * h \\
&\quad - 4\alpha\beta_l(\xi d_\xi Re\{\boldsymbol{e}_{l;i}^* \boldsymbol{d}_{l;i}\} * f_l) * h - 2\alpha^2 \beta_l(d_\xi^2 Re\{\boldsymbol{e}_{l;i}^* \boldsymbol{d}_{l;i}\} * f_l) * h \tag{B.31} \\
&\quad - \beta_l^2(\xi^2 |\boldsymbol{d}_{l;i}|^2 * f_l) * h - 2\alpha\beta_l^2(\xi d_\xi |\boldsymbol{d}_{l;i}|^2 * f_l) * h \\
&\quad - \alpha^2 \beta_l^2(d_\xi^2 |\boldsymbol{d}_{l;i}|^2 * f_l) * h\|_\Gamma^2.
\end{aligned}
$$

Noting

$$P_{0,l} = M_l - (\xi^2 |\boldsymbol{e}_{l;i}|^2 * f_l) * h$$

$$P_{1,l} = (\xi d_\xi |\boldsymbol{e}_{l;i}|^2 * f_l) * h$$

$$P_{2,l} = (d_\xi^2 |\boldsymbol{e}_{l;i}|_l^2 * f_l) * h$$

$$P_{3,l} = (\xi^2 Re\{\boldsymbol{e}_{l;i}^* \boldsymbol{d}_{l;i}\} * f_l) * h$$

$$P_{4,l} = (\xi d_\xi Re\{\boldsymbol{e}_{l;i}^* \boldsymbol{d}_{l;i}\} * f_l) * h \qquad \text{(B.32)}$$

$$P_{5,l} = (d_\xi^2 Re\{\boldsymbol{e}_{l;i}^* \boldsymbol{d}_{;i}\} * f_l) * h$$

$$P_{6,l} = (\xi^2 |\boldsymbol{d}_{l;i}|^2 * f_l) * h$$

$$P_{7,l} = (\xi d_\xi |\boldsymbol{d}_{l;i}|^2 * f_l) * h$$

$$P_{8,l} = (d_\xi^2 |\boldsymbol{d}_{l;i}|^2 * f_l) * h,$$

f_s can be rewritten as

$$f_\text{s}\big(\alpha, (\beta_l)_{l=1..L-1}\big) = W \sum_{l=1}^{L-1} \| P_{0,l} - 2\alpha P_{1,l} - \alpha^2 P_{2,l} - 2\beta_l P_{3,l} - 4\alpha\beta_l P_{4,l} - 2\alpha^2 \beta_l P_{5,l}$$

$$- \beta_l^2 P_{6,l} - 2\alpha\beta_l^2 P_{7,l} - \alpha^2 \beta_l^2 P_{8,l} \|_\Gamma^2. \qquad \text{(B.33)}$$

Noting

$$P_{ij,lm} = \langle P_{i,l} | P_{j,m} \rangle_\Gamma,$$

it can be expanded as the polynomial

$$f_\text{s}\big(\alpha, (\beta_l)_{l=1..L-1}\big) = W \sum_{l=1}^{L-1} \Big($$

$$P_{00,ll} - 4\alpha P_{01,ll} \ - 2\alpha^2 P_{02ll} \ - 4\beta_l P_{03,ll} \ - 8\alpha\beta_l P_{04,ll} \ - 4\alpha^2 \beta_l P_{05,ll} - 2\beta_l^2 P_{06,ll}$$

$$- 4\alpha\beta_l^2 P_{07,ll} - 2\alpha^2 \beta_l^2 P_{08,ll}$$

$$+ 4\alpha^2 P_{11,ll} + 4\alpha^3 P_{12,ll} + 8\alpha\beta_l P_{13,ll} + 16\alpha^2 \beta_l P_{14,ll} + 8\alpha^3 \beta_l P_{15,ll} + 4\alpha\beta_l^2 P_{16,ll}$$

$$+ 8\alpha^2 \beta_l^2 P_{17,ll} + 4\alpha^3 \beta_l^2 P_{18,ll}$$

$$+ \alpha^4 P_{22,ll} + 4\alpha^2 \beta_l P_{23,ll} + 8\alpha^3 \beta_l P_{24,ll} + 4\alpha^4 \beta_l P_{25,ll} + 2\alpha^2 \beta_l^2 P_{26,ll} + 4\alpha^3 \beta_l^2 P_{27,ll}$$

$$+ 2\alpha^4 \beta_l^2 P_{28,ll}$$

$$+ 4\beta_l^2 P_{33,ll} + 16\alpha\beta_l^2 P_{34,ll} \ + 8\alpha^2 \beta_l^2 P_{35,ll} \ + 4\beta_l^3 P_{36,ll} \ + 8\alpha\beta_l^3 P_{37,ll} \ + 4\alpha^2 \beta_l^3 P_{38,ll}$$

$$+ 16\alpha^2 \beta_l^2 P_{44,ll} + 16\alpha^3 \beta_l^2 P_{45,ll} + 8\alpha\beta_l^3 P_{46,ll} + 16\alpha^2 \beta_l^3 P_{47,ll} + 8\alpha^3 \beta_l^3 P_{48,ll}$$

$$+ 4\alpha^4 \beta_l^2 P_{55,ll} + 4\alpha^2 \beta_l^3 P_{56,ll} + 8\alpha^3 \beta_l^3 P_{57,ll} + 4\alpha^4 \beta_l^3 P_{58,ll}$$

$$+ \beta_l^4 P_{66,ll} \ + 4\alpha\beta_l^4 P_{67,ll} + 2\alpha^2 \beta_l^4 P_{68,ll}$$

$$+ 4\alpha^2 \beta_l^4 P_{77,ll} + 4\alpha^3 \beta_l^4 P_{78,ll}$$

$$+ \alpha^4 \beta_l^4 P_{88,ll} \Big).$$

The derivative $\partial f_\text{s}/\partial\alpha$ and $\partial f_\text{s}/\partial\beta_l$ can be easily calculated by term-to-term derivation of this sum.

Cross terms

f_x is defined by

$$f_\mathrm{x}\big(\alpha,(\beta_l)_{l=1..L-1}\big) = F_\mathrm{x}(\xi + \alpha d_\xi, (\boldsymbol{e}_{l;i} + \beta_l \boldsymbol{d}_{l;i})_{l=1..L-1}).$$

It can be expanded as

$$
\begin{aligned}
f_\mathrm{x}\big(\alpha,(\beta_l)_{l=1..L-1}\big) &= W \left\| M_L - \left[(\xi + \alpha d_\xi)^2 \left(LI_0 - \sum_{l=1}^{L-1} (|\boldsymbol{e}_{l;i} + \beta_l \boldsymbol{d}_{l;i}|^2 * f_l) \right) \right] * h \right\|_\Gamma^2 \\
&= W \left\| M_l - \left[(\xi^2 + 2\alpha\xi d_\xi + \alpha^2 d_\xi^2) \left(LI_0 - \sum_{l=1}^{L-1} |\boldsymbol{e}_{l;i}|^2 * f_l \right) \right] * h \right. \\
&\quad \left. + \sum_{l=1}^{L-1} \left[(\xi^2 + 2\alpha\xi d_\xi + \alpha^2 d_\xi^2)(2\beta_l Re\{\boldsymbol{e}_{l;i}^* \boldsymbol{d}_{l;i}\} * f_l + \beta_l^2 |\boldsymbol{d}_{l;i}|^2 * f_l) \right] * h \right\|_\Gamma^2 \\
&= W \left\| M_l - \left[\xi^2 \left(LI_0 - \sum_{l=1}^{L-1} |\boldsymbol{e}_{l;i}|^2 * f_l \right) \right] * h - 2\alpha \left[\xi d_\xi \left(LI_0 - \sum_{l=1}^{L-1} |\boldsymbol{e}_{l;i}|^2 * f_l \right) \right] * h \right. \\
&\quad - \alpha^2 \left[d_\xi^2 \left(LI_0 - \sum_{l=1}^{L-1} |\boldsymbol{e}_{l;i}|^2 * f_l \right) \right] * h + 2 \sum_{l=1}^{L-1} \beta_l (\xi^2 Re\{\boldsymbol{e}_{l;i}^* \boldsymbol{d}_{l;i}\} * f_l) * h \\
&\quad + 4 \sum_{l=1}^{L-1} \alpha\beta_l (\xi d_\xi Re\{\boldsymbol{e}_{l;i}^* \boldsymbol{d}_{l;i}\} * f_l) * h + 2 \sum_{l=1}^{L-1} \alpha^2 \beta_l (d_\xi^2 Re\{\boldsymbol{e}_{l;i}^* \boldsymbol{d}_{l;i}\} * f_l) * h \\
&\quad + \sum_{l=1}^{L-1} \beta_l^2 (\xi^2 |\boldsymbol{d}_{l;i}|^2 * f_l) * h + 2 \sum_{l=1}^{L-1} \alpha\beta_l^2 (\xi d_\xi |\boldsymbol{d}_{l;i}|^2 * f_l) * h \\
&\quad \left. + \sum_{l=1}^{L-1} \alpha^2 \beta_l^2 (d_\xi^2 |\boldsymbol{d}_{l;i}|^2 * f_l) * h \right\|_\Gamma^2 .
\end{aligned}
$$

Noting

$$
\begin{aligned}
P_{0,L} &= M_l - \left[\xi^2 \left(LI_0 - \sum_{l=1}^{L-1} |\boldsymbol{e}_{l;i}|^2 * f_l \right) \right] * h \\
P_{1,L} &= \left[\xi d_\xi \left(LI_0 - \sum_{l=1}^{L-1} |\boldsymbol{e}_{l;i}|^2 * f_l \right) \right] * h \\
P_{2,L} &= \left[d_\xi^2 \left(LI_0 - \sum_{l=1}^{L-1} |\boldsymbol{e}_{l;i}|^2 * f_l \right) \right] * h,
\end{aligned}
\tag{B.34}
$$

f_x can be rewritten as

$$f_\mathrm{x}\big(\alpha,(\beta_l)_{l=1..L-1}\big) = W \left\| P_{0,L} - 2\alpha P_{1,L} - \alpha^2 P_{2,L} + 2 \sum_{l=1}^{L-1} \beta_l P_{3,l} + 4 \sum_{l=1}^{L-1} \alpha\beta_l P_{4,l} \right. \tag{B.35}$$

$$\left. + 2 \sum_{l=1}^{L-1} \alpha^2 \beta_l P_{5,l} + \sum_{l=1}^{L-1} \beta_l^2 P_{6,l} + 2 \sum_{l=1}^{L-1} \alpha\beta_l^2 P_{7,l} + \sum_{l=1}^{L-1} \alpha^2 \beta_l^2 P_{8,l} \right\|_\Gamma^2 . \tag{B.36}$$

One finally obtains the polynomial

$$
f_{\mathrm{x}}\big(\alpha, (\beta_l)_{l=1..L-1}\big) = W\bigg(P_{00;LL} - 4\alpha P_{01;LL} - 2\alpha^2 P_{02;LL} + 4\alpha^2 P_{11;LL} + 4\alpha^3 P_{12;LL} + \alpha^4 P_{22;LL}
$$

$$
+ 4\sum_{l=1}^{L-1}\beta_l P_{03;Ll} \; + 8\sum_{l=1}^{L-1}\alpha\beta_l P_{04;Ll} + 4\sum_{l=1}^{L-1}\alpha^2\beta_l P_{05;Ll} \quad + 2\sum_{l=1}^{L-1}\beta_l^2 P_{06;Ll}
$$

$$
+ 4\sum_{l=1}^{L-1}\alpha\beta_l^2 P_{07;Ll} + 2\sum_{l=1}^{L-1}\alpha^2\beta_l^2 P_{08;Ll}
$$

$$
- 8\sum_{l=1}^{L-1}\alpha\beta_l P_{13;Ll} - 16\sum_{l=1}^{L-1}\alpha^2\beta_l P_{14;Ll} - 8\sum_{l=1}^{L-1}\alpha^3\beta_l P_{15;Ll} - 4\sum_{l=1}^{L-1}\alpha\beta_l^2 P_{16;Ll}
$$

$$
- 8\sum_{l=1}^{L-1}\alpha^2\beta_l^2 P_{17;Ll} - 4\sum_{l=1}^{L-1}\alpha^3\beta_l^2 P_{18;Ll}
$$

$$
- 4\sum_{l=1}^{L-1}\alpha^2\beta_l P_{23;Ll} - 8\sum_{l=1}^{L-1}\alpha^3\beta_l P_{24;Ll} - 4\sum_{l=1}^{L-1}\alpha^4\beta_l P_{25;Ll} - 2\sum_{l=1}^{L-1}\alpha^2\beta_l^2 P_{26;Ll}
$$

$$
- 4\sum_{l=1}^{L-1}\alpha^3\beta_l^2 P_{27;Ll} - 2\sum_{l=1}^{L-1}\alpha^4\beta_l^2 P_{28;Ll}
$$

$$
+ 4\sum_{l=1}^{L-1}\sum_{m=1}^{L-1}\beta_l\beta_m P_{33;lm} + 16\sum_{l=1}^{L-1}\sum_{m=1}^{L-1}\alpha\beta_l\beta_m P_{34;lm} + 8\sum_{l=1}^{L-1}\sum_{m=1}^{L-1}\alpha^2\beta_l\beta_m P_{35;lm}
$$

$$
+ 4\sum_{l=1}^{L-1}\sum_{m=1}^{L-1}\beta_l\beta_m^2 P_{36;lm} + 8\sum_{l=1}^{L-1}\sum_{m=1}^{L-1}\alpha\beta_l\beta_m^2 P_{37;lm} + 4\sum_{l=1}^{L-1}\sum_{m=1}^{L-1}\alpha^2\beta_l\beta_m^2 P_{38;lm}
$$

$$
+ 16\sum_{l=1}^{L-1}\sum_{m=1}^{L-1}\alpha^2\beta_l\beta_m P_{44;lm} + 16\sum_{l=1}^{L-1}\sum_{m=1}^{L-1}\alpha^3\beta_l\beta_m P_{45;lm} + 8\sum_{l=1}^{L-1}\sum_{m=1}^{L-1}\alpha\beta_l\beta_m^2 P_{46;lm}
$$

$$
+ 16\sum_{l=1}^{L-1}\sum_{m=1}^{L-1}\alpha^2\beta_l\beta_m^2 P_{47;lm}
$$

$$
+ 8\sum_{l=1}^{L-1}\sum_{m=1}^{L-1}\alpha^3\beta_l\beta_m^2 P_{48;lm}
$$

$$
+ 4\sum_{l=1}^{L-1}\sum_{m=1}^{L-1}\alpha^4\beta_l\beta_m P_{55;lm} + 4\sum_{l=1}^{L-1}\sum_{m=1}^{L-1}\alpha^2\beta_l\beta_m^2 P_{56;lm} + 8\sum_{l=1}^{L-1}\sum_{m=1}^{L-1}\alpha^3\beta_l\beta_m^2 P_{57;lm}
$$

$$
+ 4\sum_{l=1}^{L-1}\sum_{m=1}^{L-1}\alpha^4\beta_l\beta_m^2 P_{58;lm}
$$

$$
+ \sum_{l=1}^{L-1}\sum_{m=1}^{L-1}\beta_l^2\beta_m^2 P_{66;lm} + 4\sum_{l=1}^{L-1}\sum_{m=1}^{L-1}\alpha\beta_l^2\beta_m^2 P_{67;lm} + 2\sum_{l=1}^{L-1}\sum_{m=1}^{L-1}\alpha^2\beta_l^2\beta_m^2 P_{68;lm}
$$

$$
+ 4\sum_{l=1}^{L-1}\sum_{m=1}^{L-1}\alpha^2\beta_l^2\beta_m^2 P_{77;lm} + 4\sum_{l=1}^{L-1}\sum_{m=1}^{L-1}\alpha^3\beta_l^2\beta_m^2 P_{78;lm}
$$

$$
+ \sum_{l=1}^{L-1}\sum_{m=1}^{L-1}\alpha^4\beta_l^2\beta_m^2 P_{88;lm}\bigg).
$$

The derivative of f_x by respect to α is easily found by term-to-term derivation.

$$
\frac{\partial f_\mathrm{x}}{\partial \alpha} = W\bigg(-4P_{01,LL} - 4\alpha P_{02,LL} + 8\alpha P_{11,LL} + 12\alpha^2 P_{12,LL} + 4\alpha^3 P_{22,LL}
$$

$$
+ 8\sum_{l=1}^{L-1}\beta_l P_{04,Ll} \quad + 8\sum_{l=1}^{L-1}\alpha\beta_l P_{05,Ll} + 4\sum_{l=1}^{L-1}\beta_l^2 P_{07,Ll} + 4\sum_{l=1}^{L-1}\alpha\beta_l^2 P_{08,Ll}
$$

$$
- 8\sum_{l=1}^{L-1}\beta_l P_{13,Ll} - 32\sum_{l=1}^{L-1}\alpha\beta_l P_{14,Ll} - 24\sum_{l=1}^{L-1}\alpha^2\beta_l P_{15,Ll} - 4\sum_{l=1}^{L-1}\beta_l^2 P_{16,Ll}
$$

$$
- 16\sum_{l=1}^{L-1}\alpha\beta_l^2 P_{17,Ll} - 12\sum_{l=1}^{L-1}\alpha^2\beta_l^2 P_{18,Ll}
$$

$$
- 8\sum_{l=1}^{L-1}\alpha\beta_l P_{23,Ll} - 24\sum_{l=1}^{L-1}\alpha^2\beta_l P_{24,Ll} - 16\sum_{l=1}^{L-1}\alpha^3\beta_l P_{25,Ll} - 4\sum_{l=1}^{L-1}\alpha\beta_l^2 P_{26,Ll}
$$

$$
- 12\sum_{l=1}^{L-1}\alpha^2\beta_l^2 P_{27,Ll} - 8\sum_{l=1}^{L-1}\alpha^3\beta_l^2 P_{28,Ll}
$$

$$
+ 16\sum_{l=1}^{L-1}\sum_{m=1}^{L-1}\beta_l\beta_m P_{34,lm} + 16\sum_{l=1}^{L-1}\sum_{m=1}^{L-1}\alpha\beta_l\beta_m P_{35,lm} + 8\sum_{l=1}^{L-1}\sum_{m=1}^{L-1}\beta_l\beta_m^2 P_{37,lm}
$$

$$
+ 8\sum_{l=1}^{L-1}\sum_{m=1}^{L-1}\alpha\beta_l\beta_m^2 P_{38,lm}
$$

$$
+ 32\sum_{l=1}^{L-1}\sum_{m=1}^{L-1}\alpha\beta_l\beta_m P_{44,lm} + 48\sum_{l=1}^{L-1}\sum_{m=1}^{L-1}\alpha^2\beta_l\beta_m P_{45,lm} + 8\sum_{l=1}^{L-1}\sum_{m=1}^{L-1}\beta_l\beta_m^2 P_{46,lm}
$$

$$
+ 32\sum_{l=1}^{L-1}\sum_{m=1}^{L-1}\alpha\beta_l\beta_m^2 P_{47,lm} + 24\sum_{l=1}^{L-1}\sum_{m=1}^{L-1}\alpha^2\beta_l\beta_m^2 P_{48,lm}
$$

$$
+ 16\sum_{l=1}^{L-1}\sum_{m=1}^{L-1}\alpha^3\beta_l\beta_m P_{55,lm} + 8\sum_{l=1}^{L-1}\sum_{m=1}^{L-1}\alpha\beta_l\beta_m^2 P_{56,lm} + 24\sum_{l=1}^{L-1}\sum_{m=1}^{L-1}\alpha^2\beta_l\beta_m^2 P_{57,lm}
$$

$$
+ 16\sum_{l=1}^{L-1}\sum_{m=1}^{L-1}\alpha^3\beta_l\beta_m^2 P_{58,lm}
$$

$$
+ 4\sum_{l=1}^{L-1}\sum_{m=1}^{L-1}\beta_l^2\beta_m^2 P_{67,lm} + 4\sum_{l=1}^{L-1}\sum_{m=1}^{L-1}\alpha\beta_l^2\beta_m^2 P_{68,lm}
$$

$$
+ 8\sum_{l=1}^{L-1}\sum_{m=1}^{L-1}\alpha\beta_l^2\beta_m^2 P_{77,lm} + 12\sum_{l=1}^{L-1}\sum_{m=1}^{L-1}\alpha^2\beta_l^2\beta_m^2 P_{78,lm}
$$

$$
+ 4\sum_{l=1}^{L-1}\sum_{m=1}^{L-1}\alpha^3\beta_l^2\beta_m^2 P_{88,lm}\bigg).
$$

The derivative of f_{x} by respect to β_l is obtained as

$$
\frac{\partial f_{\mathrm{x}}}{\partial \beta_l} = 2W \Bigg\langle 2P_{3,l} + 4\alpha P_{4,l} + 2\alpha^2 P_{5,l} + 2\beta_l P_{6,l} + 4\alpha\beta_l P_{7,l} + 2\alpha^2 \beta_l P_{8,l} \Bigg|
$$

$$
P_{0,L} - 2\alpha P_{1,L} - \alpha^2 P_{2,L} + 2\sum_{m=1}^{L-1}\beta_l P_{3,m} + 4\sum_{m=1}^{L-1}\alpha\beta_l P_{4,m}
$$

$$
+2\sum_{m=1}^{L-1}\alpha^2\beta_l P_{5,m} + \sum_{m=1}^{L-1}\beta_l^2 P_{6,m} + 2\sum_{m=1}^{L-1}\alpha\beta_l^2 P_{7,m} + \sum_{m=1}^{L-1}\alpha^2\beta_l^2 P_{8,m} \Bigg\rangle_\Gamma , \quad \text{(B.37)}
$$

$$
\frac{\partial f_{\mathrm{x}}}{\partial \beta_l} = W \Bigg(4P_{03,Ll} + 8\alpha P_{04,Ll} - 4\alpha^2 P_{05,Ll} + 4\beta_l P_{06,Ll} + 8\alpha\beta_l P_{07,Ll} + 4\alpha^2\beta_l P_{08,Ll}
$$

$$
- 8\alpha P_{13,Ll} - 16\alpha^2 P_{14,Ll} - 8\alpha^3 P_{15,Ll} - 8\alpha\beta_l P_{16,Ll} - 16\alpha^2\beta_l P_{17,Ll} - 8\alpha^3\beta_l P_{18,Ll}
$$

$$
- 4\alpha^2 P_{23,Ll} - 8\alpha^3 P_{24,Ll} - 4\alpha^4 P_{25,Ll} - 4\alpha^2\beta_l P_{26,Ll} - 8\alpha^3\beta_l P_{27,Ll} - 4\alpha^4\beta_l P_{28,Ll}
$$

$$
+ 8\sum_{m=1}^{L-1}\beta_m P_{33,ml} + 16\sum_{m=1}^{L-1}\alpha\beta_m P_{34,ml} + 8\sum_{m=1}^{L-1}\alpha^2\beta_m P_{35,ml} + 8\sum_{m=1}^{L-1}\beta_l\beta_m P_{36,ml}
$$

$$
+ 16\sum_{m=1}^{L-1}\alpha\beta_l\beta_m P_{37,ml} + 8\sum_{m=1}^{L-1}\alpha^2\beta_l\beta_m P_{38,ml}
$$

$$
+ 16\sum_{m=1}^{L-1}\alpha\beta_m P_{34,lm} + 32\sum_{m=1}^{L-1}\alpha^2\beta_m P_{44,ml} + 16\sum_{m=1}^{L-1}\alpha^3\beta_m P_{45,ml} + 16\sum_{m=1}^{L-1}\alpha\beta_l\beta_m P_{46,ml}
$$

$$
+ 32\sum_{m=1}^{L-1}\alpha^2\beta_l\beta_m P_{47,ml} + 16\sum_{m=1}^{L-1}\alpha^3\beta_l\beta_m P_{48,ml}
$$

$$
+ 8\sum_{m=1}^{L-1}\alpha^2\beta_m P_{35,lm} + 16\sum_{m=1}^{L-1}\alpha^3\beta_m P_{45,lm} + 8\sum_{m=1}^{L-1}\alpha^4\beta_m P_{55,ml} + 8\sum_{m=1}^{L-1}\alpha^2\beta_l\beta_m P_{56,ml}
$$

$$
+ 16\sum_{m=1}^{L-1}\alpha^3\beta_l\beta_m P_{57,ml} + 8\sum_{m=1}^{L-1}\alpha^4\beta_l\beta_m P_{58,ml}
$$

$$
+ 4\sum_{m=1}^{L-1}\beta_m^2 P_{36,lm} + 8\sum_{m=1}^{L-1}\alpha\beta_m^2 P_{46,lm} + 4\sum_{m=1}^{L-1}\alpha^2\beta_m^2 P_{56,lm} + 4\sum_{m=1}^{L-1}\beta_l\beta_m^2 P_{66,ml}
$$

$$
+ 8\sum_{m=1}^{L-1}\alpha\beta_l\beta_m^2 P_{67,ml} + 4\sum_{m=1}^{L-1}\alpha^2\beta_l\beta_m^2 P_{68,ml}
$$

$$
+ 8\sum_{m=1}^{L-1}\alpha\beta_m^2 P_{37,lm} + 16\sum_{m=1}^{L-1}\alpha^2\beta_m^2 P_{47,lm} + 8\sum_{m=1}^{L-1}\alpha^3\beta_m^2 P_{57,lm} + 8\sum_{m=1}^{L-1}\alpha\beta_l\beta_m^2 P_{67,lm}
$$

$$
+ 16\sum_{m=1}^{L-1}\alpha^2\beta_l\beta_m^2 P_{77,ml} + 8\sum_{m=1}^{L-1}\alpha^3\beta_l\beta_m^2 P_{78,ml}
$$

$$
+ 4\sum_{m=1}^{L-1}\alpha^2\beta_m^2 P_{38,lm} + 8\sum_{m=1}^{L-1}\alpha^3\beta_m^2 P_{48,lm} + 4\sum_{m=1}^{L-1}\alpha^4\beta_m^2 P_{58,lm} + 4\sum_{m=1}^{L-1}\alpha^2\beta_l\beta_m^2 P_{68,lm}
$$

$$
+ 8\sum_{m=1}^{L-1}\alpha^3\beta_l\beta_m^2 P_{78,lm} + 4\sum_{m=1}^{L-1}\alpha^4\beta_l\beta_m^2 P_{88,ml} \Bigg).
$$

Analytical minimization in blind-SIM-SD

In this section the gradients as well as the numerical and analytical minimization of the polynoms for the blind-SIM-SD is presented.

Gradient

Using $\eta_l^2 = i_l^2 \xi^2$ the cost functional of blind-SIM-SD is modified in terms of the auxiliary functions η_l as

$$F(\eta_l) = W_l \|M_l - \eta_l^2 * h\|_\Gamma^2 = W_l \|P_0\|. \tag{C.1}$$

By definition

$$g_{\eta_l} = \arg\max_u \lim_{t \to 0} \frac{F(\eta_l + tu) - F(\eta_l)}{t} | \|u\| = 1. \tag{C.2}$$

$$
\begin{aligned}
F(\eta_l + tu) \qquad &= W_l \|M_l - (\eta_l + tu)^2 * h\| \\
& W_l \|M_l - (\eta_l^2 + 2t\eta_l u + t^2 u^2) * h\| \\
& W_l \|M_l - (\eta_l^2 * h) - 2t(\eta_l u * h) - (t^2 u^2) * h\| \\
& W_l \|P_0 - 2t(\eta_l u * h) - (t^2 u^2) * h\| \\
& W_l \|P_0\|^2 - 2t\langle P_0, \eta_l u * h\rangle + \mathcal{O}(t^2)\|.
\end{aligned}
\tag{C.3}
$$

Then using Eq. (C.2) is determined as

$$
\begin{aligned}
g_{\eta_l} \quad &= \arg\max_u -2\langle P_0, \eta_l u * h\rangle | \|u\| = 1 \\
&= \arg\max_u -2\eta_l \langle P_0 * h^\dagger, u\rangle | \|u\| = 1.
\end{aligned}
\tag{C.4}
$$

Therefore,

$$g_{\eta_l} \quad = -2\eta_l P_0 * h^\dagger. \tag{C.5}$$

Minimization of polynomials

The funtional for each illumination

$$F(\eta_l) = W_l \|M_l - \eta_l^2 * h\|_\Gamma^2, \tag{C.6}$$

is expressed at every iteration, omitting the iteration index for clarity, as

$$F(\alpha) = W_l \|M_l - (\eta_l + \alpha d_l)^2 * h\|_\Gamma^2$$
$$W_l \|M_l - (\eta_l^2 + 2\alpha \eta_l d_l + \alpha^2 d_l^2) * h\|_\Gamma^2. \tag{C.7}$$

Noting

$$\begin{aligned} P_{0,l} &= M_l - (\eta_l^2) * h \\ P_{1,l} &= \eta_l d_l * h \\ P_{2,l} &= d_l^2 * h, \end{aligned} \tag{C.8}$$

$$\begin{aligned} F(\alpha) &= W_l \|P_{0,l} - 2\alpha P_{1,l} - \alpha^2 P_{2,l}\|_\Gamma^2 \\ &= P_{00,ll} - 4P_{01,ll}\alpha + (4P_{11,ll} - 2P_{02,ll})\alpha^2 + 4P_{12,ll}\alpha^3 + P_{22,ll}\alpha^4, \end{aligned} \tag{C.9}$$

where $P_{ij,ll} = W_l \|P_{i,l} P_{j,l}\|_\Gamma^2$ and $\|P_{i,l} P_{j,l}\|_\Gamma^2 = \|P_{j,l} P_{i,l}\|_\Gamma^2$.

And the derivative $\partial F(\alpha) \partial \alpha$ is

$$\partial F(\alpha) \partial \alpha = -4P_{01,ll} + (8P_{11,ll} - 4P_{02,ll})\alpha + 12P_{12,ll}\alpha^2 + 4P_{22,ll}\alpha^3. \tag{C.10}$$

Here in order to minimize the functional $\partial F(\alpha) \partial \alpha = 0$ can be solved either numerically or analytically. We use the anlytical solution based on the principle of solving cubic functions proposed by Weisstein *et al.*[103]to speed up the reconstruction. Among the three roots of the cubic function, there xists atleast one real root. If only one root exists that root is selected. If two or three real roots exist the one which gives the minimum value of the functional is selected.

Publications

Peer-reviewed journals

1. Awoke Negash, Simon Labouesse, Nicolas Sandeau, Marc Allain, Hugues Giovannini, Jérôme Idier, Rainer Heintzmann, Patrick C. Chaumet, Kamal Belkebir and Anne Sentenac. "Improving the axial and lateral resolution of three-dimensional fluorescence microscopy using random speckle illuminations." JOSA A **33(6)**:1089-1094, (2016).

2. Simon Labouesse, Awoke Negash, Jérôme Idier, Sébastien Bourguignon, Thomas Mangeat, Penghuan Liu, Anne Sentenac and Marc Allain. "Joint reconstruction strategy for structured illumination microscopy with unknown illuminations." IEEE Transactions on Image Processing **26(5)**: 2480-2493, (2017).

International conferences

1. Awoke Negash, Simon Labouesse, *et al.*, "Separate deconvolution: for three-dimensional speckle imaging fluorescence microscopy", Imaging and Applied Optics 2016, Heidelberg, Germany, (2016).

2. Awoke Negash, Thomas Mangeat, *et al.*, "Slice-based out-of-focus reduction technique for 3D fluorescence microscopy", Focus on microscopy (FOM2017), Bordeaux, France, (2017).

3. Awoke Negash, Omar Olarte, *et al.*, "Resolution improvement in iSPIM based on novel structured illumination reconstruction strategies", Light Sheet Fluorescence Microscopy (LSFM2017), Singapore, (2017).

4. Awoke Negash, Thomas Mangeat, *et al.*, "Super-resolution using speckle illumination microscopy", Imaging and Applied Optics 2017, Sanfrancisco, California, USA, (2017).

5. Simon Labouesse, Awoke Negash, *et al.*, "Fast reconstruction in blind fluorescence structured illumination microscopy", Imaging and Applied Optics 2017, Sanfrancisco, California, USA, (2017).

Bibliography

[1] E. Abbe, "On the theory of optical images, with special reference to the microscope," Phil. Mag. Ser. 5 **42**, 167–195 (1896).

[2] M. Yamanaka, N. I. Smith, and K. Fujita, "Introduction to super-resolution microscop," Microscopy **63**, 177–192 (2014).

[3] S. Hell and M. Kroug, "Ground-state-depletion fluorscence microscopy:a concept for breaking the diffraction resolution limit," Appl. Phys. B **60**, 495–497 (1995).

[4] M. A. A. Neil, R. Juškaitis, and T. Wilson, "Method of obtaining optical sectioning by using structured light in a conventional microscope," Opt. Lett. **22**, 1905–1907 (1997).

[5] R. Heintzmann and C. G. Cremer, "Laterally modulated excitation microscopy: improvement of resolution by using a diffraction grating," Proc. SPIE **3568**, 185–196 (1999).

[6] M. Gustafsson, "Surpassing the lateral resolution limit by a factor of two using structured illumination microscopy," J. Microsc. **198**, 82–87 (2000).

[7] M. G. Gustafsson, L. Shao, P. M. Carlton, C. R. Wang, I. N. Golubovskaya, W. Z. Cande, D. A. Agard, and J. W. Sedaty, "Three-dimensional resolution doubling in wide-field fluorescence microscopy by structured illumination," Biophysical Journal **94**, 4957–4970 (2008).

[8] M. Gustafsson, "Nonlinear structured-illumination microscopy: Wide-field fluorescence imaging with theoretically unlimited resolution," P. N. A. S. **102**, 13081–13086 (2005).

[9] R. M. Barry, *The development of fluorescence microscopy* (John Wiley and Sons Ltd, 2001).

[10] E. Betzig, G. H. Patterson, P. Sougrat, W. Lindwasser, S. Olenych, J. S. Bonifacino, M. W. Davidson, and J. Lippincott-Schwartz, "Imaging intracellular fluorescent proteins at nanometer resolution," Science **313**, 1642–1645 (2006).

[11] M. J. Rust, M. Bates, and X. Zhuang, "Sub-diffraction-limit imaging by stochastic optical reconstruction microscopy," Nat. Methods **3**, 793–796 (2006).

[12] R. Henriques and M. Mhlanga, "Palm and storm: What hides beyond the rayleigh limit?" Biot. Jour. **4**, 846–857 (2009).

[13] S. T. Hess, T. P. K. Girirajan, and M. D. Mason, "Ultra-high resolution imaging by fluorescence photoactivation localization microscopy," Biophys. J. **91**, 4258–4272 (2006).

[14] L. Schermelleh, P. M. Carlton, S. Haase, L. Shao, L. Winoto, P. Kner, B. Burke, M. C. Cardoso, D. A. Agard, M. G. L. Gustafsson, H. Leonhardt, and J. W. Sedat, "Subdiffraction Multicolor Imaging of the Nuclear Periphery with 3D Structured Illumination Microscopy," Science **320**, 1332–1336 (2008).

[15] Liisa M. Hirvonen and Kai Wicker and Ondrej Mandula and Rainer Heintzmann, "Structured illumination microscopy of a living cell," European Biophys. J. **38**, 807–812 (2009).

[16] P. Kner, B. B. Chhun, E. R. Griffis, L. Winoto, and M. G. Gustafsson, "Super-resolution video microscopy of live cells by structured illumination," Nat. Methods **6**, 339–342 (2009).

[17] L. Shao, P. Kner, E. H. Rego, and M. G. Gustafsson, "Super-resolution 3d microscopy of live whole cells using structured illumination," Nature methods **8**, 1044 (2011).

[18] E. Mudry, *Resolution improvement in fluorescence and phase optical microscopy* (Institut Fresnel, équipe SEMO, Aix-Marseille Université, Marseille, France, 2012).

[19] M. Fernández-Suárez and A. Y. Ting, "Fluorescent probes for super-resolution imaging in living cells," Mol. Cell. Bio. **9**, 929–943 (2008).

[20] F. W. Rost, *Fluorescence microscopy*, vol. II (Cambridge University Press, 1995).

[21] A. Egner and S. W. Hell, "Fluorescence microscopy with super-resolved optical sections," Trends in Cell Biology **15**, 207 – 215 (2005).

[22] S. Bretschneider, C. Eggeling, and S. W. Hell, "Breaking the Diffraction Barrier in Fluorescence Microscopy by Optical Shelving," Phys. Rev. Lett. **98**, 218103–4 (2007).

[23] T. royal swedish academy of sciences, "Super-resolved fluorescence microscopy," Scientific background on the noble prize in chemistry (2014).

[24] G. Q. Xiao, T. R. Corle, and G. S. Kino, "Real time confocal scanning optical microscope," Appl. Phys. Lett. **53**, 716–718 (1988).

[25] H. J. Tiziani and H. M. Uhde, "Three-dimensional image sensing by chromatic confocal microscopy," Appl. Opt. **33**, 1838–1843 (1994).

[26] C. J. Brakenhoff, P. Blom, and P. Barends, "Confocal scanning light microscopy with high aperture immersion lenses," J. Microsc. **117**, 219–232 (1979).

[27] T. Wilson and B. R. Masters, "Confocal microscopy," App. Opt. **33**, 565–566 (1994).

[28] A. Jesacher, M. Ritsh-Marte, and R. Piestun, "Three-dimensional information from two-dimensional scans: a scanning microscope with postacquisition refocusing capability," Optica **2**, 210–213 (2015).

[29] J. Huff, "The airyscan detector from zeiss: confocal imaging with improved signal-to-noise ratio and super-resolution," Nat. Meth. **12** (2015).

[30] S. W. Hell and E. H. K. Stelzer, "Fundamental improvement of resolution with a 4pi-confocal fluorescence microscope using two-photon excitation," Optics Communications **93**, 277 – 282 (1992).

[31] D. Karadaglić and T. Wilson, "Image formation in structured illumination wide-field fluorescence microscopy," Micron **39**, 808–818 (2008).

[32] B.-J. Chang, L.-J. Chou, Y.-C. Chang, and S.-Y. Chiang, "Isotropic image in structured illumination microscopy patterned with a spatial light modulator," Opt. Exp. **17**, 14710–14721 (2009).

[33] R. Förster, H.-W. Lu-Walther, A. Jost, M. Kielhorn, K. Wicker, and R. Heintzmann, "Simple structured illumination microscope setup with high acquisition speed by using a spatial light modulator," Opt. Express **22**, 20663–20677 (2014).

[34] H.-W. Lu-Walther, M. Kielhorn, Förster, A. Jost, K. Wicker, and R. Heintzmann, "fast-sim: a practical implementation of fast structured illumination microscopy," Methods and Applications in Fluorescence **3**, 014001 (2015).

[35] L. H. Schaefer, D. Schuster, and J. Schaffer, "Structured illumination microscopy: artefact analysis and reduction utilizing a parameter optimization approach," Journal of microscopy **216**, 165–174 (2004).

[36] E. Mudry, K. Belkebir, J. Girard, J. Savatier, E. L. Moal, C. Nicoletti, M. Allain, and A. Sentenac, "Structured illumination microscopy using unknown speckle patterns," Nat. Photon. **6**, 312–315 (2012).

[37] K. Wicker, O. Mandula, G. Best, R. Fiolka, and R. Heintzmann, "Phase optimization for structured illumination microscopy," Opt. Express **21**, 2032–2049 (2013).

[38] R. Ayuk, H. Giovannini, A. Jost, E. Mudry, J. Girard, T. Mangeat, N. Sandeau, R. Heintzmann, K. Wicker, K. Belkebir *et al.*, "Structured illumination fluorescence microscopy with distorted excitations using a filtered blind-sim algorithm," Optics letters **38**, 4723–4726 (2013).

[39] X. Hao, C. Kuang, Z. Gu, Y. Wang, S. Li, Y. Ku, Y. Li, J. Ge, and X. Liu, "From microscopy to nanoscopy via visible light," Light: Science and Applications **2**, e108 (2013).

[40] J. Mertz, "Optical sectioning microscopy with planar or structured illumination," Nature methods **8**, 811–819 (2011).

[41] D. Lim, T. N. Ford, K. K. Chu, and J. Mertz, "Optically sectioned in vivo imaging with speckle illumination hilo microscopy," Journal of Biomedical Optics **16**, 016014–016014–8 (2011).

[42] M. Kim, C. Park, C. Rodriguez, Y. Park, and Y.-H. Cho, "Superresolution imaging with optical fluctuation using speckle patterns illumination," Scientific reports **5** (2015).

[43] J. Min, J. Jang, D. Keum, S.-W. Ryu, C. Choi, K.-H. Jeong, and J. C. Ye, "Fluorescent microscopy beyond diffraction limits using speckle illumination and joint support recovery," Scientific reports **3** (2013).

[44] E. J. Botcherby, R. Juškaitis, M. J. Booth, and T. Wilson, "An optical technique for remote focusing in microscopy," Optics Communications **281**, 880–887 (2008).

[45] S. Abrahamsson, J. Chen, B. Hajj, S. Stallinga, A. Y. Katsov, J. Wisniewski, G. Mizuguchi, P. Soule, F. Mueller, C. D. Darzacq *et al.*, "Fast multicolor 3d imaging using aberration-corrected multifocus microscopy," Nature methods **10**, 60–63 (2013).

[46] W. H. Press, B. P. Flannery, S. A. Teukolski, and W. T. Vetterling, *Numerical recipes. The art of scientific computing* (Cambridge University Press, 1986).

[47] M. R. Hestenes and E. Stiefel, *Methods of conjugate gradients for solving linear systems*, vol. 49 (NBS, 1952).

[48] E. Polak and G. Ribiere, "Note sur la convergence de méthodes de directions conjuguées," Revue française d'informatique et de recherche opérationnelle. Série rouge **3**, 35–43 (1969).

[49] A. Jost, E. Tolstik, P. Feldmann, K. Wicker, A. Sentenac, and R. Heintzmann, "Optical sectioning and high resolution in single-slice structured illumination microscopy by thick slice blind-sim reconstruction," PloS one **10**, e0132174 (2015).

[50] G. Cox and C. J. R. Sheppard, "Practical limits of resolution in confocal and non-linear microscopy," Micros. Res. Tech. **63**, 18–22 (2004).

[51] R. Heintzmann, "Estimating missing information by maximum likelihood deconvolution," Micron **38**, 136–144 (2007).

[52] P. C. Hansen, *Rank-deficient and discrete ill-posed problems: numerical aspects of linear inversion* (SIAM, 1998).

[53] G. H. Golub, M. Heath, and G. Wahba, "Generalized cross-validation as a method for choosing a good ridge parameter," Technometrics **21**, 215–223 (1979).

[54] Q. Ma, B. Khademhosseinieh, E. Huang, H. Qian, M. A. Bakowski, E. R. Troemel, and Z. Liu, "Three-dimensional fluorescent microscopy via simultaneous illumination and detection at multiple planes," Scientific reports **6**, 31445 (2016).

[55] P. Prabhat, S. Ram, E. S. Ward, and R. J. Ober, "Simultaneous imaging of different focal planes in fluorescence microscopy for the study of cellular dynamics in three dimensions," IEEE transactions on nanobioscience **3**, 237–242 (2004).

[56] A. Negash, S. Labouesse, N. Sandeau, M. Allain, H. Giovannini, J. Idier, R. Heintzmann, P. C. Chaumet, K. Belkebir, and A. Sentenac, JOSA A **33**, 1089–1094 (2016).

[57] E. J. Botcherby, R. J. uskaitis, M. J. Booth, and T. Wilson, "Aberration-free optical refocusing in high numerical aperture microscopy," Opt. Lett. **32** (2007).

[58] H.-W. Lu-Walther, M. Kielhorn, R. Förster, A. Jost, K. Wicker, and R. Heintzmann, "fastsim: a practical implementation of fast structured illumination microscopy," Methods and Applications in Fluorescence **3**, 014001 (2015).

[59] S. F. Gibson and F. Lanni, "Experimental test of an analytical model of aberration in an oil-immersion objective lens used in three-dimensional light microscopy," JOSA A **9**, 154–166 (1992).

[60] J. R. Swedlow, J. W. Sedat, and D. A. Agard, "Deconvolution in optical microscopy," Deconvolution of images and spectra **285**, 284–309 (1997).

[61] "http://argolight.com/argo-sim/," .

[62] M. Walde, J. Monypenny, R. Heintzmann, G. E. Jones, and S. Cox, "Vinculin binding angle in podosomes revealed by high resolution microscopy," PloS one **9**, e88251 (2014).

[63] C. Luxenburg, D. Geblinger, E. Klein, K. Anderson, D. Hanein, B. Geiger, and L. Addadi, "The architecture of the adhesive apparatus of cultured osteoclasts: from podosome formation to sealing zone assembly," PloS one **2**, e179 (2007).

[64] S. W. Hell, S. Lindek, C. Cremer, and E. H. Stelzer, "Confocal microscopy with an increased detection aperture: type-b 4pi confocal microscopy," Optics letters **19**, 222–224 (1994).

[65] M. G. Gustafsson, D. Agard, J. Sedat *et al.*, "I5m: 3d widefield light microscopy with better than 100nm axial resolution," Journal of microscopy **195**, 10–16 (1999).

[66] E. Mudry, E. L. Moal, P. Ferrand, P. C. Chaumet, and A. Sentenac, "Isotropic diffraction-limited focusing using a single objective lens," Phys. Rev. Lett. **105**, 203903 (2010).

[67] E. Le Moal, E. Mudry, P. C. Chaumet, P. Ferrand, and A. Sentenac, "Two-photon fluorescence isotropic-single-objective microscopy," Optics letters **37**, 85–87 (2012).

[68] P. T. So, C. Y. Dong, B. R. Masters, and K. M. Berland, "Two-photon excitation fluorescence microscopy," Annual review of biomedical engineering **2**, 399–429 (2000).

[69] O. Therrien, B. Aubé, S. Pagès, P. De Koninck, and D. Côté, "Wide-field multiphoton imaging of cellular dynamics in thick tissue by temporal focusing and patterned illumination," Biomedical optics express **2**, 696–704 (2011).

[70] D. Oron, E. Tal, and Y. Silberberg, "Scanningless depth-resolved microscopy," Optics express **13**, 1468–1476 (2005).

[71] A. Vaziri and C. V. Shank, "Ultrafast widefield optical sectioning microscopy by multifocal temporal focusing," Optics express **18**, 19645–19655 (2010).

[72] M. Ingaramo, A. G. York, P. Wawrzusin, O. Milberg, A. Hong, R. Weigert, H. Shroff, and G. H. Patterson, "Two-photon excitation improves multifocal structured illumination microscopy in thick scattering tissue," Proceedings of the National Academy of Sciences **111**, 5254–5259 (2014).

[73] P. W. Winter, A. G. York, D. D. Nogare, M. Ingaramo, R. Christensen, A. Chitnis, G. H. Patterson, and H. Shroff, "Two-photon instant structured illumination microscopy improves the depth penetration of super-resolution imaging in thick scattering samples," Optica **1**, 181–191 (2014).

[74] L.-C. Cheng, C.-Y. Chang, C.-Y. Lin, K.-C. Cho, W.-C. Yen, N.-S. Chang, C. Xu, C. Y. Dong, and S.-J. Chen, "Spatiotemporal focusing-based widefield multiphoton microscopy for fast optical sectioning," Optics express **20**, 8939–8948 (2012).

[75] E. Tal, D. Oron, and Y. Silberberg, "Improved depth resolution in video-rate line-scanning multiphoton microscopy using temporal focusing," Optics letters **30**, 1686–1688 (2005).

[76] J. Huisken, J. Swoger, J. W. F. Del Bene, and E. H. K. Stelzer, "Optical sectioning deep inside live embryos by selective plane illumination microscopy," Science **305**, 1007–1009 (2004).

[77] M. Neil, T. Wilson, and R. Juškaitis, "A light efficient optically sectioning microscope," Journal of Microscopy **189**, 114–117 (1998).

[78] J. Qian, M. Lei, D. Dan, B. Yao, X. Zhou, Y. Yang, S. Yan, J. Min, and X. Yu, "Full-color structured illumination optical sectioning microscopy," Scientific reports **5**, 14513 (2015).

[79] D. Lim, K. K. Chu, and J. Mertz, "Wide-field fluorescence sectioning with hybrid speckle and uniform-illumination microscopy," Opt. Lett. **33**, 1819–1821 (2008).

[80] G. Cox and C. Sheppard, "Effects of image deconvolution on optical sectioning in conventional and confocal microscopes," Bioimaging **1**, 82–95 (1993).

[81] J.-A. Conchello and J. G. McNally, "Fast regularization technique for expectation maximization algorithm for optical sectioning microscopy," in "PROCEEDINGS-SPIE THE INTERNATIONAL SOCIETY FOR OPTICAL ENGINEERING," (SPIE INTERNATIONAL SOCIETY FOR OPTICAL, 1996), pp. 199–208.

[82] M. Weinstein and K. R. Castleman, "Reconstructing 3-d specimens from 2-d section images," in "Proc. SPIE," , vol. 26 (1971), vol. 26, pp. 131–138.

[83] D. A. Agard and J. W. Sedat, "Three-dimensional architecture of a polytene nucleus," Nature **302**, 676–681 (1983).

[84] Y. Gruenbaum, M. Hochstrasser, D. Mathog, H. Saumweber, D. Agard, and J. Sedat, "Spatial organization of the drosophila nucleus: a three-dimensional cytogenetic study," J Cell Sci **1984**, 223–234 (1984).

[85] H. Siedentopf and R. Zsigmondy, "Uber sichtbarmachung und größenbestimmung ultramikoskopischer teilchen, mit besonderer anwendung auf goldrubingläser," Annalen der Physik **315**, 1–39 (1902).

[86] A. Voie, D. Burns, and F. Spelman, "Orthogonal-plane fluorescence optical sectioning: Three-dimensional imaging of macroscopic biological specimens," Journal of microscopy **170**, 229–236 (1993).

[87] C. J. Engelbrecht and E. H. Stelzer, "Resolution enhancement in a light-sheet-based microscope (spim)," Opt. Lett. **31**, 1477–1479 (2006).

[88] E. G. Reynaud, U. K. zič, K. Greger, and E. H. K. Stelzer, "Light sheet-based fluorescence microscopy: more dimensions, more photons, and less photodamage," HFSP J. **2**, 266–275 (2008).

[89] J. Huisken and D. Y. R. Stainier, "Selective plane illumination microscopy techniques in developmental biology," Development **136**, 1963–1975 (2009).

[90] P. J. Keller and H.-U. Dodt, "Light sheet microscopy of living or cleared specimens," Science Direct **22**, 138–143 (2011).

[91] P. J. Keller, A. D. Schmidt, K. K. A. Santella, J. W. Z. Bao, and E. H. K. Stelzer, "Fast, high-contrast imaging of animal development with scanned light sheet-based structured-illumination microscopy," Nat. Methods **7**, 637–642 (2010).

[92] P. J. Keller and E. H. K. Stelzer, "Quantitative in vivo imaging of entire embryos with digital scanned laser light sheet fluorescence microscopy," Curr. Opin. Neurobiol. **18**, 624–632 (2008).

[93] O. E. Olarte, J. Licea-Rodriguez, J. A. Palero, E. J. Gualda, D. Artigas, J. Mayer, J. Swoger, J. Sharpe, I. Rocha-Mendoza, R. Rangel-Rojo, and P. Loza-Alvarez, "Image formation by linear and nonlinear digital scanned light-sheet fluorescence microscopy with gaussian and bessel beam profiles," Biom. Opt. Exp. **3** (2012).

[94] T. A. Planchon, L. Gao, D. E. Milkie, M. W. Davidson, J. A. SGalbraith, C. G. Galbraith, and E. Betzig, "Rapid three-dimensional isotropic imaging of living cells using bessel beam plane illumination," Nat. Methods **8**, 417–423 (2011).

[95] P. J. Keller, A. D. Schmidt, J. Wittbrodt, and E. H. K. Stelzer, "Reconstruction of zebrafish early embryonic development by scanned light sheet microscopy," Science **322**, 1065–1069 (2008).

[96] T. J. Schröter, S. B. Johnson, K. John, and P. A. Santi, "Scanning thin-sheet laser imaging microscopy (stslim) with structured illumination and hilo background rejection," J Biom. Opt. Exp. **3** (2012).

[97] D. Bhattacharya, V. R. Singh, C. Zhi, P. T. C. So, P. Matsudaira, and G. Barbastathis, "Three dimensional hilo-based structured illumination for a digital scanned laser sheet microscopy (dslm) in thick tissue imaging," J. Opt. Exp. **20** (2012).

[98] K. Mohan, S. B. Purnapatra, and P. P. Mondal, "Three dimensional fluorescence imaging using multiple light-sheet microscopy," PLOS ONE **9** (2012).

[99] K. Mohan and P. P. Mondal, "Spatial filter based light-sheet laser interference technique for three-dimensional nanolithography," J. App. Phy. Lett. **106** (2015).

[100] B.-C. Chen, W. R. Legant, K. Wang, L. Shao, D. E. Milkie, M. W. Davidson, C. Janetopoulos, X. S. Wu, J. A. Hammer, Z. Liu *et al.*, "Lattice light-sheet microscopy: Imaging molecules to embryos at high spatiotemporal resolution," Science **246** (2014).

[101] Y. Wu, P. Wawrzusin, J. Senseney, R. S. Fischer, R. Christensen, A. Santella, A. G. York, P. W. Winter, C. M. Waterman, Z. Bao *et al.*, "Spatially isotropic four-dimensional imaging with dual-view plane illumination microscopy," Nature biotechnology **31**, 1032–1038 (2013).

[102] J. D. Manton and E. J. Rees, "trispim: light sheet microscopy with isotropic super-resolution," J. Opt. Lett. **41** (2016).

[103] E. W. Weisstein, "Cubic formula," omega **86**, 87 (2002).

Résumé

La microscopie de fluorescence optique est l'un des outils les plus puissants pour étudier les structures cellulaires et moléculaires au niveau subcellulaire. La résolution d'une image de microscope conventionnel à fluorescence est limitée par la diffraction, ce qui permet d'obtenir une résolution spatiale latérale de 200nm et axiale de 500nm. Récemment, de nombreuses techniques de microscopie de fluorescence de super-résolution ont été développées pour permettre d'observer de nombreuses structures biologiques au-delà de la limite de diffraction. La microscopie d'illumination structurée (SIM) est l'une de ces technologies. Le principe de la SIM est basé sur l'utilisation d'une grille de lumière harmonique qui permet de translater les hautes fréquences spatiales de l'échantillon vers la région d'observation du microscope. L'amélioration de la résolution de cette technologie de microscopie dépend fortement de la technique de reconstruction, qui rétablit les hautes fréquences spatiales de l'échantillon dans leur position d'origine. Les méthodes classiques de reconstruction SIM nécessitent une connaissance parfaite de l'illumination de l'échantillon. Cependant, l'implémentation d'un contrôle parfait de l'illumination harmonique sur le plan de l'échantillon n'est pas facile expérimentalement et il présente un grand défi. L'hypothèse de la connaissance parfaite de l'intensité de la lumière illuminant l'échantillon en SIM peut donc introduire des artefacts sur l'image reconstruite de l'échantillon, à cause des erreurs d'alignement de la grille qui peuvent se présenter lors de l'acquisition expérimentale. Afin de surmonter ce défi, nous avons développé dans cette thèse des stratégies de reconstruction «aveugle» qui sont indépendantes de d'illumination. À l'aide de ces stratégies de reconstruction dites «blind-SIM», nous avons étendu la SIM harmonique pour l'appliquer aux cas de «SIM-speckle» qui utilisent des illuminations aléatoires et inconnues qui contrairement à l'illumination harmonique, ne nécessitent pas de controle. Comme il est utile de récupérer des informations sur l'illumination en SIM harmonique, nous avons développé une reconstruction blind-SIM tridimensionnel et filtrée qui confine l'estimation itérative des illuminations au voisinage des pics dans l'espace de Fourier, en utilisant des masques de filtre de Fourier soigneusement conçus. En utilisant des techniques de reconstruction blind-SIM, une résolution latérale d'environ 100 nm et une résolution axiale d'environ 200 nm sont obtenues, à la fois en SIM harmonique et en SIM speckle. En outre, pour réduire le problème de focalisation dans les images de champ large, une technique de calcul simple qui repose sur la reconstruction bidimensionnel de données à partir de PSF tridimensionnel est développée. En outre, afin de combiner à la fois les fonctionnalités de la SIM et de la microscopie á nappe de lumière, en tant que preuve de concept, nous avons développé une configuration de microscope simple qui produit une nappe de lumière structurée.

Abstract

Optical fluorescence microscopy is one of the most powerful tools to study cellular structures and molecular events in subcellular level. The resolution of a conventional fluorescence microscope image is diffraction limited which achieves a spatial resolution of 200nm lateral and 500nm axial. Recently, many superresolution fluorescence microscopy techniques have been developed which allow the observation of many biological structures beyond the diffraction limit. Structured illumination microscopy (SIM) is one of them. The principle of SIM is based on using a harmonic light grid which downmodulates the high spatial frequencies of the sample into the observable region of the microscope. The resolution enhancement is highly dependent on the reconstruction technique, which restores the high spatial frequencies of the sample to their original position. Common SIM reconstructions require the perfect knowledge of the illumination pattern. However, to perfectly control the harmonic illumination patterns on the sample plane is not easy in experimental implementations and this makes the experimental setup very technical. Reconstructing SIM images assuming the perfect knowledge of the illumination intensity patterns may, therefore, introduce artifacts on the estimated sample due to the misalignment of the grid that can occur during experimental acquisitions. To tackle this drawback of SIM, in this thesis, we have developed blind-SIM reconstruction strategies which are independent of the illumination patterns. Using the 3D blind-SIM reconstruction strategies we extended the harmonic SIM to speckle illumination microscopy which uses random unknown speckle patterns that need no control, unlike the harmonic grid patterns. For harmonic-SIM images, since incorporating some information about illumination patterns is valuable, we have developed a 3D positive filtered blind-SIM reconstruction which confines the iterative estimation of the illuminations in the vicinity of the Fourier peaks (using carefully designed Fourier filter masks) in the Fourier space. Using blind-SIM reconstruction techniques a lateral resolution of about 100nm and axial resolution of about 200nm is obtained in both speckle and harmonic SIM. In addition, to reduce the out-of-focus problem in widefield images, a simple computational technique which is based on reconstructing 2D data with 3D PSF is developed based on blind-SIM reconstruction. Moreover, to combine the functionalities of SIM and light sheet microscopy, as a proof of concept, we have developed a simple microscope setup which produces a structured light sheet illumination pattern.